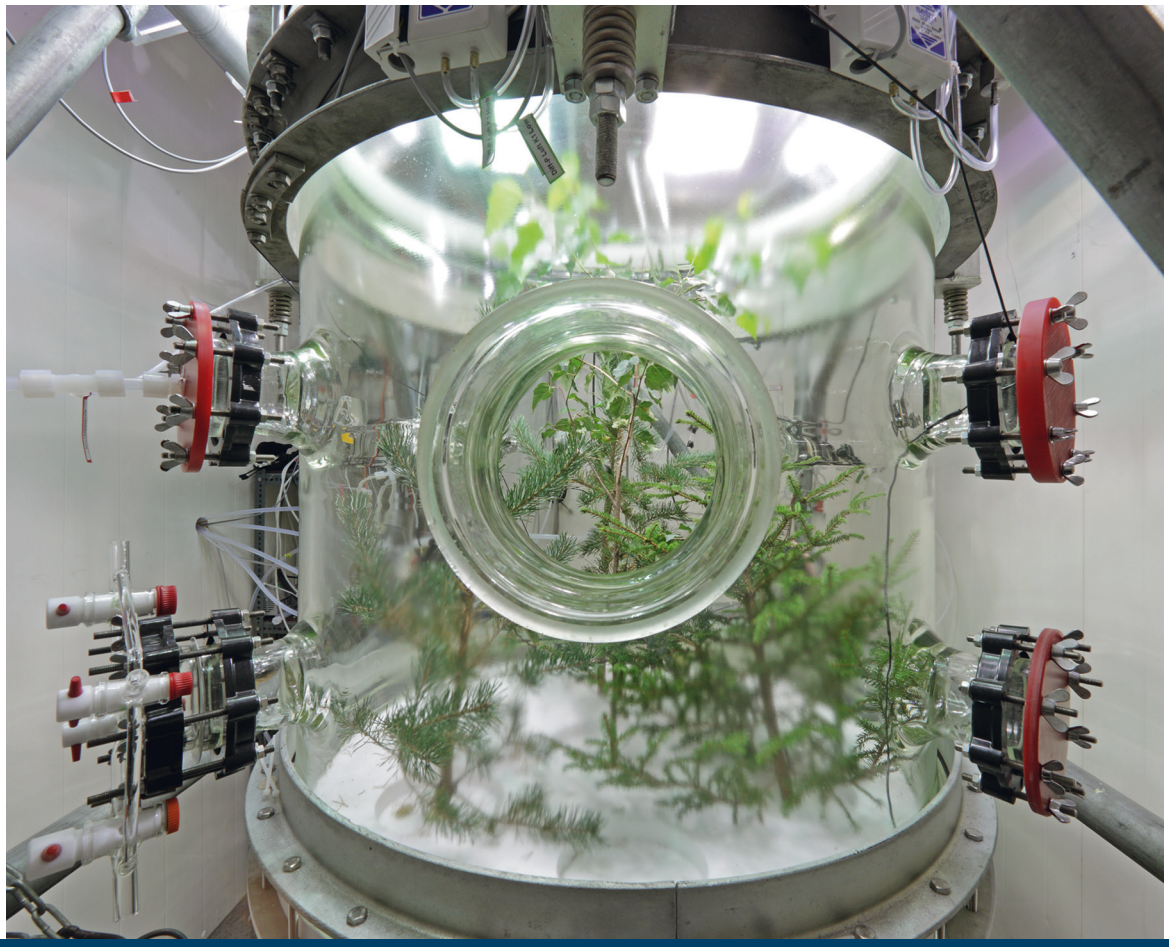

Formation of highly oxygenated organic molecules from α-pinene photochemistry

Sungah Kang

Energie & Umwelt / Energy & Environment
Band / Volume 557
ISBN 978-3-95806-596-3

Mitglied der Helmholtz-Gemeinschaft

JÜLICH
Forschungszentrum

Schriften des Forschungszentrums Jülich
Reihe Energie & Umwelt / Energy & Environment Band / Volume 557

Forschungszentrum Jülich GmbH
Institut für Energie- und Klimaforschung
Troposphäre (IEK-8)

Formation of highly oxygenated organic molecules from α-pinene photochemistry

Sungah Kang

Schriften des Forschungszentrums Jülich
Reihe Energie & Umwelt / Energy & Environment Band / Volume 557

ISSN 1866-1793 ISBN 978-3-95806-596-3

Bibliografische Information der Deutschen Nationalbibliothek.
Die Deutsche Nationalbibliothek verzeichnet diese Publikation in der Deutschen Nationalbibliografie; detaillierte Bibliografische Daten sind im Internet über http://dnb.d-nb.de abrufbar.

Herausgeber und Vertrieb:	Forschungszentrum Jülich GmbH Zentralbibliothek, Verlag 52425 Jülich Tel.: +49 2461 61-5368 Fax: +49 2461 61-6103 zb-publikation@fz-juelich.de www.fz-juelich.de/zb
Umschlaggestaltung:	Grafische Medien, Forschungszentrum Jülich GmbH
Druck:	Grafische Medien, Forschungszentrum Jülich GmbH
Copyright:	Forschungszentrum Jülich 2021

Schriften des Forschungszentrums Jülich
Reihe Energie & Umwelt / Energy & Environment, Band / Volume 557

D 468 (Diss. Wuppertal, Univ., 2021)

ISSN 1866-1793
ISBN 978-3-95806-596-3

Vollständig frei verfügbar über das Publikationsportal des Forschungszentrums Jülich (JuSER) unter www.fz-juelich.de/zb/openaccess.

This is an Open Access publication distributed under the terms of the Creative Commons Attribution License 4.0, which permits unrestricted use, distribution, and reproduction in any medium, provided the original work is properly cited.

Declaration of Authorship

I, Sungah KANG, declare that this thesis titled, "Formation of highly oxygenated organic molecules from α-pinene photochemistry" and the work presented in it are my own. I confirm that:

- This work was done wholly or mainly while in candidature for a research degree at this University.
- Where any part of this thesis has previously been submitted for a degree or any other qualification at this University or any other institution, this has been clearly stated.
- Where I have consulted the published work of others, this is always clearly attributed.
- Where I have quoted from the work of others, the source is always given. With the exception of such quotations, this thesis is entirely my own work.
- I have acknowledged all main sources of help.
- Where the thesis is based on work done by myself jointly with others, I have made clear exactly what was done by others and what I have contributed myself.

Signed:

Date:

Acknowledgements

I owed many thanks to many people. Without their help, this work would not have been possible.

First of all, I would like to thank to Prof. Dr. Thorsten Benter for accepting the supervision of this thesis and being my doctor father.

I would like to thank Prof. Dr. Astrid Kiendler-Scharr for accepting the role of the second examiner of my thesis as well.

In addition, I really appreciate the chance I got to work in IEK-8, Forschungszentrum Jülich by Prof. Dr. Andreas Wahner, Prof. Dr. Astrid Kiendler-Scharr and all their effort to improve PhD life in IEK-8.

I want to thank HiTEC as well for accepting me as a graduate student.

I would never be able to express enough gratitude to my scientific supervisor PD Dr. Thomas F. Mentel. He provided me scientific guidance, discussion, and supervision. Moreover, he always motivated me and trigger my curiosity after discussions. His passion to science (especially to HOM) really motivated me a lot and attracted me to the world of HOM which I never heard before starting my PhD work.

I must mention PD. Dr. Jürgen Wildt. Thank you for reading my thesis for correction even after the retirement. Discussions with him were always inspiring.

I am deeply grateful to Dr. Iida Pullinen and Monika Springer for introducing me to the world of CIMS. I still remember the first ice cream afternoon of the CIMS group.

I appreciate the help from Dr. Cheng Wu and Dr. Defeng Zhao in the beginning of my PhD for scientific discussions and practical supports.

I would like to thank Dr. Sebastian Schmitt and Dr. Georgios Gkatzelis who introduced me to the world of programming. Thank you for being patient teachers and introduce the fun and pain of the coding to me who didn't know programming at all. I really enjoyed and am motivated by the discussion time with you and Dr. Scarlet Stadtler.

I want to thank Silvia Proff for providing model data and her English corrections. It was such a great valuable help.

I am grateful to Dr. Anna Novelli for her valuable corrections and efforts in addition to all fun and cheerful environment.

I want to thanks my precious office mate Marvin Glowania, Vaishali Vardhan, Andreas Paul made my office very pleasant working environment.

I am thankful to Dr. Ralf Tillmann for scientific discussion and his encouragement for writing, running.

There are many colleagues I didn't mention here but my gratitude towards you are in my heart.

Last but not least, thank you for all your support my dear family.

Abstract

Understanding secondary organic aerosols (SOA) is important because of their impact on climate and human health. However, SOA formation mechanisms and SOA precursors are still not very well known. Among the precursors of SOA, highly oxygenated organic molecules (HOM) are considered as a significant contributor to SOA formation. HOM are known to have a high O:C ratio which allows them to have low to extremely low vapour pressures. The high O:C ratio is achieved by a process called autoxidation. Autoxidation comprises a series of intramolecular H-shifts in peroxy radicals followed by O_2 addition while preserving the peroxy functionality.

α-pinene is an important biogenic volatile organic compound. It contributes the largest fraction to monoterpene emissions by plants and it reacts with OH radicals which is the major oxidant during daytime. Therefore, an understanding of α-pinene photooxidation is crucial. In this study, the formation of HOM from oxidation of α-pinene by OH was investigated. HOM were observed by Chemical Ionisation high resolution Time of Flight Mass Spectrometry (CI-ToF-MS). Four factors were varied in the reaction system: OH concentration, CO addition, addition of isoprene as a second organic component, NOx concentration. The variation of [OH] and the addition of CO served to derive mechanistic aspects of the HOM formation, while the isoprene and NOx addition addressed effects of HOM on SOA formation. A detailed analysis of mass spectrometric data was performed at high resolution level and pathways leading to compound families and marker compounds were elaborated.

The HOM concentration increased as the turnover of α-pinene increased. Herein, turnover is defined as the product of rate coefficient, [OH] and [α-pinene]. However, [HOM] and turnover were not related in an linear manner. This is due to the importance of the secondary oxidation of oxidised products such as pinonaldehyde in HOM formation. The similarity of the HOM mass spectra in α-pinene OH oxidation and pinonaldehyde OH oxidation supports these findings.

A high ratio of HO_2/RO_2 was achieved by introducing CO in the system. This resulted in a preference of peroxy radicals to react with HO_2 and form hydroperoxides. In addition, we observed a substantial decrease of the concentration of HOM peroxy radicals and products which require the involvement of alkoxy radicals during their formation. Due to the lower [RO_2], less alkoxy radicals were formed by the reaction of two RO_2 and less accretion products.

The effect of small peroxy radicals on the α-pinene photooxidation was investigated by introducing isoprene to the reaction system. Isoprene addition led to SOA suppression via two factors. Firstly, isoprene effectively scavenged OH because of the twofold higher reactivity of isoprene towards OH radicals compared to α-pinene. Secondly, small peroxy radicals originating from isoprene scavenged larger HOM peroxy radicals from α-pinene leading to less volatile products.

Adding NOx to the reaction system changed a reaction pattern of the α-pinene OH oxidation. HOM organic nitrates accounted for up to 50 % of the HOM monomer signals. In

addition, an increased importance of fragmentation was observed in the presence of NOx, indicated by an increasing concentration of HOM with less than ten C-atoms. These two findings did not affect the SOA mass formation. However, a strong suppression of HOM accretion products resulted in a SOA mass suppression. In addition, the coupling of intramolecular H-shifts in peroxy and alkoxy radicals, the alkoxy-peroxy pathway, explained the high concentration of peroxy radicals even at the very high NOx concentration of up to 72 ppb.

Contents

Declaration of Authorship **iii**

Acknowledgements **v**

Abstract **vii**

1 Introduction **1**
1.1 Highly oxygenated organic molecules . . . 1
1.1.1 Volatile Organic Compounds in the atmosphere . . . 1
1.1.2 Secondary Organic Aerosol (SOA) . . . 1
1.1.3 Highly Oxygenated organic Molecules (HOM) . . . 2
1.2 HOM formation: atmospheric VOC oxidation by OH and O_3 . . . 3
1.2.1 Atmospheric oxidants . . . 3
1.2.2 Classical photochemistry and peroxy radicals . . . 5
1.2.3 Autoxidation and HOM formation . . . 7
1.2.4 Importance of alkoxy radicals . . . 9
1.3 Goals of the thesis . . . 10

2 Experiments and Methods **13**
2.1 Experimental setup . . . 13
2.1.1 Jülich Plant Atmosphere Chamber (JPAC) . . . 13
2.1.2 Experiment descriptions . . . 15
2.2 Chemical Ionisatiton Mass Spectrometer (CIMS) . . . 23
2.2.1 Introduction of the CIMS . . . 23
2.2.2 Calibration of detected HOM . . . 26
2.3 Data Evaluation . . . 28
2.3.1 High resolution peak analysis . . . 28
2.3.2 CIMS analyzer . . . 32
2.3.3 Families and markers . . . 32
2.3.4 Kendrick mass defect plot . . . 35
2.4 Corrections and assumptions . . . 37
2.4.1 Corrections for turnover and particle surface in NOx experiments . . . 37
2.4.2 Assumptions . . . 39

3 Photochemical oxidation of α-pinene: Dependency on OH concentration and effect of CO and small peroxy radicals **41**
3.1 Ozonolysis of α-pinene . . . 41
3.1.1 Mass spectrum of α-pinene ozonolysis . . . 42
3.1.2 Comparison of mass spectra of α-pinene ozonolysis in different experiments . . . 43
3.2 Photochemical oxidation of α-pinene: Dependency on OH concentration . . . 43
3.2.1 Effect of increasing turnover on the concentration of sum of HOM, monomers and accretion products . . . 46
3.2.2 Changes of families with increasing turnover . . . 48
3.2.3 Closer look into families: Marker analysis . . . 58
C_{10} peroxy radical marker analysis . . . 58
C_{20} marker analysis . . . 60
C_{10} marker analysis . . . 64
3.3 Photochemical oxidation of α-pinene: Effect of CO . . . 68
3.3.1 Mass spectrum comparison . . . 71
3.3.2 Monomer and accretion product comparison . . . 71
3.3.3 The effect of CO on C_{10} and C_{20} families . . . 72
3.3.4 The effect of CO on C_{10} and C_{20} marker compounds . . . 74
C_{10} peroxy radicals . . . 74
C_{20} marker compounds . . . 76
C_{10} marker compounds . . . 79
3.4 Photochemical oxidation of α-pinene: Effect of isoprene . . . 82

4 Photochemical oxidation of α-pinene: Impact of NOx **89**
4.1 Monomer HOM pattern change . . . 89
4.2 Fragmentation . . . 93
4.3 Accretion product suppression . . . 97
4.4 Alkoxy-peroxy pathway . . . 101
4.5 Family analysis . . . 105
4.6 Concluding the effect of NOx on α-pinene photooxidation . . . 110

5 Summary, conclusion and outlook **113**

Bibliography **119**

A Peaklists **127**
A.1 α-pinene OH oxidation . . . 127
A.2 α-pinene OH oxidation in the presence of CO . . . 127
A.3 α-pinene OH oxidation in the presence of isoprene . . . 127
A.4 α-pinene OH oxidation in the presence of NOx . . . 127

B CIMS analyzer **151**
B.1 CIMS analyzer 151

C Abbreviation **155**

List of Figures

1.1 Schematics of BVOC oxidation overview 6
1.2 Schematic illustration of autoxidation 8
1.3 Euler diagram of HOM and its relation to peroxy radical isomerisation products and relevant volatility classes 9

2.1 Schematic of JPAC 13
2.2 Time series of the j(O^1D) experiment for α-pinene OH oxidation 17
2.3 Time series of the CO experiment for α-pinene OH oxidation 19
2.4 Time series of the isoprene experiment for α-pinene OH oxidation 20
2.5 Time series of a NOx experiment for α-pinene OH oxidation 22
2.6 Schematics of Atmospheric Pressure interface Time-of-Flight Mass Spectrometer 24
2.7 Schematics of NO_3^- chemical ionisation inlet 25
2.8 Time series the summed signal of $^{14}NO_3^-$, $^{15}NO_3^-$, and their clusters in the NOx experiments 26
2.9 H_2SO_4 calibration 28
2.10 Peak shape 29
2.11 Peak width function 30
2.12 A high resolution peak fitting example 31
2.13 The map of the oxidation of α-pinene 34
2.14 Classification of products from α-pinene ozonolysis 35
2.15 The Kendrik mass defect plot for α-pinene photooxidation. 36
2.16 HOM versus turnover 38

3.1 Typical mass spectrum of α-pinene ozonolysis. 42
3.2 Comparison mass spectra observed during α-pinene ozonolysis phases. 44
3.3 Mass spectra observed at different OH concentrations in "j(O^1D)" experiment . . 45
3.4 The sum of HOM, monomers, and accretion products as a function of turnover. . 47
3.5 The sum of monomers normalised to total ion counts vs turnover 48
3.6 The sum of signal of accretion products normalised to total ion counts vs turnover 49
3.7 Model simulation of HO_2 radicals and RO_2 radicals concentration as a function of turnover. 50
3.8 Model simulation of $C_{10}H_{17}O_3$ and $C_{10}H_{15}O_4$ as a function of turnvoer 51
3.9 Turnover vs C_{10} families. 52
3.10 Turnover vs C_{20} families. 55

3.11 Overlapped mass spectrum of α-pinene ozonolysis, α-pinene OH oxidation and pinonaldehyde OH oxidation. 57
3.12 The normalised signal of family members of $C_{10}H_{15}O_z$ and $C_{10}H_{17}O_z$ vs turnover 59
3.13 The normalised signal C_{20} accretion product family as a function of turnover . . 61
3.14 The normalised signal of the C_{10} monomer families as a function of turnover . . 65
3.15 Bar graph of modeled HO_2 and RO_2 concentration 70
3.16 Mass spectrum comparison of two experiment with at similar turnover with and without CO 71
3.17 Bar graph of monomer and accretion products and its fragmentation for the comparison 72
3.18 Bar graph of C_{10} monomer families and C_{20} accretion product families 73
3.19 Bar graph of $C_{10}H_{15}O_z$ peroxy radical family members 75
3.20 Bar graph of $C_{20}H_{30}O_z$ accretion product family members 76
3.21 Bar graph of $C_{20}H_{32}O_z$ accretion product family members 77
3.22 Bar graph of $C_{20}H_{34}O_z$ accretion product family members 78
3.23 Bar graph of $C_{10}H_{14}O_z$, $C_{10}H_{16}O_z$ and $C_{10}H_{18}O_z$ family members 80
3.24 HOM monomer and accretion products distribution with and without isoprene . 83
3.25 Time dependence of sum of products with different carbon atoms 85
3.26 Relative contributions of HOM monomers and accretion products with different number of carbon in the molecule 87

4.1 Four mass spectra at different NOx concentration in the system 90
4.2 The relative intensities of HOM according to termination functional groups as a function of steady state NOx concentration 91
4.3 Effective uptake coefficients γ_{eff} for HOM-PP and HOM-ON 92
4.4 The normalised signal of monomer and accretion products and HOM resulting from fragmentation as function of NOx 94
4.5 Monomers and accretion products with fractions that went through fragmentation processes as a function of NOx 95
4.6 Mass concentration of monomers ($C_{5\text{-}10}$) and accretion products($C_{11\text{-}20}$) as a function of NOx 96
4.7 Mass spectra observed in the oxidation of α-pinene by OH at 0.3 ppb background NOx and 26 ppb NOx in steady state 98
4.8 O:C ratio of α-pinene photooxidation products with and without additional NOx 100
4.9 Reaction scheme of alkoxy-peroxy pathway 102
4.10 The normalised signal of peroxy radicals as a function of NOx 103
4.11 Oxygen based mass defect plot of both NOx and no NOx systems 104
4.12 The normalised signal of C_{10} and C_{20} families as a function of NOx 106
4.13 The normalised signal of family members of $C_{10}H_{15}O_z$ family and $C_{10}H_{17}O_z$ family as a function of NOx 107

4.14 Modeled HO_2 radicals and RO_2 radicals as a function of NOx 109

B.1 CIMS analyzer 153
B.2 High resolution stick mass spectrum 154

List of Tables

2.1 Experimental conditions for α-pinene photooxidation 16

A.1 Peaklist from α-pinene OH oxidation. 128
A.2 Peaklist from α-pinene OH oxidation (Continued). 129
A.3 Peaklist from α-pinene OH oxidation (Continued). 130
A.4 Peaklist from α-pinene OH oxidation (Continued). 131
A.5 Peaklist from α-pinene OH oxidation in the presence of CO. 132
A.6 Peaklist from α-pinene OH oxidation in the presence of CO (Continued). 133
A.7 Peaklist from α-pinene OH oxidation in the presence of CO (Continued). 134
A.8 Peaklist from α-pinene OH oxidation in the presence of CO (Continued). 135
A.9 Peaklist from α-pinene OH oxidation in the presence of Isoprene. 136
A.10 Peaklist from α-pinene OH oxidation in the presence of Isoprene (Continued). . . 137
A.11 Peaklist from α-pinene OH oxidation in the presence of Isoprene (Continued). . . 138
A.12 Peaklist from α-pinene OH oxidation in the presence of Isoprene (Continued). . . 139
A.13 Peaklist from α-pinene OH oxidation in the presence of NOx. 140
A.14 Peaklist from α-pinene OH oxidation in the presence of NOx (Continued). 141
A.15 Peaklist from α-pinene OH oxidation in the presence of NOx (Continued). 142
A.16 Peaklist from α-pinene OH oxidation in the presence of NOx (Continued). 143
A.17 Peaklist from α-pinene OH oxidation in the presence of NOx (Continued). 144
A.18 Peaklist from α-pinene OH oxidation in the presence of NOx (Continued). 145
A.19 Peaklist from α-pinene OH oxidation in the presence of NOx (Continued). 146
A.20 Peaklist from α-pinene OH oxidation in the presence of NOx (Continued). 147
A.21 Peaklist from α-pinene OH oxidation in the presence of NOx (Continued). 148
A.22 Peaklist from α-pinene OH oxidation in the presence of NOx (Continued). 149

Chapter 1

Introduction

1.1 Highly oxygenated organic molecules

1.1.1 Volatile Organic Compounds in the atmosphere

The Earth's atmosphere is an absolutely necessary component for life in earth. A dry atmosphere consist of 78.08 % of nitrogen (N_2), 20.90 % of oxygen (O_2), 0.93 % of Argon and 0.09 % of trace gas. In addition to gases, liquids and solids are present in the atmosphere. The chemical processing of gases plays a pivotal role in the removal of reactive trace gases by changing chemical, physical properties of the gases. Moreover, the gas phase chemistry affects the particle phase because of the interaction between gas phase and particle phase. Among reactive trace gases, Volatile Organic Compounds (VOCs) are key species in atmospheric chemistry with high vapor pressures. They are emitted by vegetation (Biogenic sources, BVOC) or generated by human activities (Anthropogenic sources, AVOC) (Kroll and Seinfeld, 2008). BVOC are composed of unsaturated hydrocarbons (isoprene, monoterpenes, sesquiterpenes) and oxygenated VOC such as acetone, methanol and formaldehyde (Atkinson and Arey, 2003). AVOC consist of compounds that result from vehicle emission, petrochemical sources, and solvent use. Recently, urban volatile chemical products such as personal care products, coatings or paints were realised as an important source of urban VOC (McDonald *et al.*, 2018; Shah *et al.*, 2019). On a global scale, BVOC emissions are about 10 times higher than AVOC. However, AVOC can be made up to 50 % of VOC emissions in urban areas (Atkinson and Arey, 2003; Guenther *et al.*, 2012). Both, AVOC and BVOC are important for secondary organic aerosol formation.

1.1.2 Secondary Organic Aerosol (SOA)

Atmospheric aerosols are a relatively stable suspension of solid or liquid particles in the air. Aerosol particles occur in a range of sizes with diameters from several nanometers to several ten micrometers. Chemically, atmospheric aerosols consists of inorganic and organic components. About 20-90 % of the submicron aerosols consist of organic components (Jimenez *et al.*, 2009; Zhang *et al.*, 2007; Hallquist *et al.*, 2009). Organic Aerosol (OA) can be divided into Primary Organic Aerosol (POA) and Secondary Organic Aerosol (SOA). The POA is emitted

directly from fossil fuel and biomass combustion while the SOA is formed by chemical processes from organic precursors. SOA can be formed by nucleation or precursors condensing on the existing particles, which can be composed of organic and inorganic components. Understanding SOA and its formation is important because of its impact on human health, climate, solar radiation and cloud formation (Hadley, Baumgartner, and Vedanthan, 2018; Landrigan *et al.*, 2018; Riipinen *et al.*, 2011; Jokinen *et al.*, 2015; Roldin *et al.*, 2019). For instance, aerosol particles scatter and absorb the light depending on their size and chemical composition and effect on radiation budget. SOA has a cooling impact on the Earth and compensate the global warming due to the green house gases (Stocker *et al.*, 2013).

The major source of the submicron organic aerosol is OVOC from atmospheric oxidation of VOCs (Hallquist *et al.*, 2009). The origin of those VOCs can be both anthropogenic and biogenic. In urban area, anthropogenic sources can be responsible for SOA formation (De Gouw and Jimenez, 2009; Zhang *et al.*, 2015). However, biogenic originated SOA accounts for the largest fraction of SOA (Spracklen *et al.*, 2011; Shilling *et al.*, 2013; Hoyle *et al.*, 2011). In spite of the massive study about SOA formation, its formation mechanism and the chemical composition is not fully understood.

Sulfuric acid is considered as a driving component of New Particle Formation (NPF, Kulmala *et al.*, 2004; Weber *et al.*, 1996; Sipilä *et al.*, 2010). However, additional vapours are required for the growth of newly formed particles to the Cloud Condense Nuclei (CCN) size (Kulmala *et al.*, 2013; Metzger *et al.*, 2010; Donahue *et al.*, 2012a; Ehn *et al.*, 2012; Ehn *et al.*, 2014; Paasonen *et al.*, 2010; Riipinen *et al.*, 2012). Several studies showed that Highly Oxygenated organic Molecules (HOM) contribute significantly to the particle growth (Ehn *et al.*, 2012; Ehn *et al.*, 2014; Riipinen *et al.*, 2012; Zhao *et al.*, 2015; Jokinen *et al.*, 2015; Ostrom *et al.*, 2017).

Due to the low to extremely low volatility of HOM, they condense on particles irreversibly. Ehn *et al.*, 2014 showed similar oxygen : carbon (O:C) and hydrogen : carbon (H:C) ratios in the gas phase and particle phase in accordance with HOM accounting for a substantial mass fraction of SOA. Additionally, HOM can be an important component in new particle formation (Paasonen *et al.*, 2010; Schobesberger *et al.*, 2013; Ehn *et al.*, 2014; Jokinen *et al.*, 2015; Tröstl *et al.*, 2016; Bianchi *et al.*, 2016; Riccobono *et al.*, 2014; Roldin *et al.*, 2019; Kirkby *et al.*, 2016). C_{10} monomers from α-pinene ozonolysis (and OH oxidation) have a higher volatility than previously thought and accretion products play a more prominent role in nucleation (Tröstl *et al.*, 2016; Kurtén *et al.*, 2016; Frege *et al.*, 2018).

1.1.3 Highly Oxygenated organic Molecules (HOM)

Oxidation of VOC produces classical Oxygenated Volatile Organic Compounds (OVOC) as e.g. described and predicted in the Master Chemical Mechanism (MCM v3.3.1, Saunders *et al.*, 2003). However, those compounds have too high volatility to participate in the particle formation. Therefore, less volatile compounds with higher oxidation degrees are needed to explain the observed particle growth rates and secondary organic aerosol formation.

It was proposed that lower volatility could be obtained by sequential oxidation (higher degree of oxidation) or oligomerisation of OVOCs (higher molecular weight) (Hallquist *et al.*, 2009). However, these processes are too slow and too diverse to explain the fast particle formation rate. New insights were provided by the development of Atmospheric Pressure interface Time of Flight Mass Spectrometer (APi-ToF-MS, Junninen *et al.*, 2010). Ehn *et al.*, 2012; Ehn *et al.*, 2014 found a group of molecules called Highly Oxygenated organic Molecules (HOM) with extremely low volatility. HOM have high O:C ratio and high molecular masses. For example, α-pinene ozonolysis fastly produces HOM products (Kurtén *et al.*, 2015; Jokinen *et al.*, 2014; Ehn *et al.*, 2014; Mentel *et al.*, 2015; Molteni *et al.*, 2019; Berndt *et al.*, 2015). Mentel *et al.*, 2015 proposed the vinylhydroperoxide path in ozonolysis as a starting point of HOM formation. Autoxidation (H-shift in peroxy radicals followed by O_2 addition) was investigated for OH oxidation of α-pinene (Peeters, Vereecken, and Fantechi, 2001; Crounse *et al.*, 2013; Vereecken, Müller, and Peeters, 2007; Berndt *et al.*, 2016; Zhao *et al.*, 2015; Kristensen *et al.*, 2014; Donahue *et al.*, 2012b). As HOM are highly functionalised, as one can see from high O:C ratio and usually multiple hydroperoxides, (Rissanen *et al.*, 2014; Berndt *et al.*, 2016), their vapour pressures are low or even extremely low. This is because of the increase of molecular mass and the ability to make multiple hydrogen bonding (Kroll *et al.*, 2011). Autoxidation which is a key process for HOM formation will be introduced in more detail in Chapter 1.2.3. Due to their low volatility, HOM play an important role in the formation of secondary organic aerosol (SOA) (Ehn *et al.*, 2014; McFiggans *et al.*, 2019).

1.2 HOM formation: atmospheric VOC oxidation by OH and O_3

1.2.1 Atmospheric oxidants

VOCs are oxidised in the atmosphere by oxidants such as hydroxyl radicals (OH), ozone (O_3), and nitrate radical (NO_3). The OH radicals and O_3 are the major daytime oxidants while the NO_3 radicals and O_3 are major oxidants in nighttime chemistry of VOCs (Finlayson-Pitts and Pitts Jr, 1999).

Tropospheric O_3 is mainly formed by the photolysis of NO_2.

$$\begin{aligned} &\mathrm{NO_2} + h\nu\,(\lambda < 420\,\mathrm{nm}) \longrightarrow \mathrm{O(^3P)} + \mathrm{NO} \\ &\mathrm{O(^3P)} + \mathrm{O_2} \xrightarrow{\mathrm{M}} \mathrm{O_3} \end{aligned} \qquad \text{R1.2.1}$$

A major source of OH radicals is the photolysis reaction of O_3 in both, clean remote and polluted urban areas.

$$\mathrm{O_3} + h\nu\,(\lambda < 340\,\mathrm{nm}) \longrightarrow \mathrm{O(^1D)} + \mathrm{O_2} \qquad \text{R1.2.2}$$

$$O(^1D) + H_2O \longrightarrow 2\,OH \qquad \text{R1.2.3}$$

Photolysis of O_3 produces electronically excited oxygen atoms (O^1D). OH radicals are formed when O^1D react with atmospheric water vapor before they are quenched by collisions with N_2 and O_2 molecules. A source of OH radicals in polluted areas is photo-dissociation of nitrous acid (HONO) as a major channel and hydrogen peroxide as a minor channel (H_2O_2).

$$HONO + hv\,(\lambda < 370\,nm) \longrightarrow OH + NO \qquad \text{R1.2.4}$$

$$H_2O_2 + hv\,(\lambda < 370\,nm) \longrightarrow 2\,OH \qquad \text{R1.2.5}$$

Another important chemical source of OH is the reaction of HO_2 with NO when the nitrogen oxides (NOx = NO + NO_2) concentration is high.

$$HO_2 + NO \longrightarrow OH + NO_2 \qquad \text{R1.2.6}$$

The reaction of O_3 with alkenes is a source of nighttime OH radicals (Finlayson, Pitts Jr, and Akimoto, 1972).

The rate coefficients of O_3 with alkenes are several orders of magnitude slower than those of OH radicals. However, ozonolysis is important because of the higher concentration of O_3 compared to OH radicals. O_3 has a selectivity for C-C double bonds (Finlayson-Pitts and Pitts Jr, 1999) since O_3 can only react with C-C double bond, unlike OH radicals. Breaking the double bond produces aldehydes or ketones on one end and Criegee Intermediates (CI) on the other, whereby substitution of the double bond determines the formation of CI or carbonyl (Criegee, 1975). CI can undergo further reactions including the vinylhydroperoxide pathway which produces radicals with mesomeric structures. Addition of O_2 result in the formation of peroxy radicals (Johnson and Marston, 2008; Vereecken and Francisco, 2012). Peroxy radicals from the vinylhydroperoxide pathway play a critical role in HOM formation (Mentel *et al.*, 2015).

Unlike ozonolysis, OH radicals have no selectivity towards the C-C double bond (in the sense that OH radical can oxidise molecules without C-C double bond). As a result, OH radicals can attack the molecule multiple times. There are two possibilities for the initial step of OH oxidation. One is electrophilic addition to the double bond and the other one is hydrogen atom abstraction resulting in an alkyl radical and H_2O. For example the BVOC α-pinene reacts in the the first step to 92.5 % by OH radical addition to the double bond and to 7.5 % by hydrogen abstraction (MCM v3.3.1, Saunders *et al.*, 2003). OVOC products can be further attacked by OH via H-abstraction leading to chemical aging and producing higher O:C ratios.

1.2.2 Classical photochemistry and peroxy radicals

The peroxy radicals (RO_2) formed in ozonolysis and OH oxidation are key components in atmospheric chemistry. They can undergo many further reactions. The lifetime and the fate of RO_2 highly depend on the relative mixing ratios of the reaction partners. Most important, a high or a low concentration of NOx changes the product pattern significantly. NO concentration can be as high as 200 ppb which is measured at rush hour in New York (Ren *et al.*, 2003), and as low as 20 ppt which is measured in Amazon forest (Lelieveld *et al.*, 2008).

At the low NOx regime, peroxy radicals react mainly with HO_2 and other RO_2 radicals forming hydroperoxides (R1.2.7), ketones and alcohols (R1.2.8).

$$\mathrm{RO_2 + HO_2 \longrightarrow ROOH + O_2} \qquad \text{R1.2.7}$$

$$\mathrm{RO_2 + RO_2 \longrightarrow R_H{=}O + R{-}OH + O_2} \qquad \text{R1.2.8}$$

In addition, the recombination of two peroxy radicals can lead to the formation of oligomers called dimers or accretion products. As recently shown by Berndt *et al.*, 2018b, this pathway is more likely for functionalised peroxy radicals (R1.2.9).

$$\mathrm{RO_2 + RO_2 \longrightarrow ROOR + O_2} \qquad \text{R1.2.9}$$

The reaction between two peroxy radicals can produce not only closed shell products but also alkoxy radicals (R1.2.10).

$$\mathrm{RO_2 + RO_2 \longrightarrow RO\cdot + O_2} \qquad \text{R1.2.10}$$

In the presence of NOx, other pathways gain more importance. Peroxy radicals react fastly with NO and form organic nitrates (R1.2.11) and alkoxy radicals (R1.2.12).

$$\mathrm{RO_2 + NO \longrightarrow RO_2NO} \qquad \text{R1.2.11}$$

$$\mathrm{RO_2 + NO \longrightarrow RO + NO_2} \qquad \text{R1.2.12}$$

If the peroxy radicals are acyl peroxy radicals, they react with NO_2 and form peroxy acyl nitrates (PAN)-like organic nitrates (R1.2.13).

$$\mathrm{R(=O)O_2 + NO_2 \longrightarrow RO_2NO_2} \qquad \text{R1.2.13}$$

Figure 1.1 shows an overview of the oxidation of BVOC by O_3 and OH.

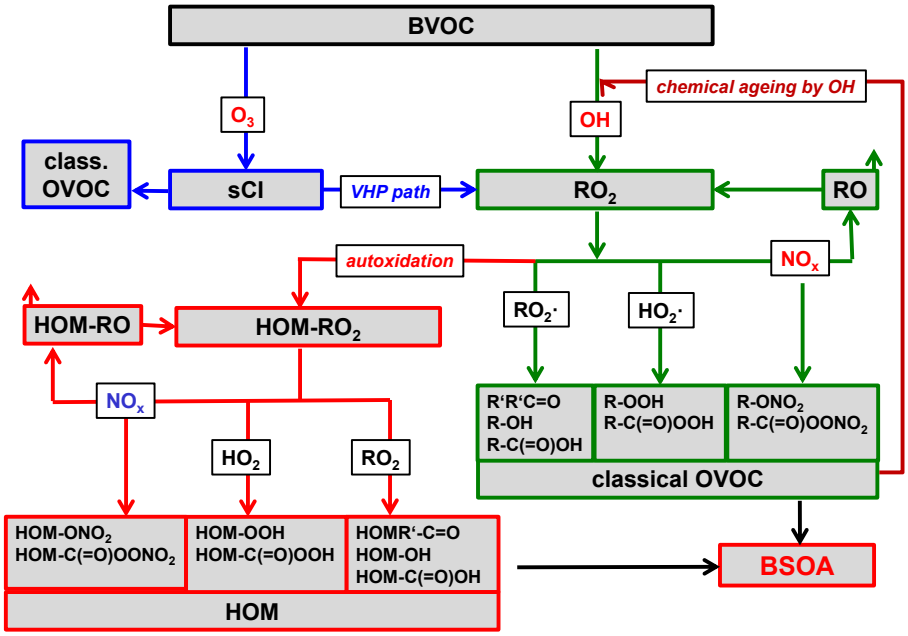

Figure 1.1: Reaction pathways of BVOC oxidation by O_3 and OH radicals. Blue boxes show a simplified ozonolysis path and green boxes show classical photochemical reactions that result in various closed-shell products (classical OVOC). These products can condense on particles if their volatility is sufficiently low. Red boxes represent a new class of highly oxygenated organic molecules which are connected to classical photochemistry by the process called autoxidation involving highly oxygenated peroxy radicals (HOM-RO_2).

Blue boxes in Figure 1.1 show a simplified ozonolysis pathway via stabilised Criegee Intermediates (sCI) resulting in classical Oxygenated Volatile Organic Compounds (OVOCs) after several reaction steps. sCI can form peroxy radicals by the vinylhydroperoxide pathway (VHP path, Johnson and Marston, 2008; Vereecken and Francisco, 2012).

Peroxy radicals (RO_2) are produced by the oxidation of BVOC by OH as shown in the green boxes in Figure 1.1. The RO_2 react with the various reaction partners such as other RO_2, HO_2 and NOx. The actual branching ratio for each reaction channel is dependent on the conditions of the system, e.g., by relative mixing ratios of RO_2, HO_2 and NOx (Orlando and Tyndall, 2012). At low NOx conditions, reactions with RO_2 and HO_2 are dominant and produce ketones (RR′C=O), hydroperoxides (R-OOH), alcohols (R-OH), carboxylic acids (R-C(=O)OH), and percarboxylic acids (R-C(=O)OOH). However, when the concentration of NOx is high, reactions leading to organic nitrates (R-ONO_2) or PAN-like compounds (R-C(=O)$OONO_2$) become prominent. The reaction of RO_2 with NO also produces alkoxy radicals (RO). According

to MCM v3.3.1, the RO_2 + NO reaction generates alkoxy radicals with yields up to 70 %. Yet, the importance of alkoxy radicals has been somewhat overlooked in HOM formation. Therefore, the importance of alkoxy radical and its potential role in the HOM formation is a topic of this thesis. The importance of alkoxy radicals will be introduced in Chapter 1.2.4.

RO_2 react along classical reaction pathways and form closed-shell products with low degree of oxidation. However, these compounds are often too volatile to effectively condense on the particle. Recently, HOM were recognised as important source of particle formation and growth by organic compounds. HOM are formed by a process called autoxidation under atmospheric conditions (Crounse *et al.*, 2012; Crounse *et al.*, 2013; Ehn *et al.*, 2014; Mentel *et al.*, 2015). Autoxidation will be explained in the next section.

1.2.3 Autoxidation and HOM formation

Autoxidation is defined as the process in which a peroxy radical first undergoes an intramolecular hydrogen-atom shift forming hydroperoxide and an alkyl radical. Molecular oxygen rapidly attaches to alkyl radical and a new peroxy radical with higher oxidiation degree is formed (Crounse *et al.*, 2012; Crounse *et al.*, 2013; Bianchi *et al.*, 2019). Autoxidation allows for the fast formation of peroxy radicals with high O:C ratios (O:C > 1). One can assume that HOM-RO_2 undergo the same classical termination reactions to form closed-shell products as other RO_2 (Bianchi *et al.*, 2019). The difference between HOM-RO_2 and RO_2 is that HOM-RO_2 form closed-shell products with a high O:C ratio (HOM) which will condense effectively on the existing particles or even form new particles with higher chances than classical OVOC.

HOM formation (red boxes in Figure 1.1) is connected with the classical OVOC photooxidation scheme by autoxidation. Autoxidation is well known in combustion chemistry but was only recently recognised as an important process in atmospheric chemistry (Crounse *et al.*, 2012; Crounse *et al.*, 2013; Ehn *et al.*, 2014; Rissanen *et al.*, 2014; Mentel *et al.*, 2015). Autoxidation steps can occur several times until all abstractable H-atoms are consumed and the resulting HOM-RO_2 is terminated as a stable closed-shell HOM product. The process is illustrated in Figure 1.2. The presence of functional groups near the peroxy radical or the shifted H-atom lowers the barrier height of H-shift (Crounse *et al.*, 2013; Møller *et al.*, 2020; Otkjær *et al.*, 2018; Vereecken and Nozière, 2020).

Ehn *et al.*, 2014 showed the importance of autoxidation for HOM formation. However, highly oxygenated organic molecules could include a broad range of compounds without specific criteria. Bianchi *et al.*, 2019 suggest key criteria to define atmospheric relevant HOM. 1) The formation process should be engaged with organic peroxy radicals involving autoxidation. 2) HOM are formed at atmospheric relevant conditions. 3) HOM typically contain six or more oxygen atoms.

Figure 1.3 shows the relation of HOM with peroxy radical isomerisation products and various volatility classes. HOM include compounds that belong to ELVOC and LVOC. Not all

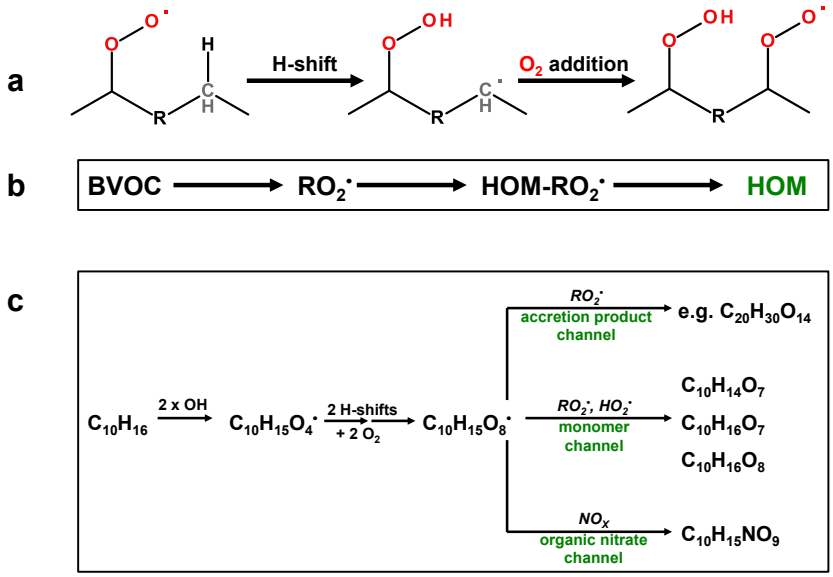

Figure 1.2: Schematic illustration of HOM formation adapted and modified form Ehn *et al.*, 2014. Panel a shows the process hydrogen shift and oxygen molecule addition at the alkyl radical cite. Panel b shows a general scheme of formation of HOM and panel c shows the mechanism for the oxidation of α-pinene by OH specifically (include secondary oxidation of OVOC).

peroxy radical isomerisation products are HOM. However, this classification is rather a suggestion than a rule, and a precise and clean separation needs more studies.

Ozonolysis of alkenes can in general produce HOM by peroxy radical formation and autoxidation via the vinyl hydroperoxide pathway. Ehn *et al.*, 2014 showed the role of HOM formed by ozonolysis of α-pinene in SOA formation. In addition, many studies showed that the reaction of VOC with O_3 can produce HOM (Ehn *et al.*, 2012; Jokinen *et al.*, 2014; Mentel *et al.*, 2015; Berndt *et al.*, 2015; Rissanen *et al.*, 2015; Hyttinen *et al.*, 2015; Zhang *et al.*, 2017).

As mentioned before, Mentel *et al.*, 2015 proposed a detailed mechanism for ozonolysis based HOM formation at the example of cyclic alkenes. First, ozonolysis of the endocyclic double bond leads to ring opening and results in a sCI at one end and a carbonyl group at the other end. The sCI can form a vinyl hydroperoxide which decomposes and produces an oxo-alkyl radical (with mesomeric structures). Finally, the addition of molecular O_2 produces a peroxy radical which can undergo autoxidation and HOM formation.

Unlike for ozonolysis, fewer studies show the HOM formation from OH oxidation (Berndt *et al.*, 2016; Pye *et al.*, 2019). This is because OH oxidation is less specific than ozonolysis since

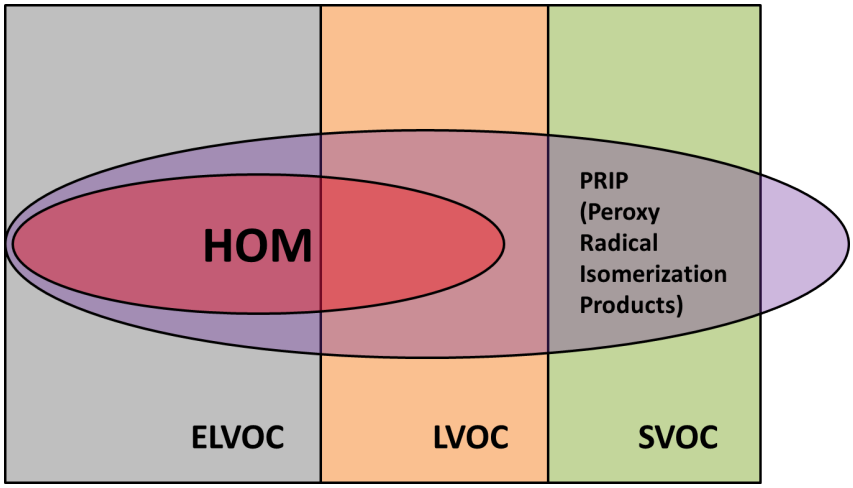

Figure 1.3: Euler diagram of HOM and relation to peroxy radical isomerisation products and relevant volatility classes. HOM is part of peroxy radical isomerisation products (PRIP). HOM partially consists of extremely low volatile organic compounds (ELVOC) and partially consists of low volatile organic compounds (LVOC). Figure adapted from Bianchi *et al.*, 2019.

OH can attack double bonds and also abstract hydrogens to form radicals. In addition, sequential oxidation is possible by OH and this makes the elucidation of the HOM formation mechanism initiated by OH difficult. However, it is important to understand the HOM formation by oxidation of VOC by OH in order to explain particle formation and a substantial amount of SOA mass during daytime (Kulmala *et al.*, 2013).

1.2.4 Importance of alkoxy radicals

Alkoxy radicals are intermediates in the atmospheric degradation of VOCs. Various oxidants can attack VOCs and form alkyl radicals. By the addition of O_2, peroxy radicals are formed and react with NO, HO_2, and RO_2. Each of those reactions can be a source of alkoxy radicals. In addition, the photolysis of hydroperoxides provides a minor contributes to alkoxy radical formation.

$$RO_2 + NO \longrightarrow RO + NO_2 \qquad \text{R1.2.14}$$

$$RO_2 + R'O_2 \longrightarrow RO + R'O + O_2 \qquad \text{R1.2.15}$$

$$RO_2 + HO_2 \longrightarrow RO + OH + O_2 \qquad \text{R1.2.16}$$

$$\mathrm{ROOH} + hv \longrightarrow \mathrm{RO} + \mathrm{OH} \qquad \text{R1.2.17}$$

By which path alkoxy radicals are formed depends on the relative abundance of the reaction partners.

After being formed, alkoxy radicals have three possible pathways. The first one is the reaction with O_2, the second one is isomerisation (H-migration), and the third one is decomposition. The fate and the relative reaction coefficients are highly dependent on structure and substitution of the alkoxy radicals (Vereecken and Peeters, 2010). Even for two alkoxy radicals sharing the same carbon skeleton (isomers), the branching ratio between the pathways can be significantly dissimilar (Carrasquillo *et al.*, 2014).

Reaction with O_2 occurs by the abstraction of a hydrogen atom from the alkoxy site with the generation of an HO_2 radical and a carbonyl compound. This reaction is more frequent in short chained alkoxy radicals (Finlayson-Pitts and Pitts Jr, 1999). Typical reaction coefficients are in a range of 3-8 $\times$ 10^4 s^{-1} for nearly all alkoxy radicals in typical atmospheric condition.

Vereecken and Peeters, 2010 showed that the H-migration is sensitive to geometry, substitution, and structure. The most important unimolecular rearrangement is 1,5-H-migration (Vereecken and Peeters, 2010). This will result in an OH group and an alkyl radical site in or directly in a peroxy radical when the H-atom is abstracted from a hydroperoxide group. The alkyl radical becomes a peroxy radical by adding an oxygen molecule. The peroxy radicals can undergo autoxidation or termination reactions and become closed-shell products. If the peroxy radicals which were formed by the rearrangement of alkoxy radicals undergo autoxidation and this is called the alkoxy peroxy path. It will be shown in this thesis that the alkoxy peroxy path plays an important role especially when massive amounts of alkoxy radicals are formed by the reaction of RO_2 and NO.

Since alkoxy radicals contain excessive energy and are highly unstable, they can undergo fragmentation e.g. by α-bond scission as well. This results in molecules with smaller carbon numbers such as C_7, C_8 and C_9 in the case of α-pinene. Fragmentation can be thus a very important indicator to investigate the involvement of alkoxy radicals. Like H-migration, the rate of decomposition is highly dependent on the structure and substitution of the alkoxy radicals. Vereecken and Peeters, 2009 showed that especially the substitution at the α- and β- carbon on either side of the breaking C-C bond affects the decomposition rate of alkoxy radicals significantly.

1.3 Goals of the thesis

The task of the thesis is to investigate HOM formation under different chemical regimes. Among monoterpenes, α-pinene is chosen in this work because it is one of the most abundantly emitted species (34 % of global emission, Sindelarova *et al.*, 2014). In addition, α-pinene oxidation by OH radical has been only rarely studied.

In this study, the chemical environment was varied by modifying the OH source strength and by adding other components to shift the peroxy radical chemistry: CO, isoprene, and NOx. The major work is the detailed evaluation of high-resolution mass spectra with chemical ionisation by the nitrate reagent ion for all four regimes. The advantage of NO_3^--CIMS is that it is highly selective for HOM with about uniform sensitivity (Hyttinen *et al.*, 2015). The goal of the thesis is to classify the detected HOM in families and investigate the formation of the HOM families and specific HOM molecules (markers) along with the current understanding of the chemistry of peroxy radicals. Herein, the Master Chemical Mechanism (MCM v 3.3.1.) served as a guideline. However, since MCM v3.3.1 does not contain the most updated mechanisms, e.g. HOM chemistry, the results of the thesis will serve as a basis for future detailed mechanism development of HOM formation. The thesis will present a semi-quantitative mechanistic understanding of HOM formation and its reflection in SOA formation. The focus lies on the role of second step oxidation, accretion product formation, and the possible role of alkoxy radicals in autoxidation processes.

This will be presented as follows.

1. The dependency of HOM formation on the OH radical concentration and its product pattern change will be investigated. This will provide more detailed insight into HOM formation chemistry at the low NOx conditions. By family and marker analysis, the importance of secondary OH chemistry and alkoxy radicals will be shown.

2. The effect of a high HO_2/RO_2 ratio and its impact on the parity of oxygen in molecules will be investigated. A high HO_2/RO_2 results in the decrease of RO_2 + RO_2 reaction and as a consequence, there will be a less alkoxy radical formation. In this way, the importance of alkoxy radicals which are formed from RO_2 + RO_2 will be shown.

3. The impact of the presence of small chain radicals ($C_{\leq 5}$ from isoprene) on the product formation pattern and SOA mass formation will be demonstrated.

4. The effect of NOx on the product distribution and the changes in the chemistry of RO_2 will be discussed. Additionally, it will be demonstrated how the changes impact on SOA mass formation.

Chapter 2

Experiments and Methods

2.1 Experimental setup

2.1.1 Jülich Plant Atmosphere Chamber (JPAC)

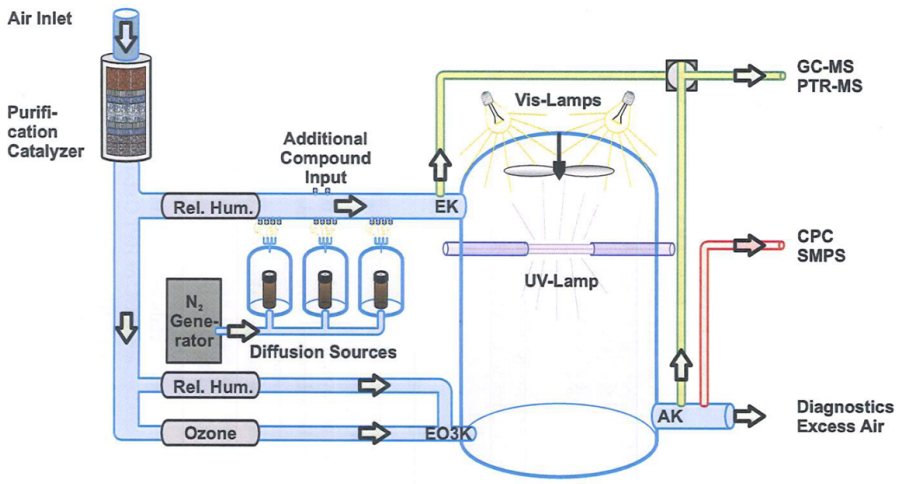

Figure 2.1: Schematic of the Jülich Plant Atmosphere Chamber (JPAC). The chamber was made of borosilicate glass. Purified air was provided by two main inlet lines. Both air flows were humidified before entering the chamber. The upper inlet flow carried the VOC of interest coming from diffusion sources. Other trace gases such as NOx or CO were added via the VOC inlet line. The lower inlet carried the ozone in to the chamber. The fan in the chamber assured the mixing in the chamber within two minutes. There were three different types of lamps providing UVC (λ_{max} = 254 nm), UVA (λ_{max}=365 nm, not shown), and visible light.

The experiments discussed within this study were all conducted in the Jülich Plant Atmosphere Chamber (JPAC) which is schematically shown in Figure 2.1. The reaction chamber was made of borosilicate glass and had a volume of 1450 L. The bottom of the chamber was made of teflon but it was covered with a glass plate. Clean air flushed the space between the teflon and

the glass plate to reduce memory effects due to the absorption of materials by the teflon surface. The chamber was placed in a temperature-controlled housing. During the experiments, the temperature was about 16 °C. JPAC was operated as a continuously stirred tank reactor.

To avoid possible wall losses, teflon (PFA, PTEE) was used for all connections and tubings. There were two separate inlet flows which went into the chamber (see Figure 2.1) in order to prevent possible reactions of ozone and VOCs in the gas lines. A total of about 31 l min^{-1} of purified air was pumped through the chamber resulting in a residence time of about 46 minutes. A fan in the chamber was used to assure the mixing in the chamber and the mixing time was 2 minutes. The flows were humidified by temperature-controlled evaporation of double-distilled water which resulted in a typical relative humidity of about 63 %.

The VOCs (α-pinene, isoprene) were added to the first flow (upper inlet in Figure 2.1) using clean N_2 as a carrier gas. VOCs were introduced into the carrier gas stream by the aid of diffusion sources. The concentration of the VOCs were varied by changing emission strength and dilution. Depending on the type of experiments, NOx or CO gas were added to the first flow. The second flow (lower inlet in Figure 2.1) served to add ozone to the chamber. In a few cases, aerosol was added to the chamber to force "controlled" condensation of HOM onto the seed surfaces. The seed aerosol was produced by atomising ammonium sulfate solutions with an aerosol generator (TSI, Aerosol Generator 3076). The aerosol was dried in a silica gel diffusion dryer and injected via a separate inlet line. The humidity in the two other inlets lines were regulated accordingly to keep the relative humidity at 63 %.

Three types of lamps were used to provide visible light, to produce OH radicals, and to photolyse NO_2 to generate NO. One or two discharge lamps (Osram, HQI400 W/D) were used to provide visible light. Twelve UVA discharge lamps (Philips, TL 60W/10-R, 60W, λ_{max}=365 nm) were mounted outside around the chamber walls and were used to photolyse NO_2 to NO. A maximum photolysis frequency j(NO_2) of about 4.3 $\times$ 10^{-3} s^{-1} could be achieved. A UVC lamp (Philips, TUV 40W, λ_{max}=254 nm) was located in a quartz tube inside the chamber and was used to photolyse ozone for the OH production. Herein, ozone is photolysed to O(^{1}D) which forms OH by reaction with the water vapor in the chamber. Two adjustable glass tubes shielded the TUV lamp from both ends. In this way the photolysis frequency j(O^{1}D) and the OH concentration could be varied by adjusting the gap between these glass tubes. The maximum j(O^{1}D) that could be achieved was about 5 $\times$ 10^{-3} s^{-1}.

The glass walls of the chamber had a wavelength cut-off near 350 nm. This means there was no radiation with short enough wavelength to produce OH radicals by photolysis of ozone when the UVC lamp was turned off. The UVC lamp contributes three orders of magnitude less to j(NO_2) than the UVA lamp so that j(O^{1}D) and j(NO_2) could be operated truly independent of each other.

The OH concentration was determined from the consumption of the VOC in the experiment. It was calculated by the following equation 2.1.1.

$$\frac{d[VOC]}{dt} = \frac{F}{V} \cdot ([VOC]_{\text{in}} - [VOC]) - (k_{OH} \cdot [OH] \cdot [VOC] + k_{O3} \cdot [O_3] \cdot [VOC]) \tag{2.1.1}$$

When the system reached steady-state condition $\frac{d[VOC]}{dt} = 0$, the equation 2.1.2 is derived from equation 2.1.1.

$$[OH] = \frac{\frac{F}{V} \cdot \frac{([VOC]_{\text{in}} - [VOC])}{[VOC]} - k_{O3} \cdot [O_3]}{k_{OH}} \tag{2.1.2}$$

$[VOC]_{in}$ and [VOC] refer to the initial concentration and the actual concentration of the VOC in the chamber, respectively. F is the total air flow through the chamber and V is the volume of the chamber. k_{OH} and k_{O3} are the reaction rate coefficients of OH and O_3 with the corresponding VOC. k_{OH} and k_{O3} for α-pinene were 5.37 $\times$ 10^{-11} cm^3 s^{-1} and 8.79 $\times$ 10^{-17} cm^3 s^{-1} at $16\,°\mathrm{C}$, respectively ((Atkinson and Arey, 2003)).

The VOC concentration was measured by Gas Chromatography Mass Spectrometry (GC-MS, Agilent), a Proton Transfer Reaction Quadrupole Mass Spectrometer (Q-PTR-MS, Ionicon) and a Proton Transfer Reaction Time-of-Flight Mass Spectrometer (PTR-ToF-MS, Ionicon). The instruments were switched from inlet to outlet to measure the source strength of the VOC and the concentration of the VOC in the chamber. O_3 was measured by UV absorption (Thermo Environment 49). NO was measured by chemiluminescence (Eco Physics, CLD 770 AL) and NO_2 after photolytic conversion (Eco Physics, PLC 760) to NO. The water vapour concentration was measured by the dew point mirror (TP-2, Walz). For particle number concentrations a CPC was used (TSI 3783, d_p>3nm) and the particle size distribution was measured by an SMPS (TSI 3081 electrostatic classifier combined with CPC TSI 3025). For HOM measurements a Chemical Ionization Atmospheric Pressure interface Time-of-Flight Mass Spectrometer (CIMS form now on) was used. This will be introduced in more detail in Chapter 2.2.

2.1.2 Experiment descriptions

The investigation of HOM formation from α-pinene photooxidation was performed under several different boundary conditions.

Table 2.1 shows the experimental conditions for the α-pinene photooxidation experiments. α-pinene and ozone concentrations are the concentrations at the inlet, which would be the "hypothetical" steady-state conditions before any action took place. The OH radical concentrations shows the range of steady-state concentrations for the different conditions within the experiment series. However, only steady-state OH radical concentration is shown in CO experiment. Isoprene and NOx concentrations give the range of concentrations applied within the experiment series. Temperature and relative humidity were kept in all experiment series around $16\,°\mathrm{C}$ and 63 %, respectively. The photolysis rate of O_3 was only varied in the OH dependency experiments series and kept constant in the other experiment series. To investigate the photooxidation of α-pinene and the effect of increasing OH radical concentrations on HOM formation, the OH concentration was varied by opening and closing the gap of the UVC lamp changing j(O^1D) (Column 1). The results of the study will be shown and discussed in Chapter 3.2.

Table 2.1: Experimental conditions for α-pinene photooxidation

	j(O^1D)	**CO**	**isoprene**	**NOx**
[α-pinene] (ppb)	8.1	12	1-8	18
[Ozone] (ppb)	32.2	60	22-33	90-230
[OH] (cm^{-3})	0.9×10^6 -4.4×10^7	7.4×10^6	2.3×10^6 -3.6×10^7	3.0×10^7 -9.0×10^7
[CO] (ppm)	-	3	-	-
[Isoprene] (ppb)	-	-	0-20	-
[NOx] (ppb)	-	-	-	0.3-140
Temperature °C	16	16	16	16
RH (%)	63	63	63	63

Since the atmosphere does not consist of just one volatile organic compound, the effects of various additional components were investigated.

CO was added to the system to investigate the effect of the high HO_2/RO_2 ratio on the HOM formation in α-pinene OH oxidation (Column 2). This will be described and discussed in Chapter 3.3. The effect of small peroxy radicals on the HOM formation and SOA yields in the α-pinene photooxidation will be presented in Chapter 3.4. The concentration of small peroxy radicals was achieved by the addition of isoprene to the system (Column 3). Finally, the effect of NOx in the system on HOM formation and SOA yields will be dealt with in Chapter 4 (Column 4).

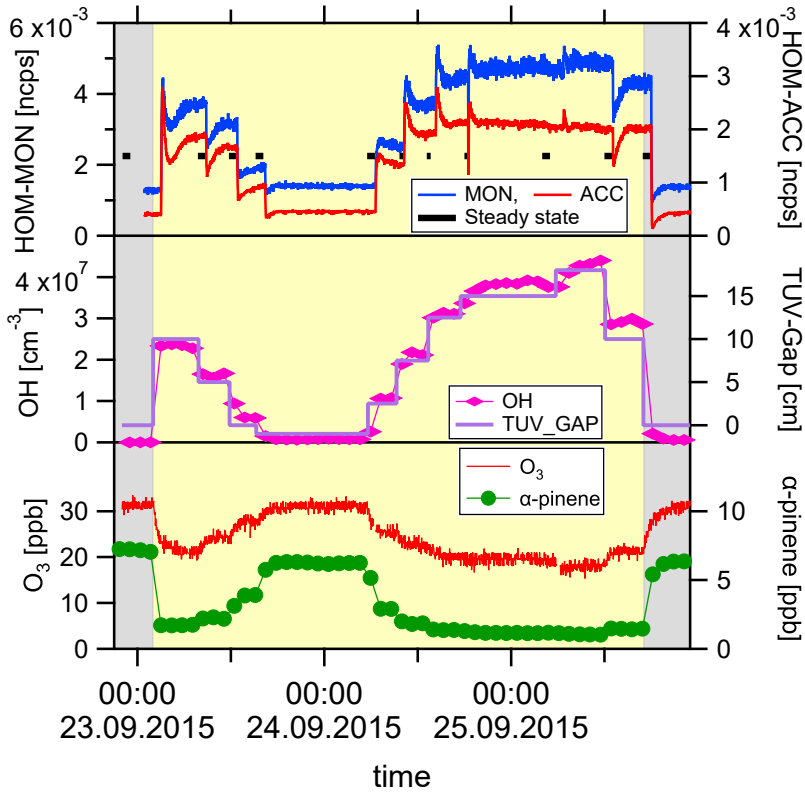

Figure 2.2: Time series of the α-pinene OH oxidation experiment with varying j(O^1D). The yellow shaded area represents the duration when UVC light was switched on for the production of OH radicals and the grey shaded area shows when UVC light was off. At the lowest graph, the measured concentration of α-pinene (green circles) and O_3 (red line) concentration are shown. As UVC light is on, the concentration of α-pinene and O_3 decreased because of the reaction with OH and being photolysed respectively. In the middle graph, the OH concentration (pink rhombus) and TUV gap (violet line) are shown. TUV gap means the gap between lamp shielding glasses and the higher TUV gap means the higher photolysis rate. On the top graph, the normalised signal of HOM (monomer (blue line) and accretion products (red line)) and the steady-state interval (black line) are shown. HOM concentration increased and decreased with varying OH concentrations.

Figure 2.2 shows the time series of measured concentrations and normalised HOM signal for α-pinene photooxidation at varying OH concentration. Before the photochemical OH production began (before UVC light was switched on), the chamber reached steady-state in a phase of α-pinene ozonolysis. When UVC lamp switched on, the OH production and photooxidation of α-pinene started. As soon as the photooxidation started, massive HOM production was observed. The HOM concentration went through a transient maximum and reached (nearly) steady-state. After reaching (nearly) steady-state the OH radical concentration was varied by changing the TUV gap and therewith the j(O^1D). As one can infer from the signal of HOM, j(O^1D) stepwise increased and decreased with the passage of time. After the

last steady-state period of α-pinene OH photooxidation, UVC light was switched off and the OH production stopped. Almost immediately HOM production decreased and the ozonolysis phase before the photooxidation was reproduced.

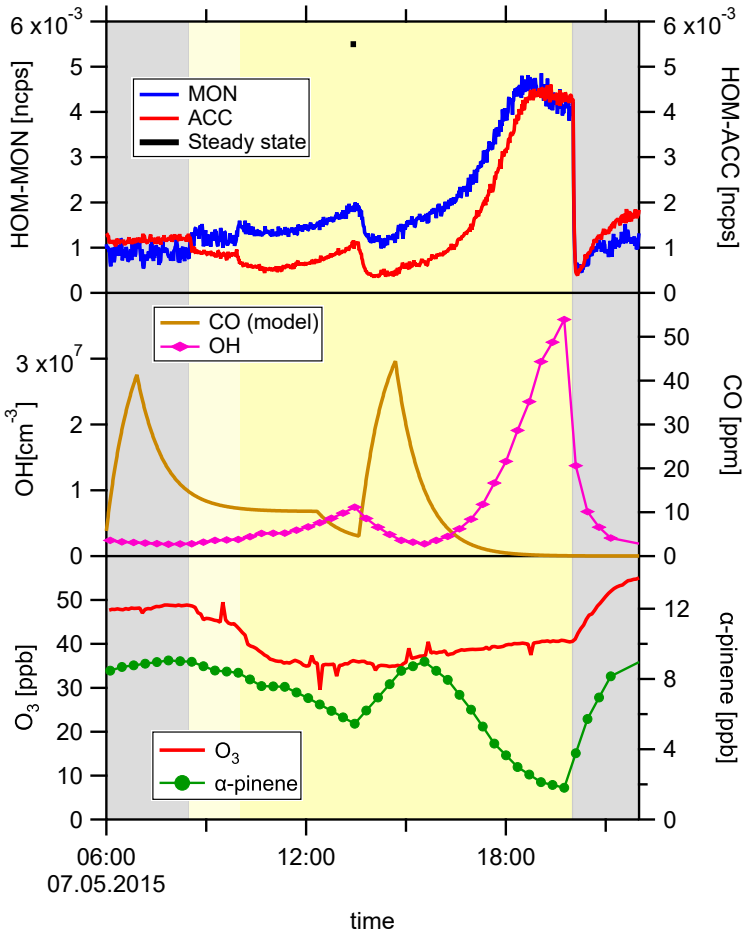

Figure 2.3: Time series of the α-pinene OH oxidation experiment in the presence of CO. The yellow shaded area represents the duration when UVC light was switched on for the production of OH radicals and the grey shaded area shows when UVC light was off. At the lowest graph, the measured concentration of α-pinene (green circles) and O_3 (red line) concentration are shown. As UVC light is on, the concentration of O_3 decreased because O_3 was photolysed. α-pinene concentration did not decrease as dramatic as in the OH varying experiment because of the scavenging effect of CO on OH radical (pink rhombus in the middle graph). In the middle graph, CO (orange line) concentrations are shown as well. The concentration of CO is taken from the model calculation. In the presence of high CO concentration, OH was scavenged. However, OH radical concentration increased when CO was flushed out. On the top graph, the normalised signal of HOM (monomer (blue line) and accretion products (red line)) and the steady-state interval (black line) are shown. Changes in CO and OH radical concentration resulted in the changes in normalised HOM concentrations.

Figure 2.3 displays the time series of measured experimental conditions and modeled CO

concentration in α-pinene OH oxidation experiment in the presence of CO. Before the photooxidation started, steady-state was established for α-pinene ozonolysis in the presence of CO. The UVC light was switched on to start the photooxidation. The HOM concentration did not increase significantly in the presence of CO because of low OH concentrations (in the middle graph, pink rhombus). The CO concentration was varied as given in Figure 2.3 with the effects on OH and HOM concentrations.

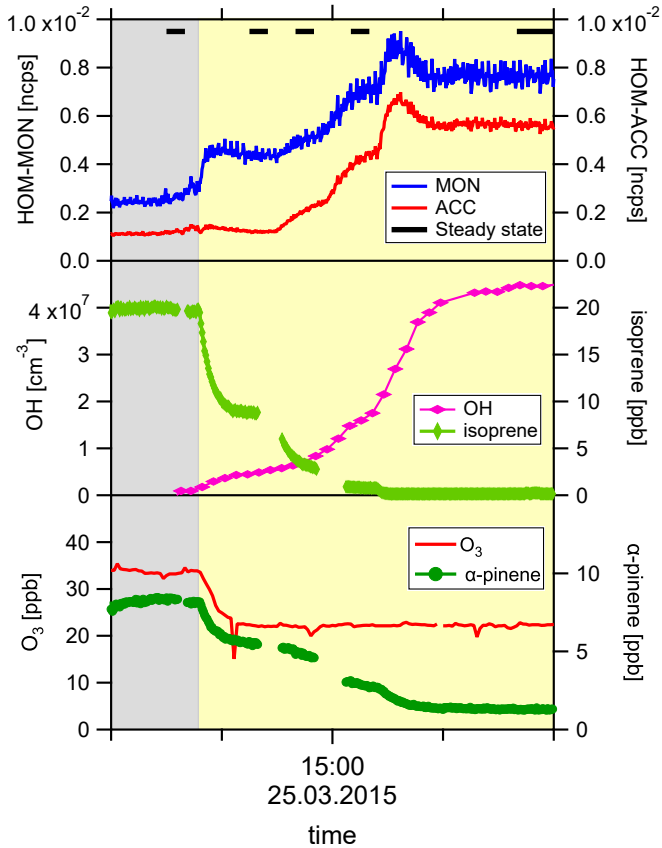

Figure 2.4: Time series of the α-pinene OH oxidation experiment in the presence of isoprene. The yellow shaded area represents the duration when UVC light was switched on for the production of OH radicals and the grey shaded area shows when UVC light was off. At the lowest graph, the measured concentration of α-pinene (green circles) and O_3 (red line) concentration are shown. As UVC light is on, the concentration of O_3 decreased because it was photolysed. In the middle graph, the OH (pink rhombus) and isoprene (light green diamonds) concentrations are shown. Isoprene concentration decreased dramatically because of the reaction with OH (OH scavenging effect of isoprene). As isoprene concentration decreased, OH concentration increased. On the top graph, normalised signal of HOM (monomer (blue line) and accretion products (red line)) and the steady-state interval (black line) are shown.

Figure 2.4 shows the time series of HOM production for α-pinene OH oxidation in the isoprene experiment. At first, steady-state was established for α-pinene ozonolysis in the presence of isoprene. As soon as the UVC lamp was switched on, the OH production started. The HOM signal increased less than in the j(O^1D) experiment because isoprene scavenged the OH radicals and kept their concentration low (the rate coefficient of OH reaction for isoprene is about twice as high than the one for α-pinene). Accretion products were suppressed because of the product scavenging effect of small peroxy radicals originating from isoprene (McFiggans *et al.*, 2019). The isoprene addition was stepwise decreased and OH- and product- scavenging lost their importance. Isoprene addition was stopped and after 18:00 h. After that, the steady-state for α-pinene OH oxidation was established. It served as photooxidation reference since the condition was same except the absence of isoprene.

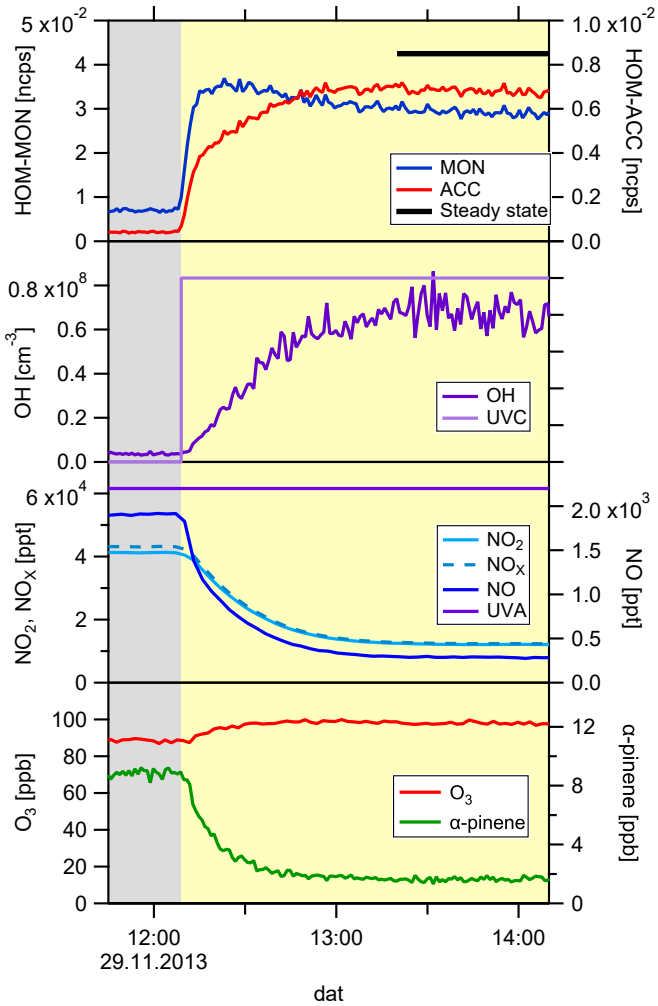

Figure 2.5: Time series of the α-pinene OH oxidation experiment in the presence of NOx. Among various NOx experiments, 12.8 ppb of NOx was used in this example. The yellow shaded area represents the duration when UVC light was switched on for the production of OH radicals and the grey shaded area shows when UVC light was off. At the lowest graph, the measured concentration of α-pinene (green circles) and O_3 (red line) concentration are shown. In the second-lowest graph, the concentrations of NO_2 (light blue line), NO (blue line) and NOx (light blue dashed line) are shown. The UVA light (violet line) was switched on the whole period to photolyse NO_2 and to generate NO. In the third graph, OH concentrations (violet line) are shown in addition to UVC light (light violet line). As UVC light was on, OH production began and the normalised signal of HOM monomer (blue line), accretion products (red line) increased (on the top graph). Black line on the top graph shows the time interval used for steady-state.

The NOx experiment series extended over more than one month. Figure 2.5 shows an example for the time series of a single NOx experiment day ([NOx] = 12.8 ppb). Before OH

production started, steady-state of α-pinene ozonolysis was established with the UVA light switched on. Then, NO was added to the system and a new steady-state for ozonolysis in the presence of NO_2 and NO was established. This period served for checks and controls in other contexts and will not be further considered here. Finally, the UVC light was switched on and OH production started. After an instantaneous and significant increase of normalised HOM signals, the system entered a steady-state. In the detailed analysis, only steady-state data at the end of this phase were considered.

2.2 Chemical Ionisatiton Mass Spectrometer (CIMS)

2.2.1 Introduction of the CIMS

The development of the Atmospheric Pressure interface Time-of-Flight Mass Spectrometer with a Chemical Ionisation inlet enabled the discovery of HOM (Ehn *et al.*, 2012; Ehn *et al.*, 2014; Schobesberger *et al.*, 2013) and initiated vigorously HOM studies. The CIMS consists of two parts, the APi-ToF-MS (Figure 2.6, Junninen *et al.*, 2010) and the chemical ionisation source (Figure 2.7, Eisele and Tanner, 1993).

As shown in Figure 2.6, ions enter the APi part through a critical orifice after being ionised in the chemical ionisation inlet. The amount of air that enters the APi-ToF-MS is determined by the diameter of critical orifice. In this work, a diameter of 0.3 μm was used allowing a sampling air flow of 0.8 l min^{-1} into the APi-ToF-MS.

In the first stage, a small segmented quadrupole serves to guide the ions. It is operated at about 2 mbar so that collisional dissociation of ion clusters with water can occur. The second stage has a big segmented quadrupole which is operated at 1.5×10^{-2} mbar. In this stage, the declustering of analyte-reagent ion clusters is controlled. The next stage has a stack of electrical lenses to focus and accelerate the ion beam into the extraction region of ToF. ToF region is operated at about 1×10^{-6} mbar. All the pressures are controlled by differential pumping by a scroll pump and a three-staged turbo pump. Ions are focused and filtered based on the voltage settings along the three-stages.

After entering the ToF part, the ions are extracted perpendicularly by a pulser and separated by the different time of flight based on their mass per charge ratio. APi-ToF-MS has two modes of operation, V mode and W mode, depending on the shape of the flight path of the ions. The W mode has a higher resolving power (8000 Th/Th) but is less sensitive, so only the V mode was used in this study. The V mode has a better sensitivity and higher time resolution at a resolving power of 4000-5000 Th/Th. Herein resolving power is defined as $\frac{M}{\Delta M}$, wherein M is mass per charge ratio and ΔM is the width of the peak at its half maximum.

Negative ion CI is a soft ionisation method with only a little fragmentation compared to other ionisation methods such as electron impact or the Proton Transfer Reaction Mass Spectrometry. Based on the fact that HOM were detected as stable clusters with natural NO_3^- ions

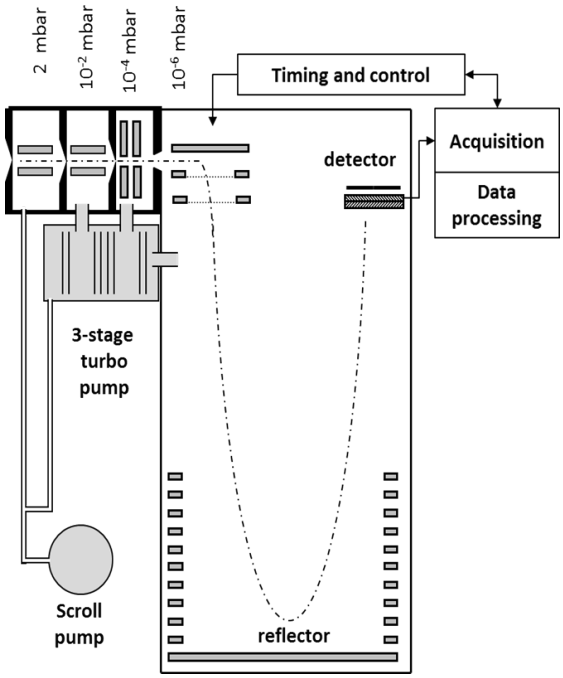

Figure 2.6: Schematics of the Atmospheric Pressure interface Time-of-Flight Mass Spectrometer. Sample air enters the first chamber through a critical orifice. Two quadrupoles and an electrical lens system guide the ions into the extraction region of the ToF-MS. The ToF path is folded by using a reflectron. Ions are detected by a multi-channel plate detector. A scroll pump and a three-stage turbo pump allow for a reduction of the pressure in four steps from atmospheric pressure to 10^{-6} mbar. Junninen *et al.*, 2010

(Junninen *et al.*, 2010; Ehn *et al.*, 2012), CI with nitrate ions is the method of choice to measure highly functionalised organic molecules.

Therefore, nitrate CI was applied to detect HOM in the field studies and laboratory studies (Ehn *et al.*, 2014; Jokinen *et al.*, 2012; Jokinen *et al.*, 2015). Since HOM are mostly multiple hydroperoxides with additional alcohol, carboxyl or percarboxyl groups, HOM and NO_3^- reagent ions form stable clusters by means of multiple hydrogen bonds (Hyttinen *et al.*, 2015).

An eisele type inlet was used in this thesis. The eisele type inlet was originally designed for the measurement of atmospheric sulfuric acid using NO_3^- ions (Eisele and Tanner, 1993). Figure 2.7 shows the schematics of the Eisele inlet, modified for the use with ToF-MS by Jokinen *et al.*, 2012. The inlet is built from stainless steel, with Polymethyl methacrylate (PMMA) spacers for electrical isolation. It consists of the ionisation region (left) and the ion drift tube (right). The ionisation region is embedded in PMMA housing. The whole assembly is mounted to the APi-ToF-MS by a polyvinylidene fluoride (PVDF) foot (green, right). About 10 l min^{-1} of sample flow enters through the inlet. From the side, 20 l min^{-1} purified air containing the

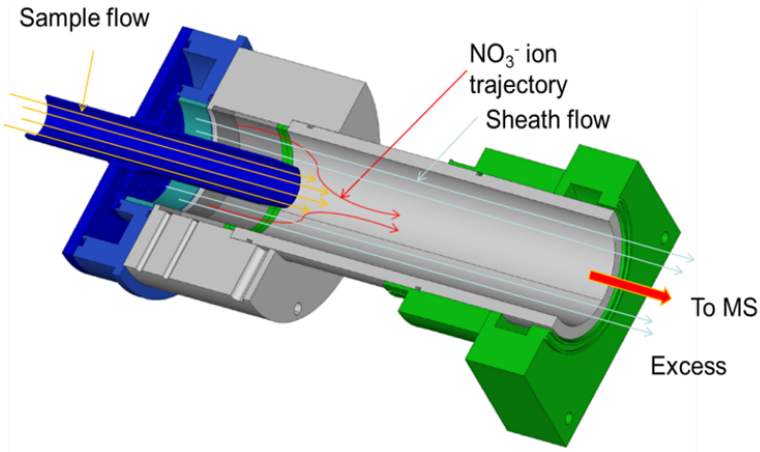

Figure 2.7: Schematics of the Eisele type NO_3^- chemical ionisation inlet. About 10 l min^{-1} sample flow enters through the sampling line (blue tube). 20 l min^{-1} purified air containing HNO_3 enter from the side (not shown) into the left part of the inlet (blue). HNO_3 molecules are ionised by α-radiation of an ^{241}Am radioactive source. The 20 l min^{-1} purified air containing NO_3^- ions enters the ion drift tube as sheath air surrounding the sample flow. An electrical field pushes the NO_3^- ions into the sample stream containing the HOM. Excess air are pumped out by total flow (29.2 l min^{-1}) and about 0.8 l min^{-1} enters through the critical orifice into the APi-ToF-MS. Adapted from Jokinen *et al.*, 2015.

HNO_3 vapor are introduced. HNO_3 is ionised by the exposure to α-radiation from a radioactive ^{241}Am source. Nitrate ions are mixed with HOM in the sample flow by pushing them to the center of the ion drift tube. For that, an electric field is applied between the walls of the drift tube and the grounded critical orifice of the APi-ToF-MS.

The Eisele type inlet has a coaxial laminar flow and the strong sheath airflow minimises any interactions of the sample flow containing the HOM with the walls of the drift tube. In addition, the applied electric field repels the reagent ions to the center of the drift tube reducing wall losses and reactions of the analyte with OH radicals, which are also formed by the radioactive source. A design to minimise the wall loss is critical for the detection of molecules with very low vapour pressure such as HOM. The nitrate ions exist as monomers (NO_3^-), dimers ($HNO_3 \cdot NO_3^-$) and trimers ($(HNO_3)_2 \cdot NO_3^-$). Typical distributions during the experiments were 60 % monomers, 25% dimers, and 15% trimers. Most of the analyte molecules were detected as clusters with monomer NO_3^- ions and only the compounds with high concentrations were detected as a monomer and dimer nitrate ion cluster.

For the experiments of α-pinene photooxidation with NOx, isotopically labeled nitric acid ($H^{15}NO_3$, 98% ^{15}N) was used to distinguish N-atoms from reagent ions and from organic nitrates formed by HOM peroxy radicals reacting with NO or NO_2. However, while labeling with ^{15}N was effective to distinguish the origin of N-atoms in low and moderate NOx concentration experiments, it did not work as well as intended under high NOx conditions because of a fast charge exchange with the $H^{14}NO_3$ formed in the reaction of NO_2 with OH in the chamber.

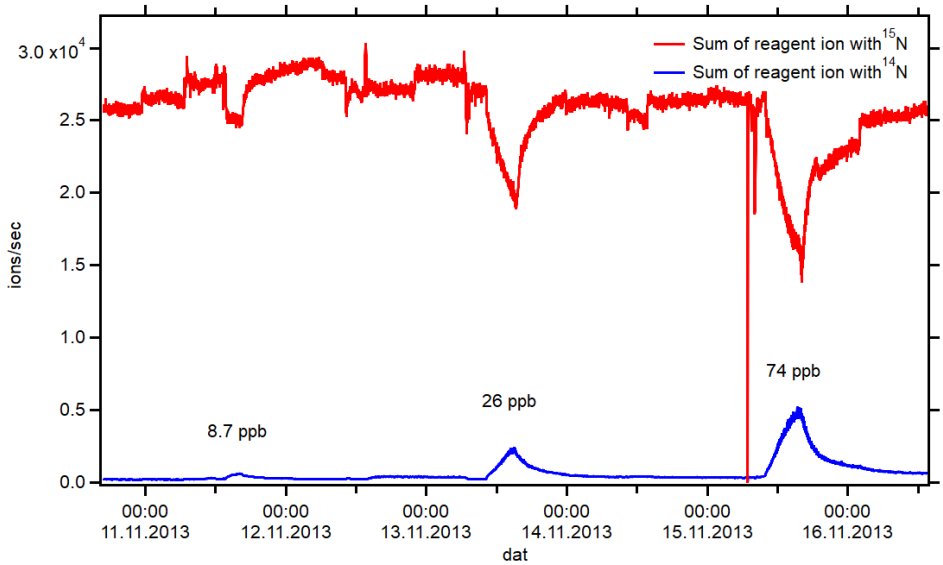

Figure 2.8: Time series of the summed up signal of $^{14}NO_3^-$ (blue), $^{15}NO_3^-$ (red), and their clusters in three different NOx experiments. The concentration of NOx was 8.7, 26 and 72 ppb, respectively. The percentage of ^{14}N nitrate reagent ions increased from 1.9 %, 10 % and 25 %.

Figure 2.8 shows the increasing contribution by ^{14}N containing reagent ions. The fraction of ^{14}N containing reagent ions increased with the concentration of NOx due to an increase of $H^{14}NO_3$ formed in the chamber. As a result, HOM were detected as clusters with both $^{14}NO_3^-$ and $^{15}NO_3^-$ nitrate ions. The loss of labeling of the reagent ion prohibited an easy separation of the origin of nitrate atom (reagent ion or organic nitrate) and increased the difficulties of molecular identification. However, the majority of HOM were still detected as $^{15}NO_3^-$ cluster and $^{14}NO_3^-$ contributions were considered in the high resolution peak identification.

2.2.2 Calibration of detected HOM

Calibration of the NO_3^--CIMS for HOM is a challenge due to their very low vapour pressure and the high probability of loss of HOM in tubings and at the inlet walls. Therefore, a suited absolute calibration method for HOM measurement is not existing yet. However, indirect calibration using the measurement of H_2SO_4 with the NO_3^--CIMS was applied in other studies (Ehn *et al.*, 2014; Jokinen *et al.*, 2014; Mutzel *et al.*, 2015; Berndt *et al.*, 2016). The sensitivity of the NO_3^--CIMS to HOM is supposedly similar to the sensitivity of H_2SO_4 under the assumption that the charging efficiencies for HOM and H_2SO_4 are both near to the kinetic limit (Viggiano *et al.*, 1997; Ehn *et al.*, 2014; Kirkby *et al.*, 2016). Therefore, in this work, calibration of the CIMS with H_2SO_4 was used to obtain concentrations of the detected HOM.

H_2SO_4 was formed in-situ by oxidation of SO_2 by OH in the JPAC according to the following reactions.

$$\begin{aligned} &SO_2 + OH \xrightarrow{M} HOSO_2 \\ &HOSO_2 + O_2 \longrightarrow HO_2 + SO_3 \\ &SO_3 + H_2O \longrightarrow H_2SO_4 \end{aligned} \qquad \text{R2.2.18}$$

OH radicals were produced by photolysis of O_3 in the presence of water vapour as described before. Since the reactions of $HOSO_2$ + O_2 and SO_3 + H_2O are much faster than the oxidation of SO_2 by OH at the mixing ratio of water vapour of 1.06 %, the SO_2 + OH reaction was the rate determining step. Therefore, the production of H_2SO_4 can be expressed as follows.

$$P(\mathrm{H_2SO_4}) = k_{\mathrm{SO_2}} \cdot [\mathrm{SO_2}] \cdot [OH] \qquad (2.2.1)$$

(E)-2-butene was added as an OH radical tracer to estimate the concentration of OH radicals. (E)-2-butene was chosen because it does not form a detectable amount of new particles and its oxidation products do not overlap with the sulfuric acid ion masses. The determined OH radical concentration was (3.3 ± 0.8) × 10^7 molecule cm^{-3}. Even though SO_2 was oxidised by OH radicals, the OH radical concentration was not much affected because of the low reactivity of SO_2 towards OH radicals compared to (E)-2-butene.

In the mass spectrum, H_2SO_4 was detected as clusters of NO_3^- monomers ($H_2SO_4 \cdot NO_3^-$), dimers ($H_2SO_4 \cdot HNO_3 \cdot NO_3^-$) and trimers ($H_2SO_4 \cdot HNO_3 \cdot HNO_3 \cdot NO_3^-$). All clusters were summed up and normalised to the total ion counts to remove possible uncertainty caused by instrumental performance.

At the end of the measurement, SO_2 was flushed out and eventually became zero so that the background H_2SO_4 could be determined (0.05 normalised counts per second (ncps) = 2 x 10^6 cm^{-3}) and possible interferences from (E)-2-butene oxidation products could be excluded. The wall loss of H_2SO_4 was determined by stopping the OH production and measuring the decay of H_2SO_4 in an additional experiment. An exponential decay of H_2SO_4 with a lifetime of 87 ± 5 s (loss rate $L(H_2SO_4) = 1/\tau = 0.012 \pm 0.001\ s^{-1}$) was observed.

The H_2SO_4 concentrations were calculated from the production rates (8.03 x 10^5 cm^{-3} s^{-1} and 4.15 x 10^5 cm^{-3} s^{-1}) divided by the first order loss rate of H_2SO_4.

$$[\mathrm{H_2SO_4}] = \frac{P(\mathrm{H_2SO_4})}{L(\mathrm{H_2SO_4})} = \frac{P(\mathrm{H_2SO_4})}{L(\mathrm{H_2SO_4})} \qquad (2.2.2)$$

In Figure 2.9, the sum of the detected H_2SO_4 as clusters with monomer, dimer and trimer reagent ions is plotted as a function of the H_2SO_4 concentration. The solid line shows the linear regression forced through zero. The inverse of the slope was used to determine the calibration factor in units of molecules cm^{-3} nc^{-1}. The calibration factor C_{H2SO4} was (3.7 ± 1.2) × 10^{10} molecules cm^{-3} nc^{-1}. The overall uncertainty was due to the uncertainty of $[H_2SO_4]$ of ±37 %, calculated by error propagation from the contributions by the uncertainty of the OH radical concentration (∼20 %), of the SO_2 concentration (∼5 %) and the uncertainty of the loss of H_2SO_4 (∼25 %).

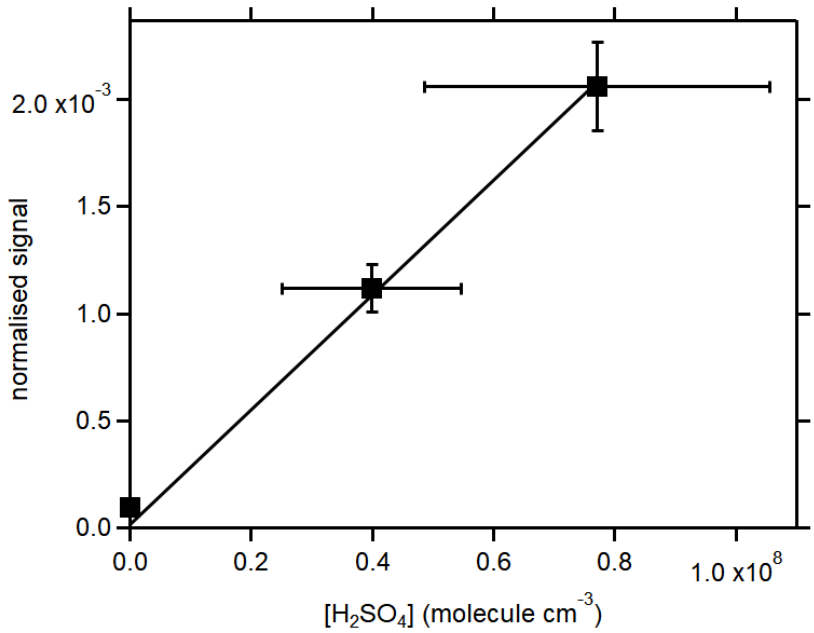

Figure 2.9: The normalised sum of H_2SO_4 clusters with monomer, dimer and trimer NO_3^- ion as a function of H_2SO_4 concentration. Solid line represents the linear regression forced through zero at the no SO_2 addition point. The inverse of the slope was used to determine the calibration factor C_{H2SO4}. The uncertainty was estimated to ±37 % due to the uncertainty of $[H_2SO_4]$.

As described in Ehn *et al.*, 2014 and Hyttinen *et al.*, 2017, HOM with six or more oxygen atoms in the molecule are detected with similar sensitivity as H_2SO_4. Therefore, C_{H2SO4} was used to calculate the concentrations of detected HOM (C_{H2SO4}=C_{HOM}).

2.3 Data Evaluation

2.3.1 High resolution peak analysis

The high resolution data was analysed by using Tofware (v2.5.11, Tofwerk AG and Aerodyne Research, Inc.) and Igor Pro(7.08)(Wavemetrics). The data were averaged over one minute using the pre-averaging function in Tofware. The instrument functions (peak shape, peak width and baseline) were calculated by built-in functions which are described in Stark *et al.*, 2015. The first step was to select the reference mass spectrum that represents the steady-state of the experiment well and has high enough signal. Within the reference mass spectrum, peak shape and peak width function were determined. The peak shape was determined by using about 10-20 large peaks in the mass spectrum. Even though the reagent ion peak at mass per charge ratio (m/z or Th) = 62 (NO_3^-) was the highest peak in the mass spectrum, it was excluded because of its satellite peak in the front.

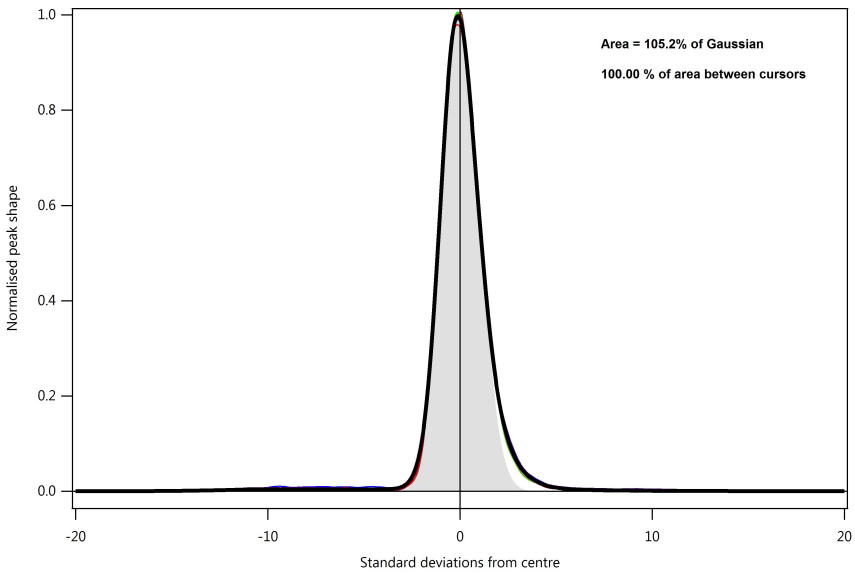

Figure 2.10: Peak shape determined for j(O^1D) experiment series. Selected peaks are normalised to 1. The thick coloured lines show selected peaks and the black thick line shows averaged peak shape of selected peaks. Grey area shows the Gaussian graph and the area of peak shape was calculated to be 105.2 % of Gaussian graph area.

Figure 2.10 shows a representative example of the peak shape determined from the 14 large peaks. The coloured lines show the normalised peak shapes from different m/z and the black line shows the average peak shape which was derived and applied in the peak fitting.

Figure 2.11 shows the full width at half maximum of the peaks in the mass spectrum as a function of the mass to charge ratio (left) and the resolution function (right). The upper right panel shows one example of the peaks used to determine the peak width function. Black dots represent the lower bound of the full width at half maximum of all peaks. These peaks were considered as single peaks and used to calculate the peak width function which is a red line. Grey open circles are all other peaks which have a broader full width at half maximum. The left panel in Figure 2.11 indicates a high possibility of multiple and overlapping peaks under a unit mass resolution signal. The graph with the resolution function shows that our instrument had a resolving power of 4000 Th/Th in the j(O^1D) experiment series.

After the peak shape and the peak width function were determined, a post-measurement mass calibration was carried out. The monomer, monomer water cluster, dimer, and trimer of the NO_3^- ion were used as mass calibrants. The mean residual error was less than 5 ppm. A three-parameter fit ($p1 \times m^{p3} + p2$) was applied to convert the time of flight base into a mass base. Since the trimer reagent ion only covered masses up to 188 m/z, more peaks were added as mass calibrants which had a high intensity and was clearly single peak with a known single molecular formula.

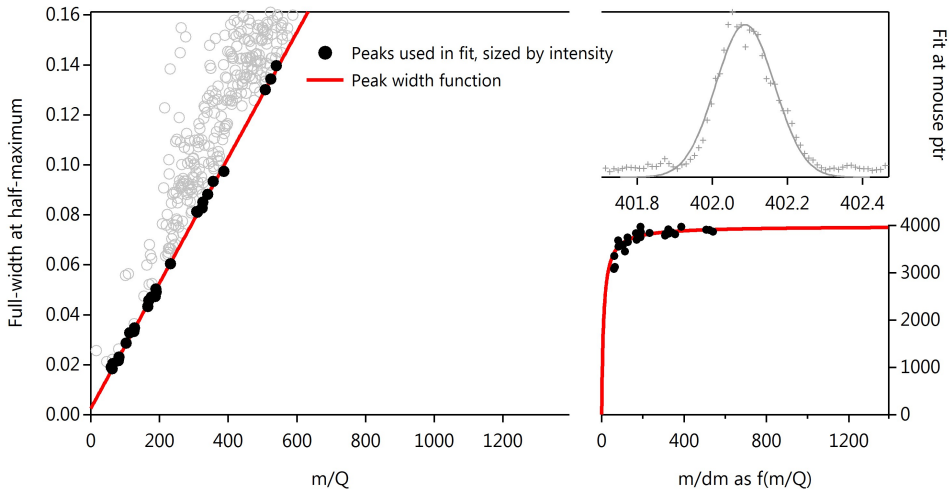

Figure 2.11: Peak width function and resolution function determined for the j(O^1D) experiment series.

For the peak identification, the following procedure was performed. The target peak was fitted by applying the previously determined peak shape and peak width function. If the target peak was a single peak, this resulted in a very small residual (the difference between measured peak and fitted peak). If a large residual remained in the peak fitting and the peak had a broad full width at half maximum, one more peak was added for the fitting. This procedure was repeated until the residual was reasonably small. Since the residuals will be always smaller when more peaks are added, the number of peaks that were fitted to the target peak was kept as small as possible. After the number of peaks that fitted the target peak was decided, possible candidates for the peaks within "expected" atoms and their number of appearances were calculated. For example, C, O, N, H were selected in this study and a built-in program searched for molecules with combinations of 0-20 for each atom. The molecular formula was determined by minimising the difference between expected mass for the combinations and exact positions of fitted peaks. The selection was accepted when the error was less than 15 ppm. The results for each unit mass resolution signal were inspected visually and several more criteria were deployed for the crosschecking of the peak identification;

1. Molecular formulae from similar experiments in the literature were taken into account.

2. The suggested molecular formula was supposed to be convertible to a chemically possible molecule. For example, the number of hydrogen should be equal or less than that of a saturated hydrocarbon with the same carbon number (2n+2, n is the number of carbon atoms). In turn, the suggested molecular formulae should have more than minimum hydrogen as well. If the candidate molecule showed a very small error but impossible molecular formula, it was excluded. In case of uncertain, molecular formulae

were double checked with NIST chemistry webBook (`https://webbook.nist.gov/chemistry/form-ser/`)

3. Expected isotope patterns for the proposed molecular formulae were inspected as well, especially the ^{13}C isotope. Stable carbon isotopes are made to 98.9 % of ^{12}C and 1.1 % ^{13}C. For example, for a C_{10} molecule at mass per charge M, about 11 % of C_{10} signal should appear at M+1 Th. The built-in peak identification function showed directly the ^{13}C isotope signal at the next integer mass. Therefore, if the isotope satellite of the candidate molecule was bigger than the observed signal, the candidate molecule was excluded.

4. Experimental changes (like turning on the UVC light to start photochemistry or adding NOx) were considered as well in the peak identification process. This was especially helpful for assigning odd integer masses in the NOx experiment series since odd masses can be originated from either organic nitrate or from peroxy radicals.

   Figure 2.12 shows mass peaks at molecular mass 277 Da from NOx experiment series. Panel A shows the background NOx concentration of 0.3 ppb and panel B shows the same peak at the NOx concentration of 8.7 ppb.

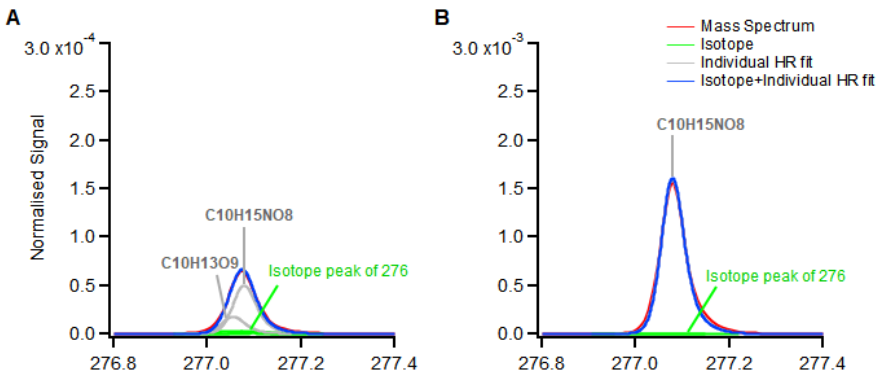

Figure 2.12: Comparison of peak identification at molecular mass 277 Da in the NOx experiment. The concentration of NOx was 0.3 ppb (A) and 8.7 ppb (B). The red line shows the measured mass spectrum and the grey lines show each individual peak. The green line shows the isotope signal from previous integer mass and the blue line is the sum of the signal from individual peaks and isotope signal (Grey and Green). Signals were normalised to the sum of all ions.

Assuming a resolving power of 4000 Th/Th, full resolution at 277 Da was achieved when the mass difference of the two peaks was bigger than 0.07 Th.

However, the mass difference between the $C_{10}H_{15}NO_8$ and the $C_{10}H_{13}O_9$ was only 0.0238 Th, therefore the separation was insufficient. The inspection of the time series of each peak helped at this point. Organic nitrate peaks increased dramatically under the addition of NOx, whereas the changes in peroxy radicals were less strong. The different

temporal behaviour of the organic nitrate and the peroxy radical reduced the uncertainty in the peak identification.

2.3.2 CIMS analyzer

Tofware is a useful tool for high resolution analysis. Tofware helps to assign molecular formulae, perform peak fitting, and generate time series of the intensity under the each assigned peak. In addition, it is a valuable tool to obtain a (averaged) mass spectra in the steady-state period of interest. Tofware offers functions as well to filter peaks by certain criteria such as mass to charge ratio range or carbon numbers or oxygen to carbon ratio. However, there are limitations for the handling of the data, especially a classification of molecules according to more complex criteria, e.g., the chemical origin or chemical functionality such as whether the products arising from peroxy peroxy reactions (HOM-PP), from peroxy NO reactions (organic nitrates, HOM-ON), or peroxy radicals (HOM-RO_2) themselves. There is a function to select species and save them as a group in Tofware but selection must be done by hand which is a time consuming task. This is cumbersome if long experiment series provide a large amount of data and a large number of molecules and molecule classes of interest.

To have better and specific data handling, a program called CIMS analyzer was developed in our group. The program is based on Igor Pro (7.08) (Wavemetrics). Details will be described in the appendix B. Using the CIMS analyzer program made the data handling easy, less time consuming, and less susceptible to errors, especially in obtaining normalised signals or mass weighted signals for all species. The CIMS analyzer was extensively used to generate all the normalised data and mass weighted data shown in this thesis.

2.3.3 Families and markers

Even though mass spectrometry cannot provide the exact structure of the molecule, it can provide the chemical formula of a compound. As α-pinene undergoes oxidation, products with the typical formulae of type $C_xH_yO_z$ would be formed. Analysis and classification of molecules according to x, y, z can provide important mechanistic information. For example, the number of carbon x in α-pinene equals 10. However, if the molecule with $x < 10$ was observed, it must have undergone a fragmentation process. In addition, if the molecule is fragmented, the number x gives a rough idea which part of molecule went through bond scission (central, if x is C_5 or C_6 or terminal, if x is C_8 or C_9).

The number of hydrogen (y) can give the information about the reaction which terminanted the autoxidation process. This is useful information especially for C_{10} α-pinene oxidation products. The hydrogen number of the fragmented molecules are more complicated since the structures of the fragmented molecules are less known than those of C_{10} molecules. Therefore, only C_{10} monomers and C_{20} accretion products will be treated in this thesis. Depending on the reaction pathway, the number of hydrogen in radicals can be either 15 or 17. Ozonolysis of

α-pinene gives H_{15} peroxy radicals and OH addition reaction gives H_{17} peroxy radicals as first generation peroxy radicals. In case of a second OH attack by H-abstraction on closed shell oxidation products (such as pinonaldehyde), peroxy radicals with 15 H-atoms can be produced as well in the OH oxidation. This allows for separation of the first and the higher generation contributions in the photooxidation of α-pinene.

The number of oxygen (z) provides a hint whether an alkoxy radical formation is possibly involved in the formation mechanism of the peroxy radicals. This is because autoxidation adds 2 oxygen atoms to the molecule which does not change the parity of oxygen number while involving the formation of one alkoxy radical changes the parity of oxygen number. In other words, if there is only straight autoxidation during the formation mechanism of the compound, the parity of the oxygen number will be the same as in the starting peroxy radical. There is a possibility that the formation of two alkoxy radicals is involved which would set back parity of oxygen. However, this will not be considered in this work since the possibility is low.

Analysis of closed shell products is complicated. e.g., the $C_{10}H_{15}O_z$ peroxy radical can lose one oxygen and one hydrogen atom which results in a carbonyl group as termination functionality with the chemical formula of $C_{10}H_{14}O_{z\text{-}1}$. In the disproportionation reactions, the peroxy radicals can yield hydroxyl groups which results in molecular formulae of the $C_{10}H_{16}O_{z\text{-}1}$ (R1.2.8). When $C_{10}H_{15}O_z$ peroxy radicals react with HO_2, hydroperoxides with chemical formulas of $C_{10}H_{16}O_z$ are produced. In the photochemical system, the first generation peroxy radicals are $C_{10}H_{17}O_3$. Such radicals can undergo autoxidation which results in peroxy radicals with the chemical formula of $C_{10}H_{17}O_z$. These radicals will produce $C_{10}H_{16}O_{z\text{-}1}$ as carbonyl compounds, $C_{10}H_{18}O_{z\text{-}1}$ as alcohols and $C_{10}H_{18}O_z$ as hydroperoxides. The mixture of the different termination products with the same molecular formulae introduces complexity in the analysis. Despite of the complexity, some systematic information can be derived from the analysis.

The entire framework of the α-pinene oxidation by ozonolysis and OH oxidation which classifies of the data in this work is shown below.(Fig 2.13)

Based on the x, y, z numbers, classification and division into the different families by the given chemical formula is possible. This was already shown by Molteni *et al.*, 2019 who classified α-pinene ozonolysis C_{10} compounds into 10 classes (Figure 2.14).

The number of carbon atoms in the compounds will be used to investigate the fragmentation of α-pinene (oxidation products) in this thesis. An increasing fragmentation can be a clue for the increase of the formation of alkoxy radicals. The number of hydrogen of the compounds will be discussed to see the importance of the different termination reactions. Finally, the number of oxygen will be considered to see the number of autoxidation steps and the involvement of alkoxy-peroxy pathway.

For the analysis, "Family" is defined here as a group of compounds that have the same number of carbon and hydrogen with a different number of oxygen. The grouping and the classification is a useful tool. However, the information from the different oxygen number is lost since it shows only the averaged behaviour of the compounds in the same family. The

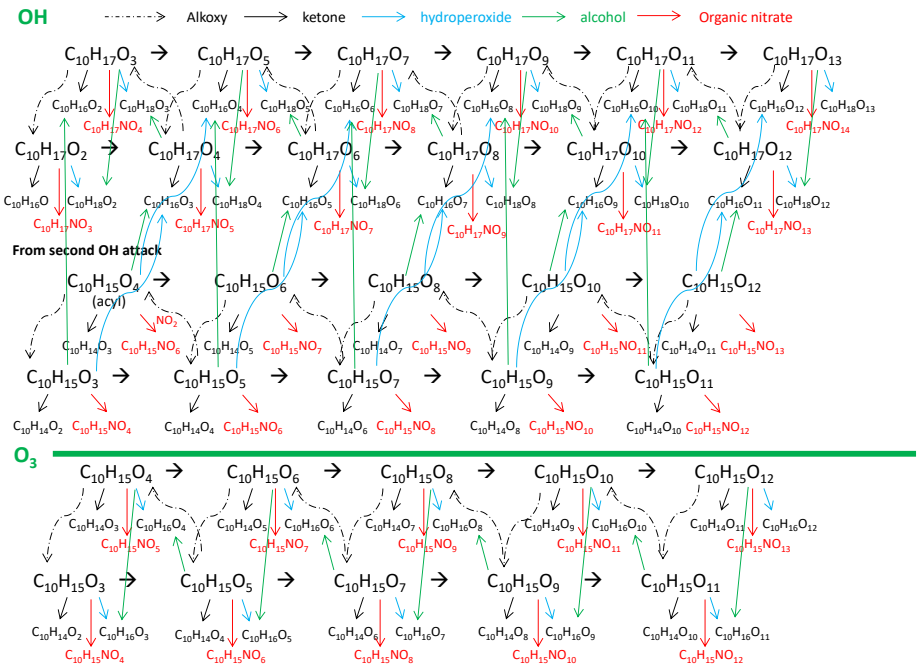

Figure 2.13: The map of the α-pinene oxidation by the OH radical and O_3. The upper part shows the oxidation of α-pinene by the OH radical and the lower part shows the ozonolysis. Peroxy radicals, reaction pathways, and resulting products are shown. The $C_{10}H_{15}O_4$ peroxy radical in the beginning of the ozonolysis is formed via VHP. Autoxidation goes from the left to the right and increases the oxygen number by two. Dashed lined arrow indicates the alkoxy radical involving path. The black arrow pathways produce carbonyl termination products, while blue arrows pathways produce hydroperoxides. The green and red arrows pathway produce alcohols and organic nitrates, respectively. In this way, the potential origin of an observed compound can be tracked and possible information on the formation mechanism can be achieved.

mass spectra show a limited number of analyte peaks that constitute a dominant portion of total signal in the steady-state. For example, the peak of $C_{10}H_{16}O_7$ is the dominant peak in the mass spectra of α-pinene photooxidation. As a consequence, the $C_{10}H_{16}O_7$ as a major compound points out the specific tendency of its family ($C_{10}H_{16}O_z$). However, not all $C_{10}H_{16}O_z$ family members behave the same way as $C_{10}H_{16}O_7$. Therefore, the behaviour of individual compounds needs to be investigated as well. This is why the marker analysis beyond family analysis is needed for better understanding of oxidation mechanism. Here, the "Marker analysis" is defined as an investigation of individual compounds in each family with focus on the major compound(s) in each family. This will allow us to derive mechanistic information of HOM formation on molecular level in addition to the understanding of the major flows in the formation mechanisms.

Table 1. C_{10} Monomer Classification*

	14 hydrogens	15 hydrogens	16 hydrogens	17 hydrogens	18 hydrogens
Even O	unimolecular R2, carbonyl R4a, alkoxy-O_2 R5	primary radical R1	hydroperoxyl R3a, hydroxyl R4a, unimolecular R2, carbonyl R4a, alkoxy-O2 R5	alkoxy R1	hydroxyl R4a
Odd O	unimolecular R2, carbonyl R4a, alkoxy-O_2 R5	alkoxy R1	hydroxyl R4a, hydroperoxyl R3a	primary radical R1	hydroperoxyl R3a

*In gray, first-generation products from the AP ozonolysis without the alkoxy autoxidation pathway (Scheme S1 of the Supporting Information); in blue, products from the AP ozonolysis that went through an alkoxy rearrangement step (Scheme S2 of the Supporting Information); and in orange, first-generation products from the OH addition autoxidation mechanism (Scheme S3 of the Supporting Information). The reaction pathway to the products is also indicated.

Figure 2.14: Classification of products from α-pinene(AP) ozonolysis. Adapted from Molteni *et al.*, 2019.

2.3.4 Kendrick mass defect plot

A mass defect is defined as a difference between the integer mass and the exact mass of a compound. A mass defect can be either positive or negative depending on the atoms in the compounds. Mass defect is a key feature for a high resolution mass analysis and it can be very useful.

A Kendrick mass is defined by setting the mass of a certain molecular unit to an integer value (typically, setting -CH_2- to 14.000 Da). The purpose of the Kendrick mass is to help the visualisation of the data by aligning compounds that have the same Kendrick mass defect in a collinear manner. In the case of CH_2 unit, Kendrick mass is defined as follows.

$$Kendrikmass = IUPACmass \times \frac{14.00000}{14.01565} \tag{2.3.1}$$

The unit of CH_2 is used mostly in the petroleomics. The CO_2, H_2, or O-atom can be used as a Kendrick mass base as well. The Kendrick mass defect is the difference between integer mass and Kendrick exact mass. In Kendrick mass analysis, the Kendrick mass defect is plotted against Kendrick mass. The O-atom was used in this work because the number of O-atoms is a key parameter to elucidate the mechanisms of HOM formation. The Kendrick plot adds one dimension to the mass spectra and make it easier to recognise series of compound groups. The following figure shows an example of the Kendrick mass defect plot.

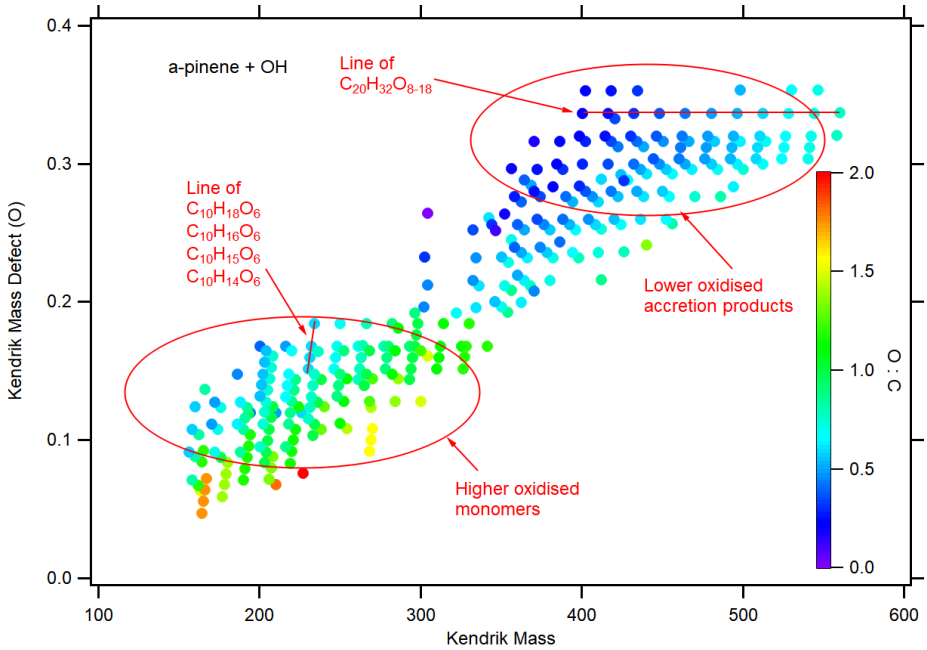

Figure 2.15: An example of the Kendrick mass defect plot for α-pinene photooxidation. The x-axis shows Kendrick mass and the y-axis shows Kendrick mass defect. Reagent ions were not considered in the calculation. The O-atom was used as a unit. Color code represents the O:C ratio of the compounds.

Figure 2.15 shows the Kendrick mass defect plot for the α-pinene photooxidation. Each dot represents one compound. The Kendrick mass defect of each compound is plotted against Kendrick mass (base unit: oxygen). In low Kendrick mass range (160-210 Da), monomers with carbon numbers less than 10 are located. As colour code of monomer range shows, monomers have higher oxidation degree than accretion products. A vertical line in monomer range shows a pattern of $C_{10}H_yO_6$ monomers with different H-atoms. On the other hand, compounds with the same carbon and hydrogen number and only different oxygen number are located on the same horizontal lines as shown in the series of $C_{20}H_{32}O_{8\text{-}18}$. This is because the base unit is oxygen which makes only integer difference in the Kendrick mass defect for the compounds in the same family. Accretion products with the high carbon and hydrogen numbers with relatively low O:C ratio are located in higher Kendrick mass range (350 Da-580 Da). Since hydrogen has a large positive mass defect and oxygen has a small negative mass defect, accretion products which have a low degree of oxidation show a large positive Kendrick mass defect. As one can see, Kendrick mass defect plots are a very helpful visualisation tool to find certain series of compounds or to investigate chemical properties of compounds. Therefore, the Kendrick mass defect plot will be used in this thesis for analysis.

2.4 Corrections and assumptions

2.4.1 Corrections for turnover and particle surface in NOx experiments

In this section, the correction factors used in Chapter 4 will be described.

The presence or absence of the NOx in the system controls the OH radical concentration by following reactions (Finlayson-Pitts and Pitts Jr, 1999).

$$HO_2 + NO \longrightarrow OH + NO_2 \qquad \text{R2.4.19}$$

$$OH + NO_2 \longrightarrow HNO_3 \qquad \text{R2.4.20}$$

A lower or a higher OH radical concentrations affect the turnover which is here defined as the product of the reaction coefficient (α-pinene + OH), the α-pinene concentration and the OH radical concentration (k_{OH}·[OH]·[α-pinene]). The turnover determines the production rate of RO_2, thus the HOM production rate. In HOM experiments sometime new particle formation driven by HOM cannot be avoided. Besides regulating OH radical concentration, NOx suppresses a new particle formation (Wildt *et al.*, 2014) which can cause a reduction of loss of HOM to particles with increasing NOx concentration. Both effects have an impact on the HOM concentration in the gas phase and make the evaluation of the changes in HOM chemistry induced by NOx itself difficult. Therefore, the corrections for both effects are needed for the comparisons of chemistry at different NOx concentrations. The correction for the impact of NOx on the OH radical concentration was derived by measuring the relation between HOM concentration and turnover. The OH concentration and therewith the turnover was changed by varying the photolysis rate of O_3, j(O^1D) (The same set of experiments was used in Chapter 3 to investigate the dependency of HOM on OH radical concentrations).

Figure 2.16 shows the power-law plot of the HOM concentration (c(HOM)) and the turnover of the α-pinene by the OH radicals. A non-linear dependence of ln(c(HOM)) on ln(turnover) was observed. The main reason is the contribution to HOM by ozonolysis of α-pinene. Therefore, only the data obtained at turnover higher than 4.1 $\times$ 10^7 cm^{-3} s^{-1} (ln(turnover) > 17.5) were selected to minimise the influence of the ozonolysis. In this range, the turnover by the OH radicals was an order of magnitude higher than the turnover by the ozone (In all the NOx experiments, the oxidation by the OH radicals was dominant). Fitting to the power-law plot gave a slope of 1.47 $\pm$ 0.07. Using this slope, a normalisation to the turnover of HOM at zero NOx was achieved by the following equation.

$$C_{\mathrm{R}}(HOM) = \frac{Tnv_R^{1.47}}{Tnv_M^{1.47}} \cdot C_{\mathrm{M}}(HOM) \qquad (2.4.1)$$

$C_{\mathrm{R}}(HOM)$ is the HOM concentration at the reference turnover Tnv_R while $C_{\mathrm{M}}(HOM)$ is the HOM concentration at the actually measured turnover Tnv_M. The correction factor is given by

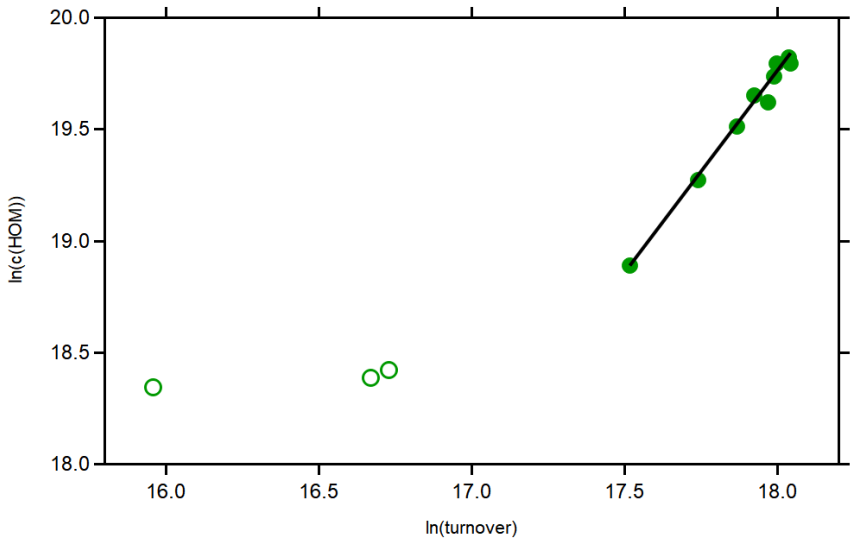

Figure 2.16: Plot of the ln(C(HOM)) versus ln(turnover). Open circles shows where the oxidation of α-pinene by ozonolysis was significant compared to the oxidation by OH radical. Here, only filled circles were used where the turnover by OH oxidation was dominant. The fitting to the power law gave a slope of 1.47 $\pm$ 0.07. Adapted from Pullinen *et al.*, 2020.

the ratio of the reference turnover to the actual measured turnover to the power of 1.47: $\frac{Tnv_R^{1.47}}{Tnv_M^{1.47}}$. The correction factor varied by less than 30 % within the NOx experiment series.

For the correction of the HOM loss onto newly formed particles, a normalisation of the HOM concentration to particle-free condition was performed. The method is similar to the methods to determine the effective uptake coefficients of HOM (Pullinen *et al.*, 2020) and the wall loss of HOM (Sarrafzadeh *et al.*, 2016). $C(HOM)$ is determined by its production rate ($P(HOM)$) and the first-order loss rate ($L(HOM)$).

$$C(HOM) = \frac{P(HOM)}{L(HOM)} \tag{2.4.2}$$

When there are no particles in the system, the total loss rate $L(HOM)$ is solely determined by the loss to the walls $L_w(HOM)$. However, in the presence of particles, loss of HOM is determined by a loss to the wall and by loss to the particles ($L_w(HOM)$+$L_p(HOM)$). When the production rate of HOM is constant, the ratio of the HOM concentrations in the absence and in the presence of particles is proportional to the inverse of the ratio of their loss rates.

$$\frac{C(HOM)^0}{C(HOM)} = \frac{L_w(HOM) + L_p(HOM))}{L_w(HOM)} \tag{2.4.3}$$

In equation 2.4.3, the $C(HOM)^0$ is the HOM concentration at the particle-free conditions and the $C(HOM)$ is the HOM concentration in the presence of particles. Since signal and concentration is proportional, the following equation can be derived.

$$\frac{S(HOM)^0}{S(HOM)} = \frac{C(HOM)^0}{C(HOM)} = \frac{L_w(HOM) + L_p(HOM))}{L_w(HOM)} \tag{2.4.4}$$

In equation 2.4.4, the $S(HOM)^0$ is the measured signal of HOM in the absence of particles and $S(HOM)$ is the HOM signal when there are particles present. $L_w(HOM)$ could be determined from the loss of HOM after stopping a HOM production, the $L_p(HOM)$ can be calculated by the equation 2.4.4. Once knowing the $L_w(HOM)$ and the $L_p(HOM)$ as a function of particle surface, the $C(HOM)^0$ can be extrapolated from measured $C(HOM)$ during in any other experiment by applying the correction factor $\frac{L_w(HOM)+L_p(HOM))}{L_w(HOM)}$.

The corrected HOM signal is achieved by multiplying the two correction factors.

$$S(HOM)^0 = S_M(HOM) \cdot \frac{L_w(HOM) + L_p(HOM))}{L_w(HOM)} \cdot \frac{Tnv_R^{1.47}}{Tnv_M^{1.47}} \tag{2.4.5}$$

This correction was applied in Chapter 4 to compare the effects of NOx itself under various NOx conditions after removing the OH effect and particle sink effect.

2.4.2 Assumptions

There are a few assumptions that need to be clarified for a better understanding of the approaches and methodology in this study. Firstly, the HOM with six or more oxygen atoms in the molecules are detected with the same sensitivity by NO_3^- CIMS (Hyttinen *et al.*, 2017; Riva *et al.*, 2019). In this way, the semi-quantitative comparisons of mass spectral information can be conducted. Secondly, it is assumed that HOM-RO_2 react in a similar way as classical, less oxygenated RO_2. In addition, the mechanisms in the master chemical mechanism (MCMv v3.3.1.) was adopted for conclusions based on chemical analogy for the unknown HOM chemistry. These assumptions gave a possibility to predict which type of HOM closed-shell products can be expected. Thirdly, the "disproportionation" reaction of a RO_2 with another peroxy radicals (R1.2.8) is anticipated to produce alcohol and carbonyl compounds with equal probability, even though there might be a structural preference (for example, a peroxy radical which does not have an H-atom to be abstracted will prefer become alcohol). 50/50 chance for the alcohols and carbonyls are statistically likely if RO_2 of all kinds are involved. Finally, It is assumed that the accretion product formation (R1.2.9) involves a pre-stabilised cluster of two RO_2 in a coarse analogy to the Lindemann-Hinshelwood mechanism which describe an unimolecular reaction by two elementary steps (Steinfeld, Francisco, and Hase, 1999).

Chapter 3

Photochemical oxidation of α-pinene: Dependency on OH concentration and effect of CO and small peroxy radicals

In this chapter, results from the different α-pinene photochemical systems will be investigated. Time traces for HOM moonmers and accretion products were shown in Figure 2.2. Two hypotheses are pursed : HOM are (majorly) formed from α-pinene oxidation products and alkoxy radicals play a role in HOM formation.

In all experiment sets, contributions by ozonolysis of α-pinene were observed. Therefore, the mass spectra of α-pinene ozonolysis experiments will be discussed before focusing on the effects of an increasing OH concentration. In addition, the effect of CO and small peroxy radicals from isoprene on photochemical HOM formation by α-pinene will be discussed in two chapters.

3.1 Ozonolysis of α-pinene

Since OH radicals were produced by O_3 photolysis in our experiments, there will be a (varying) contribution of ozonolysis in all experiments. α-pinene can form HOM via ozonolysis: in the first step Criegee Intermediates (CI) are formed. One important pathway of CI is to form vinylhydroperoxides that decompose to peroxy radicals with aldehyde functionality (Johnson and Marston, 2008). These peroxy radicals undergo several internal H-shifts followed by O_2 addition (autoxidation, Mentel *et al.*, 2015). In this section, mass spectra taken during α-pinene ozonolysis and major ozonolysis products will be introduced. In addition, the signal of the most abundant products and their precursors will be discussed in order to suggest formation mechanisms of the compounds.

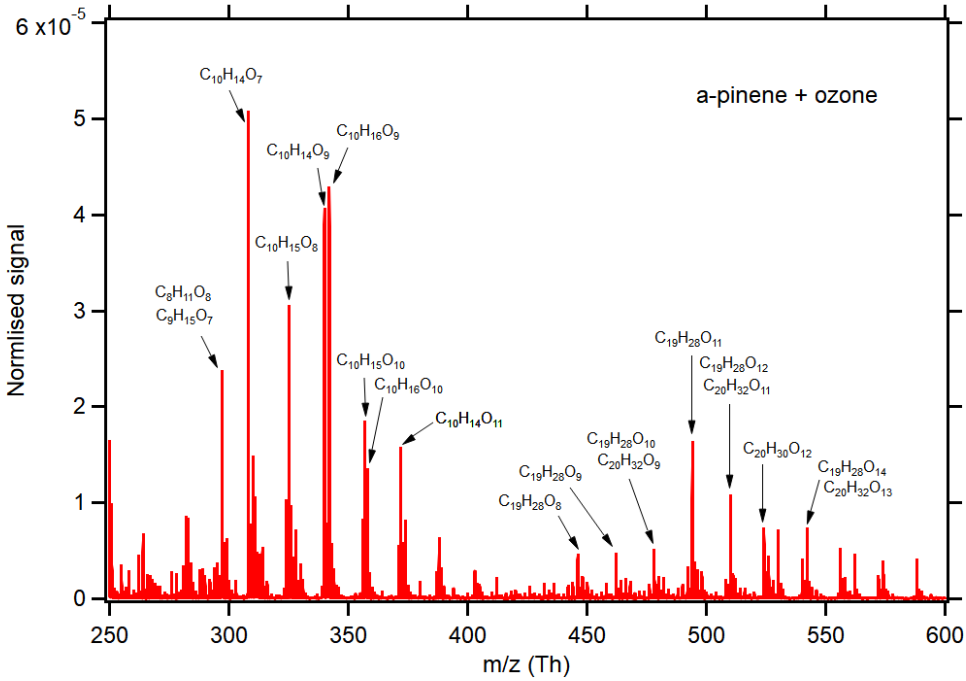

Figure 3.1: Typical mass spectrum of α-pinene ozonolysis. The x-axis shows mass to charge ratio (m/z) and the y-axis shows the signal normalised to the total ion signal. The m/z shown is including the nitrate ion (NO_3^-). Compounds with relatively high signal are shown.

3.1.1 Mass spectrum of α-pinene ozonolysis

Figure 3.1 shows a mass spectrum during steady state in an α-pinene ozonolysis experiment. The x-axis shows the mass to charge ratio and the y-axis shows the normalised signal of detected compounds. Most of the identified compounds were detected as clusters with a nitrate ion (NO_3^-). One can clearly recognise the region of monomers which is dominated by C_{10} compounds and the region of accretion products which comprises C_{19} and C_{20} compounds.

The most abundant molecules have the sum formula $C_{10}H_{14}O_7$ which is likely carbonyl compounds. They are termination products arising from the reaction R1.2.8. Their mother peroxy radical is $C_{10}H_{15}O_8$ which appeared to be the most abundant peroxy radicals in the mass spectra. The even number of oxygen in the $C_{10}H_{15}O_8$ can be rationalised by the fact that the first peroxy radical in α-pinene ozonolysis is $C_{10}H_{15}O_4$ which has an even number of oxygen. This radical can undergo two steps of autoxidation adding two more molecular oxygen and become $C_{10}H_{15}O_8$. It is noteworthy that the expected alcohol product from the disproportionation reaction R1.2.8, $C_{10}H_{16}O_7$, was found in large concentrations. One would expect a similar signal of $C_{10}H_{14}O_7$ and $C_{10}H_{16}O_7$ in the disproportionation reaction of $C_{10}H_{15}O_8$ with all other RO_2 if the chances to form alcohol $C_{10}H_{16}O_7$ or carbonyl $C_{10}H_{14}O_7$ are similar for both reaction partners. Therefore, it is a question why $C_{10}H_{16}O_7$ showed relatively lower concentration than

$C_{10}H_{14}O_7$. One possibility could be that carbonyl formation is preferred because of a specific structure of the $C_{10}H_{15}O_8$ peroxy radicals.

The second highest set of peroxy radicals and their termination products from the reaction R1.2.8 are $C_{10}H_{15}O_{10}$, $C_{10}H_{14}O_9$ and $C_{10}H_{16}O_9$. Here, the ratios of carbonyl compound and alcohol are almost equal. $C_{10}H_{16}O_9$ had a somewhat higher signal. This is possibly because $C_{10}H_{16}O_9$ could be originated from the $C_{10}H_{15}O_9$ peroxy radicals by reaction with HO_2 radicals as well.

In case of accretion products, a clear progression pattern was observed. The highest signal in each progression came from the $C_{19}H_{28}O_z$ family. This family can be formed from the combination of two peroxy radicals such as $C_{10}H_{15}O_x$ and $C_9H_{13}O_y$ (with z=x+y-2). The other families which had large signals were the $C_{20}H_{30}O_z$ family and the $C_{20}H_{32}O_z$ family. The $C_{20}H_{30}O_z$ family can be formed from two $C_{10}H_{15}O_{x,y}$ peroxy radicals and the $C_{20}H_{32}O_z$ family can be formed from the combination of the $C_{10}H_{15}O_x$ and $C_{10}H_{17}O_x$ peroxy radical families. Peroxy radicals with a lower degree of oxidation were likely participating in the process of forming accretion products. This is supported by the lower O:C ratio of accretion products compared to monomers, even after considering the loss of two O-atoms in the formation process.

3.1.2 Comparison of mass spectra of α-pinene ozonolysis in different experiments

The experiment protocols always included an ozonolysis phase in the photooxidation experiments. The reproducibility of the ozonolysis contribution was confirmed for different experiments and examples of mass spectra are shown in Figure 3.2.

Experiments were performed at different α-pinene and ozone concentrations, which means they had different α-pinene turnovers. Therefore, the relative intensity of individual peaks in the mass spectra varied somewhat. For example, the relative intensity of $C_{10}H_{14}O_9$ at 340 Th and $C_{10}H_{16}O_9$ at 342 Th compared to $C_{10}H_{14}O_7$ at 308 Th was dissimilar in the NOx experiment and in the j(O^1D) experiment (the ratio of $C_{10}H_{14}O_9$ / $C_{10}H_{16}O_9$ was 0.95 in j(O^1D) experiment and 0.85 in NOx experiment). Additionally, the relative importance of $C_{10}H_{15}O_8$ at 325 Th varied (the ratio of $C_{10}H_{15}O_8/C_{10}H_{14}O_7$ was 0.625 in j(O^1D) experiment and 0.25 in NOx experiment). Despite these variations, it is concluded that the resulting product pattern was the same throughout all experiment series.

3.2 Photochemical oxidation of α-pinene: Dependency on OH concentration

Unlike O_3, the OH radical can attack α-pinene molecules by addition to the double bond and by H-abstraction. Moreover, OH attack can happen multiple times. Pullinen, 2016 investigated the effect of the OH concentration and product pattern on unit mass resolution level under aspects

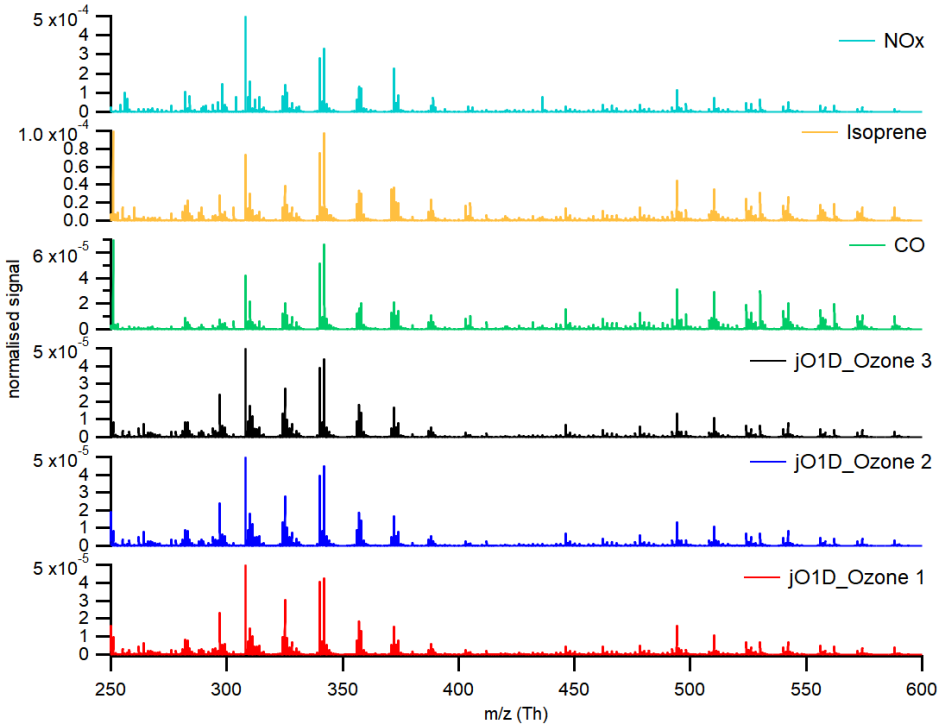

Figure 3.2: Comparison of mass spectra observed during α-pinene ozonolysis phases. Three lower mass spectra (red, blue and black) are from the ozonolysis phase of different "j(O^1D)" experiments. The green mass spectrum is from the "CO experiment" (without CO). The yellow mass spectrum is from "α-pinene + isoprene" experiment series. This spectrum was taken before isoprene injection and OH production. Finally, the most upper mass spectrum in turquoise is from "α-pinene + NOx" series. It was taken before NOx injection and OH production. Because $^{15}NO_3^-$ was used as a reagent ion in the NOx experiments, the mass spectrum was shifted by 0.99704 Th to lower m/z for the direct comparison.

of the competition of autoxidation and sequential OH addition. It was shown that autoxidation has more importance than sequential OH addition because the relative intensity of different oxygenated compounds was not inclined to a higher oxidation state with higher OH radical concentration. Here, the analysis will be extended to high resolution and the systematic effect of the OH concentration on the product distribution will be investigated.

As it was explained in Chapter 2, the OH concentration was controlled by varying the gap between two UV absorbing glasses shielding the TUV lamp. That means the bigger the gap, the higher was the O_3 photolysis frequency (j(O^1D)) and the OH production. Figure 3.3 shows the mass spectra observed at steady state conditions with an increasing TUV gap, thus increasing OH concentration and α-pinene turnover. Because the peak at 310 Th was the highest peak compared to other peaks, it is clipped here for easier comparison of other peaks, with the intensity of peak at 310 Th given by number. At the lowest OH concentration (6.7×10^6

molecules cm^{-3}), the fewest HOM were observed. When the OH concentration reached 2.32 $\times$ 10^{7} molecules cm^{-3}, the mass spectra started to look similar: there was one major peak at 310 Th ($C_{10}H_{16}O_7$ as nitrate ion cluster) and sequences of additional peaks with a difference of 16 Th with increasing m/z.

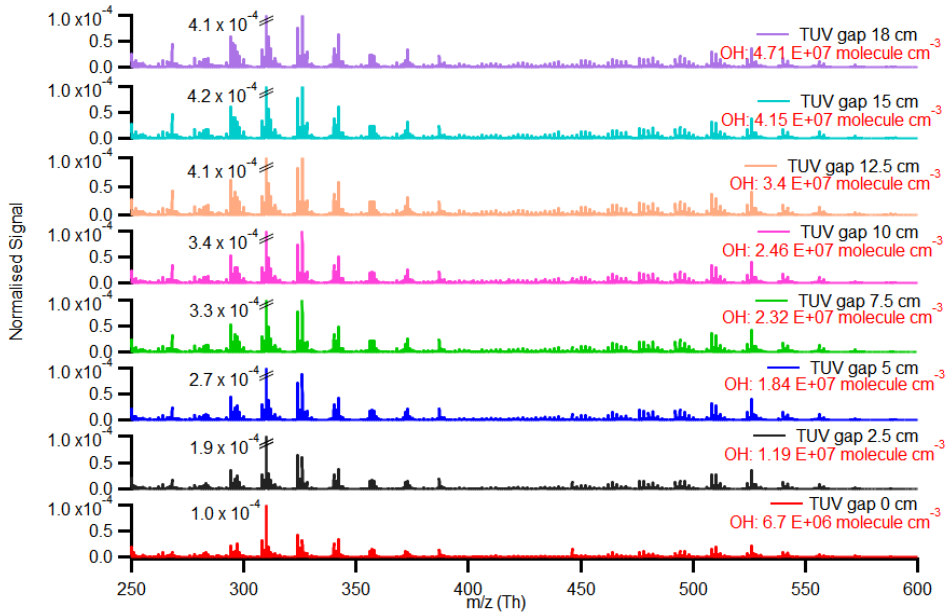

Figure 3.3: Mass spectra observed at different OH concentrations in "j(O^1D)" experiment. The mass spectra was averaged over 30-60 minutes for steady state periods. The y-axis shows signal normalised to the total ion signal and the x-axis shows mass per charge ratio, including the reagent ion. On the right upper corner of each mass spectrum, TUV gap and OH radical concentration during steady state are given. Note that highest peak at 310 Th is cut off. The normalised signal of $C_{10}H_{16}O_7$ is written next to the peak.

In the monomer range (250 Th to 400 Th), the pattern of the mass spectra did not change much. There is no evidence of a higher degree of oxidation of termination products caused by higher OH concentrations.

However, the small relative changes between peaks were observed, e.g. notable for the two peaks at m/z 324 Th and 326 Th with the molecular formulas $C_{10}H_{14}O_8$ and $C_{10}H_{16}O_8$. At the lowest OH concentration, which is shown in red in Figure 3.3, the intensity of $C_{10}H_{14}O_8$ at 324 Th was slightly higher than that of $C_{10}H_{16}O_8$ at 326 Th. However, as OH concentration was increasing, the concentration of $C_{10}H_{16}O_8$ started to grow and surpass the concentration of $C_{10}H_{14}O_8$. Another example of change can be seen for the signal at 295 Th which increased with OH. This peak has an odd mass per charge ratio which indicates that it arises from peroxy radicals. The high resolution peak analysis showed that the peak at 295 Th had overlapping contributions by $C_8H_9O_8$ and $C_9H_{13}O_7$, both peroxy radicals and that there was a negligible

contribution by the $C_{10}H_{17}O_6$ peroxy radical. The increase of $C_8H_9O_8$ and $C_9H_{13}O_7$ peroxy radicals with increasing OH concentration indicates already in the mass spectra an increasing importance of alkoxy radicals and their fragmentation according to the reaction R1.2.10. The increase of fragmentation will be discussed in the next section.

In the accretion product range (450 Th - 600 Th), there were almost no differences except for the mass spectrum at the lowest OH concentration. At low OH concentration, there were fewer accretion products because there were less RO_2 radicals available for accretion products. For the same reason, there were less monomers in the mass spectrum at the lowest OH concentration Despite of minor changes, termination product patterns in the mass spectra look very similar for different OH concentrations. Moreover, there was no distinct evidence of any stronger oxidation degree because of the increase of multiple OH reactions of α-pinene.

3.2.1 Effect of increasing turnover on the concentration of sum of HOM, monomers and accretion products

The increase of steady state OH concentrations lead to increasing α-pinene consumption and increasing turnover. Turnover will be used in this analysis because turnover indicates how many peroxy radicals were produced from α-pinene and OH radical reaction. In the following, the observed changes in the concentration of HOM as a function of the turnover will be shown and discussed.

Figure 3.4 shows the normalised signals for the sum of HOM, HOM monomers, and HOM accretion products on a logarithmic scale as a function of turnover. At turnovers higher than 4 $\times$ 10^7 cm^{-3} s^{-1} more than 90% of the α-pinene is consumed by OH radicals, i.e. in this range the contributions by ozonolysis became negligible. The monomer concentration increased strongly with turnover in a non-linear fashion. The non-linear increase with turnover supports the hypothesis that OH attack on oxidation products like pinonaldehyde contributes to HOM formation. Increasing concentration of peroxy radicals with increasing turnover escalates termination reactions between two RO_2, R1.2.8. However, not all families increased in a similar manner.

Accretion products increased non-linearly with turnover as well in the beginning. At turnover higher than 5.75 $\times$ 10^7 cm^{-3} s^{-1}, new particle formation was observed. The saturation of accretion products at high turnover can thus possibly be explained by new particle formation aided by accretion products. The specific role of accretion products in new particle formation was also observed in other studies (Schobesberger *et al.*, 2013; Riccobono *et al.*, 2014; Bianchi *et al.*, 2016; Tröstl *et al.*, 2016; Kirkby *et al.*, 2016).

Figure 3.5 analyses the sum of monomers as a function of the turnover. Monomers were divided into two different groups. One group comprised monomers with ten carbon atoms, the other groups comprised of monomers with five to nine carbon atoms resulting from fragmentation processes. Fragmented monomers can be formed via alkoxy radicals from the reaction between two peroxy radicals (R1.2.10). Both C_{10} monomers and $C_{5\text{-}9}$ monomers increased with

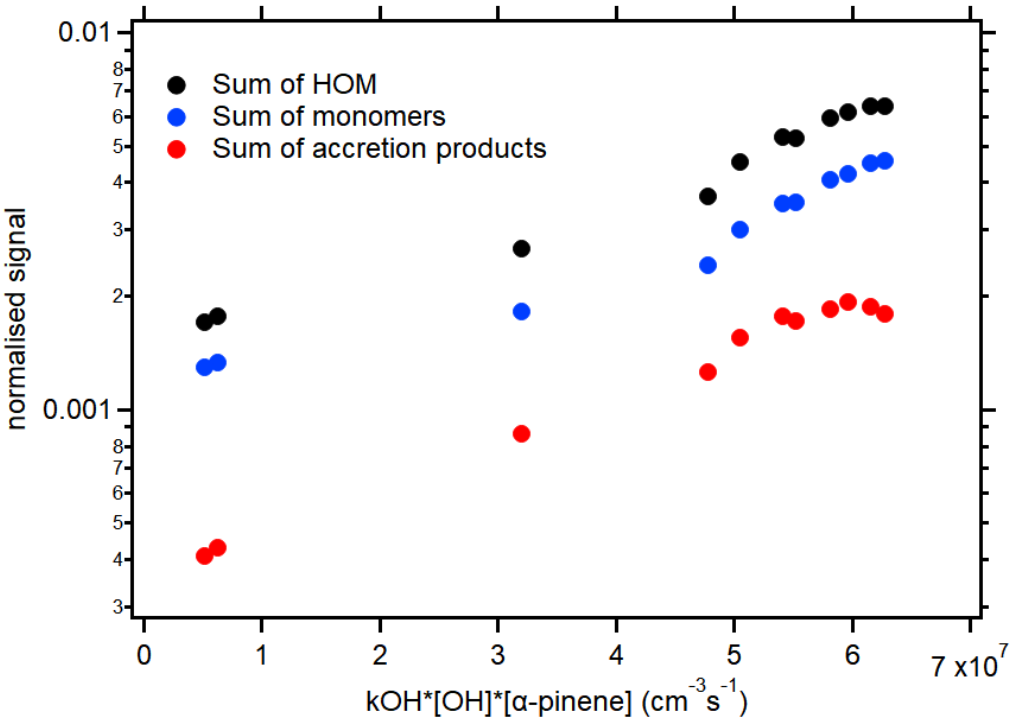

Figure 3.4: The sum of HOM, monomers, and accretion products as a function of turnover. The signals were normalised to total ion counts. As turnover increased, the sum of HOM, monomers increased in nonlinear manner and accretion products showed saturation at high turnovers.

turnover. At the highest turnovers (> 5×10^7 cm^{-3} s^{-1}) where OH was the major oxidant (>90 %), the slope of increase was steeper for fragmented monomers (7.7×10^{-11}) than for C_{10} monomers (5.7×10^{-11}). This can be explained by the increased importance of alkoxy radicals formed by reaction R1.2.10.

As for monomers, also a non-linear increase of accretion products with increasing turnover was observed as shown in Figure 3.6. Unlike monomers, the concentration of accretion products showed a saturation effect at high turnovers. Especially C_{20} accretion products strongly saturated in the graph. The effect is less expressed for $C_{11\text{-}19}$ accretion products. There could be two reasons why C_{20} and $C_{11\text{-}19}$ accretion products showed different behaviour. One reason is an increase of smaller peroxy radicals as turnover increased, because of the fragmentation processes via alkoxy radicals. Smaller peroxy radicals formed smaller accretion products with less than 20 carbon atoms in the molecule. As a consequence, a higher formation of smaller accretion products made the curve less bent. Another reason could be that the smaller accretion products with less than 20 carbons have higher vapour pressure than C_{20} accretion products. That means the loss of smaller accretion products by new particle formation is smaller than that of C_{20} accretion products. In short, despite of possible condensation on the newly formed

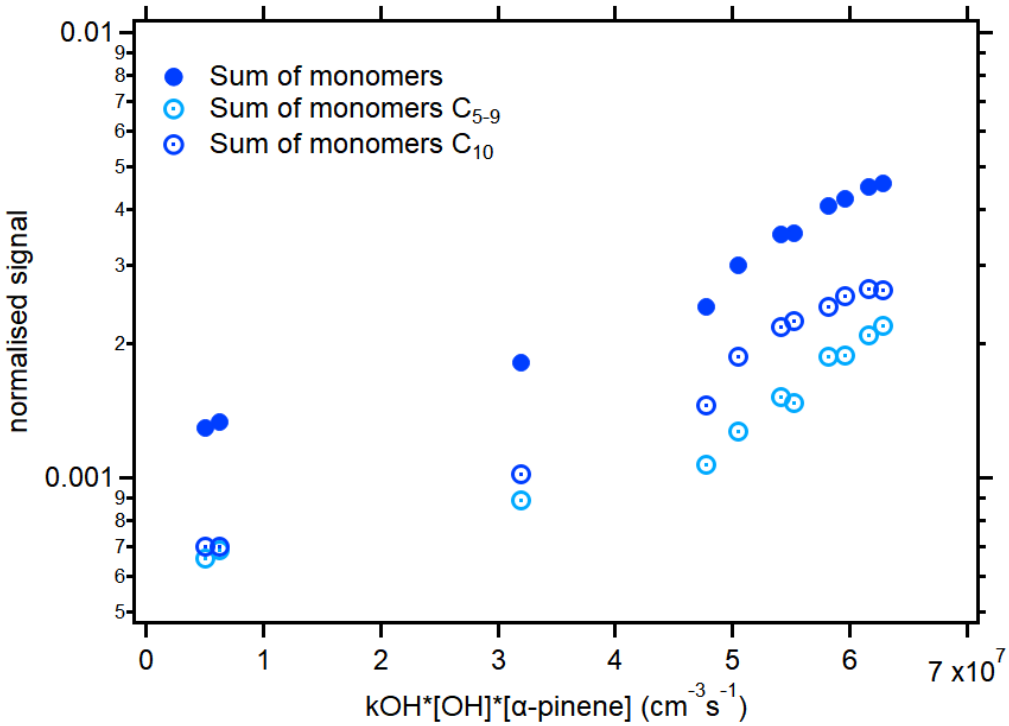

Figure 3.5: The sum of monomers vs turnover. Signals were normalised to total ion counts. Blue filled circles represent the sum of all monomers. Light blue open circles show the sum signal of fragmented monomers that have 5-9 carbon atoms. Blue open circles show monomers with 10 carbon atoms.

particle, smaller accretion products showed increased signal or milder bend over than C_{20} accretion products, because of stronger production from the increased concentration of smaller peroxy radicals and diminished loss than C_{20} accretion products.

3.2.2 Changes of families with increasing turnover

In this chapter, the effect of increasing OH concentrations and turnover on the C_{10} and C_{20} families will be described.

As explained in Chapter 2, families refer to molecules with same number of carbon-, hydrogen atoms but different number of oxygen atoms: in the molecular formula $C_xH_yO_z$, members of same family have same x, y but different z. In the C_{10} group, there were five families, namely $C_{10}H_{14}O_z$, $C_{10}H_{15}O_z$, $C_{10}H_{16}O_z$, $C_{10}H_{17}O_z$ and, $C_{10}H_{18}O_z$. The intensities of the signals of different families will be compared to deduce origin and formation mechanism of each family.

Expected behaviour of each family with increasing OH concentration, thus increasing turnover, will be analysed considering the peroxy radical chemistry as implemented in the chemical master mechanism (MCM v3.3.1) and HO_2 and RO_2 concentrations predicted by box model calculations. I.e. the chemistry of HOM formation will be compared to expectations from classical

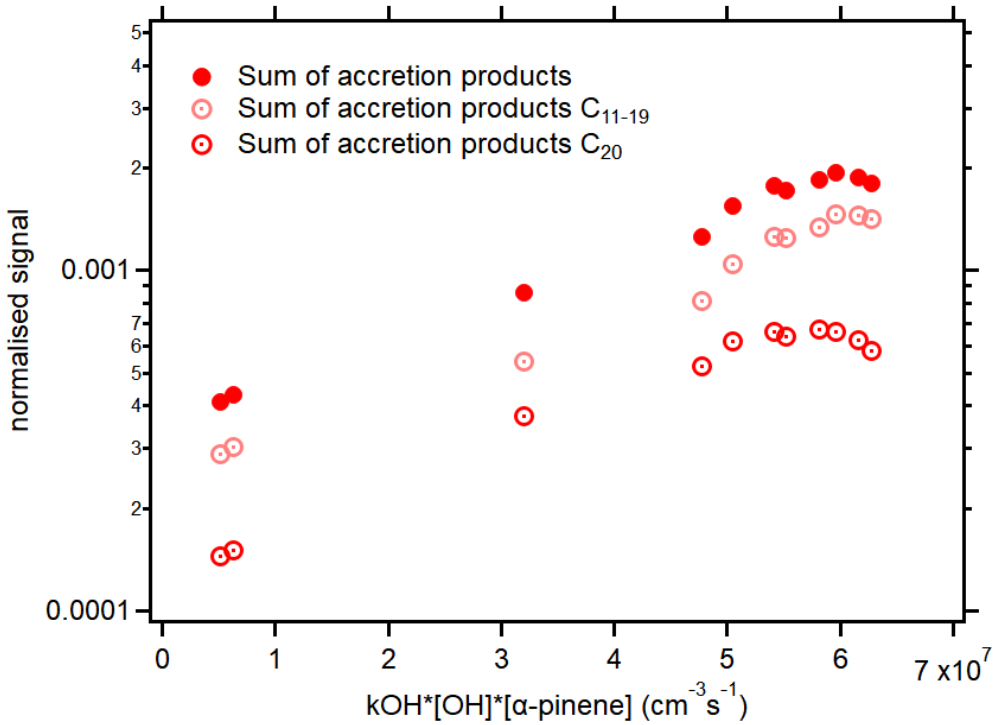

Figure 3.6: The sum of the signal of accretion products normalised to total ion counts vs turnover. Red filled circles represent the sum of all accretion products. Pink open circles show sum signal of accretion products with less than 20 carbons in the molecule($C_{11\text{-}19}$). Red open circles show accretion products that had 20 carbons in the molecule.

peroxy chemistry. The box model calculations were performed applying MCM v3.3.1 under the boundary conditions of the JPAC chamber and prediction of O_3, OH, α-pinene, and NO_X within the experimental errors (box model calculations were provided by S.Proff). HO_2 and RO_2 concentrations are shown in Figure 3.7.

Figure 3.7 shows the calculated RO_2 (grey hashtag) and HO_2 (green star) concentration as a function of turnover. As turnover increased, both RO_2 and HO_2 increased. The concentration of RO_2 was two orders of magnitude higher than HO_2 as can be seen in the ratio of HO_2 and RO_2 (blue filled circles). Since the degree of increase in [HO_2] was higher than that of [RO_2], the ratio HO_2/RO_2 increased as a function of turnover.

Figure 3.8 shows groups of RO_2 predicted by model calculation based on MCM v3.3.1. $C_{10}H_{17}O_3$ (light green circles) which are the primary peroxy radicals from α-pinene OH oxidation increased linearly as turnover increased. On the other hand, $C_{10}H_{15}O_4$ peroxy radicals from Criegee Intermediates (CI) in α-pinene ozonolysis (red triangles) show a decrease with increasing turnover. The concentration of $C_{10}H_{15}O_4$ peroxy radicals that are formed in the second attack of oxidation products show an increase in non-linear manner. Autoxidation of $C_{10}H_{15}O_4$ will lead to a family of peroxy radicals with formula $C_{10}H_{15}O_{z=even}$. In reaction with

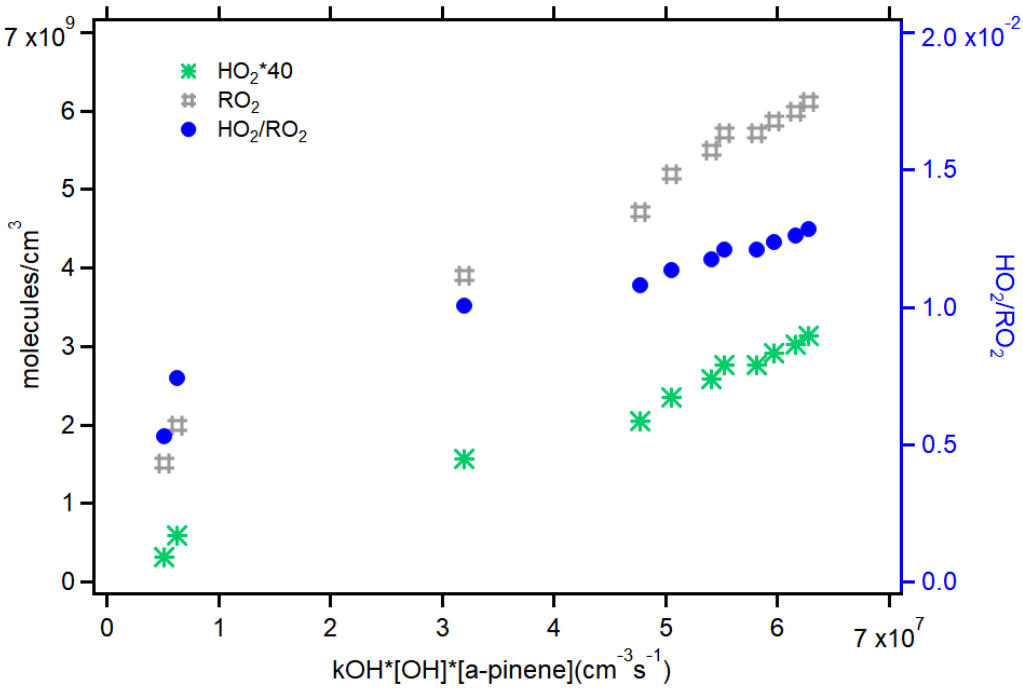

Figure 3.7: HO_2 radicals and RO_2 radicals concentration simulated by a box model. Green stars represent HO_2 radical concentration multiplied 40 to be on the same scale with RO_2 radicals. Grey hashtag symbols represent the concentration of RO_2 radicals. Both RO_2 and HO_2 multiplied by 40 can be read on the left y-axis. Blue filled circles show the ratio of HO_2 and RO_2 radicals which can be read on the right y-axis.

other peroxy radicals, $C_{10}H_{15}O_z$ peroxy radicals can produce $C_{10}H_{14}O_{z-1}$ which is attributed to carbonyl compounds such as ketones and aldehydes and $C_{10}H_{16}O_{z-1}$ which is attributed to alcohols (reaction R1.2.8). $C_{10}H_{15}O_{z-1}$ peroxy radicals can also produce $C_{10}H_{16}O_z$ by reaction with HO_2 (R1.2.7) which is attributed to hydroperoxides.

As a result, the detected signals of $C_{10}H_{15}O_z$, $C_{10}H_{14}O_{z-1}$, and $C_{10}H_{16}O_{z-1}$ are anticipated to be high during ozonolysis. In general, HO_2 is low in dark ozonolyis experiments (Figure 3.7) and not much contribution to the formation of the $C_{10}H_{16}O_z$ family is expected. The OH concentration during dark ozonolysis of α-pinene will not be zero, because of "dark OH" which is produced from CI as well. $C_{10}H_{17}O_{z=3}$ peroxy radicals are the primary peroxy radicals from the oxidation of α-pinene by OH (Figure 3.8) and $C_{10}H_{17}O_z$ is the according family arising from autoxidation. During ozonolysis, $C_{10}H_{17}O_z$ and the termination products from the reaction with HO_2 $C_{10}H_{18}O_z$ are expected to show low signals compared to $C_{10}H_{15}O_z$ peroxy radicals and their termination products. Since $C_{10}H_{15}O_z$ are expected to be the major peroxy radicals, the $C_{20}H_{30}O_p$ family is anticipated to form the major accretion products. In addition, there can be a small amounts of $C_{20}H_{32}O_p$ from the reactions between $C_{10}H_{15}O_z$ peroxy radicals and $C_{10}H_{17}O_q$ peroxy radicals ($p = z + q - 2$).

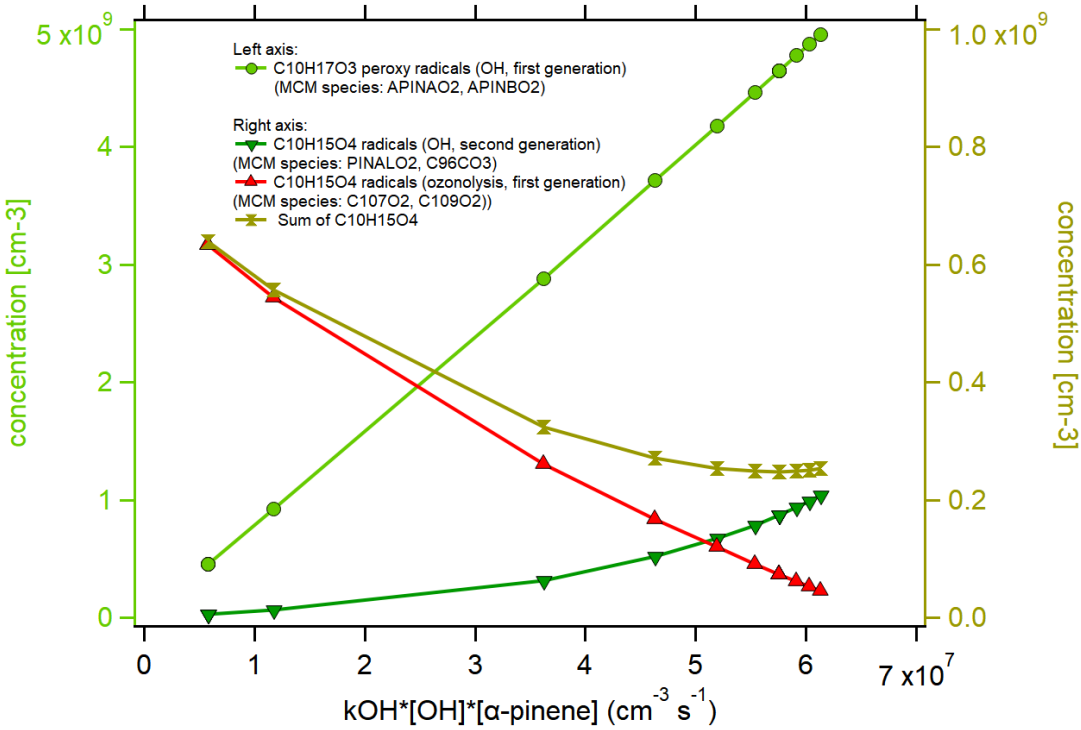

Figure 3.8: The modeled concentration of $C_{10}H_{17}O_3$ (light green circles), the primary peroxy radical of α-pinene and OH, and $C_{10}H_{15}O_4$, the peroxy radical from ozonolysis (red triangles) and secondary OH attack of oxidation product like pinonaldehyde (green upside down triangle) and sum of $C_{10}H_{15}O_4$ (olive green hourglass) as a function of turnover. The left y-axis represents the concentration of $C_{10}H_{17}O_3$ peroxy radicals and the right y-axis represents $C_{10}H_{15}O_4$ peroxy radicals from different sources.

However, in the photooxidation phase, $C_{10}H_{17}O_{z=3}$ are the main primary peroxy radicals from the reaction between α-pinene and OH radicals according to MCM v3.3.1.(Figure 3.8). And by reaction with other peroxy radicals the according autoxidation family $C_{10}H_{17}O_z$ produces $C_{10}H_{16}O_{z-1}$, i.e. carbonyls and $C_{10}H_{18}O_{z-1}$ i.e. alcohols. In addition, $C_{10}H_{17}O_z$ peroxy radicals react with HO_2 radicals and form $C_{10}H_{18}O_z$ i.e. hydroperoxides. $C_{20}H_{34}O_p$ accretion products are predicted to be the major accretion products if $C_{10}H_{17}O_z$ peroxy radicals are the major peroxy radicals.

Figure 3.9 shows the observed behaviour of C_{10} families with increasing turnover. The two data points close to turnover 5×10^6 cm^{-3} s^{-1} were results from dark experiments where ozonolysis was dominant. As expected, $C_{10}H_{15}O_z$ peroxy radicals (orange squares) showed here a higher signal compared to $C_{10}H_{17}O_z$ peroxy radicals (green squares) in panel B. The $C_{10}H_{14}O_z$ family (black circles) which was attributed to carbonyl compounds and the $C_{10}H_{16}O_z$ family (red triangles) which was attributed to alcohols or hydroperoxides from $C_{10}H_{15}O_z$ peroxy radicals (and some carbonyls from $C_{10}H_{17}O_z$ peroxy radicals) showed the top two highest signals

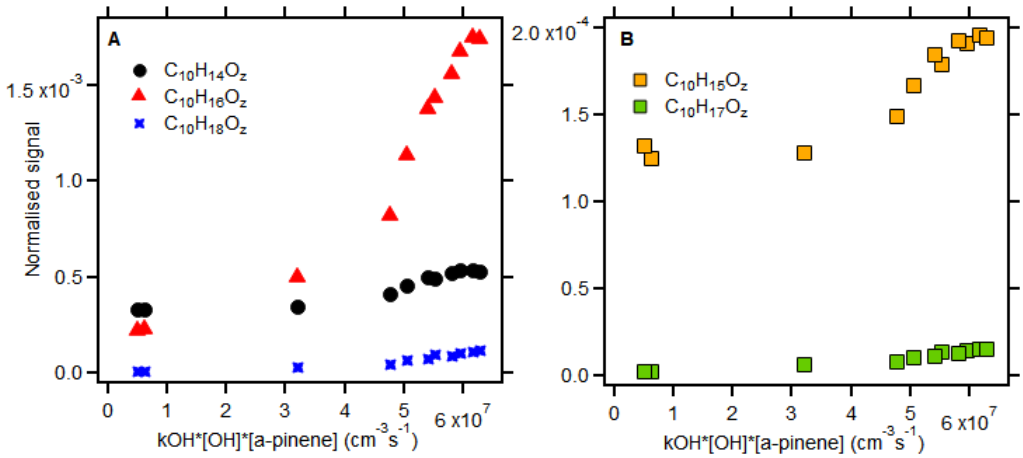

Figure 3.9: The signal of each C_{10} family normalised to total ion counts are plotted as a function of turnover. In panel A, the black circles represent normalised signal of $C_{10}H_{14}O_z$ family and red triangles, blue stars show the normalised signal of $C_{10}H_{16}O_z$, and $C_{10}H_{18}O_z$ respectively. Panel b shows the normalised signal of $C_{10}H_{15}O_z$ and $C_{10}H_{17}O_z$ family in orange and green squares.

among the C_{10} families during the dark ozonolysis phase. The $C_{10}H_{17}O_z$ peroxy radical family (green squares) and their termination products, the $C_{10}H_{18}O_z$ family (blue crosses), which can be alcohols or hydroperoxides, showed a very low signal compared to that of other families in the C_{10} group.

With increasing OH and turnover, ozonolysis becomes less important and the contribution by OH was higher than 90 % at turnover higher than 4.5×10^7 cm^{-3} s^{-1}. Despite the high photochemical turnover, $C_{10}H_{17}O_z$ peroxy radicals did not become the major peroxy radicals, as could be expected by looking at the modeled concentration of $C_{10}H_{17}O_3$ in Figure 3.8. Instead, $C_{10}H_{15}O_z$ peroxy radicals remained most abundant. In accordance, the $C_{10}H_{16}O_z$ family, alcohols and hydroperoxides, and the $C_{10}H_{14}O_z$ family, carbonyl compounds, all termination products of $C_{10}H_{15}O_z$ peroxy radicals, account for the top two highest signal of all C_{10} families. These results confirmed that $C_{10}H_{15}O_z$ peroxy radicals were the most important peroxy radicals for HOM formation, whereas $C_{10}H_{17}O_z$ peroxy radicals and their termination products, the $C_{10}H_{18}O_z$ family consisting of alcohols and hydroperoxides, showed very low signal compared to the other C_{10} families. The latter confirms a minor role of the $C_{10}H_{17}O_z$ peroxy radicals. Interestingly, the $C_{10}H_{14}O_z$ family behaves similar to the sum of $C_{10}H_{15}O_4$ radicals in the model and showed minor change with α-pinene turnover.

The $C_{10}H_{16}O_z$ family showed a strongly rising signal with increasing turnover. Three channels contribute to the formation of the $C_{10}H_{16}O_z$ family. The first channel is alcohol formation in the disproportionation reaction of $C_{10}H_{15}O_z$ peroxy radicals and other RO_2 radicals (R1.2.8). The second channel is the hydroperoxide formation from $C_{10}H_{15}O_z$ peroxy radicals reacting

with HO_2. The third channel is the formation of a carbonyl compound in the disproportionation reaction of $C_{10}H_{17}O_z$ peroxy radicals (R1.2.8).

If two same structured $C_{10}H_{15}O_z$ peroxy radicals undergo a disproportionation reaction, chances to form alcohol or carbonyl are about the same for both of them. However, if two peroxy radicals with different molecular structures undergo a disproportionation reaction, there can be preferences for each of the peroxy radical towards either an alcohol or a carbonyl group. For example, if one peroxy radical has no hydrogen to be subtracted to become carbonyl, it will preferably become alcohol. Nonetheless, considering the number of peroxy radicals behind the $C_{10}H_{15}O_z$ or $C_{10}H_{17}O_z$ peroxy radical families and the huge number of RO_2 radicals they can react with, half and half chances for the formation of carbonyl and alcohol are not too unlikely.

Based on the 50/50 chance for the formation of alcohol and carbonyl, a strong increase of the carbonyl channel, i.e. of the $C_{10}H_{14}O_z$ family is missing. This implies that the strong increase of the $C_{10}H_{16}O_z$ family might be the result of the formation of hydroperoxides from $C_{10}H_{15}O_z$ peroxy radicals. The $C_{10}H_{18}O_z$ family did not show such a behaviour despite the contribution of hydroperoxide from $C_{10}H_{17}O_z$ peroxy radical. This might be a result of the lower signal of $C_{10}H_{17}O_z$. Since the amount of $C_{10}H_{17}O_z$ was too small, the formation of $C_{10}H_{18}O_z$ was not visible.

The box model calculations showed that both HO_2 and RO_2 radicals increased with turnover (Master thesis S.Proff, Figure 3.7). Note that the HO_2 concentration is about at least a factor of 80 lower than the RO_2 concentration, but the rate coefficient for reactions of HO_2 with RO_2 (R1.2.7) is about one order of magnitude larger then that for RO_2 + RO_2 in reaction (R1.2.8). Figure 3.7 shows that the ratio of HO_2 and RO_2 radicals was indeed increasing with increasing turnover which means the degree of increase of HO_2 radical concentration was higher (a factor of 6-7) than that of RO_2 radicals (a factor of 3-5). Larger increase of [HO_2] than [RO_2] favours reactions between RO_2 and HO_2 radicals over reactions of RO_2 radicals and RO_2 radicals. As a result, the hydroperoxide formation channel (R1.2.7) increases while the disproportionation channel (R1.2.8) decreases in importance. From this point of view an increasing hydroperoxide formation from $C_{10}H_{15}O_z$ contributing to the $C_{10}H_{16}O_z$ family with increasing turnover is supported by the simulation of peroxy radicals in the experiments. Therefore, one can assume that at least some of the increase in the $C_{10}H_{16}O_z$ family happened because of the increase of hydroperoxides. The analogous increase of $C_{10}H_{18}O_z$ from $C_{10}H_{17}O_z$ peroxy radicals was a factor of a 16 which is higher compared to $C_{10}H_{16}O_z$ which was a factor of 8. However, if the assumption that peroxy radicals have 50/50 chances for the formation of alcohol and carbonyl is not valid, strong hydroperoxide formation is not required to explain the signal of $C_{10}H_{16}O_z$. If the major peroxy radicals had a preference to form alcohol rather than carbonyl, $C_{10}H_{16}O_z$ may as well consist of a considerable amount of alcohols.

A similar argument holds for the third channel contributing to $C_{10}H_{16}O_z$. If increasing disportionation of $C_{10}H_{17}O_z$ to carbonyls contributed significantly then one would expect an increase of the alcohol channel $C_{10}H_{18}O_z$ as well. Since this was not the case, one would have to claim preferential carbonyl formation in disproportionation of $C_{10}H_{17}O_z$, whereas $C_{10}H_{15}O_z$

prefer the alcohol channel. This seems not very likely.

With the help of the model data, a conclusion can be made that the huge increase of the $C_{10}H_{16}O_z$ family compared to other families may be the result of increasing hydroperoxide formation from $C_{10}H_{15}O_z$ peroxy radicals with increasing turnover, and/or a preference for alcohol formation of $C_{10}H_{15}O_z$ peroxy radicals. It seems that $C_{10}H_{17}O_z$ radicals do not contribute a lot to $C_{10}H_{16}O_z$. As described above, pathways to the $C_{10}H_{16}O_z$ family were complicated and there might be some contribution from all three channels. The question, where does all the $C_{10}H_{15}O_z$ come from despite the fact that $C_{10}H_{17}O_3$ peroxy radical is the primary peroxy radical from α-pinene OH oxidation, is not answered yet. Before answering the question, the accretion products will be discussed to get more diagnostics at hand.

In addition to current implementations in MCM v3.3.1, two peroxy radicals can undergo an accretion product formation (R1.2.9) besides the disproportionation reaction (R1.2.8). The term 'dimer' is used in literature but the notation 'accretion product' is used in this thesis. This is because "dimer" can give a wrong impression that it is only formed from self reaction of alike peroxy radicals while the observations indicate that accretion products are formed by all kinds of combinations of peroxy radicals. The formation mechanism of accretion products is still unclear. However, they are most likely directly formed by the reaction of two HOM peroxy radicals including self-reactions or a combination of a HOM-RO_2 and another functionalized and/ or abundant peroxy radical (Berndt *et al.*, 2018a; McFiggans *et al.*, 2019; Pullinen *et al.*, 2020). Valiev *et al.*, 2019 showed that two peroxy radicals can form tetroxide cluster with triplet state of oxygen in the middle ($RO\cdots O_2\cdots OR\prime$). Since the recombination of two RO in triplet state is a forbidden process, one would expect a slower reaction rate for accretion products than observed by Berndt *et al.*, 2018b. However, Valiev *et al.*, 2019 showed that intersystem crossing and thus accretion product formation can be very fast.

It is assumed here that in cross reactions of peroxy radicals, the number of hydrogen atoms observed in HOM-accretion products, must be built up by a combination of precursors peroxy radicals with odd number of H-atoms. This puts some constraints on the precursor HOM-RO_2 that are possibly involved in the formation of the observed accretion products.

In Figure 3.10, the signal normalised to total ion counts for C_{20} families is shown. Four different families were observed which are $C_{20}H_{28}O_z$, $C_{20}H_{30}O_z$, $C_{20}H_{32}O_z$ and $C_{20}H_{34}O_z$.

When ozonolysis dominates at the first two data points near turnover 5×10^6 cm^{-3} s^{-1}, the two most abundant accretion product families were the $C_{20}H_{30}O_z$ and $C_{20}H_{32}O_z$ family. The $C_{20}H_{30}O_z$ family should mainly stem from the combination of $C_{10}H_{15}O_p$ peroxy radicals and $C_{10}H_{15}O_q$ peroxy radicals, where z=p+q-2 (p and q can be same or different) since two oxygen atoms are lost when accretion products are formed by two peroxy radicals. Since $C_{10}H_{15}O_p$ peroxy radicals are most abundant in ozonolysis, it is a comprehensible that $C_{20}H_{30}O_z$ were the most abundant accretion products. In principle, there is still a possibility that combinations of $C_{10}H_{13}O_p$ and $C_{10}H_{17}O_q$ peroxy radicals contributed to the $C_{20}H_{30}O_z$ accretion product family. However, the chances should be low supported by the fact that the $C_{20}H_{28}O_z$ and $C_{20}H_{34}O_z$ families showed very low intensity and they were supposedly formed by $C_{10}H_{13}O_z$

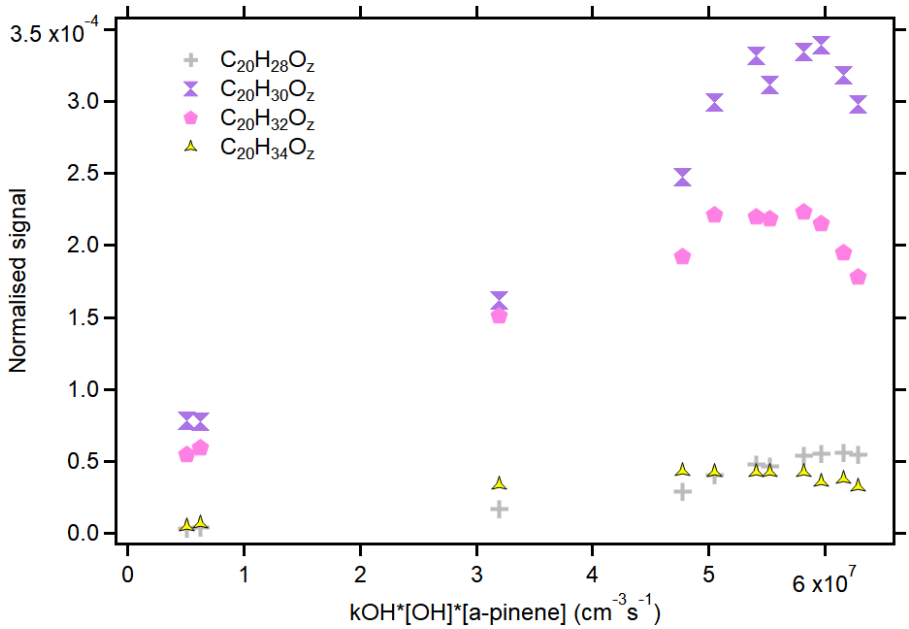

Figure 3.10: Signal of each C_{20} family normalised to total ion counts are plotted as a function of turnover. The grey crosses and the lilac hourglasses represents $C_{20}H_{28}O_z$ and $C_{20}H_{30}O_z$ family respectively. The pink pentagons and yellow triangular symbols shows normalised signal of $C_{20}H_{32}O_z$ and $C_{20}H_{34}O_z$ family.

and $C_{10}H_{17}O_z$ peroxy radicals pairing with $C_{10}H_{15}O_z$ and $C_{10}H_{17}O_z$ peroxy radicals, respectively.

On the other hand, a high signal from $C_{20}H_{32}O_z$ accretion products in the ozonolysis phase was somewhat unexpected. $C_{20}H_{32}O_z$ accretion products were probably formed in the reaction between $C_{10}H_{15}O_p$ peroxy radicals and $C_{10}H_{17}O_q$ peroxy radicals where z=p+q-2. $C_{10}H_{17}O_q$ peroxy radicals were formed in the oxidation of α-pinene by "dark OH" produced from α-pinene CI in the ozonolysis. The question arises why the $C_{20}H_{32}O_z$ accretion product family showed a relatively high signal despite the low concentration of $C_{10}H_{17}O_z$ peroxy radicals compared to the $C_{10}H_{18}O_z$ family. One reason could be that it was more likely for $C_{10}H_{17}O_z$ peroxy radicals to form accretion products with $C_{10}H_{15}O_z$ peroxy radicals because of the high abundance of $C_{10}H_{15}O_z$ peroxy radicals in the ozonolysis phase. This implies, that the reaction rate of the formation of accretion products (R1.2.9) might be fast enough to efficiently compete with termination reactions (R1.2.8 and R1.2.7) and the formation of monomers such as carbonyls, alcohols and hydroperoxides. This is supported by studies of Berndt *et al.*, 2018b who reports accretion formation rate coffecients close to the collision limit for HOM-RO_2 + HOM-RO_2.

At higher turnover where OH oxidation was predominant, $C_{20}H_{30}O_z$ accretion products remained the most prominent family followed by the $C_{20}H_{32}O_z$ family, similar to the ozonolysis phase. The high signal of $C_{20}H_{30}O_z$ family among C_{20} accretion product families supports the fact that $C_{10}H_{15}O_z$ peroxy radicals were the major peroxy radicals in HOM formation and

$C_{10}H_{17}O_z$ peroxy radicals were of minor importance.

The concentration of $C_{20}H_{32}O_z$ family increased also as turnover rose. This was the case because $C_{10}H_{17}O_z$ peroxy radicals increased with turnover. (Figure 3.9 in panel D). However, the increase of $C_{20}H_{30}O_z$ was more prominent than the increase of the $C_{20}H_{32}O_z$ and the $C_{20}H_{34}O_z$ family flattened between turnover 6.8×10^7 to 7.8×10^7 cm^{-3} s^{-1}. This observation showed that $C_{20}H_{30}O_z$ family increased in importance which is related to the importance of the $C_{10}H_{15}O_z$ peroxy radical family.

The concentration of $C_{20}H_{34}O_z$ family was expected to increase as $C_{10}H_{17}O_3$ is the primary peroxy radical from OH addition and autoxidation should lead fast to $C_{10}H_{17}O_z$ peroxy radicals. Actually, it was expected to show quadratic growth because two $C_{10}H_{17}O_z$ peroxy radicals form $C_{20}H_{34}O_z$ accretion products. However, this was not supported by the data. The majority of $C_{10}H_{17}O_z$ peroxy radicals obviously prefers to produce $C_{20}H_{32}O_z$ accretion products instead of $C_{20}H_{34}O_z$ accretion products or even monomer $C_{10}H_{18}O_z$ termination products (Figure3.9). One reason can be again the extensive abundance of $C_{10}H_{15}O_z$ peroxy radicals. Because there were quite high concentrations of $C_{10}H_{15}O_z$ peroxy radicals, $C_{10}H_{17}O_z$ family members find easily $C_{10}H_{15}O_z$ peroxy radical family members to react with. In addition, the formation of accretion products depends of course on the relation of the rate coefficients for the competing channels. As mentioned before, reaction coefficients for accretion are often close to the collision limit Berndt *et al.*, 2018b and thus favor branching into the accretion product channel. Therefore, higher reaction rates into accretion products must be the reason for $C_{10}H_{17}O_z$ peroxy radicals to form $C_{20}H_{32}O_z$ accretion products instead of contributing to the $C_{10}H_{18}O_z$ family.

Interestingly the concentration of $C_{20}H_{28}O_z$ family showed an increase with increasing turnover. According to the assumptions which are made in this work, $C_{20}H_{28}O_z$ accretion product should be formed by combinations of $C_{10}H_{13}O_z$ and $C_{10}H_{15}O_z$ peroxy radicals. I.e. the observation of $C_{20}H_{28}O_z$ accretion products indicated the existence of the $C_{10}H_{13}O_z$ peroxy radical family, which was not observed as a major peroxy radical in the mass spectrum. This is similar to the $C_{20}H_{32}O_z$ family, which indicated a larger importance of the $C_{10}H_{17}O_z$ family than deduced from the analysis of the monomer families alone.

The conclusion can be made that accretion products are good indicators in terms of the behaviour and importance of peroxy radicals. The family analysis of C_{20} accretion products indicated that the major peroxy radicals were $C_{10}H_{15}O_z$ peroxy radicals instead of $C_{10}H_{17}O_z$ peroxy radicals. The observation of the $C_{20}H_{28}O_z$ family showed the existence of the $C_{10}H_{13}O_z$ peroxy radical family. Both, analysis of the monomer families and the accretion products underline that $C_{10}H_{15}O_z$ peroxy radicals were the major peroxy radical family and not $C_{10}H_{17}O_z$, despite the fact that $C_{10}H_{17}O_z$ peroxy radicals should be formed by autoxidation of $C_{10}H_{17}O_3$, the first generation peroxy radicals from the α-pinene OH oxidation.

As a consequence of what have discussed up to here, one reason that $C_{10}H_{17}O_z$ peroxy radicals showed a low signal could be that $C_{10}H_{17}O_z$ peroxy radicals react very fast and form monomer closed shell carbonyl products, $C_{10}H_{16}O_{z<5}$, or accretion products, $C_{20}H_{32}O_z$. Since only a signal strength (concentrations) of molecules were observed, fast destruction can result

in a low concentration of molecules even though their production is efficient and fast. However, the observation of the small signal of products from $C_{10}H_{17}O_z$ peroxy radicals such as the $C_{10}H_{18}O_z$ family and $C_{20}H_{34}O_z$ family suggests that this was probably not the case. Besides, $C_{10}H_{15}O_z$ peroxy radical showed a strong signal even though their termination products such as the $C_{10}H_{14}O_z$ family or the $C_{20}H_{30}O_z$ family showed the strongest signals. It is more likely that $C_{10}H_{15}O_z$ peroxy radicals were the major peroxy radicals.

The question what is the source of the $C_{10}H_{15}O_z$ peroxy radicals can be thrown. Since the relative importance of ozonolysis decreases with increasing OH, primary radicals arising from ozonolysis decrease strongly as shown in Figure 3.8, and their autoxidation cannot be the source of the increasing $C_{10}H_{15}O_z$ peroxy radicals with turnover. However, with increasing OH, the second attack of OH radicals on first generation products is becoming more likely leading to an increasing second generation peroxy radicals concentration (green upside down triangles in Figure 3.8). Oxidation of e.g. pinonaldehyde by OH radicals under H-abstraction indeed leads to $C_{10}H_{15}O_4$ peroxy radicals, which can then undergo autoxidation. Pinonaldehyde is a major primary oxidation product from α-pinene oxidation by OH (Peeters, Vereecken, and Fantechi, 2001; Capouet *et al.*, 2004).

Pullinen, 2016 measured a mass spectrum of HOM formed by oxidation of pinonaldehyde by OH.

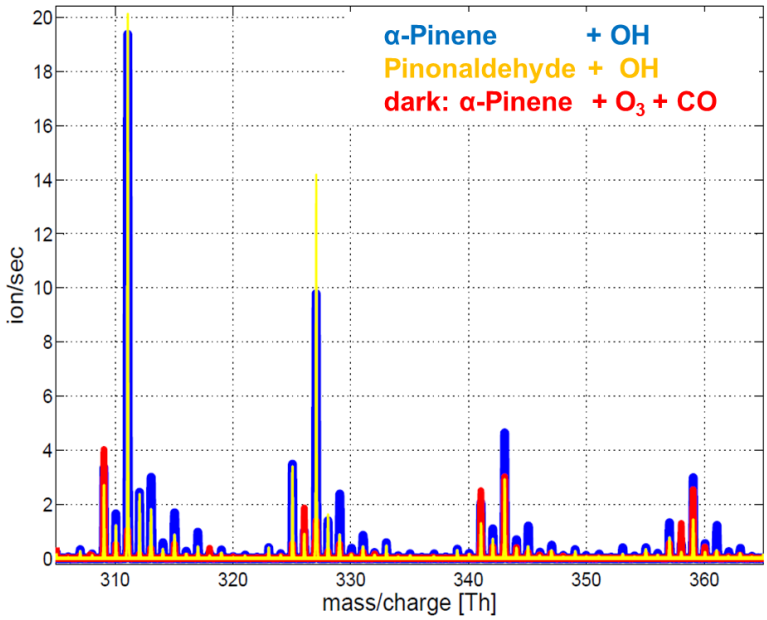

Figure 3.11: Overlapped mass spectrum of α-pinene ozonolysis(red), α-pinene OH oxidation(blue) and pinonaldehyde OH oxidation (yellow). The x-axis shows mass per charge ratio and the y-axis shows non-normalised signal. Pinonaldehyde mass spectrum was scaled to match the α-pinene peak at 310 Th. Compound's mass/charge is shown with a cluster with NO_3^- ion. Data from Iida Pullinen.

This mass spectrum of pinonaldehyde under OH radical reaction looked very similar to that of α-pinene under OH radical reaction (Figure 3.11), while α-pinene ozonolysis showed a different mass spectrum with a different pattern. According to MCM v3.3.1, OH radicals abstract hydrogen from pinonaldehyde ($C_{10}H_{16}O_2$) and produces either an acyl peroxy radical (branching ratio 0.77) or a peroxy radical located at the four-membered ring (branching ratio 0.23). From the observation of a similar pattern in mass spectra in oxidation of pinonaldehyde and α-pinene by OH, it is probable that a significant portion of $C_{10}H_{15}O_z$ peroxy radicals were formed in a second attack of OH with oxidation products such as pinonaldehyde. As a consequence, a significant portion of HOM is probably formed by secondary attack of OH to oxidation products and subsequent autoxidation. This result is supported by the study of Eddingsaas *et al.*, 2012. They found about 33 % yield of pinonaldehyde from α-pinene phooxidation in a low NOx experiment. Pinonaldehyde was also found to be a major product in a high NOx experiment. Comparing the modeled $C_{10}H_{15}O_{even}$ peroxy radicals (Figure 3.8) with the observed $C_{10}H_{15}O_z$ family (Figure 3.9), the drop with turnover in the $C_{10}H_{15}O_z$ family concentration was not observed. This indicates that there are either more channels to $C_{10}H_{15}O_z$ peroxy radicals than currently implemented in the MCM v3.3.1., or that the autoxidation of second generation peroxy radicals arising from OH oxidation is more efficient than autoxidation of the first generation of peroxy radicals from ozonolysis.

3.2.3 Closer look into families: Marker analysis

In the previous section, changes in the families with an increasing turnover were discussed. Family analysis can only show an averaged behaviour of the family members. In other words, if the concentration of one family member increased and the concentration of other family members decreased this changes will be canceled out and not clearly observed in the family analysis. In this section, a deepened analysis by studying individual family members with an increasing turnover will be shown. The several outstanding compounds (marker compounds) with a particularly high signal will be discussed. The analysis will include the parity of oxygen in the molecular formulae of family members as a new parameter. Oxygen parity can be an important parameter, as it does not change in an autoxidation step, but it changes as soon as alkoxy radicals are involved in the formation mechanism of the molecule. A goal is to elucidate the importance of alkoxy radicals in the process of HOM formation. In the next section, the concentration of members of the peroxy radical families will be shown.

C_{10} peroxy radical marker analysis

When ozonolysis is the dominant process in the system, $C_{10}H_{15}O_4$ peroxy radicals are formed from CI via the vinylhydroperoxide path and $C_{10}H_{15}O_4$ are the first generation peroxy radicals (Johnson and Marston, 2008). Therefore $C_{10}H_{15}O_{even}$ peroxy radicals are expected as major peroxy radicals and the peroxy radicals resulted from the autoxidation of $C_{10}H_{15}O_4$. Additionally, some $C_{10}H_{17}O_z$ peroxy radicals could result from dark OH reacting with α-pinene. Since the

first generation peroxy radicals are $C_{10}H_{17}O_3$, it is expected that $C_{10}H_{17}O_{odd}$ peroxy radicals from the autoxidation of $C_{10}H_{17}O_3$ will be dominant in the $C_{10}H_{17}O_z$ family.

In the phase where OH oxidation is dominant, it is expected to detect members of the two different peroxy radicals families. From the result described before, a minor contribution of $C_{10}H_{17}O_{odd}$ peroxy radicals is expected from autoxidation of $C_{10}H_{17}O_3$ which are the first generation peroxy radicals formed by the addition of OH to the double bond of the α-pinene. The major contribution should comprise $C_{10}H_{15}O_{even}$ peroxy radicals formed by an autoxidation of $C_{10}H_{15}O_4$ peroxy radicals, which are formed by H-abstraction in the oxidation of products such as pinonaldehyde by OH radicals.

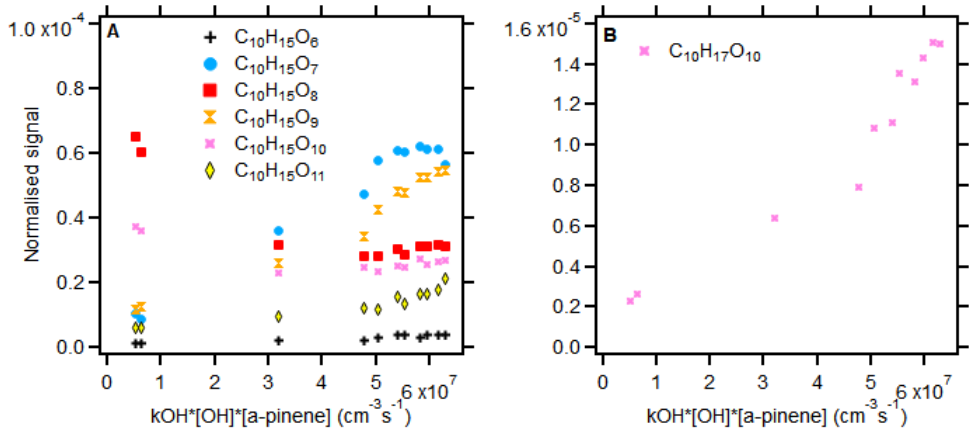

Figure 3.12: The normalised signal of family members of $C_{10}H_{15}O_z$(panel A) and $C_{10}H_{17}O_z$(panel B) as function of turnover.

In Figure 3.12, the normalised signal of the members of $C_{10}H_{15}O_z$ and $C_{10}H_{17}O_z$ peroxy radicals families are shown. Six individual members of the $C_{10}H_{15}O_z$ family could be detected (Figure 3.12, Panel A). In the turnover range dominated by ozonolysis, the largest contributions was observed by $C_{10}H_{15}O_8$ and the second largest contributions were by $C_{10}H_{15}O_{10}$ followed by $C10H15O_{7,9,11}$. The highly abundant $C_{10}H_{15}O_8$ and $CH_{10}H_{15}O_{10}$ were the products formed from the straight autoxidation of the primary $C_{10}H_{15}O_4$ radicals as expected, with addition of two or three O_2 molecules. Observation of $C_{10}H_{15}O_{7,9,11}$ with odd oxygen numbers indicate some involvement of alkoxy radical during their formation mechanism ((Mentel *et al.*, 2015).

In the photochemical phase, $C_{10}H_{15}O_{8,10}$ showed strong signals, but lower than in the ozonolysis phase. They followed qualitatively the behavior of the modeled $C_{10}H_{15}O_4$ in Figure 3.8. Instead, the peroxy radicals $C_{10}H_{15}O_{7,11,9}$ gain in importance. In general, all the signal of $C_{10}H_{15}O_{odd}$ rise with an increasing turnover ($C_{10}H_{15}O_{7,9,11}$).

The observation of strong signals of $C_{10}H_{15}O_{7,9,11}$ with odd oxygen numbers and their increase with an increase in turnover, indicates an increasing importance of alkoxy radicals in their formation mechanism. The formation of an alkoxy radical from the peroxy radicals

(R1.2.10) changes the O-atom parity, here from even to odd. The alkoxy radicals can undergo H-shifts reforming a peroxy radical under O_2 addition. The latter could continue the autoxidation chain, leading to the observed large number of O-atoms with an odd parity in the HOM.

For the $C_{10}H_{17}O_z$ family, only one member was detected directly: $C_{10}H_{17}O_{10}$ (Figure 3.12, panel B). In contrast to expectation, it has an even number of O-atoms, indicating that an alkoxy radical formation is probably involved in its formation.

There could be a reason for the limited detection of $C_{10}H_{17}O_z$ peroxy radicals. There were huge peaks 1 Da in front of the $C_{10}H_{17}O_z$ peroxy radicals, which came from $C_{10}H_{16}O_z$ family members. The ^{13}C isotope signal of $C_{10}H_{16}O_z$ family appeared near the m/z where the $C_{10}H_{17}O_z$ family should be detected. This could disturb the high resolution analysis of $C_{10}H_{17}O_z$ family, when the signal of $C_{10}H_{16}O_z$ is high and thus their ^{13}C satellite, which is about 11 % of the ^{12}C signal. However, if there was a high signal from a $C_{10}H_{17}O_z$ peroxy radials, it should be detected since the software used for high resolution analysis, calculates the isotopic signal from the ^{12}C peak at M and considers the isotope signal in the fit of the peak signal (M+1). (For example, $C_{10}H_{14}O_z$ family showed also quite high signal in ozonolysis experiments but still the $C_{10}H_{15}O_z$ peroxy radical family could be detected.) As a consequence, it can be concluded that the concentration of $C_{10}H_{17}O_z$ family was indeed low or even not detectable, indicating a minor role of this species. However, as mentioned before, the conclusions made from the concentrations of intermediate products like peroxy radicals and their importance are limited. That is because if an efficient loss paths exist for the intermediate species, a low concentration does not automatically means low level of production.

As described in the previous chapter, the accretion products are important and efficiently indicate the role of certain peroxy radicals. In this respect, members contributing to accretion product families will be discussed in the next section, before the analysis of the closed shell C_{10} families.

C_{20} marker analysis

In this section, the behaviour of individual family members of C_{20} families will be discussed. Based on the abundance of the detected peroxy radicals, the reaction partner will be inferred. In this way, the hints of the precursors of accretion products formation can be achieved and the possible mechanisms for accretion product formation. In addition, the parity of O-atoms in the molecular formulae gives a information of the involvement of a alkoxy-peroxy pathway. First the observation in the ozonolysis phase will be discussed followed by the observation in the photooxidation phase.

As described before, the accretion products are formed by the recombination of two peroxy radicals (R1.2.9). Therefore, the parity of oxygen in the accretion products reflects the involvement of alkoxy radicals in the formation of precursor peroxy radicals. It is expected that the peroxy radicals shown in Figure 3.12 are involved in the accretion product formation. In addition, less oxidised RO_2 were supposedly trapped in accretion products. Figure 3.13 shows the

normalised signal of the members of each accretion product family as a function of turnover.

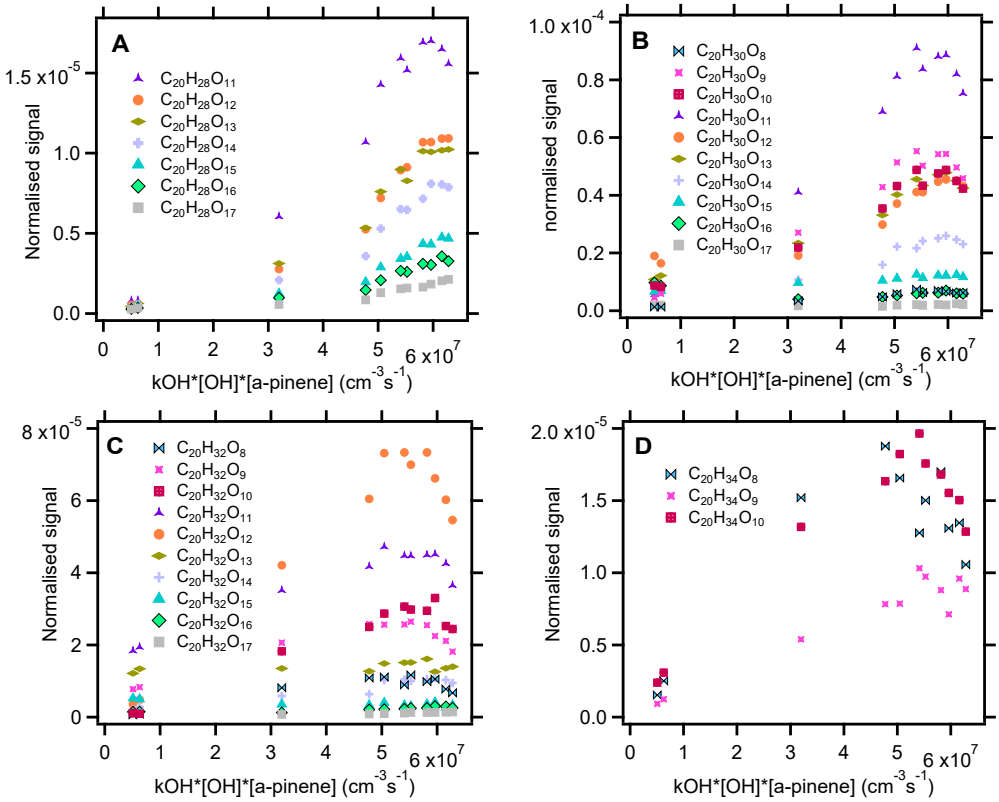

Figure 3.13: The normalised signal of C_{20} family versus turnover. Panel A and B show the signal of the $C_{20}H_{28}O_z$ and the $C_{20}H_{30z}$ family members. Panel C and D show the normalised signal of $C_{20}H_{32}O_z$ and $C_{20}H_{34}O_z$ family members respectively.

In panel A, the $C_{20}H_{28}O_z$ accretion product family with seven family members are shown. In the ozonolysis phase, only small concentration of the $C_{20}H_{28}O_z$ family was observed. The $C_{20}H_{28}O_z$ accretion products are likely formed by the recombination of $C_{10}H_{15}O_z$ and $C_{10}H_{13}O_z$. Since $C_{10}H_{15}O_z$ peroxy radicals were the major peroxy radicals in the ozonolysis phase, the small concentration of the $C_{20}H_{28}O_z$ is supposed to be a result of the low concentration of $C_{10}H_{13}O_z$. The concentration of $C_{10}H_{15}O_z$ peroxy radical was not lower in the ozonolysis phase compared to OH oxidation dominant phase which confirms that the low concentration in the ozonolysis phase must be a result of the lacking $C_{10}H_{13}O_z$ peroxy radicals. In other words, the higher concentration of $C_{20}H_{28}O_z$ family is caused by an increase of $C_{10}H_{13}O_z$ peroxy radicals in the OH oxidation dominant phase.

In the high turnover range, $C_{20}H_{28}O_{11}$ showed the highest signal followed by $C_{20}H_{28}O_{12}$,

and $C_{20}H_{28}O_{13}$. Since the $C_{10}H_{15}O_z$ peroxy radicals were measured, the partner $C_{10}H_{13}O_z$ peroxy raidcals can be inferred based on the abundance of $C_{10}H_{15}O_z$ peroxy radical family members. $C_{10}H_{15}O_7$, $C_{10}H_{15}O_9$, $C_{10}H_{15}O_8$ and $C_{10}H_{15}O_{10}$ were the major peroxy radicals in the OH oxidation dominant phase (Figure 3.12, panel A). For example, pairing of $C_{10}H_{15}O_9$ with the $C_{10}H_{13}O_{4\text{-}6}$ peroxy radicals could explain the $C_{20}H_{28}O_{11\text{-}13}$ accretion products. In pairs with $C_{10}H_{15}O_{8,9,10}$ the $C_{10}H_{13}O_z$ would have a relatively low oxygen content, meaning that HOM-RO_2 recombined with less oxidised RO_2. Indeed, the signal strength of the $C_{20}H_{28}O_z$ scales inversely with the number of oxygen atoms (Figure 3.13). Since peroxy radicals with low O-atom numbers arise earlier in the reaction chain, they are expected to have higher concentrations.

It is interesting to see the fall off of $C_{20}H_{28}O_{11}$ accretion product at a high turnover while other $C_{20}H_{28}O_z$ family members did not show such a dramatic drop down. Partitioning to the particle cannot solely explain this observation because less volatile $C_{20}H_{28}O_{>11}$ members with higher oxygen contents did not show the signal reduction. It is unclear at the moment why only the $C_{20}H_{28}O_{11}$ molecule was showing such a decrease, but possibly the concentration of recombination partner(s) decreased at the highest OH concentrations.

In Figure 3.13, panel B, the 10 detected members of the $C_{20}H_{30}O_z$ accretion product family are shown. In the ozonolysis phase, it is expected that the $C_{20}H_{30}O_{even}$ show more prominent signals than $C_{20}H_{30}O_{odd}$ family members. That is because the $C_{10}H_{15}O_{even}$ peroxy radicals were main peroxy radicals and recombination of two even O-atom peroxy radical would form $C_{20}H_{30}O_{even}$ accretion products. It was observed that $C_{20}H_{30}O_{12}$ was the compound with the highest signal although it does not have much higher signal than many other family members. Since the $C_{10}H_{15}O_8$ and the $C_{10}H_{15}O_{10}$ were the major peroxy radicals in ozonolysis phase, the peroxy radicals $C_{10}H_{15}O_{4\text{-}7}$ would be needed to form $C_{20}H_{30}O_{12}$ and $C_{20}H_{30}O_{13}$ accretion products. In order to form $C_{20}H_{30}O_{13}$ and other $C_{20}H_{30}O_{odd}$ accretion products, peroxy radicals with odd numbers of O-atoms are required, and one alkoxy radical step must have been involved in their formation in addition to straight autoxidation. Observation of a strong signal of the $C_{20}H_{30}O_{13}$ with odd number of oxygen is another indication for the involvement of alkoxy steps under ozonolysis conditions.

On the other hand, the concentration of $C_{20}H_{30}O_{11}$ accretion products were the highest among the $C_{20}H_{30}O_z$ family members in the OH oxidation dominant phase. The three accretion products with odd numbers of O-atoms, $C_{20}H_{30}O_9$, $C_{20}H_{30}O_{13}$ and $C_{20}H_{30}O_{11}$, were under the top 5 abundant family members. They appeared in almost the same abundance as the accretion products with even O-atom numbers, $C_{20}H_{30}O_{10}$ and $C_{20}H_{30}O_{12}$.

Considering that the $C_{10}H_{15}O_{7,9}$ were the major peroxy radicals in the photooxidation phase, the partners of the recombination pairs should be $C_{10}H_{15}O_{4,6,5}$ to form $C_{20}H_{30}O_z$ in the observed decreasing order of intensity. They could be peroxy radicals formed in the second OH attack of closed shell oxidation products ($C_{10}H_{15}O_4$), followed by one step of autoxidation ($C_{10}H_{15}O_6$). In addition, there could be an alkoxy-peroxy pathway forming the alkoxy radical $C_{10}H_{15}O_3$ followed by the addition of O_2 to form peroxy radical ($C_{10}H_{15}O_5$) as well. Additionally, a peroxy radical with the molecular formula $C_{10}H_{15}O_3$ is formed by OH if the H-shift in the alkoxy

radical with the same molecular formula occurred from a hydroperoxide functional group.

The recombination of the two most abundant HOM-RO_2, $C_{10}H_{15}O_{7,9}$ should lead to the $C_{20}H_{30}O_{14}$. $C_{20}H_{30}O_{14}$ was observed as a 6th highest signal (+ lylac symbols in Figure 3.13, panel B). Based on the observation, it should be noted that in the $C_{20}H_{30}O_z$ family, the recombinations of less oxygenated RO_2 with HOM-RO_2 must play a role in the formation process of accretion product.

In panel C of Figure 3.13, the behaviour of the $C_{20}H_{32}O_z$ family members with turnover is shown. In the ozonolysis dominant phase, the $C_{20}H_{32}O_{11}$, $C_{20}H_{32}O_{13}$ and $C_{20}H_{32}O_9$ with odd number of oxygen show the largest signals. Since $C_{10}H_{15}O_8$ and $C_{10}H_{15}O_{10}$ were the major peroxy radicals, the other recombination partners were likely to be the $C_{10}H_{17}O_{5,7,3}$. These radicals are the first generation peroxy radicals formed by reaction of dark OH and α-pinene ($C_{10}H_{17}O_3$) and their products after one or two autoxidation process.

$C_{20}H_{32}O_{12}$ and $C_{20}H_{32}O_{11}$ are the members of the $C_{20}H_{32}O_z$ family with the highest concentrations in high turnover phase. Considering that the major peroxy radical were $C_{10}H_{15}O_{7,9}$ peroxy radicals, the other partners for recombination should be $C_{10}H_{17}O_{5,3,7,6,4}$ in order of the decreasing intensity of the observed $C_{20}H_{32}O_z$ accretion products. These peroxy radicals are mixture of first generation peroxy radical and their products after one or two process of autoxidation ($C_{10}H_{17}O_3$, $C_{10}H_{17}O_5$ and $C_{10}H_{17}O_7$) and including in addition one alkoxy step ($C_{10}H_{17}O_4$, $C_{10}H_{17}O_6$).

In both the ozonolysis phase and the photooxidation phase, the involvement of alkoxy radical formation step and the recombination with less oxygenated peroxy $C_{10}H_{17}O_z$ peroxy radicals must be involved in the formation of $C_{20}H_{32}O_z$ accretion products. However, the large signals of $C_{20}H_{32}O_{12}$ and $C_{20}H_{32}O_{11}$ indicate that radicals from autoxidation of $C_{10}H_{17}O_3$ must exist at likely higher concentrations than the only detectable $C_{10}H_{17}O_{10}$ peroxy radicals. An explanation could be that the concentration of $C_{10}H_{17}O_z$ remains low because they were efficiently scavenged by the most abundant members of the $C_{10}H_{15}O_z$ family.

In Figure 3.13 D, the three detected members of the $C_{20}H_{34}O_z$ family are shown. Their concentrations were low in the ozonolysis phase, the $C_{20}H_{34}O_{10}$ showing slightly higher intensity. In the higher turnover phase, signals were scattered. Nonetheless, all family members displayed higher signal in oxidation by OH radicals compared to the oxidiaton by ozone. The $C_{20}H_{34}O_{10}$ which shows the highest signal among the family members of $C_{20}H_{34}O_z$ could be formed by the recombination of $C_{10}H_{17}O_5$ and $C_{10}H_{17}O_7$ peroxy radicals or a self-reaction of two $C_{10}H_{17}O_6$ peroxy radicals. The former with odd numbers of O-atoms should arise from the autoxidation of first generation peroxy radicals from OH and α-pinene. The recombination of two $C_{10}H_{17}O_6$ should involve one alkoxy radical step for each because of their even number of oxygen. $C_{20}H_{34}O_8$ can be formed from the combination from the self-reaction of two $C_{10}H_{17}O_5$ peroxy radicals or $C_{10}H_{17}O_6$ and $C_{10}H_{17}O_4$ peroxy radicals. The latter option would again require one alkoxy radical step in the formation of both peroxy radicals.

The explanations for the behaviour of the concentrations of $C_{20}H_{32}O_z$ and $C_{20}H_{34}O_z$ family members are speculative, since only the $C_{10}H_{17}O_{10}$ peroxy radicals were detected. However,

the findings support the major conclusions derived from the pattern analysis of all four HOM accretion product families. Firstly, HOM peroxy radicals produce the accretion products by the recombination of HOM-RO_2 with less oxygenated peroxy radicals. This was derived from the lower O:C ratio for accretion products and by pointing out the possible recombination partners. Secondly, often an alkoxy radical step is involved in combination with autoxidation in the formation of less functionalised and HOM-RO_2, as was shown by the many major HOM accretion products with odd oxygen numbers under accretion product family members. In the next section, the changes of the marker compounds in the C_{10} families with an increasing turnover will be discussed.

C_{10} marker analysis

In this section, the behaviour of the individual family members of the C_{10} families as a function of turnvoer will be investigated. This allows to get information of the formation mechanism of HOM monomers. In addition, the preference of reaction (R1.2.8 or R1.2.7) will be investigated by comparing the normalised signal. Besides, the involvement of a alkoxy-peroxy pathway will be dealt with by discussing the parity of the number of O-atoms in the molecular formulae.

The HOM peroxy radicals which could be directly detected were treated in the Chapter 3.2.3. The findings were related to the first and the second generation peroxy radicals established in the current RO_2 chemistry by referring to box model calculations with MCM v3.3.1. The analysis of C_{20} marker compounds showed additional hints about the abundance and the existence of peroxy radicals, which could not be directly detected. In this chapter, these findings will be applied in order to analyse the behaviour of monomer C_{10} marker compounds as a function of turnover.

When the ozonolysis is dominant, $C_{10}H_{15}O_4$ peroxy radicals are formed from CI and $C_{10}H_{15}$ -O_{even} peroxy radicals are formed by straight autoxidation process. Whenever $C_{10}H_{15}O_{even}$ peroxy radicals form an intermediate alkoxy radical in reactions with other RO_2, H-shifts can occur which leads to the formation of the $C_{10}H_{15}O_{odd}$ peroxy radicals. In the reaction of dark OH with α-pinene, a second peroxy radical family is formed from the first generation peroxy radical $C_{10}H_{17}O_3$ and $C_{10}H_{17}O_{odd}$ peroxy radicals from straight autoxidation. In this case, involvement of alkoxy radical steps changes the parity of the O-atoms in the peroxy radicals from odd to even ($C_{10}H_{17}O_{even}$). In the OH oxidation dominant phase, there are contributions of three different peroxy radical families: $C_{10}H_{13}O_z$(from the observation of $C_{20}H_{28}O_z$), $C_{10}H_{15}O_z$ and $C_{10}H_{17}O_z$. The changes in O-atom parity by an alkoxy radical step applies here as well. The $C_{10}H_{13}O_z$ peroxy radicals are not documented in the MCM v3.3.1 mechanism. They are of potential importance in this study because of their reaction with RO_2 and HO_2 may contribute to compounds with molecular formulae of $C_{10}H_{14}O_{z-1}$ (alcohols) or to $C_{10}H_{14}O_z$ (hydroperoxides), respectively. Compounds with molecular formulae $C_{10}H_{12}O_{z-1}$ (carbonyl compounds), however, were not detected in a significant amount.

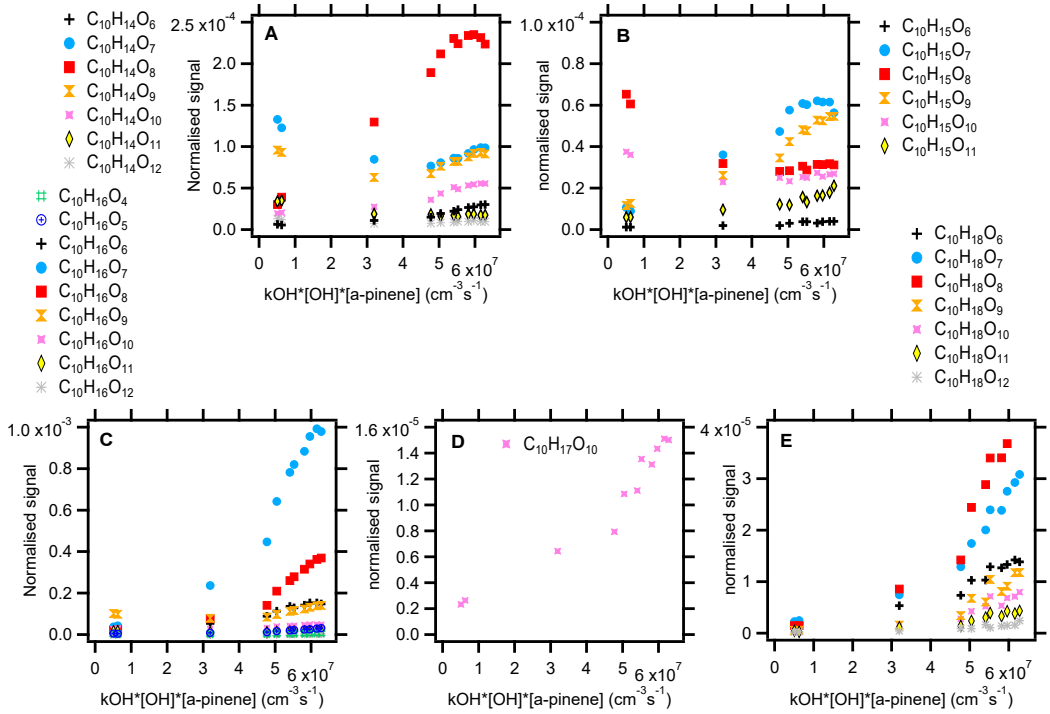

Figure 3.14: The normalised signal of the C_{10} family members versus turnover. Panel A shows $C_{10}H_{14}O_z$ family members and panel B shows members of $C_{10}H_{15}O_z$ peroxy radical family. Panel C shows $C_{10}H_{16}O_z$ family members which was attributed to the mixture of alcohol, hydroperoxide and carbonyl from different peroxy radicals. Panel D shows $C_{10}H_{17}O_z$ peroxy radical family members and panel E shows $C_{10}H_{18}O_z$ family members which is the mixture of the alcohol and the hydroperoxide. Mind that the scale of the y-axes are not same.

Figure 3.14 shows the behaviour of the C_{10} family members in different panels. Panel B and D represents the signals from the $C_{10}H_{15}O_z$ and the $C_{10}H_{17}O_z$ family members which were described before. However, it is shown here again for an easy reference. In panel A, C, E, the normalised signal of $C_{10}H_{14}O_z$, $C_{10}H_{16}O_z$ and $C_{10}H_{18}O_z$ family members are shown. These families belong to termination products from $C_{10}H_{15}O_z$ and $C_{10}H_{17}O_z$ peroxy radicals. The same symbols represent that the molecules that have same number of O-atoms. It should be noted that the order of the signal intensities and the signals itself is important factor in this analysis. That is because the aim of this work is to find and elucidate the precursors of termination products.

In the *ozonolysis* phase the $C_{10}H_{15}O_8$ peroxy radical concentration were the highest. Accordingly, $C_{10}H_{14}O_7$ (carbonyl) and $C_{10}H_{16}O_7$ (alcohol) from disproportionation reaction R1.2.8 shows high signal in panel A and C. $C_{10}H_{16}O_8$, which was attributed to hydroperoxides, shows only a low signal. As second highest, $C_{10}H_{15}O_{10}$ peroxy radicals produced $C_{10}H_{14}O_9$ (carbonyl products) and $C_{10}H_{16}O_9$ (alcohols). The alcohols $C_{10}H_{16}O_7$ and $C_{10}H_{16}O_9$ shows the relatively

highest signals in the ozonolysis dominant phase but were very low compared to OH oxidation phase. Considering the high intensity of $C_{10}H_{15}O_8$ and $C_{10}H_{15}O_{10}$, it can be concluded that significant contribution to the $C_{10}H_{16}O_9$ and $C_{10}H_{16}O_7$ signal should come from alcohol termination products of $C_{10}H_{15}O_{10}$ and $C_{10}H_{15}O_8$ respectively. It is not clear why $C_{10}H_{16}O_7$ showed lower signal than $C_{10}H_{16}O_9$ despite of higher signal of $C_{10}H_{15}O_8$ compared to $C_{10}H_{15}O_{10}$.

The normalised signal of $C_{10}H_{14}O_z$ and $C_{10}H_{16}O_z$ family members can be compared, keeping in mind that they are related by the disproportionation reaction R1.2.8. The signals of the carbonyls were for $C_{10}H_{14}O_7$ = 1.16 $\times$ 10^{-4} and for $C_{10}H_{14}O_9$ = 0.9 $\times$ 10^{-4}. The corresponding alcohols $C_{10}H_{16}O_7$ and $C_{10}H_{16}O_9$ showed signals of 0.4 $\times$ 10^{-4} and 0.9 $\times$ 10^{-4}, respectively. The latter were upper limits as they include possible contributions by hydroperoxides. $C_{10}H_{14}O_7$ carbonyl compounds showed three times higher signal than $C_{10}H_{16}O_7$ despite of the fact that $C_{10}H_{16}O_7$ may include signals from hydroperoxides. There can be two reasons for the discrepancy between $C_{10}H_{14}O_7$, $C_{10}H_{16}O_7$ and $C_{10}H_{14}O_9$, $C_{10}H_{16}O_9$. One reason is the above mentioned preference for the carbonyl functionality depending on the molecular structure, i.e. $C_{10}H_{15}O_8$ may comprise peroxy radicals with molecular structures with a preference towards carbonyl formation. The second reason is possible formation of alcohol and hydroperoxide from $C_{10}H_{13}O_{8,10}$ peroxy radicals. However, the possibility of the second is low in the ozonolysis phase, supported by the very low signal of $C_{20}H_{28}O_z$ family.

From $C_{10}H_{17}O_z$ family, only $C_{10}H_{17}O_{10}$ peroxy radical was detected with a decent signal. As expected, $C_{10}H_{17}O_{10}$ peroxy radical and $C_{10}H_{18}O_z$ family members showed only low signal in the dark phase. However, C_{20} family analysis indicated $C_{20}H_{32}O_z$ and $C_{20}H_{30}O_z$ accretion products with similar signal strength (Figure 3.10). This means that $C_{10}H_{17}O_z$ peroxy radicals were produced from α-pinene and dark OH, but preferred forming accretion products instead of monomer termination products. In conclusion, accretion product formation reactions are competitive if not faster than termination reactions with RO_2 and HO_2. This is in accordance with Berndt *et al.*, 2018b who observed rate coefficients up to the collision limit in accretion product formation of HOM-RO_2.

In the *photooxidation*, the situation was more complicated. We know from the C_{10} and C_{20} family analysis that $C_{10}H_{15}O_z$ were the major peroxy radicals. Therefore, the analysis will begin with the markers of $C_{10}H_{14}O_z$ and $C_{10}H_{16}O_z$ family members formed from $C_{10}H_{15}O_z$ peroxy radicals. In Figure 3.14 panel B, the $C_{10}H_{15}O_7$ and the $C_{10}H_{15}O_9$ peroxy radicals with an odd number of O-atoms showed the strongest signal. The $C_{10}H_{15}O_{even}$ peroxy radicals ($C_{10}H_{15}O_8$ and $C_{10}H_{15}O_{10}$) from the autoxidation of $C_{10}H_{15}O_4$ peroxy radicals showed only intermediate strong signals. As mentioned before, the strong signal from $C_{10}H_{15}O_{odd}$ peroxy radicals is an indication of the importance of alkoxy-peroxy pathway.

The $C_{10}H_{15}O_7$ peroxy radical could produce $C_{10}H_{14}O_6$ which was attributed to carbonyls and $C_{10}H_{16}O_6$ which was attributed to alcohols. Both $C_{10}H_{14}O_6$ and $C_{10}H_{16}O_6$ showed a relatively low signal intensity in the high turnover range. On the other hand, the signal of $C_{10}H_{16}O_7$ which was partially produced from the reaction between $C_{10}H_{15}O_7$ and HO_2 showed a very strong increase with increasing turnover and it was the most outstanding peak in the mass

spectra in the OH oxidation phase (Figure 3.3). A high concentration of the $C_{10}H_{15}O_7$ peroxy radicals and an increasing HO_2/RO_2 ratio (Figure 3.7) suggested that a significant portion of the increase of the $C_{10}H_{16}O_7$ might come from the hydroperoxides formation from $C_{10}H_{15}O_7$. However, the conclusion cannot be made that $C_{10}H_{16}O_7$ was increased solely by the increase of hydroperoxide formation from $C_{10}H_{15}O_7$ peroxy radicals because there are two more formation channels of the $C_{10}H_{16}O_7$. $C_{10}H_{15}O_8$ peroxy radicals and $C_{10}H_{17}O_8$ peroxy radicals can be the precursors of the $C_{10}H_{16}O_7$ as well, if they are terminated as alcohols and carbonyls, respectively. The signal of the $C_{10}H_{15}O_8$ peroxy radicals were detected as a third highest thus likely to contribute substantially to the formation of the $C_{10}H_{16}O_7$. $C_{10}H_{17}O_8$ as not detected directly but could be important for several reasons: their immediate autoxidation products $C_{10}H_{17}O_{10}$ as directly detected, and their termination products with RO_2 ($C_{10}H_{18}O_7$, R1.2.8) and with HO_2 ($C_{10}H_{18}O_8$, R1.2.7), respectively, where the most abundant $C_{10}H_{18}O_z$ family members (Figure 3.14, panel E). So there are good reasons that the carbonyl termination product in R1.2.8 is formed as well and contributes substantially to the $C_{10}H_{16}O_7$ concentration. Since $C_{10}H_{16}O_7$ provided by far the highest signal in the OH oxidation phase, the prediction of its strength and its relation to $C_{10}H_{15}O_7$, $C_{10}H_{15}O_8$, and $C_{10}H_{17}O_8$ peroxy radicals will be a key to the mechanistic understanding of HOM formation.

The $C_{10}H_{15}O_9$ peroxy radical which has the second highest peroxy radical signal from $C_{10}H_{15}O_z$ family can produce $C_{10}H_{14}O_8$ and $C_{10}H_{16}O_8$ (carbonyls and alcohols, respectively). The $C_{10}H_{14}O_8$ showed the highest signal among the $C_{10}H_{14}O_z$ family members and the $C_{10}H_{16}O_8$ showed the second highest signal among the $C_{10}H_{16}O_z$ family members, both with similar intensity. In a cautious conclusion, the $C_{10}H_{14}O_8$ and the $C_{10}H_{16}O_8$ were mainly produced from the $C_{10}H_{15}O_9$ peroxy radicals. However, it cannot be excluded that $C_{10}H_{14}O_8$ were formed as alcohols or hydroperoxides from $C_{10}H_{13}O_9$ or $C_{10}H_{13}O_8$ peroxy radicals, respectively ($C_{10}H_{13}O_z$ may play a role as indicated by the marker analysis of the accretion products). In addition, hydroperoxide formation from the $C_{10}H_{15}O_8$ can produce the $C_{10}H_{16}O_8$ which might be an important channel. In addition, it is not clear why $C_{10}H_{15}O_7$ and $C_{10}H_{15}O_9$ showed a different preference for the reaction channels (the first seem to prefer hydroperoxide formation, while the other seem to undergo the disproportionation reaction to carbonyls and alcohols), but this preference depends on the detailed structure of the $C_{10}H_{15}O_7$ and $C_{10}H_{15}O_9$ peroxy radicals. That is the limitation of the mass spectrometer based analysis since it is not able to elucidate the detailed structure between isobaric compounds. The $C_{10}H_{16}O_8$ which is partially attributed to hydroperoxides from $C_{10}H_{15}O_8$ peroxy radicals showed only intermediate strong intensity despite the high intensity of $C_{10}H_{15}O_8$.

In Figure 3.14 panel A, the $C_{10}H_{14}O_7$ and the $C_{10}H_{14}O_9$ showed the second highest and similar normalised signal. The peroxy radicals $C_{10}H_{15}O_8$ and $C_{10}H_{15}O_{10}$ showed the third and fourth highest but similar signal in Figure 3.14 panel B. Thus, it is likely that $C_{10}H_{14}O_7$ and $C_{10}H_{14}O_9$ were arising as carbonyl disproportionation products from the precursor peroxy radicals $C_{10}H_{15}O_8$ and $C_{10}H_{15}O_{10}$. However, only $C_{10}H_{16}O_9$ from the corresponding alcohols appeared at about the expected signal strength in Figure 3.14, panel C. As was already discussed,

the formation of $C_{10}H_{16}O_7$ has multiple pathways, that enhances the signal of the compound strongly.

Only one compound of the $C_{10}H_{17}O_z$ family could be directly detected. The compound was $C_{10}H_{17}O_{10}$ and had even number of oxygen atoms. In addition, lack of abundance could be seen in the relatively small signals of the $C_{10}H_{18}O_z$ family members compared to other closed shell products. On the other hand, the concentration of the $C_{10}H_{14}O_z$ and the $C_{10}H_{16}O_z$ families are relatively high.

In Figure 3.14, panel E, the $C_{10}H_{18}O_8$ and the $C_{10}H_{18}O_7$ family members had the highest signal among the seven $C_{10}H_{18}O_z$ family members. The $C_{10}H_{18}O_8$ could be formed from $C_{10}H_{17}O_9$ peroxy radicals and $C_{10}H_{17}O_8$ peroxy radicals. The $C_{10}H_{18}O_7$ could be formed from $C_{10}H_{17}O_8$ peroxy radicals or $C_{10}H_{17}O_7$ peroxy radicals. As mentioned, $C_{10}H_{17}O_8$ was possibly an important peroxy radical which contributed to the strong signal of $C_{10}H_{16}O_7$ by the reaction R1.2.8. It could form the major products observed $C_{10}H_{18}O_7$ as alcohol and $C_{10}H_{18}O_8$ as hydroperoxide as well. However, the reason why these products of $C_{10}H_{17}O_8$ are higher than $C_{10}H_{18}O_{10}$ or $C_{10}H_{18}O_9$ which were the analogous products of the detected $C_{10}H_{17}O_{10}$ peroxy radical is not clear. Among the precursor peroxy radicals of the four major $C_{10}H_{18}O_z$ family members, the $C_{10}H_{17}O_8$ peroxy radicals and the $C_{10}H_{17}O_{10}$ peroxy radicals which have an even number of O-atoms showed again the importance of alkoxy-peroxy pathway.

Up to here, the changes in families and marker compounds with an increasing turnover by OH radical was anlaysed. The $C_{10}H_{15}O_z$ peroxy radicals were observed as the major peroxy radicals rather than $C_{10}H_{17}O_z$ peroxy radicals. This is attributed to the importance of the H-abstraction by OH radicals in oxidation products such as pinonaldehyde, and and possibly hindered autoxidation of $C_{10}H_{17}O_3$ peroxy radicals which have two intact ring systems (Rissanen *et al.*, 2015). In addition, it was observed that accretion products can form very fast and possibly even faster than monomers in termination reactions ($C_{10}H_{17}O_z$ form more accretion products than monomer termination products). In addition, it was observed that peroxy radicals that could either not be directly detected or that have a lower degree of oxidation were involved in the accretion products formation. In this way, indirect hints were found for the existence of $C_{10}H_{13}O_z$ peroxy radicals. By investigating the O-atom parity of marker compounds, either peroxy radical or monomers or accretion products, the importance of alkoxy-peroxy pathway was supported.

In the next section, the OH oxidation of α-pinene in high HO_2/RO_2 regime will be described by comparing two experiments with and without CO at similar turnover.

3.3 Photochemical oxidation of α-pinene: Effect of CO

As shown in Figure 1.1, HOM-RO_2 peroxy radicals have different reaction channels. The branching ratio into each channel depends on the experimental conditions and can be varied. In the previous section, an α-pinene OH radical oxidation experiment was analysed. Model

simulations showed that this experiment was performed under conditions of a peroxy radical rich regime (Figure 3.7). In this section, the effect of a high HO_2/RO_2 ratio on HOM formation in the photooxidation of α-pinene will be investigated. The HO_2/RO_2 ratio will be shifted to high HO_2 by adding CO into the system.

HOM-RO_2 peroxy radicals will undergo reactions with RO_2 peroxy radicals or HO_2 hydroperoxy radicals (R1.2.8 or R1.2.7) at low NOx concentrations in the system. Reactions with peroxy radicals produce carbonyl compounds, alcohols and accretion products, while reactions with HO_2 form hydroperoxides as a closed shell product. The role of CO molecules was to produce HO_2 radicals by converting OH radicals according to the following reactions.

$$\begin{aligned}
&\mathrm{CO + OH \longleftrightarrow HOCO\cdot} \\
&\mathrm{HOCO\cdot \longrightarrow H + CO_2, H + O_2 + M \longrightarrow HO_2 + M} \\
&\mathrm{HOCO\cdot \longrightarrow HOCO + M, HOCO + O_2 \longrightarrow HO_2 + CO_2}
\end{aligned} \qquad \text{R3.3.21}$$

As a result, the OH and thus the RO_2 concentrations decreases and the HO_2 radical concentration increases, which results in an increase of the HO_2/RO_2 ratio. To minimize other effects on the HOM chemistry besides that of HO_2/RO_2RO2, two experiments, with and without CO addition, were selected which had about the same steady state α-pinene turnover by OH. The steady state period in the J(O^1D) experiments with a turnover of 5.53×10^7 cm^{-3} s^{-1}, was chosen as a reference for the comparison to a steady state period in the CO experiment with a turnover of 5.60×10^7 cm^{-3} s^{-1}. The turnover of the OH varying experiments was achieved at an α-pinene steady state concentration of 2 ppb and an OH concentration of 2.57×10^7 cm^{-3}. Due to the OH scavenging effect of CO, the same turnover in the CO experiment (at 3 ppm CO) was reached at a lower steady state OH concentration of about 1×10^7 cm^{-3} and a higher α-pinene steady state concentration of about 5 ppb. Thus, the RO_2 concentration was lowered and the HO_2 concentration was enhanced and HO_2/RO_2 increased from 0.012 to 3.1, a factor of about 250.

Figure 3.15 shows the modeled HO_2 radical and RO_2 peroxy radical concentration in the reference experiment and in the CO experiment. The black bars show the concentration of HO_2 radicals and RO_2 peroxy radicals from reference experiment. The red bars show the concentration of HO_2 radicals and RO_2 peroxy radicals from the CO experiment. The color code "black" for the reference and "red" for the CO experiment will be kept in the following figures. Despite the similar turnover, the concentrations of HO_2 and RO_2 were very different in the CO and the reference experiment.

The increase of the HO_2/RO_2 ratio triggered changes in the closed shell product patterns. As the RO_2 concentration decreased, the whole HOM concentration was expected to decrease. In addition, a shift to HOM hydroperoxides was expected because of the higher HO_2 concentration.

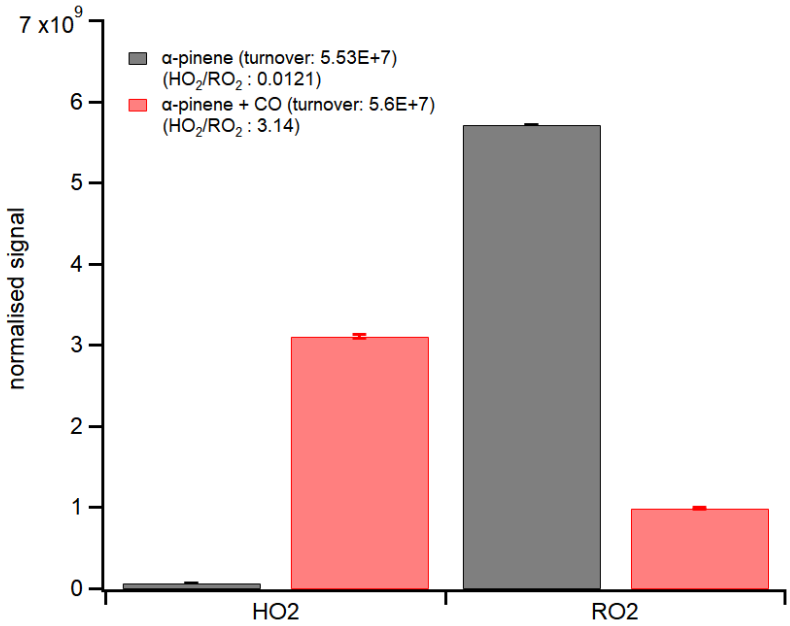

Figure 3.15: Bar graph of modeled HO_2 and RO_2 concentration of two experiments. The HO_2/RO_2 ratio was 0.012 for the reference experiment and 3.1 for the CO experiment. (Model data were provided by Silvia Proff)

3.3.1 Mass spectrum comparison

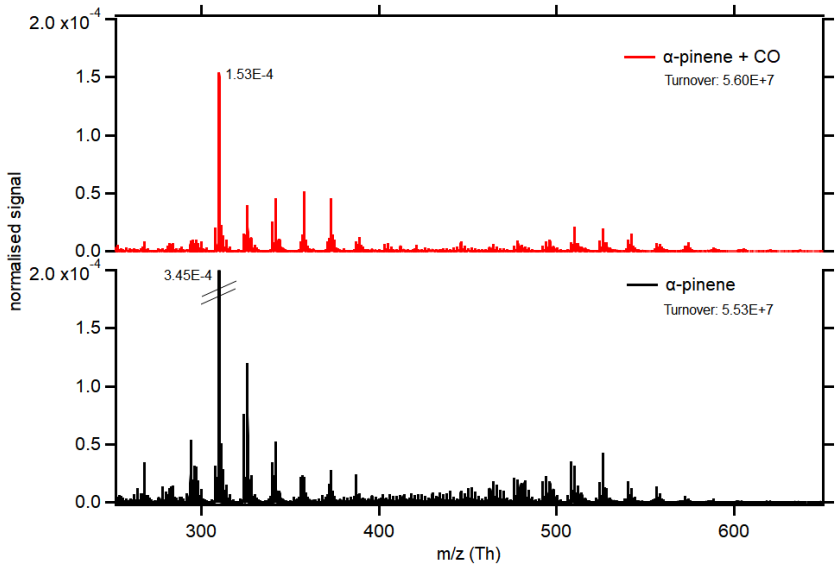

Figure 3.16: Mass spectra obtained for experiments with (red) and without CO (black) at steady state conditions and at similar turnover. Lower black mass spectrum was taken at a turnover of 5.53×10^7 $cm^{-3}s^{-1}$ (reference mass spectrum). Upper red mass spectrum shows the situation of an experiment with 3 ppm of CO with turnover 5.60×10^7 $cm^{-3}s^{-1}$. The x-axis shows the mass per charge ratio. Compounds were detected as nitrate clusters. The y-axis shows the signal normalised to the total ion count. Because of the high signal at 310 Th in the reference mass spectra (normalised signal 3.45×10^{-4} ncps), not the entire peak is shown in the mass spectrum for better comparison.

Figure 3.16 shows mass spectra of the reference experiment and the CO experiment. The lower mass spectrum (black) shows the steady state situation of the reference experiment and the upper mass spectrum (red) shows the steady state situation in the CO experiment. Since the peak at 310 Th in the reference mass spectrum was showing a very high signal, it was clipped. As can be directly seen, the addition of CO reduced the signal of monomers and accretion products (450 Th - 550 Th). The accretion product envelope is shifted towards higher mass range and the monomer envelope was also overall shifted to higher masses. In other words, the oxidation degree of HOM monomers and HOM accretion products increased in the presence of CO.

3.3.2 Monomer and accretion product comparison

The signal intensities of monomers and accretion products are compared in Figure 3.17. As shown in panel A, the sum of monomers (sum of normalised signal of $C_{5\text{-}10}$) decreased to about one half when CO was added to the system. Herein C_{10} monomers decreased by 40 % while

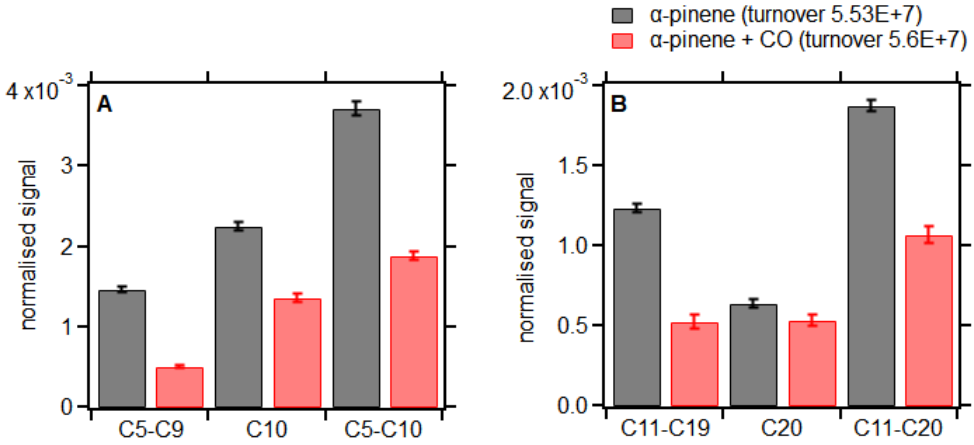

Figure 3.17: Bar graph of monomer and accretion products of two experiments are shown here. On the left side, panel A shows the comparison of monomers. $C_{5\text{-}9}$ shows the fragmented monomers and $C_{5\text{-}10}$ shows the sum of monomers. On the right side, panel B shows the comparison of accretion products. $C_{11\text{-}19}$ shows the smaller accretion products and $C_{11\text{-}20}$ shows the sum of all accretion products.

$C_{5\text{-}9}$ monomers resulting from fragmentation processes decreased by 65 %. In panel B, the sum of accretion products (sum of normalised signal of $C_{11\text{-}20}$) features a signal decrease by 43 % in the presence of CO. Smaller accretion products declined by 58 % whereas C_{20} accretion products showed only a 15 % reduction. Both, monomers and accretion products were showing diminished signals and a considerable amount of the reduction was accounted for by the decrease of monomers and accretion products which went through a step of fragmentation. The reason for reduced fragmentation was the decrease of RO_2 in the CO experiment. The decrease of RO_2 resulted in slower RO_2+RO_2 reactions and as a consequence, alkoxy radical formation (R1.2.10) was reduced which led to less fragmentation. In the next section, it will described how C_{10} monomer and C_{20} accretion product families were affected by CO.

3.3.3 The effect of CO on C_{10} and C_{20} families

It can be anticipated that the $C_{10}H_{14}O_z$ family would show a decreased signal. That is because the $C_{10}H_{14}O_z$ family comprised mainly carbonyl compounds formed by the $C_{10}H_{15}O_z$ peroxy radical family in reactions with RO_2. The expected behaviour of the $C_{10}H_{16}O_z$ family is difficult to predict because some members of the $C_{10}H_{16}O_z$ family which are attributed to hydroperoxides should show an increased signal while other members which are attributed to alcohols and carbonyls from $C_{10}H_{15}O_z$ and $C_{10}H_{17}O_z$ peroxy radicals, respectively, should decrease in signal. The $C_{10}H_{18}O_z$ family is expected to increase or remain similar to the reference system because hydroperoxides are attributed to it (from reactions with HO_2) and alcohols (from disproportionation reactions with RO_2). The C_{20} families were expected to decrease in general

because the competition between termination reactions at higher HO_2 and lower RO_2 would make accretion product formation less probable.

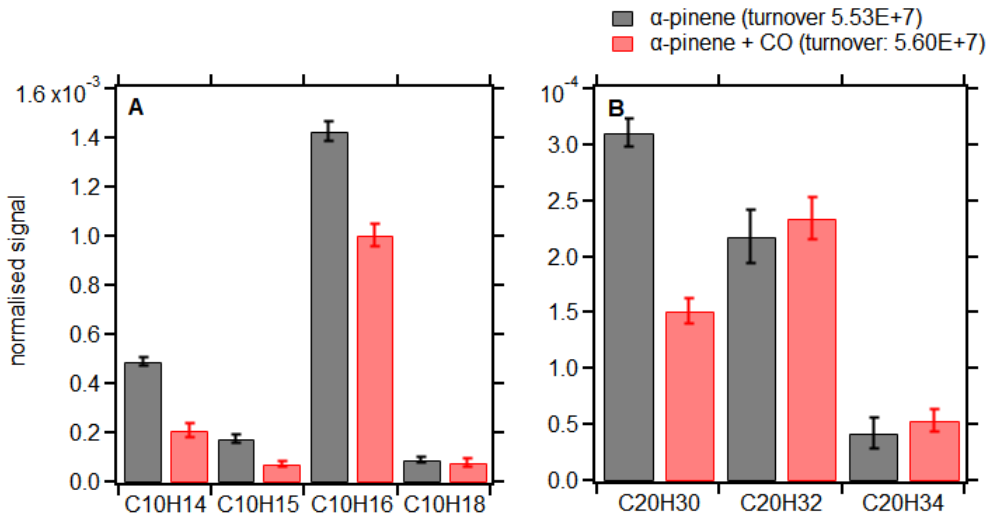

Figure 3.18: Bar graph of C_{10} monomer families and C_{20} accretion product families of two experiments are shown here. $C_{10}H_{17}O_z$ family and $C_{20}H_{28}O_z$ family did not shown here because they were not detected in CO experiment.

In panel A of Figure 3.18, the four monomer families which were detected are shown. On the right side, in panel B, the detected three accretion product families are displayed. Only the $C_{10}H_{15}O_z$ peroxy radical family was detected directly and the signals of the $C_{10}H_{17}O_z$ family were below the detection limit. The signal of the $C_{10}H_{15}O_z$ peroxy radical family was decreased by more than a half in the CO experiment (in Panel A). Based on the results in previous chapter that accretion products are a good indicator of peroxy radicals, the changes in accretion products in panel B will be discussed first. $C_{20}H_{30}O_z$ accretion products are decreased by more than a half at high HO_2/RO_2 ratio. Since $C_{20}H_{30}O_z$ were produced by the reaction between two $C_{10}H_{15}O_z$ peroxy radicals, this result is in agreement with the strong decrease of $C_{10}H_{15}O_z$ peroxy radicals in panel A. However, the $C_{20}H_{32}O_z$ and the $C_{20}H_{34}O_z$ accretion product families were somewhat increased in the CO experiment compared to the reference experiment. The $C_{20}H_{32}O_z$ accretion products were formed in reactions between $C_{10}H_{15}O_z$ and $C_{10}H_{17}O_z$ peroxy radicals. Since $C_{10}H_{15}O_z$ peroxy radicals decreased which is reflected in a reduced $C_{20}H_{30}O_z$ family, the reason for the increase of $C_{20}H_{32}O_z$ accretion products must be an over proportional relative increase of the $C_{10}H_{17}O_z$ peroxy radical family. The increased signal of the $C_{20}H_{34}O_z$ accretion products family confirmed such an increase of the $C_{10}H_{17}O_z$ peroxy radical family. From the C_{20} family analysis, it can be seen that the $C_{10}H_{15}O_z$ peroxy radical family decreased in importance while the impact of the $C_{10}H_{17}O_z$ peroxy radical family increased. This result

means that there is less contribution by the secondary oxidation of oxidation products, which can be understood since the OH level is lower.

In panel A, generally, all monomer families showed a decreased signal at high HO_2/RO_2 ratio. The $C_{10}H_{14}O_z$ family showed a signal reduced by about a half. The $C_{10}H_{14}O_z$ family was attributed to carbonyl compounds resulting from the disproportionation reaction between $C_{10}H_{15}O_z$ peroxy radicals and other peroxy radicals. Thus, it is reasonable that the $C_{10}H_{14}O_z$ family decreased because the $C_{10}H_{15}O_z$ peroxy radicals concentration decreased. The $C_{10}H_{16}O_z$ family also showed a decreased signal in the CO experiment, but the reduction was only about 25 %. The smaller reduction is probably an overlap of decreasing alcohol formation (R1.2.8) and increasing hydroperoxide formation (R1.2.7) from the $C_{10}H_{15}O_z$ peroxy radical family. Since the overall loss of C_{10}-HOM was 40 %, the $C_{10}H_{16}O_z$ family showed a relative gain within the C_{10} families while the $C_{10}H_{15}O_z$ signal showed an over proportional loss. The $C_{10}H_{18}O_z$ family showed no change of signal in the CO experiment. Since it is known from the accretion product family analysis that the importance of $C_{10}H_{17}O_z$ peroxy radicals increased in the CO experiment, the conclusion can be made that a decrease of alcohol formation by reaction of $C_{10}H_{17}O_z$ with RO_2 was compensated by an increase of hydroperoxides by reactions of $C_{10}H_{17}O_z$ with HO_2. Also here, a constant signal with respect to the reference experiment means relative gain in importance for the $C_{10}H_{18}O_z$ family.

There are two possible reasons for a generally decreased signal of the monomer families. The first one is the reduced RO_2 concentration in the presence of CO ratio as shown in modeled RO_2 result (Figure 3.15) and by reduced concentration of the $C_{10}H_{15}O_z$ family (Figure 3.18). There are less detected HOM termination products because there are less detected HOM-RO_2. The second reason can be an increased importance of the termination reactions by HO_2 in competition to autoxidation. However, the reduced RO_2 concentration will counteract this effect. The shift of the peak envelopes in the mass spectra (Figure 3.16) for monomers as well as accretion products at reduced OH concentration suggests that autoxidation is not suppressed if not enhanced in the presence of CO.

3.3.4 The effect of CO on C_{10} and C_{20} marker compounds

The overall monomers and accretion products showed already less fragmentation thus less formation of alkoxy radicals in the presence of CO. In this section, it will be investigated if less alkoxy radical formation can be detected by the parity of C_{10} and C_{20} marker compounds. Moreover, it will be analysed whether increased of $[HO_2]$ while decreasing $[RO_2]$ can compete with the autoxidation.

C_{10} peroxy radicals

As a reminder, it should be repeat here: the first generation peroxy radicals in α-pinene oxidation by OH radical has the molecular formula $C_{10}H_{17}O_3$ and their autoxidation products will

have odd numbers of O-atoms, $C_{10}H_{17}O_{odd}$. In contrast, $C_{10}H_{15}O_4$ is the molecular formula for the first peroxy radicals formed by H-abstraction from oxidation products like pinonaldehyde. The corresponding autoxidation products will have even numbers of O-atoms, $C_{10}H_{15}O_{even}$. An alkoxy step in the autoxidation chain will change the parity of the numbers of O-atoms.

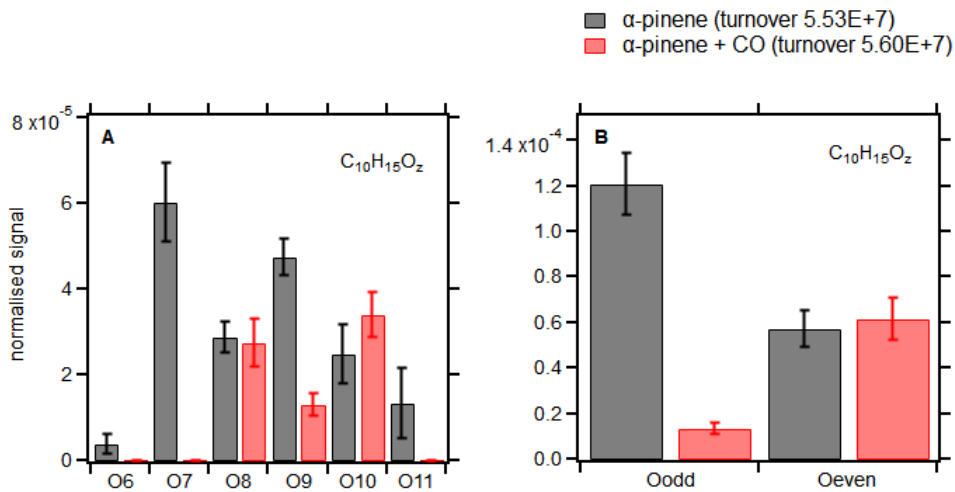

Figure 3.19: Bar graph of $C_{10}H_{15}O_z$ accretion product family members of two experiments are shown here. On the left side, panel A shows the normalised signal of each member in the two experiments is shown. The x-axis shows the number of O-atoms in the family members' molecular formula and the y-axis shows the normalised signal. On the right side, sum of family members which have an odd or even number of oxygen in the molecule was shown for two experiments.

In Figure 3.19, panel A shows the signals of the members of the $C_{10}H_{15}O_z$ family with and without CO. The $C_{10}H_{15}O_7$ peroxy radical showed a significantly decreased signal in the CO experiment compared to the reference experiment. On the other hand, $C_{10}H_{15}O_8$ and $C_{10}H_{15}O_{10}$ peroxy radicals with even numbers of O-atoms showed a stable or even increased signal in the CO experiment. Panel B shows that the concentration of the $C_{10}H_{15}O_{odd}$ peroxy radicals was strongly reduced while that of the $C_{10}H_{15}O_{even}$ peroxy radicals were even slightly increased despite the generally reduced $[RO_2]$ in the CO experiment (Figure 3.15). In other words, $C_{10}H_{15}O_z$ peroxy radicals were decreased mainly because of the decrease of $C_{10}H_{15}O_{odd}$ peroxy radicals which were produced by one alkoxy step in the alkoxy-peroxy pathway. This is the case because lower RO_2 concentration and an enhanced HO_2 concentration reduced the paths to alkoxy radicals (R1.2.10) and thus the formation of $C_{10}H_{15}O_{odd}$ in favour of hydroperoxide formation.

C_{20} marker compounds

It was observed in the family analysis that the $C_{20}H_{30}O_z$ accretion product family showed a lower signal, while both, $C_{20}H_{32}O_z$ and $C_{20}H_{34}O_z$ families showed a higher signal in the presence of CO.

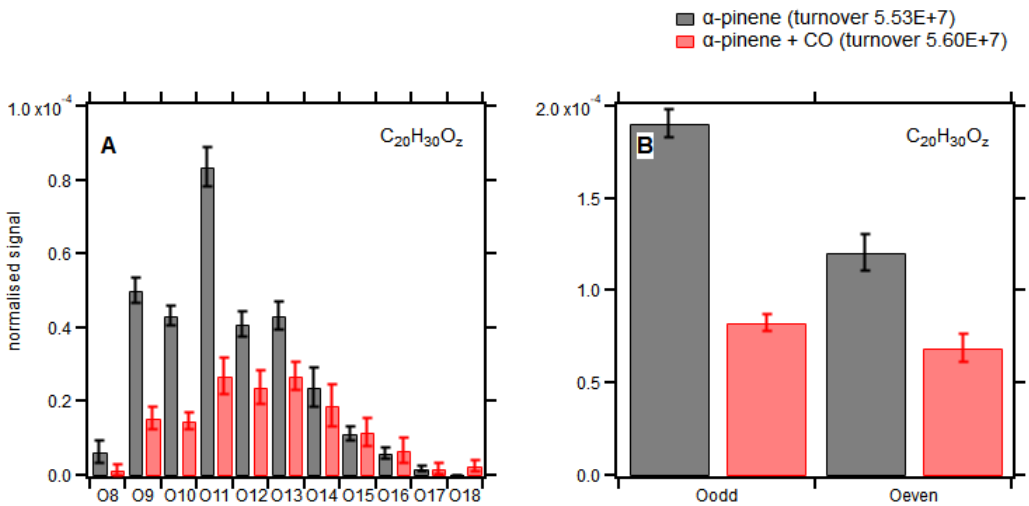

Figure 3.20: Bar graph of $C_{20}H_{30}O_z$ accretion product family members of two experiments. On the left side, panel A shows the normalised signal of each member in the two experiments is shown. The x-axis is the number of O-atoms in the family members' molecular formula. On the right side, sum of family members which have an odd or even number of oxygen in the molecule is shown for two experiments.

In Figure 3.20, panel A shows the detected family members in the $C_{20}H_{30}O_z$ accretion product family, with and without CO addition. In the presence of CO, $C_{20}H_{30}O_z$ family members showed a shift towards a higher oxidation state in general. This can be seen from the strongly decreased signal of less oxygenated $C_{20}H_{30}O_{8\text{-}11}$ family members and the milder decrease or even increase of the more oxygenated family members, $C_{20}H_{30}O_{13\text{-}18}$. In Figure 3.20, panel B shows how $C_{20}H_{30}O_{odd}$ and $C_{20}H_{30}O_{even}$ are affected by the additions of CO. As expected, $C_{20}H_{30}O_{odd}$ was showing a stronger decrease than $C_{20}H_{30}O_{even}$. This is the case that the $C_{20}H_{30}O_{odd}$ accretion products are formed from the recombination of $C_{10}H_{15}O_{odd}$ and $C_{10}H_{15}O_{even}$ peroxy radicals. The lower RO_2 concentration and enhanced HO_2 concentration reduce the path to alkoxy radicals (R1.2.10). As a consequence, less $C_{10}H_{15}O_{odd}$ resulted in lower $C_{20}H_{30}O_{odd}$ accretion products.

$C_{20}H_{32}O_z$ accretion products are produced in the reaction between $C_{10}H_{15}O_p$ and $C_{10}H_{17}O_q$ peroxy radicals where z=p+q-2. The reason for changes in [$C_{20}H_{32}O_{odd}$] are difficult to figure

out. $C_{20}H_{32}O_{odd}$ formed from the recombination of $C_{10}H_{15}O_{odd}$ and $C_{10}H_{17}O_{even}$ would be decreased in concentration because of the reduced alkoxy-peroxy pathway (both $C_{10}H_{15}O_{odd}$ and $C_{10}H_{17}O_{even}$ peroxy radicals are produced via alkoxy-peroxy pathway) while $C_{10}H_{15}O_{even}$ and $C_{10}H_{17}O_{odd}$ recombination would remain similar or even increased (because $C_{10}H_{17}O_z$ in general increased as can be seen in the $C_{20}H_{34}O_z$ family analysis). However, $C_{20}H_{32}O_{even}$ accretion products are expected to be decreased since $C_{20}H_{32}O_{even}$ accretion products need one peroxy radical from the alkoxy peroxy pathway ($C_{10}H_{17}O_{odd}$ and $C_{10}H_{15}O_{odd}$ from alkxoy peroxy pathway or $C_{10}H_{15}O_{even}$ and $C_{10}H_{17}O_{even}$ from alkxoy peroxy pathway).

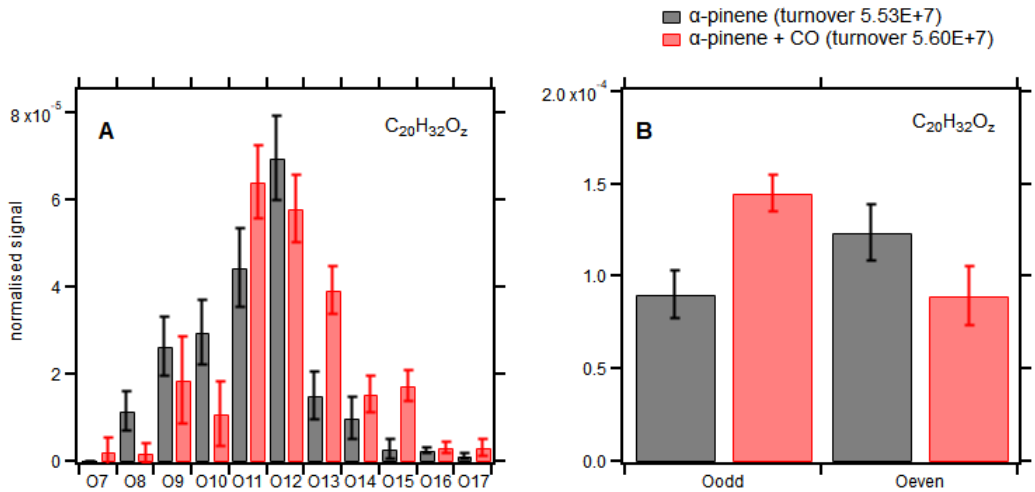

Figure 3.21: Bar graph of $C_{20}H_{32}O_z$ accretion product family members of two experiments are shown here. On the left side, panel A shows the normalised signal of each member. The x-axis is the number of O-atoms in the family members' molecular formula. On the right side, the sum of family members which have odd or even number of oxygen in the molecule is shown for two experiments.

Figure 3.21 shows the changes in $C_{20}H_{32}O_z$ accretion products marker compounds. $C_{20}H_{32}O_z$ family members showed a higher degree of oxidation during CO addition than during the reference experiment. $C_{20}H_{32}O_{7,11,13,15}$ accretion products with an odd number of O-atoms showed a higher a signal in the CO experiments. In addition, $C_{20}H_{32}O_{8,10,12}$ with an even number of O-atoms showed a decreased signal in the CO experiment, as expected. In conclusion, $C_{20}H_{32}O_{odd}$ accretion products are formed in a reaction of $C_{10}H_{15}O_{even}$ and $C_{10}H_{17}O_{odd}$ peroxy radicals which did not involve an alkoxy radical step. $C_{20}H_{32}O_{even}$ accretion products were formed from either a pair of $C_{10}H_{15}O_{odd}$ and $C_{10}H_{17}O_{odd}$ peroxy radicals or $C_{10}H_{15}O_{even}$ and $C_{10}H_{17}O_{even}$ peroxy radicals and they decreased because both pairs include one peroxy radical which is formed in the alkoxy peroxy pathway ($C_{10}H_{15}O_{odd}$ or $C_{10}H_{17}O_{even}$). Panel B shows the obvious increase of $C_{20}H_{32}O_{odd}$ and the decrease of $C_{20}H_{32}O_{even}$ accretion products.

It shows again that at high HO_2/RO_2 ratio, less alkoxy radicals were formed. $C_{20}H_{32}O_{14,16}$ accretion products showed an increased signal in the CO experiment even though they had an even number of oxygen. Since a decrease of $C_{10}H_{15}O_z$ peroxy radicals (from Figure 3.18) was observed, the increase of $C_{20}H_{32}O_z$ accretion products must come from an increase of $C_{10}H_{17}O_z$ peroxy radicals. Additionally, the increase of $C_{20}H_{32}O_{14,16}$ can be a result of a higher concentrations of $C_{10}H_{17}O_z$.

In the case of the $C_{20}H_{34}O_z$ accretion product family which is formed from the reaction between two $C_{10}H_{17}O_z$ peroxy radicals, $C_{20}H_{34}O_{even}$ accretion products are anticipated to increase while $C_{20}H_{34}O_{odd}$ accretion products should decrease. That is the case because $C_{10}H_{17}O_{odd}$ peroxy radicals, which are not involving an alkoxy radical step in the formation, would increase and as a result, $C_{20}H_{34}O_{even}$ accretion products would increase from two $C_{10}H_{17}O_{odd}$ peroxy radicals. On the other hand, $C_{10}H_{17}O_{even}$ peroxy radicals would decrease and $C_{20}H_{34}O_{odd}$ from $C_{10}H_{17}O_{even}$ and $C_{10}H_{17}O_{odd}$ peroxy radicals might be decreased as well.

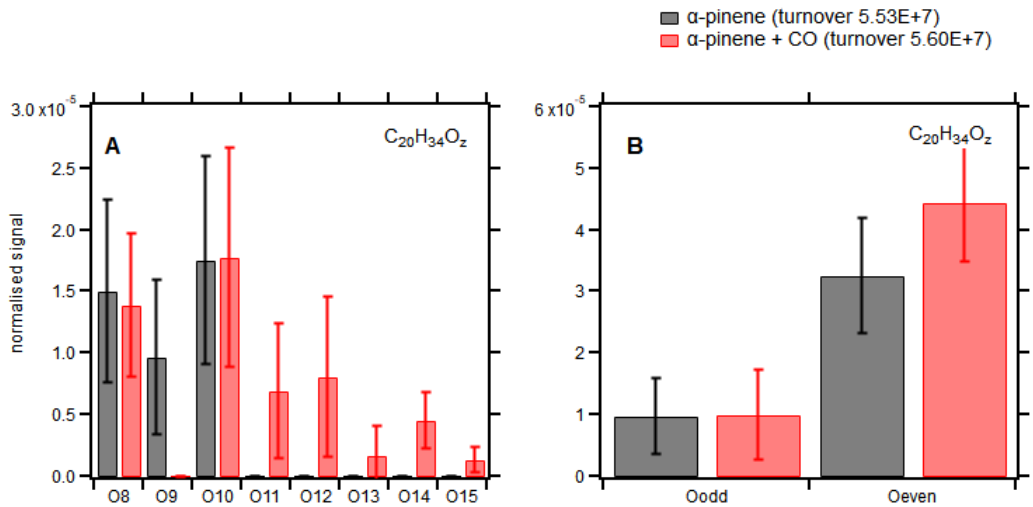

Figure 3.22: Bar graph of $C_{20}H_{34}O_z$ accretion product family members of two experiments. Panel A shows the normalised signal of each member in the two experiments. The x-axis is the number of O-atoms in the family members' molecular formula. On the right side, sum of family members which have an odd or even number of oxygen in the molecule is shown for two experiments.

Figure 3.22 shows the changes of $C_{20}H_{34}O_z$ family members with a higher HO_2/RO_2 ratio. In the reference experiment (black bars), only three family members were detected ($C_{20}H_{34}O_8$, $C_{20}H_{34}O_9$ and $C_{20}H_{34}O_{10}$). However, there were more $C_{20}H_{34}O_z$ family members with a higher number of O-atoms, up to 15 O-atoms during the CO experiment, showing a higher degree of oxidation. As expected, $C_{20}H_{34}O_{even}$ accretion products increased while $C_{20}H_{34}O_{odd}$ accretion products concentration was constant (panel B of Figure 3.22). The increase of $C_{20}H_{34}O_{even}$

probably comes from an increase of $C_{10}H_{17}O_{odd}$ peroxy radicals. That is the case because $C_{20}H_{34}O_{even}$ could be produced from the reaction of two $C_{10}H_{17}O_{odd}$ peroxy radicals, and the $C_{10}H_{17}O_{odd}$ peroxy radicals can be formed without alkoxy radicals being involved. $C_{20}H_{34}O_{odd}$ was increased as well and that might be a result of the increase of the $C_{10}H_{17}O_z$ peroxy radical in general.

One possible explanation of a higher degree of oxidation in all three accretion product families is the lower concentrations of less oxygenated peroxy radicals like $C_{10}H_{15}O_4$ because of fast termination by HO_2 at the increased HO_2/RO_2 ratio. Only autoxidation can compete with termination by HO_2 and peroxy radicals which did not terminated by HO_2 manage to undergo autoxidation and become HOM-RO_2. As a result, preferably two HOM-RO_2 peroxy radicals form accretion products resulting in accretion products with a high O:C ratio. In contrast, accretion products in the reference experiment were formed as well from classical RO_2 with smaller O:C ratio and HOM-RO_2 which resulted in a lower degree of oxidation. As shown already in j(O^1D) experiments, the formation of accretion products can be very fast. Therefore, accretion products formation cannot completely suppressed even at a high HO_2/RO_2 ratio.

C_{10} marker compounds

By studying the parity of oxygen for $C_{10}H_{15}O_z$ and C_{20} family markers, clear indications of a reduced alkoxy radical formation was observed. Now, the impact of a higher HO_2/RO_2 ratio on C_{10} marker compounds will be described. The decrease of the [$C_{10}H_{15}O_z$] in general but a stronger suppression of [$C_{10}H_{15}O_{odd}$] was observed since the formation of $C_{10}H_{15}O_{odd}$ peroxy radicals involve one alkoxy radical formation step. The impacts on C_{10}-termination products are shown in Figure 3.23.

$C_{10}H_{14}O_6$, $C_{10}H_{14}O_8$ and $C_{10}H_{14}O_{10}$ which are attributed to carbonyls formed from $C_{10}H_{15}O_7$, $C_{10}H_{15}O_9$ and $C_{10}H_{15}O_{11}$ peroxy radicals showed a strongly reduced signal in the CO experiment (panel A). In contrast, $C_{10}H_{14}O_7$ and $C_{10}H_{14}O_9$ which are attributed to carbonyls formed from $C_{10}H_{15}O_8$ and $C_{10}H_{15}O_{10}$ peroxy radicals were reduced only weakly. As a result, $C_{10}H_{14}O_{even}$ showed a stronger reduction compared to $C_{10}H_{14}O_{odd}$ (Figure 3.23 panel B). This is the case because of, a) decreased $C_{10}H_{15}O_{odd}$ peroxy radicals and b) decreased importance of RO_2 + RO_2 reactions (R1.2.8). One interesting point is that even though the $C_{10}H_{15}O_{10}$ peroxy radicals showed an increase in the CO experiment, $C_{10}H_{14}O_9$ did not show increased signal. Because of the increased HO_2 concentrations, more hydroperoxides are produced from these peroxy radicals instead of carbonyls.

The $C_{10}H_{16}O_z$ family has three sources. The family members can be formed as alcohols by $C_{10}H_{15}O_z$ peroxy radicals in reactions with other RO_2 peroxy radicals. They can also be formed as hydroperoxides if $C_{10}H_{15}O_z$ peroxy radicals react with HO_2. Finally, they will be formed as carbonyls when $C_{10}H_{17}O_z$ peroxy radicals react with other RO_2 peroxy radicals. Regarding

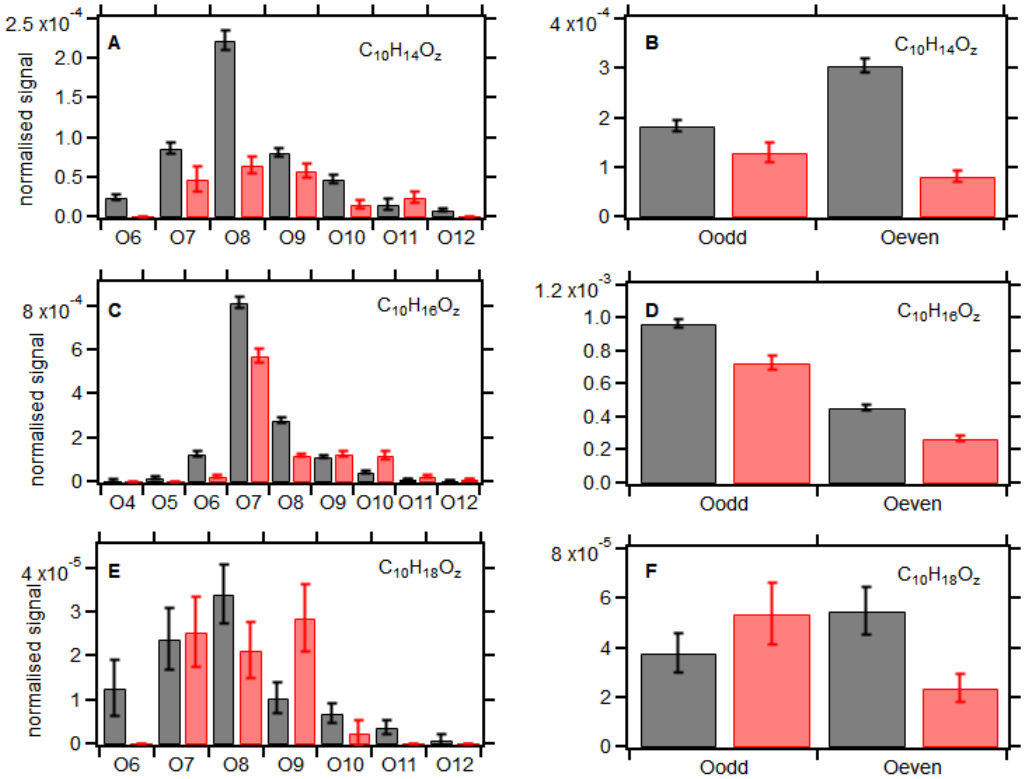

Figure 3.23: Bar graph of $C_{10}H_{14}O_z$, $C_{10}H_{16}O_z$ and $C_{10}H_{18}O_z$ family members of two experiments. Panel A, C and E show the normalised signal of each family member in two experiments. The x-axis is the number of O-atoms in the family members' molecular formula. Panel B, D and F show the sum of family members which have an odd or even number of oxygen in the molecule in the two experiments.

the even/odd parity of their O-atoms, $C_{10}H_{16}O_{odd}$ can be formed from $C_{10}H_{15}O_{even}$ as alcohols, from $C_{10}H_{15}O_{odd}$ as hydroperoxides and from $C_{10}H_{17}O_{even}$ as carbonyl compounds. The alcohol channel could either increase or decrease because the increase of $C_{10}H_{15}O_{even}$ and the decrease of the RO_2 + RO_2 reaction channel counteract. Similar arguments hold for the hydroperoxide channel, here $C_{10}H_{15}O_{odd}$ peroxy radicals were decreased while the HO_2 radical concentration increased. It is likely that the carbonyl formation from the reaction of the $C_{10}H_{17}O_{even}$ peroxy radical will be decreased since both the $C_{10}H_{17}O_{even}$ peroxy radical and a disproportionation reaction were decreased. In the same sense $C_{10}H_{16}O_{even}$ can be formed from $C_{10}H_{15}O_{odd}$ as alcohols, $C_{10}H_{15}O_{even}$ as hydroperoxides or from $C_{10}H_{17}O_{odd}$ as carbonyl compounds.

Figure 3.23 panel C shows the changes in nine $C_{10}H_{16}O_z$ marker compounds. Again the concentration of less oxygenated family members $C_{10}H_{16}O_{6\text{-}8}$ decreased strongly while those of more oxygenated $C_{10}H_{16}O_{9\text{-}12}$ showed only a mild decrease or even an increase. Panel D

shows that both $C_{10}H_{16}O_{odd}$ and $C_{10}H_{16}O_{even}$ family members decreased by a similar fraction. $C_{10}H_{16}O_7$ which was the most abundant peak in the reference experiment showed a decreased signal that could be the result of decreased $C_{10}H_{15}O_7$ peroxy radicals and reduced disproportionation reactions of $C_{10}H_{15}O_8$ peroxy radicals. However, $C_{10}H_{16}O_7$ was still the most abundant peak in the CO experiment. Both, $C_{10}H_{16}O_9$ and $C_{10}H_{16}O_{10}$ showed increased signals. The increase of $C_{10}H_{16}O_9$ could be the result of an increased hydroperoxide formation from the $C_{10}H_{15}O_9$ peroxy radical and an increased alcohol formation from the $C_{10}H_{15}O_{10}$ peroxy radical. Even though the RO_2 + RO_2 reaction channel diminished, the increase of $C_{10}H_{15}O_{10}$ was quite strong. $C_{10}H_{16}O_{10}$ showed a three times higher signal than in the reference case, because there were obviously still sufficient RO_2 to react with and contributions by the hydroperoxide formation from $C_{10}H_{15}O_{10}$ peroxy radicals. Pullinen, 2016 described $C_{10}H_{16}O_{10}$ as a contamination from the CO gas inlet. However, it is not clear how compounds like $C_{10}H_{16}O_{10}$ with such a low vapour pressure can evaporate from the gas line.

In Figure 3.23, panel E shows the seven detected members of the $C_{10}H_{18}O_z$ family. The $C_{10}H_{18}O_7$ and $C_{10}H_{18}O_9$ family members which have an odd number of O-atoms in the molecular formula showed an increase in the signal while the $C_{10}H_{18}O_6$, $C_{10}H_{18}O_8$ and $C_{10}H_{18}O_{10}$ family members with an even number of O-atoms showed a decreased signal in CO experiment. Panel F shows that $C_{10}H_{18}O_{odd}$ indeed increased while $C_{10}H_{18}O_{even}$ decreased by more than a half.

$C_{10}H_{18}O_7$ and $C_{10}H_{18}O_9$ were the strongest members of the $C_{10}H_{18}O_z$ family. Both compounds were asigned to hydroperoxides which were formed from $C_{10}H_{17}O_7$ and $C_{10}H_{17}O_9$ peroxy radicals, ($C_{10}H_{18}O_{7,9}$ could also be alcohols coming from $C_{10}H_{17}O_8$ and $C_{10}H_{17}O_{10}$ peroxy radicals but it is more likely that they are hydroperoxides because of a higher HO_2/RO_2 ratio and less alkoxy radical formation which is needed to form $C_{10}H_{17}O_{even}$ peroxy radicals).

Assuming that $C_{10}H_{18}O_{odd}$ were mainly hydroperoxides, their precursors, the $C_{10}H_{17}O_{odd}$ peroxy radicals, were straight autoxidation products of $C_{10}H_{17}O_3$ and do not involve an alkoxy step. In contrast, $C_{10}H_{17}O_{even}$ peroxy radicals need to undergo alkoxy step. Obviously, there were more $C_{10}H_{17}O_{odd}$ peroxy radicals than $C_{10}H_{17}O_{even}$ peroxy radicals which explains the increase of $C_{10}H_{18}O_{odd}$ and the decrease of $C_{10}H_{18}O_{even}$. These observations about $C_{10}H_{17}O_{odd,\ even}$ are in accordance with the analysis of the $C_{20}H_{34}O_z$ accretion products (Figure 3.22).

In summary, it was shown that how the higher HO_2/RO_2 ratios affected the concentration of marker compounds in the photochemical system of α-pinene by comparing the reference experiment and the CO experiment at the same turnover. More $C_{10}H_{17}O_z$ peroxy radicals were observed indirectly (from the C_{20} accretion product analysis). Besides, because of the decreased RO_2 concentration in the CO experiment, there was less formation of alkoxy radicals which resulted in less products that went through fragmentation processes. A lower alkoxy radical formation was in accordance with the analysis of the O-atom parity in peroxy radicals and HOM products. There were stronger decreases in the concentrations of the products that were expected from the alkoxy-peroxy pathway than in concentrations of products originating from straight autoxidation in peroxy radicals.

A higher degree of oxidation was observed in monomers and accretion products in the presence of CO, despite a smaller contribution by $C_{10}H_{15}O_z$ formed in a second step of oxidation by OH. The markers in the directly observed $C_{10}H_{15}O_z$ family were shifted by one O-atom. Accretion products of the $C_{20}H_{30}O_z$ family were shifted by one O-atom as well. Moreover, the $C_{20}H_{32}O_z$ and $C_{20}H_{34}O_z$ family members show more of the higher oxidised accretion products, pointing to higher oxidised $C_{10}H_{17}O_z$ peroxy radicals. This means that the autoxidation can take more steps. This is the case because of the overall smaller loss of HOM-RO_2 relative to the autoxidation itself. Since HO_2 increased, the smaller loss must be related to the decreasing importance of RO_2 + RO_2 reactions. According to Jenkin *et al.*, 2019, the rate coefficients for RO_2 + RO_2 are a factor of ten or smaller than the RO_2 + HO_2 rate coefficients (e.g. 2.0×10^{-12} cm^3 molecule^{-1} s^{-1} vs 2.38×10^{-11} cm^3 molecule^{-1} s^{-1} for $C_{10}H_{15}O_6$). Since [HO_2] increased by a factor of more than 100 while [RO_2] decreased by only a factor of four, the simple termination reactions (R1.2.7 and R1.2.8) cannot be the reason. It leaves the accretion product formation (R1.2.9) as a main reason, which must be fast as we already showed and can have rate coefficients up to the collision limit (Berndt *et al.*, 2018a). In addition, a recombination of two HOM-RO_2 gains more relative importance because of less RO_2 in the presence of CO.

3.4 Photochemical oxidation of α-pinene: Effect of isoprene

In the previous sections, the impacts of an increasing OH concentration and α-pinene turnover as well as a higher HO_2/RO_2 ratios on the product pattern of α-pinene photooxidation was analysed. The abundance of peroxy radicals and their termination reactions were modified by external factors. In this section, changes in the product pattern in the presence of smaller carbon chain peroxy radicals originating from isoprene will be described with a focus on the impact on accretion products and on SOA formation. Parts of this chapter contributed to McFiggans *et al.*, 2019 and was published in the journal Nature, 2019.

Kiendler-Scharr *et al.*, 2009 showed that the new particle formation from plant emission was inhibited by introducing isoprene in to the JPAC. They found that a main reason for the suppression of the new particle formation was a decrease of OH radical concentration. Since isoprene has an about two times higher rate coefficient than α-pinene at 16 °C (isoprene 1.04×10^{-10} and α-pinene 5.50×10^{-11} cm^3 molecule^{-1} s^{-1}), OH radicals reacted fast with isoprene. Less OH reacts with α-pinene and limited oxidation of α-pinene led to less products with very low volatility which in return reduced new particle formation. This is called OH scavenging effect of isoprene.

McFiggans *et al.*, 2019 showed that in α-pinene/isoprene mixtures a second effect prevents new particle formation and reduces SOA formation: the product scavenging. Product scavenging refers to a situation were low volatility condensable products are not formed because the precursors were scavenged in other reactions.

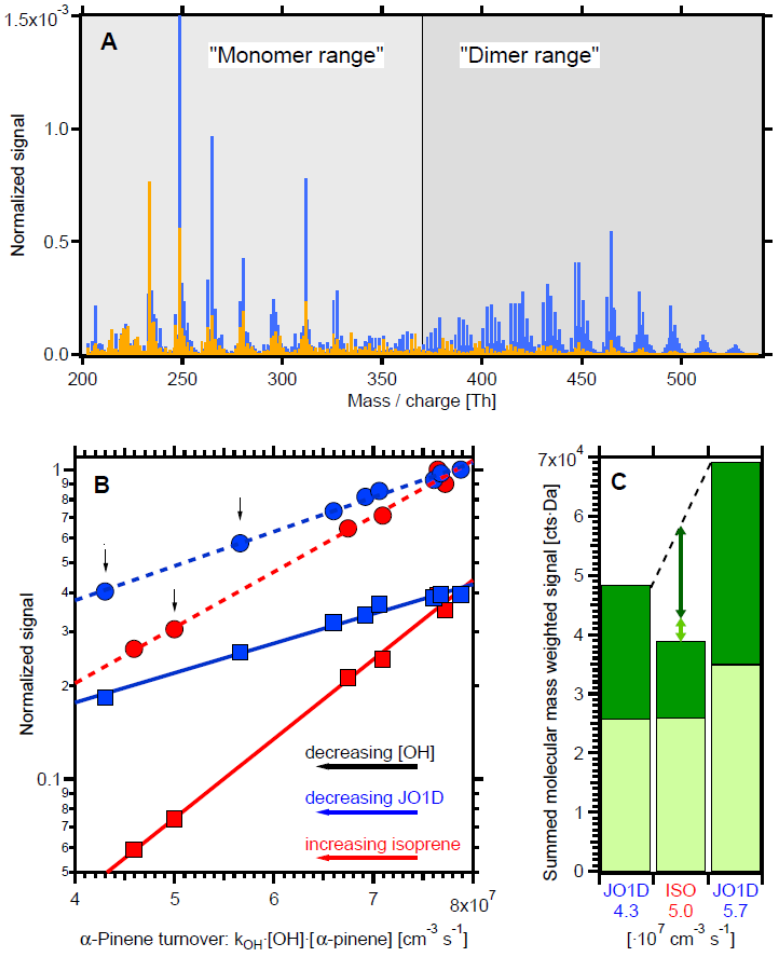

Figure 3.24: HOM monomer and accretion products distribution with and without isoprene. Panel A shows normalised mass spectra of α-pinene OH oxidation with(orange) and without(blue) isoprene. Total HOM (circles) and accretion products (squares) as a function of turnover forj(O^1D) experiment and isoprene experiments are shown in the panel B. Turnover was varied by changing the photolysis rate of O_3 (j(O^1D)) (blue points) and turnover was varied by varying the amount of isoprene added to the system (red points). Panel C shows mass weighted signal of two j(O^1D) experiments and one isoprene added experiment (turnover written under the names of experiments). The mass weighted signal obtained by multiplying signal of each molecule and mass weight. Light green bars are the signal of monomer and dark green bars are the signal from accretion products. The result of two j(O^1D) experiments were interpolated to estimate the expected total HOM mass weighted signal (dashed line). The light green arrow shows the suppression of monomer and the dark green arrow shows the suppress of accretion products by product scavenging. Adapted from McFiggans *et al.*, 2019.

Figure 3.24 demonstrates the observed product scavenging effect in α-pinene OH oxidation. In panel A, two normalised mass spectra are shown taken into account experiments of

α-pinene oxidation by OH in the presence and absence of isoprene. The blue mass spectrum shows the experiment without isoprene and the orange mass spectrum shows the experiment with isoprene. The total HOM signal decreased in the presence of isoprene as both monomers and accretion products concentration decreased. In the mass range of the accretion products from 370 Th to 550 Th, accretion products were showing strong suppression in the presence of isoprene. The same information is displayed by the normalised signal of total HOM (circles) and accretion products (squares) in panel B for different α-pinene turnover with OH. Two sets of experiments are shown in this figure, both, with a deceasing turnover by decreasing the OH radical concentration. However, the method to decrease OH radical concentration was different: blue points were obtained by controlling the photolysis frequency of O_3 while red points were obtained by varying the amount of added isoprene. If isoprene had only an OH scavenging effect, both sets of experiments should show the same slope for decreasing total HOM and accretion products. However, the degree of reduction in the isoprene experiment was higher than in the j(O^1D) experiment. In case of accretion products (squares), the slope of the isoprene experiment was steeper than that of the j(O^1D) experiment which means there is an additional suppression effect caused by the presence of isoprene. In the isoprene experiment, the accretion product concentration was obviously suppressed with increasing isoprene as a result of scavenging precursors of accretion products. Panel C is showing how much the mass concentration of total HOM and specifically monomers and accretion products were decreased by the product scavenging effect. Two points from the j(O^1D) experiment (shown in the downside arrows in panel B) were chosen as the reference experiments. The two experiments had a turnover of 4.3×10^7 cm^{-3} s^{-1} and 5.7×10^7 cm^{-3} s^{-1} respectively. The two points were interpolated and compared to one isoprene experiment in the middle (also marked in panel B) which had a turnover of 5.0×10^7 cm^{-3} s^{-1}. The isoprene experiment showed 33 % lower mass concentration of total HOM than expected by linear interpolation. The reduction of total HOM mass is made up by only 7 % less monomers and 26 % less accretion products. This result shows the product scavenging effect which was revealed for the accretion products more strongly than for the monomers. Here, the reduction of total HOM concentrations, particularly those of accretion products are investigated in the molecular level.

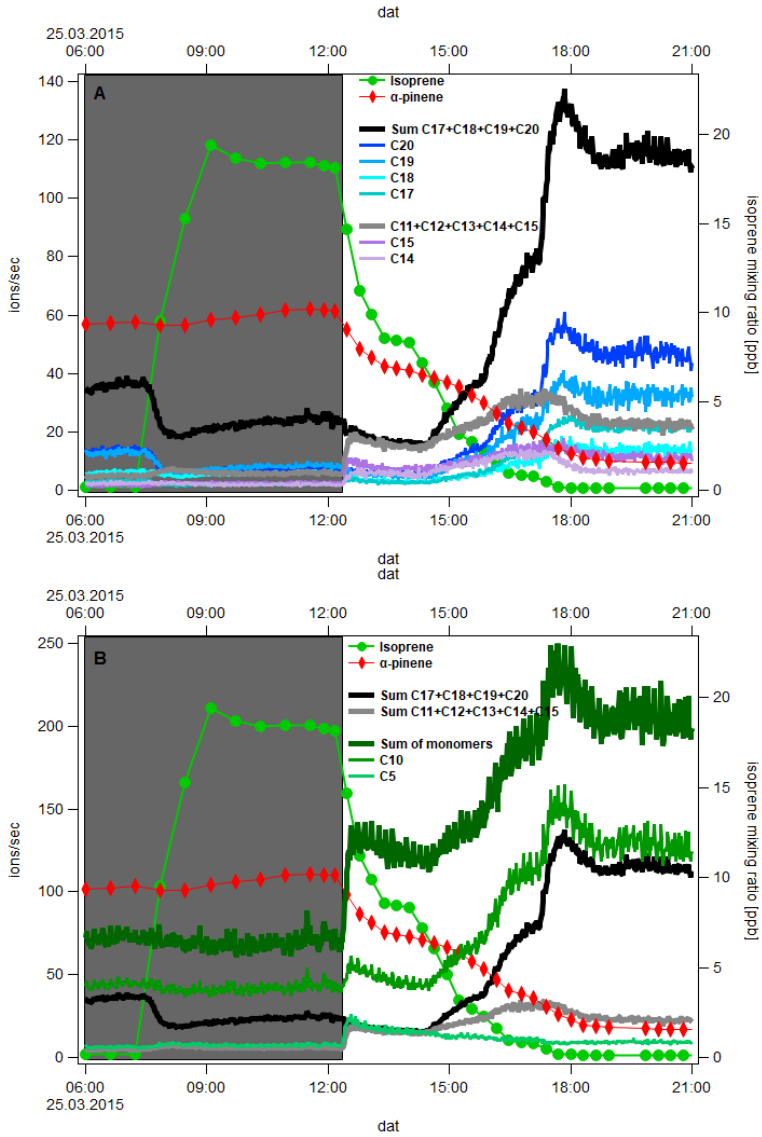

Figure 3.25: The time dependence of the sum of products with different carbon atoms. The green circles and red diamonds show the measured concentration of isoprene and α-pinene in both panels A and B. Panel A shows signals of accretion products with different carbon atoms. It is likely that α-pinene oxidation products contribute mostly to the sum of $C_{17\text{-}20}$ compounds and isoprene oxidation products contribute mainly to the sum of $C_{11\text{-}15}$ compounds. In panel B, not only accretion products but also C_{10}, C_5 and the sum of monomers are shown. As described in chapter 2.1.2, this experiment started with a dark ozonolysis phase with only α-pinene in the system. About 7:20 UTC isoprene was added to the α-pinene ozonolysis system and at 12:20 UTC, photooxidation was initiated. As can be seen in isoprene concentration (green circles with lines), isoprene addition was reduced step wise and stopped completely after around 18:00 UTC.

Figure 3.25 shows the temporal behaviour of monomers and accretion products. In panel A, the time series of $C_{17\text{-}20}$ accretion products (black line) is shown as well as the time series of $C_{11\text{-}15}$ (grey line). In addition, C_{14} and C_{15} which are the main contributors to sum of the $C_{11\text{-}15}$ are shown in violet and lilac lines. It is assumed that $C_{17\text{-}20}$ accretion products mostly arise from α-pinene while $C_{11\text{-}15}$ accretion products can be formed from isoprene originated peroxy radicals ($C_{\leq 5}$) reacting with α-pinene originated peroxy radicals ($C_{\leq 10}$). In panel A, the signal of $C_{17\text{-}20}$ accretion products dropped even in the dark ozonolysis phase when isoprene is added to the system while $C_{11\text{-}15}$ accretion products increased slightly. The reason is the reaction of isoprene with "dark OH" produced from α-pinene ozonolysis. This reaction produces more C_5 and C_4 peroxy radicals and thus C_{15} and C_{14} accretion products.

As photochemistry started, isoprene consumed OH heavily and $C_{11\text{-}15}$ increased notably (with huge contribution of C_{15} to this increase), while $C_{17\text{-}20}$ accretion products decreased slightly. As the amount of isoprene addition was reduced step wise, $C_{17\text{-}20}$ accretion products from α-pinene OH oxidation gained in importance and reached the highest value in the steady state in the absence of the isorpene (peak at around 18:00 was not considered as it was the adapting phase of the system to steady state). It should be noted that $C_{11\text{-}15}$ hit a maximum when isoprene was still in the system. This is clearly showing that C_{15} accretion products are formed substantially by C_5 peroxy radicals from isoprene. There was still a relatively high levels of $C_{11\text{-}15}$ accretion products in the pure α-pinene OH oxidation phase (at the end of the experiment) which confirms the role of fragmentation via alkoxy radicals that enables the formation of accretion products with less than 20 carbons.

In panel B, the result for monomers is shown. The dark green line shows the sum of monomers and green and light green shows the sum of C_{10} and C_5 respectively. Monomers were not much affected by the presence of isoprene and did not show such a decrease like $C_{17\text{-}20}$ (black line in panel B). Both, C_{10} and C_5 monomers, were increased. Accretion products formed from C_5 + C_5 peroxy radicals could have contributed to the increase of C_{10}. Monomer traces are determined by the OH scavenging. It is evident that isoprene forms some amount of C_5-HOM and α-pinene can form C_5-HOM as well via alkoxy radical formation. However, the difference of the C_5 signal in the presence and absence of the isoprene showed that a substantial portion of C_5 compounds came from isoprene.

In conclusion, the C_5 peroxy radicals scavenge the C_9 or C_{10} peroxy radicals by RO_2 + RO_2 termination reactions and prevent the formation of C_{20} or C_{19} accretion products in the presence of isoprene. Only a small fraction of $C_{10,9}$ peroxy radicals react with $C_{5,4}$ and form accretion products which is shown by the accretion product suppression in Figure 3.24.

Figure 3.26 summarises the relative contributions of HOM monomers and accretion products with and without isoprene. As shown before, monomers showed a 40 % decrease in the presence of isoprene mainly because of the OH scavenging effect. The fraction of monomers increased in the presence of isoprene because of stronger suppression of accretion products. The concentration of accretion products with $C_{17\text{-}20}$ decreased by 90 % because of both OH

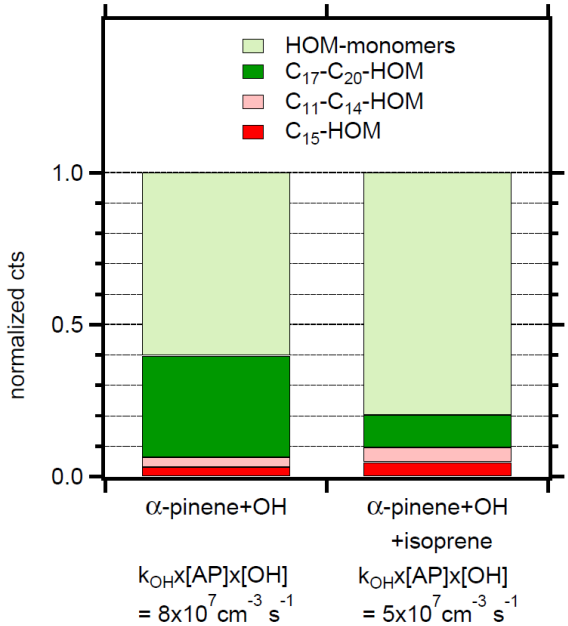

Figure 3.26: Relative contributions of HOM monomers and accretion products with a different numbers of carbon in the molecule. Left bar shows the fraction of HOM monomers (light green), $C_{17\text{-}20}$ accretion products(dark green) which were derived from α-pinene OH oxidation. Pink bar showed the fraction of $C_{11\text{-}14}$ which were most likely coming from the reaction of mixed peroxy radicals from α-pinene and isoprene OH oxidation. Right bar shows the fraction of each group in isoprene addition experiment. The data of two experiments were normalised by 344 cts (left) and 151 cts (right) respectively. Adapted from McFiggans *et al.*, 2019.

and product scavenging, and their fraction of the total decreased from 33 % to 10 %. Accretion products with 11 to 14 carbons were potentially formed in the mixture by recombination of α-pinene originated peroxy radicals and isoprene originated peroxy radicals. C_{15} accretion products are shown as a direct marker for the reaction between non-fragmented α-pinene peroxy radicals and isoprene peroxy radicals forming accretion products. The fraction of C_{15} marker accretion products or $C_{11\text{-}14}$ accretion products were increased slightly in the mixture with isoprene. Even though those increases were overall small, the relative increase of C_{15} and $C_{11\text{-}14}$ accretion products was large in the context of accretion products. Therefore, despite strongly suppressed accretion products in general, C_{15} and $C_{11\text{-}14}$ accretion products were actually increasing in their relative importance. Note, there were C_{15} and $C_{11\text{-}14}$ accretion products even without isoprene. As already mentioned they are supposed to come from peroxy radicals which result from fragmentation of alkoxy radicals formed by the reaction of two RO_2 peroxy radicals (R1.2.10).

In mixtures of α-pinene and isoprene, the SOA yield was lower than in the system that involves only α-pinene (Figure 2 in McFiggans *et al.*, 2019). Lower SOA yields resulted from

both, OH and product scavenging effect. The reactivity of isoprene towards OH radical is twice as high than that of α-pinene at similar concentration. The OH scavenging effect leads to fewer peroxy radicals formed from α-pinene and as a result less HOM. Isoprene oxidation products are less efficient at SOA mass formation so this will result in SOA mass reduction.

By comparing the j(O^1D) reference experiment with the isoprene experiment, it is shown that the product scavenging effect reduces the formation of accretion products especially from α-pinene. This is the other important reason for the SOA yield reduction in α-pinene - isoprene mixtures. Accretion products contribute up to 50 % to HOM mass and condense likely to 100 % because of their extremely low volatility. As a result, suppression of accretion products can reduce SOA yield efficiently. In the context of the previous discussions, conclusion can be made that a high ratio of $C_{\leq 5}/C_{10}$ peroxy radicals favour permutation reactions leading to monomer HOM over recombination reactions to form accretion products. This is similar to the high HO_2 case in the CO experiments. In the next section, the investigation of how the presence of NOx changes the product spectrum will be shown.

Chapter 4

Photochemical oxidation of α-pinene: Impact of NOx

In the previous sections, the effect of varying the OH concentration, CO and isoprene in the HOM formation of α-pinene was discussed. In this section, the impact of nitrogen oxides(NOx = NO + NO_2) on the HOM formation of α-pinene will be investigated. NOx is known to have an important effect on the suppression of new particles (Wildt *et al.*, 2014). In addition, NOx affects the SOA formation by controlling the OH concentration within the HOx cycle and by decreasing the SOA yield (Sarrafzadeh *et al.*, 2016; Kroll *et al.*, 2006; Kanaya, Matsumoto, and Akimoto, 2002; Stone *et al.*, 2010; Elshorbany *et al.*, 2012). However, Sarrafzadeh *et al.*, 2016 showed that without the OH scavenging effect by NO_2, the decrease of the SOA yield was only moderate. The molecular mechanism behind it will be demonstrated from the viewpoint of HOM in the following five subsections. First, it will be presented, how increasing NOx affects the monomer HOM pattern. Secondly, the impact of NOx on fragmentation processes in the chemical system will be shown for HOM. Thirdly, it will be shown how the presence of NOx affects the formation of accretion products. Fourthly, the importance of the alkoxy-peroxy pathway will be demonstrated. The four points above mentioned are connected to SOA yields and the impact of each point on the SOA yield will be described. In addition, the family analysis in terms of the increasing NOx concentration will be discussed. Parts of this chapter contributed significantly to Pullinen *et al.*, 2020 and was published in the journal Atmospheric Physics and Chemistry, 2020.

4.1 Monomer HOM pattern change

In the absence of NOx, the reactions of peroxy radicals with other peroxy radicals including hydroperoxyl radicals (R1.2.7, R1.2.8 and R1.2.9) are the major pathways for peroxy radicals to produce closed shell products. For shortness, such reactions will be called as peroxy permutation reactions and their products HOM-PP. When NOx is present, the reaction of NO with peroxy radicals as well as the reactions of NO_2 with acyl peroxy radicals strongly competes with permutation reactions. Efficient reactions of RO_2 (including acyl peroxy radicals) with

NOx will change the product pattern of HOM. This is demonstrated for HOM monomers in Figure 4.1.

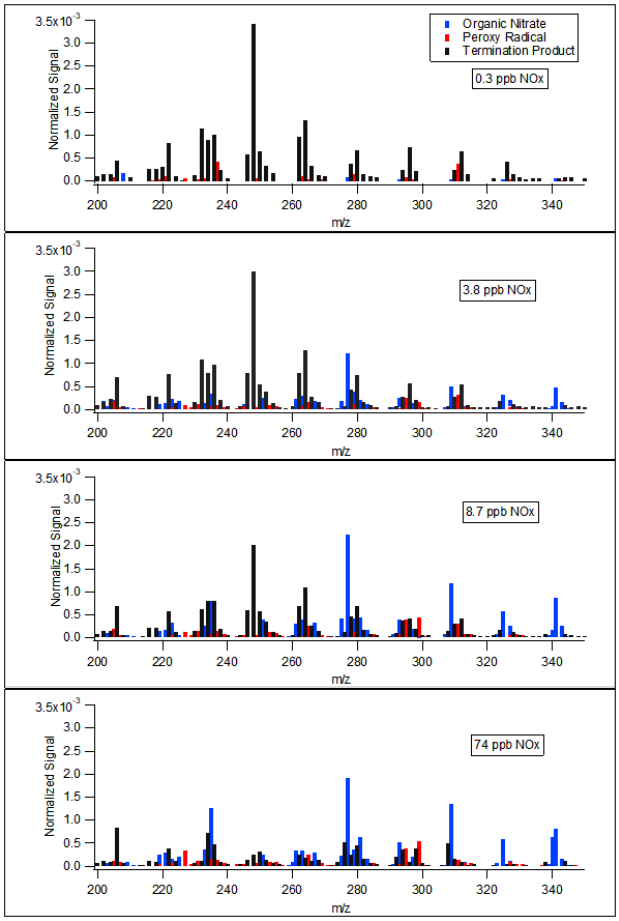

Figure 4.1: Four mass spectra at different steady state NOx concentrations. From top to bottom, the steady state mixing ratio of NOx increased from 0.3 ppb over 3.8 ppb and 8.7 ppb to 72 ppb. Different species are colour coded. The black bars represent termination closed shell products like alcohol, carbonyl and hydroperoxide (HOM-PP). The red bars show the signal from peroxy radicals(HOM-RO_2) and blue bars represent the signals from organic nitrate and peroxy acyl nitrates(PAN like) (HOM-ON). The x-axis is mass per charge ratio and peaks show the molecular mass without the reagent ion. The y-axis shows a signal normalised to the total ion counts

Figure 4.1 shows four mass spectra at different steady state mixing ratios of NOx. The normalised signal is colour coded according to the termination functional groups (permutation reaction products (HOM-PP) in black and organic nitrates (HOM-ON) in blue) or indicating HOM-peroxy radicals (HOM-RO_2 in red). The top graph shows a mass spectrum in the presence of 0.3 ppb of NOx, which was the minimum NOx that could be achieved.

At a background NOx concentration of 0.3 ppb, only little organic nitrate was formed, which can be recognized by the small blue peaks on the top mass spectrum. The majority of the "no NOx addition" mass spectrum was consisting of RO_2 and HO_2 termination products (HOM-PP, black bars). The situation changed when an increasing concentration of NOx was added to the system. As the concentrations of NOx increased and the organic nitrates became the most prominent peaks, as can be seen by the increasing blue bars.The relative contributions of different termination functional groups were calculated and are shown in Figure 4.2.

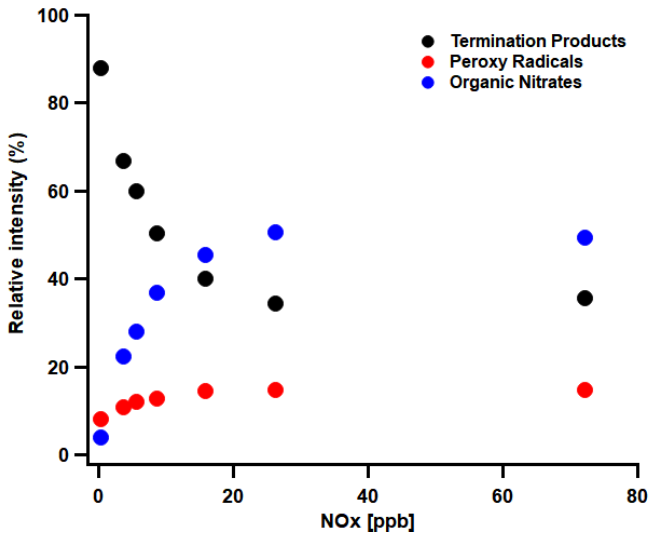

Figure 4.2: The relative intensity of HOM according to termination functional groups: HOM-ON (blue), HOM-PP (black), and HOM peroxy radicals (HOM-RO_2, red) are shown as a function of steady state NOx concentration.

As can be seen in Figure 4.2, the relative intensity of HOM-ON was about 4 % at the background level of NOx and it increased up to 50 % at the highest NOx level. On the other hand, the signal of termination products (HOM-PP) dropped from 88 % to 35 %. This result shows that the termination reactions of monomer HOM-RO_2 switched from termination by other peroxy radicals or HO_2 to termination by the reaction with NO or NO_2. One would expect that the introduction of a fast sink for peroxy radicals, here reactions with NO and NO_2, would lead to a reduction of their steady state concentrations. It is therefore remarkable that even at the very high NOx concentrations, it was possible to detect still quite a substantial amount of HOM-RO_2 (red circles). Also many closed shell HOM-PP without nitrate groups survived, although the rate coefficient for RO_2+ NO (around 9×10^{-12} cm^3 $molecule^{-1}$ s^{-1} for less oxygenated peroxy radicals, IUPAC Task Group recommendation (http://iupac.pole-ether.fr/)) is twice as high than the one for RO_2+ RO_2 (around 5.0×10^{-12} cm^3 $molecule^{-1}$ s^{-1} between less oxygenated peroxy radicals. However, rate coefficients highly depend on the peroxy radicals, Jenkin *et al.*, 2019) and the concentration of NO was much higher than that of RO_2. The possible reasons

for such a high steady state concentration of HOM-RO_2 even in the presence of a high NOx concentration will be discussed in Chapter 4.4.

Pullinen *et al.*, 2020 show that HOM makes up a large portion of SOA under the conditions in the experiments that are used in this chapter. The question arises whether the change of reaction patterns from the formation of HOM-PP to the formation of HOM-ON will affect the SOA formation. In short, that is not the case because of the special characteristics of HOM. HOM-PP consist in most cases of several hydroperoxide groups, alcohol or percarboxylic acid groups (Bianchi *et al.*, 2019). When HOM-RO_2 were formed by autoxidation they are already highly functionalised, mostly with multiple hydroperoxide groups. Therefore, there is no reason why the final termination functional group should greatly alter the volatility of the resulting termination products, thus its effect on the SOA formation. Pullinen *et al.*, 2020 observed similar effective uptake coefficients (γ_{eff}) of HOM originating from β-pinene oxidation and with different termination functional groups with increasing O-atoms in the molecule, as shown in Figure 4.3.

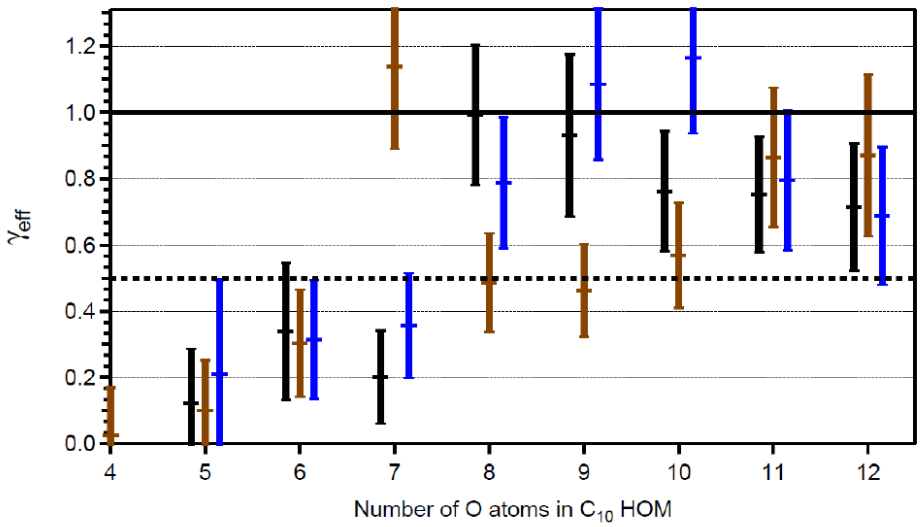

Figure 4.3: Effective uptake coefficients γ_{eff} for HOM-PP ($C_{10}H_{14}O_z$ (black bars), $C_{10}H_{16}O_z$ (brown bars)) and HOM-ON ($C_{10}H_{15}O_zNO_2$, (blue bars)) are shown as a function of the number of O-atoms in the mother C_{10} peroxy radical. Because of the limited mass spectral resolution C_9-HOM where one carbon and four hydrogens were replaced by one oxygen atom, e.g., $C_{10}H_{16}O_8$ and $C_9H_{12}O_9$, are treated together. The black line indicate γ_{eff} = 1 and 0.5. The average Fuchs-Sutugin correction factor of 0.70 (for a median surface diameter d_p=175 nm) was applied to γ_{eff}.

In the calculation of γ_{eff}, the Fuchs-Sutugin correction factor was applied in order to correct for diffusion limitations since γ_{eff} were close to unity and the median diameter of the observed particle surface distribution was 175 nm. The effective uptake coefficients of $C_{10}H_{14}O_z$ and

$C_{10}H_{16}O_z$ (black and brown, respectively) showed a similar trend as C_{10} HOM-ON products (blue). Regardless of the termination functionality, the γ_{eff} increased with an increasing number of O-atoms in the C_{10} HOM until they reached unity. In fact, if compounds have seven or more O-atoms, they will likely condense in every collision on the particle surfaces. The result is due to the multifunctional character of HOM and HOM-RO_2 as described above. In conclusion, the changes in the pattern from HOM-PP and HOM-ON will not have a great impact on the SOA yield based on the observation.

4.2 Fragmentation

Alkoxy radicals, RO$\cdot$, are formed by the reaction of two peroxy radicals (RO_2+ RO_2, R1.2.10) and to a smaller extent by the reaction of peroxy radicals with hydroperoxyl radicals (RO_2+ HO_2), when NO concentrations are low. However, with an increasing NO concentration in the system, the reaction RO_2 + NO (R1.2.12) gains importance. As a consequence, with increasing NOx, RO$\cdot$ are formed predominantly by reaction R1.2.12. Alkoxy radicals have three principal reaction pathways, depending on their size and functionalisation: H-abstraction by O_2 (primarily small alkoxy radicals), rearrangement, and decomposition. Alkoxy radicals tend to decompose since they have excess energy and thus are highly unstable. This often leads to a break of the C-C bond to a C-atom adjacent to the alkoxy group (α-scission). Fragmentation will eventually result in the formation of smaller molecules with a lower number of carbon atoms in the backbone. In other words, as the formation of alkoxy radicals increases by a reaction of RO_2 + NO, it is expected to detect an increasing number of smaller oxidation products with less than ten carbons. And this aspect was investigated in the NOx experiment series.

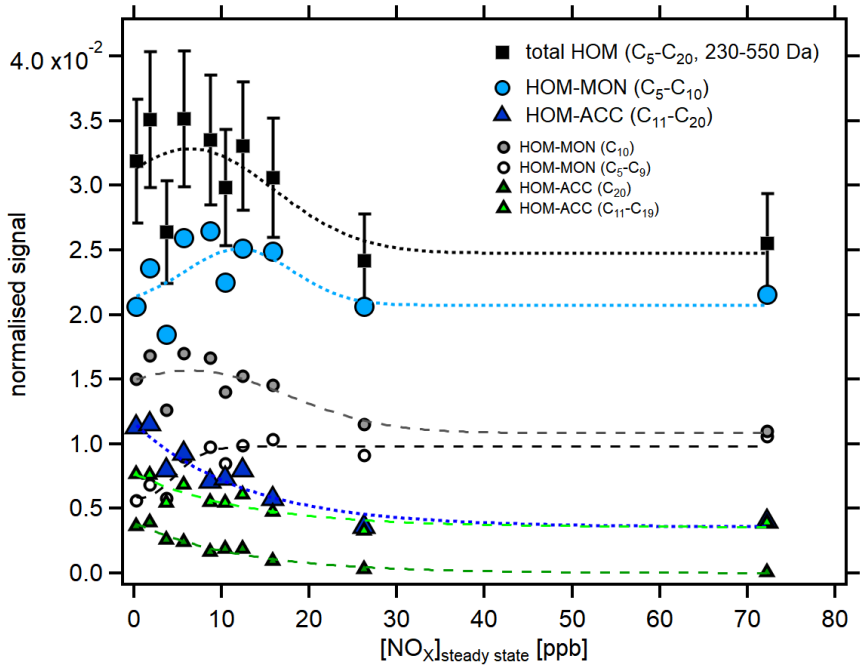

Figure 4.4: The normalised signals of total HOM, monomers, accretion products and HOM that resulted from fragmentation processes, in the mass range of 230 Da to 550 Da as a function of NOx. Black squares show total HOM, blue circles and triangles represent HOM monomers (HOM-MON) and accretion products (HOM-ACC). HOM-MON did not change much as NOx concentration increased while HOM-ACC decreased by $\frac{2}{3}$ at the highest NOx level (72 ppb) compared to reference NOx level (0.3 ppb). Smaller grey and white circles show the signal of C_{10} monomers and $C_{5\text{-}9}$ monomers, respectively. Smaller light green and dark green triangles represent C_{20} accretion products and $C_{11\text{-}19}$ accretion products. From the gain of $C_{5\text{-}9}$ monomers and the relative gain of $C_{11\text{-}19}$ accretion products, the increasing importance of fragmentation is deduced. Dashed and dotted lines serve only to guide the eye and have no further meaning. All data presented here were corrected for turnover and particle surface as described in Chapter 2.4.1

Figure 4.4 shows the normalised signal of total HOM, monomers, and accretion products. The molecular mass range of 230 to 550 Da was selected in order to cover the concentrations of those HOM that should contribute to SOA (HOM with composition $C_{10}H_{14}O_6$ have a molecular mass of 230 Da). The figure includes the splits of monomers in C_{10} and $C_{5\text{-}9}$ compounds and of accretion products in C_{20} and $C_{11\text{-}19}$ compounds, both as indicators for fragmentation processes. Total HOM (black squares) decreased by 20 % as the NOx level increased. Monomers (light blue circles) showed an only 4 % decrease with increasing NOx concentration. This was the result of two factors. C_{10} monomers (grey small circles) showed a 25 % decrease while $C_{5\text{-}9}$ monomers, which must result from fragmentation processes, almost doubled (white small circles). The increasing importance of fragmentation is related to more efficient alkoxy radical formation by the RO_2 + NO reaction with increasing NOx. The increasing importance of

fragmentation processes was more evident in accretion products. As the NOx level increased, accretion products decreased by 65 %. Small accretion products ($C_{11\text{-}19}$) decreased by only 50 % while C_{20} accretion products decreased by 98 %. This means that at high NOx concentrations most accretion products contained moieties arising from fragmentation processes. Again, an explanation is the increased production of alkoxy radicals at high NOx concentrations. The suppression of accretion products will be dealt with in the next section.

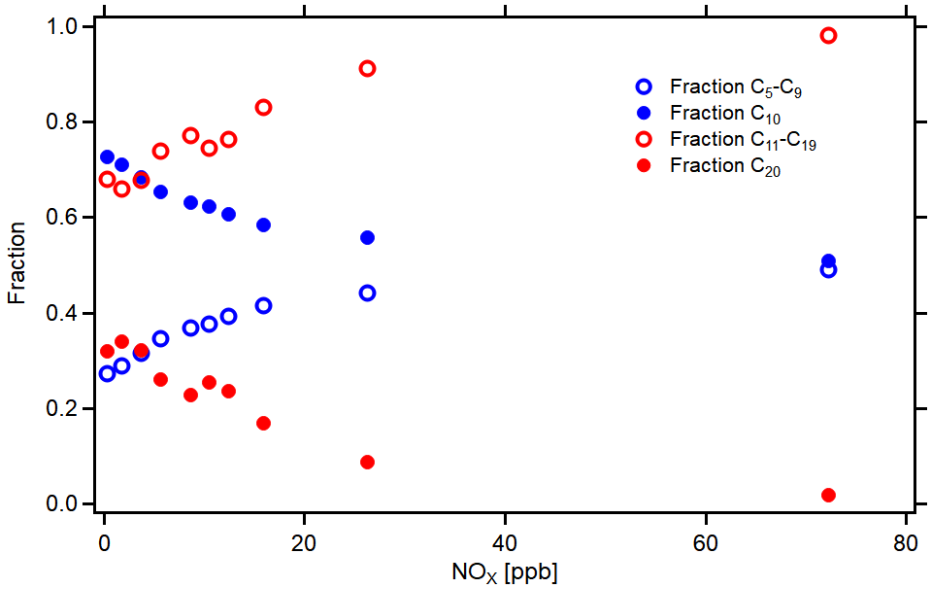

Figure 4.5: Monomers and accretion products with fractions that went through fragmentation processes as a function of NOx. The blue filled circles and blue open circles show the contributions of C_{10} and $C_{5\text{-}9}$ monomers respectively. The red filled circles and red open circles show the contributions of C_{20} and $C_{11\text{-}19}$ accretion products, respectively.

The relative changes of the players in Figure 4.5 underline the increasing importance of fragmentation with increasing NOx. The figure shows the fractions of C_{10} monomers and fragmented monomers $C_{5\text{-}9}$ as well as the fractions of C_{20} accretion products and fragmented accretion products $C_{11\text{-}19}$ as a function of NOx. The contributions by C_{10} monomers decreased from 73 % to 50 % while those by $C_{5\text{-}9}$ monomers increased from 27 % to 50 % with increasing NOx. The increasing importance of fragmentation processes was thus evident for monomers. The increasing importance of fragmentation was even more distinct for the accretion products. In the reference case with a NOx level of 0.3 ppb, there were already 70 % of accretion products with less than 20 C-atoms. They mainly come from alkoxy radicals produced by RO_2 + RO_2 reactions (as discussed in Chapter 3). With increasing NOx, the fraction of C_{20} decreased from 32 % to 2 %. zero. However, signals measured for smaller accretion products $C_{11\text{-}19}$ increased from 68 % to 98 %, and they were accounting for almost all accretion products at high NOx level. As mentioned above, this was a result of the increase of alkoxy radical formation.

The question arises, how the increase of fragmentation processes that are forming smaller monomers and accretion products will impact SOA yields. One would expect that smaller molecules have higher volatilities than the C_{10} monomers or C_{20} accretion products and less tendency to condense on particles or even to form new particles (McFiggans *et al.*, 2019). As a consequence, an increase of fragmentation processes should result in a reduction of SOA yields. Referring to Figure 4.3, it is assumed that HOM monomers with six or more O-atoms and accretion products will quantitatively contribute to SOA formation. To investigate the effect of increasing fragmentation on SOA mass yield, the mass concentrations of HOM monomers ($C_{5\text{-}10}$) and HOM accretion products ($C_{11\text{-}20}$) were calculated in the molecular mass range 230 to 550 Da. In order to do so, normalised signals were weighted by their molecular mass (calculated using the CIMS analyzer) and the calibration factor of 3.7 x 10^{10} cm^{-3} $ncps^{-1}$ was applied.

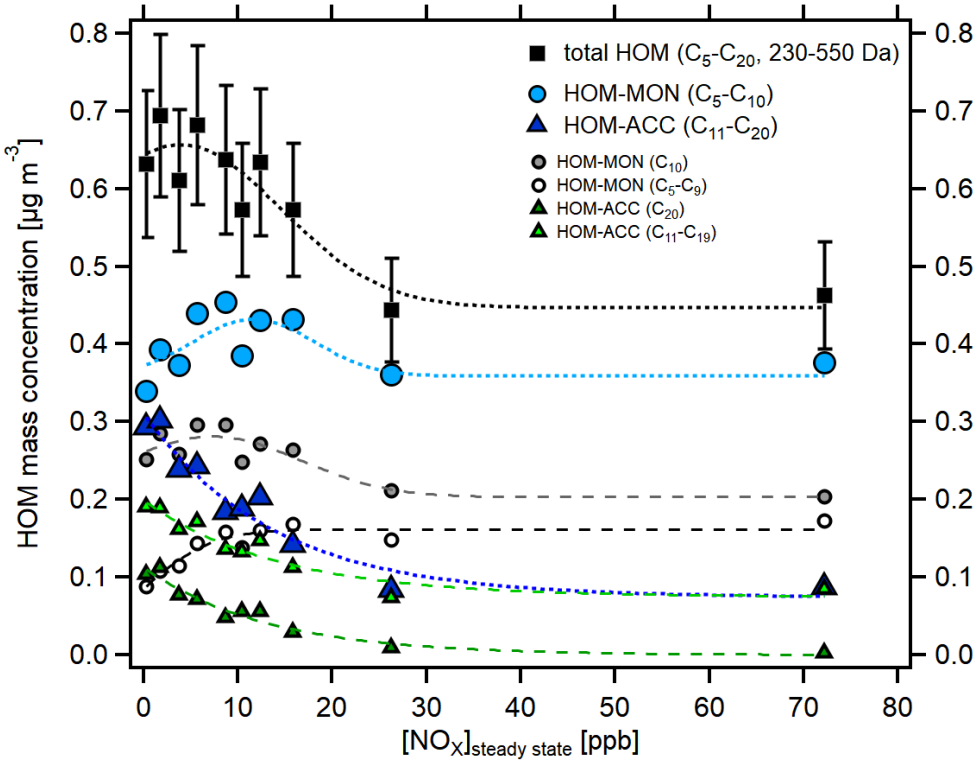

Figure 4.6: The plot shows mass concentrations of total HOM (black squares), HOM monomers ($C_{5\text{-}10}$, light blue filled circles) and accretion products ($C_{11\text{-}20}$, dark blue triangles) as a function of NOx. Additionally, the split in C_{10} (small grey circles) and $C_{5\text{-}9}$ (white small circles) monomers is shown as well as the split in C_{20} (light green triangles) and $C_{11\text{-}19}$ (dark green triangles) accretion products.

Figure 4.6 shows the same data as Figure 4.4, however, the normalised signals were converted into mass concentrations. The mass concentrations of the shown monomers and accretion products are a direct measure of the SOA mass that can be generated by them assuming

a γ_{eff} of unity. The total HOM mass concentration ($C_{5\text{-}20}$) decreased from 0.63 μg m^{-3} to 0.46 μg m^{-3} showing about 30 % reduction. The main reason is a decrease of accretion products which will be discussed in the next section. Small white circles and small light green triangles represent the mass contribution of monomers and accretion products that went through fragmentation processes. $C_{5\text{-}9}$ monomers increased in absolute terms as a function of NOx. Since they must be highly functionalised molecules to fall within the mass range 230 to 550 Da, they will contribute to SOA mass formation in the same way as C_{10} compounds of the same molecular mass. Even though the mass concentrations of small fragmented accretion products decreased, they were not suppressed as severely as C_{20} accretion products and their relative importance increased. In conclusion, an increasing fragmentation processes initiated by RO$\cdot$ do not play a significant role in SOA mass reduction with increasing NOx concentration.

4.3 Accretion product suppression

Accretion products play an important role in the formation and the growth of new particles (McFiggans *et al.*, 2019; Mohr *et al.*, 2017; Hall IV and Johnston, 2011; Kristensen *et al.*, 2013; Kristensen *et al.*, 2016; Tröstl *et al.*, 2016; Müller *et al.*, 2008; Zhao *et al.*, 2013). The composition of fresh SOA particles can be explained from 5 up to 50 % by HOM accretion products depending on the stage of the particle formation process (Zhao *et al.*, 2018; Mohr *et al.*, 2017; Kalberer *et al.*, 2004; Hall IV and Johnston, 2011). Therefore, changes in accretion products are critical to SOA yields.

As shown in Figure 4.4, the normalised signal of the accretion products decreased by 65 %. The decrease of accretion products is obviously seen in the mass spectra. In the high resolution analysis of the observed mass spectra, accretion products are found in a molecular mass range from about 350 Da to 500 Da. In the upper black mass spectrum in Figure 4.7, the mass envelope with two clear maxima allows for easy separation of monomers (200-340 Da) and accretion products (400-500 Da). On the other hand, in the lower red mass spectrum in the presence of 26 ppb NOx, the clear separation between monomer and accretion product disappeared. Instead, the monomers seem to be shifted to a higher mass range. In addition, the signal in the middle mass range (350-400 Da) increased quite strongly.

There are a few reasons for these observations. Firstly, the signal in the mass range 400 Th to 500 Th decreased because of the competition between the accretion product channel and the organic nitrate channel. As the NOx concentration increased, the peroxy radicals react more frequently with NOx. This leads to organic nitrate and alkoxy radical formation instead of accretion product formation by reactions with other peroxy radicals. As a result, the branching ratio into accretion product formation dramatically decreases. Secondly, the signal in the middle mass range (300-400 Da) showed an increase because an increasing number of smaller accretion products were formed, which have less than 20 carbon atoms. As was shown in Figure 4.5, the ratio between $C_{15\text{-}19}$ and C_{20} indeed increased from 2 to 9.5. Another reason why

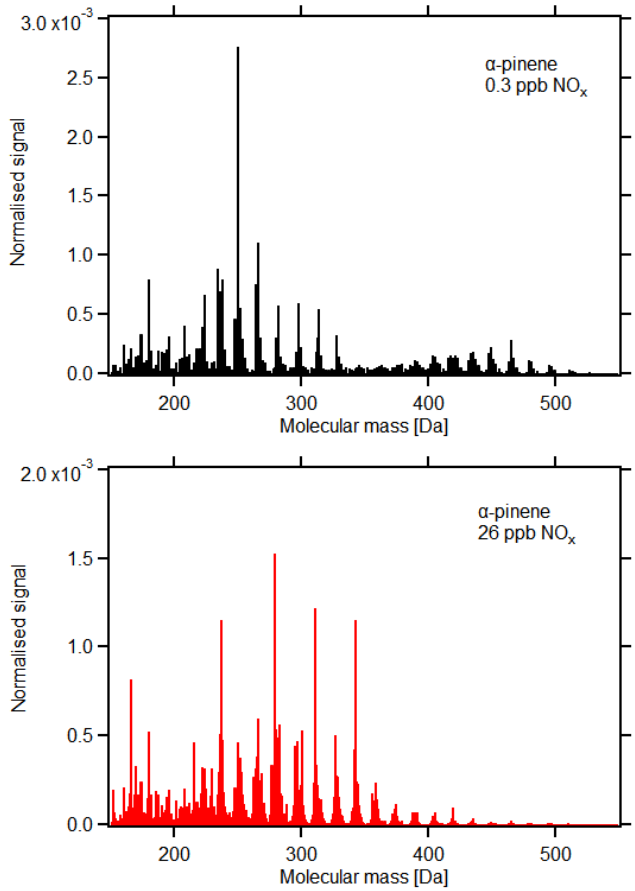

Figure 4.7: Mass spectra observed in the oxidation of α-pinene by OH at 0.3 ppb background NOx (upper black mass spectrum) and in the presence of 26 ppb NOx (lower red mass spectrum) under steady state conditions. The x-axis represents the molecular mass without the mass of the reagent ion NO_3^- and the y-axis shows normalised signal.

the signals in the middle range increased is related to the shift of the monomer envelope to a higher mass range. This is due to the formation of (monomer) HOM-ON with heavier termination groups. If a peroxy radical (RO_2) has a molecular mass of M, formation of carbonyls, alcohols and hydroperoxides would result in molecular masses of M-17, M-15, and M+1 respectively. However, the formation of organic nitrates or PAN-like compounds will increase the molecular mass to M+30 or M+46. (the latter happens, if the peroxy radical is an acyl peroxy radical and reacts with NO_2). In addition, our hypothesis is that - related to the rearrangement channel of alkoxy radicals - a higher oxidation degree can be achieved by the alkoxy-peroxy pathway, i.e. the coupling of alkoxy H-shifts and autoxidation (peroxy H-shifts). This coupling shifts the molecular mass of monomers to a higher mass range by enhancing the radical chain length. The alkoxy-peroxy pathway will be further investigated in the next section.

The question can be asked, how the accretion products suppression will affect SOA yields. First, it can be seen from Figure 4.6 that the mass concentration of accretion products ($C_{11\text{-}20}$) decreased more than 70 %. As a consequence, the contribution to SOA mass by accretion products will also decrease. To better understand the effect of NOx on SOA of accretion products suppression, the formation mechanism of accretion products will be discussed. Accretion products are formed from two peroxy radicals (Berndt *et al.*, 2018b; Berndt *et al.*, 2018a). In case of two HOM-RO_2 forming HOM-ON instead of accretion products, SOA mass yields should increase. First of all, there will be no loss of one oxygen molecule(O_2) during accretion product formation in the process of forming two monomers. In addition, if two HOM-RO_2 peroxy radicals form organic nitrates by attaching NO or NO_2, the mass gain can be 92 Da (adding 2 x NO (30 Da) and loss of O_2 (32 Da) does not occur) even 124 Da (2 x NO_2 (46 Da) and loss of O_2 does not occur).
However, if accretion products are produced by the reaction of one HOM-RO_2 peroxy radical and one less oxygenated RO_2, the suppression of accretion products will lead to SOA mass reduction by loss of the less oxygenated RO_2. That is the case because the termination products of the less oxygenated RO_2 will have too high volatility to efficiently condense, because of too low O/C ratio and functionalisation. In the case of two intermediate oxygenated RO_2 forming accretion products, resulting accretion products will condense on the particle. However, two intermediate oxygenated peroxy radicals are not likely to condense on the particle because of their relatively high volatility. In other words, suppressing of such an accretion product might lead to the mass loss of the two intermediate oxygenated RO_2 in SOA formation. This effect plays a role on the suppressing impact of SOA mass formation.

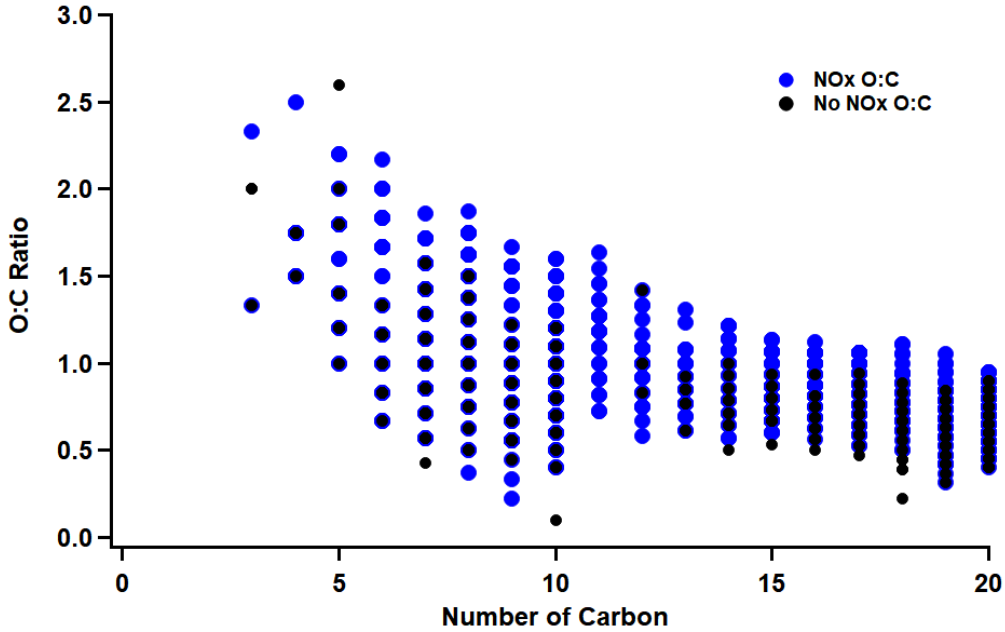

Figure 4.8: O:C ratio of α-pinene photooxidation products in the presence of background level NOx (0.3 ppb, black circles) and 8.7 ppb of NOx (blue circles) as a function of the number of carbon atoms. Each point represents detected molecules during the experiment and identified with high resolution analysis. The x-axis shows the number of carbon in the compounds and the y-axis shows the ratio between oxygen and carbon in the molecule.

The contribution of less oxygenated precursor peroxy radicals to accretion products can be confirmed by the observed of O:C ratios of HOM accretion products in comparison to HOM monomers. Figure 4.8 shows the O:C ratio of products from α-pinene photooxidation in the presence of background NOx level (black circles) and the 8.7 ppb of NOx (blue circles). The O:C ratio of accretion products is lower than that of the monomers. The average O:C ratio was 0.97 for monomers and 0.68 for accretion products under condition of background level of NOx. For higher NOx levels, the average O:C ratio is 1.16 and 0.83 for monomer and accretion products, respectively. The loss of one oxygen molecule in the accretion product formation reaction will lower the O:C ratio in average by only 0.1. Compared to that, the differences of the O:C ratio between monomer and accretion products were 0.29 for background NOx condition and 0.33 for higher NOx conditions. Thus the low O:C ratios of accretion products indicate indeed a substantial contribution of less oxygenated peroxy radicals to their formation.

Berndt *et al.*, 2018b showed that the reaction rate coefficient for accretion product formation varies two order of magnitudes depending on the degree of functionalisation. Based on Berndt *et al.*, 2018b, one could imagine three types of pathways to form accretion products. It is assumed that the involved RO_2 form a pre-existing cluster before they react to the accretion products. The first pathway would be that the accretion products are formed by two HOM-RO_2

(Mentel *et al.*, 2015). This channel would be driven by the formation of a relatively stable pre-existing cluster by two HOM-RO_2 with strong intermolecular interaction, living long enough to be stabilised and become the accretion product. The second pathway is the reaction between HOM-RO_2 and intermediate oxygenated RO_2. The pre-existing cluster maybe less stable compared to the first channel due to the lack of functionality of the second partner, so that it will fall apart faster. However, its formation rate can be (much) faster because of the larger concentration of intermediate oxygenated RO_2. The third pathway is the reaction between two intermediate oxygenated peroxy radicals. The chances for the third channel are probably low because they can form only unstable pre-existing clusters. However, it may still contribute to accretion products by the excessive number of collisions of intermediate oxygenated RO_2 and thus high formation rates of the pre-existing cluster (compensated by a fast decay rate, though). Since accretion products suppression prevents less oxygenated peroxy radicals from having a chance to condense on particles, it will result in a decrease of the SOA yield. This is in accordance with the results described by McFiggans *et al.*, 2019.

4.4 Alkoxy-peroxy pathway

As demonstrated above, the presence of NOx will favor the formation of alkoxy radicals. Alkoxy radicals have three principal reaction pathways. The first pathway is hydrogen abstraction by O_2 to form carbonyl compounds. This is usually the reaction of less functionalised, small alkoxy radicals. More functionalised, larger alkoxy radicals can undergo internal hydrogen migration from C-H bonds to form an alcohol group and an alkyl radical followed by O_2 addition (analogous to autoxidation). When the shifted hydrogen migrated from a hydroperoxide group the peroxy radical will be formed directly, and does not require the bimolecular step of the reaction with O_2. The last pathway is decomposition. Alkoxy radicals are highly unstable with excess energy and often α-bond scission takes places.

The second pathway will change the parity of the oxygen number in the resulting peroxy radicals because of the formation of the alcohol group (whereas straight autoxidation will only generate hydroperoxide groups, i.e. increase the number of O-atoms by two.). The third pathway produces increasing amounts of smaller molecules with increasing NOx, reflected in both monomer and accretion products with smaller carbon numbers than C_{10} and C_{20}, respectively. Smaller molecules with less oxygen may not be able to develop a sufficient number of hydrogen bonds with the reagent ion NO_3^- to form stable clusters and to be detected. Therefore, one would expect that the observable total HOM concentration should be lower at high NOx because smaller molecules from fragmentation processes are not detected with the nitrate CIMS. However, this was not observed.

As shown in the previous section, the total HOM signal (black squres) decreases by 20% (Figure 4.5, black squares). Considering that the accretion product concentration decreased

by 65 %, the decrease of total HOM is not very significant. In addition, considering an increased fragmentation via alkoxy radicals may lead to smaller monomers outside of our range of detection, the reduction of the total HOM concentration is an upper limit. In this sense, the decrease in HOM concentration appears to be indeed fairly small. As a consequence, there must be another source of HOM which keeps up the HOM concentration at high NOx despite the increasing NOx leading to smaller molecules by alkoxy fragmentation.

Our hypothesis is that rearrangement of alkoxy radicals plays a role and here the alkoxy-peroxy pathway comes into the play: an increasing amount of alkoxy radicals are formed with increasing NOx and the branching into fast H-migration of alkoxy radicals allows for forming the next step of peroxy radicals. The alkoxy-rearrangement is obviously able to compete strongly with C-C bond scission (Vereecken and Peeters, 2010) and keeps up the peroxy radical concentration and possibly the autoxidation process. The alkoxy-peroxy path was postulated before by Mentel *et al.*, 2015 in the ozonolysis of cyclopentene and substituted cyclohexenes.

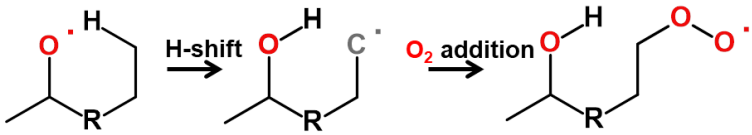

Figure 4.9: Reaction scheme of the alkoxy-peroxy pathway. Intramolecular hydrogen shift to the alkoxy site generates an alkyl radical site. It is followed by O_2 addition forming another peroxy radical, which could undergo autoxidation. By this way, alkoxy radicals do not fragment and maintain its carbon backbone with 10 C-atoms for α-pinene.

Figure 4.9 sketches how the alkoxy-peroxy pathway is working. The alkoxy radical goes through a fast internal hydrogen shift and becomes alcohol while a new alkyl radical site is created. An oxygen molecule is added to the alkyl radical and forms a new peroxy radical which has one more oxygen atom than the mother peroxy radical of the alkoxy radical. However, it is not necessary to form an alkyl radical. A hydrogen from a hydroperoxide functional group can be shifted to the alkoxy site and form directly a peroxy radical at the former hydroperoxide position. This peroxy radical would have one oxygen less than the mother peroxy radical of the alkoxy radical. In these ways, alkoxy radicals form new peroxy radicals with one more or one less oxygen atom compared to their mother peroxy radicals instead of fragmenting and yielding smaller compounds. The newly formed peroxy radicals can undergo autoxidation. Peroxy radicals formed via the alkoxy-peroxy pathway will have different parity in the number of oxygen atoms in the molecule compared to the mother peroxy radical.

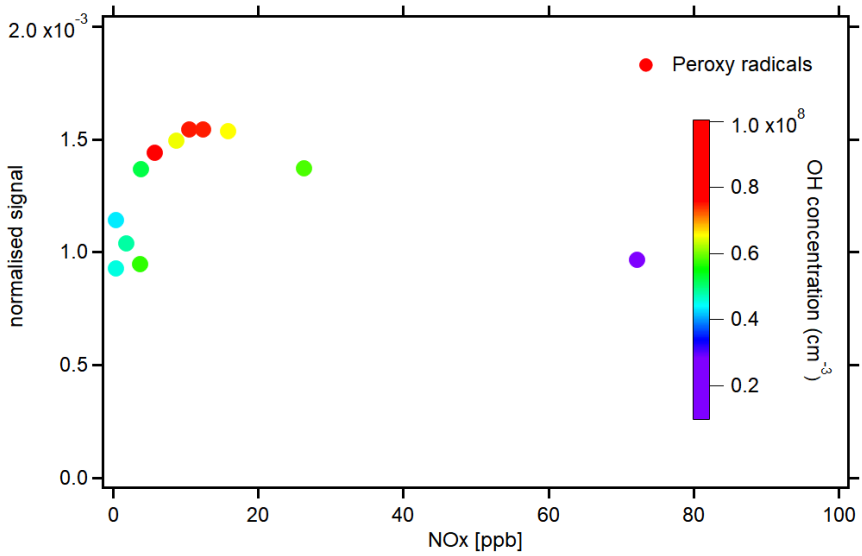

Figure 4.10: The normalised signal of peroxy radicals as a function of NOx. Colour code shows the OH concentration in units of molecules cm^{-3}.

Figure 4.10 demonstrates the signal intensity of peroxy radicals as a function of NOx. As described before, OH concentration increased until 16 ppb NOx and decreased by more than a factor of two at the point of highest NOx. The OH concentrations were about 4.3×10^7 molecules cm^{-3} at 0.3 ppb NOx, and 6.6×10^7 molecules cm^{-3} at 16 ppb NOx and about 2.8×10^7 molecules cm^{-3} at 72 ppb NOx. Despite the low OH concentration, the peroxy radical concentration at 72 ppb NOx was as high as at 2 times higher OH radical concentration at at 3.78 ppb NOx (5.20×10^7 molecules cm^{-3}). Actually, one would expect that the fast reaction with NO and NO_2 at high NOx concentrations should reduce the RO_2 concentration and the autoxidation process by fast converting peroxy radicals into closed shell organic nitrates, but this was obviously not the case.

These unexpected high amounts of peroxy radicals can be explained by an efficient alkoxy-peroxy pathway. According to MCM v3.3.1, alkoxy radicals are formed from the reaction between RO_2 and NO (with branching ratio about 70 %). And alkoxy radicals go through alkoxy-peroxy pathway to form another peroxy radical. Despite of low OH concentrations, peroxy radicals formed by the alkoxy-peroxy pathway keep the peroxy radical concentrations up. New peroxy radicals formed by the alkoxy-peroxy pathway do have one more oxygen in the molecule if they were formed via the alkyl radical path. In addition to subsequent autoxidation, this increases the degree of oxidation which could be observed in the mass spectra. That is the second reason why the monomer range in the mass spectrum is shifted to a higher mass range (besides carrying a heavier termination group). The enhancement of the oxidation degree at high NOx and the separation from smaller accretion products, is demonstrated in the mass defect plot of NOx and no NOx systems.

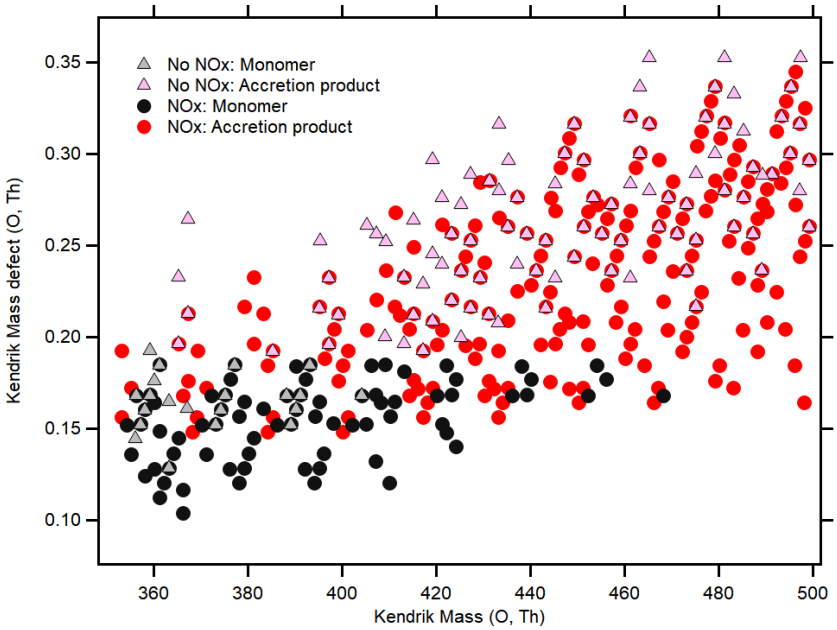

Figure 4.11: Oxygen based mass defect plot of both NOx and no NOx systems. The x-axis shows the calculated Kendrick Mass based on the integer molecular mass of oxygen atoms of 16.0000 Da. The m/z range between 350 Th-500 Th was selected. Molecular masses include the $^{15}NO_3^-$ reagent ion. The y-axis is showing Kendrick mass defect which is the difference between O based Kendrick mass and integer mass of each molecule. Grey triangles represent monomer compounds detected in the no NOx addition experiment, while pink triangles represent accretion products found in the NOx experiment ([NOx] = 8.7 ppb). Black and red closed circles show monomers and accretion products detected in NOx experiment, respectively.

Figure 4.11 represents a mass defect plot of monomer and accretion products in both no NOx and NOx experiments. Oxygen with a molecular mass of 16.0000 Da was chosen as Kendrick mass base so that compounds which differ only in the number O-atoms are appearing on horizontal lines (Oxygen based Kendrik masses are obtained by multiplying carbon based masses by $\frac{16.00000}{15.99492}$). Only the middle mass range is shown, where highly oxygenated monomers and small accretion products are overlapped. In the m/z range 360-405 Th, there were monomers in both no NOx (grey triangles) and NOx (black closed circles) experiment. In the no NOx case, three consecutive patterns at around 358 Th, 374 Th and 390 Th were found. They were C_{10} monomer progressions with one oxygen increase. The same pattern exists also with NOx in the system. However, in the m/z range between 410-470 Th, only the NOx system has monomer peaks. These indicate that monomers in the NOx experiments have indeed a higher degree of oxidation compared to the no NOx case, as expected for an efficient alkoxy-peroxy pathway.

In the m/z range of 360 Th-400 Th, some molecules with a smaller mass defect in the NOx

experiments were found. They were smaller monomer molecules that have less carbon and hydrogen but more oxygen such as $C_8H_{12}O_{14}$ at 395 Th. The reason why lower mass defects point to smaller molecules in the shown middle m/z range is explained by the following. Hydrogen has mass defect 0.00783 Th, oxygen has -0.00508 Th and carbon has 0 Th as mass defect. If in molecules one oxygen atom replaces one carbon atom and four hydrogen atoms (to be detected at same integer mass), it will have a -0.0364 Th, more negative mass defect in the carbon based Kendrik mass defect plot. In the oxygen based Kendrik mass plot, this converts to a -0.364115 Th more negative mass defect.

A similar argument holds for the separation of accretion products and highly oxygenated monomers appearing in the same m/z range: accretion products have more CH_2 and must thus have less oxygen to appear in the same m/z range. Therefore, once can conclude from the mass defect plot (Figure 4.11): even though there are many peaks which can be observed in both no NOx and NOx experiments, the NOx experiment showed a trend to smaller but higher oxidised accretion products in the m/z range above 440 Th (detected in the lower mass defect regime). As postulated above, smaller accretion products stem from recombination reactions involving peroxy radicals after fragmentation processes, wherein either one or both have less than 10 C atoms. The separation of monomers and small accretion products is also seen in the mass range between 360 Th and 400 Th. For no NOx experiments, monomer and accretion products are clearly separated at mass defect 0.19 Th. Accretion products exist above mass defect 0.19 Th and monomers showed mass defects smaller than 0.19 Th. On the other hand, monomers and accretion products showed overlap when NOx was added. This is mainly because of an increase of smaller accretion products like C_{12}, C_{13} or even C_{11}. The Kendrick mass defect plots are showing the same analytic result as derived from the mass spectra itself but clearer because of the one dimension more.

The alkoxy-peroxy pathway leads to higher oxidised products with C_{10} and with $C_{<10}$ with higher mass thus compensating the SOA mass loss expected from fragmentation processes. In the alkoxy-peroxy pathway rearrangement of alkoxy radicals competes with simple alkoxy radical decomposition. Fast H-migration kept the size of the carbon backbone and in combination with autoxidation explained the substantial amount of C_{10} RO_2 and C_{10} HOM-PP, even at high NOx. These highly oxidised HOM-PP will condense on particles and prevent the (strong) suppression of SOA yields.

4.5 Family analysis

Until now, the effect of increasing NOx on the HOM product distribution, fragmentation and HOM accretion products was discussed. In chapter 4.1, an increase of HOM-ON was observed and a decrease of HOM-PP as NOx level increased. It is evident that NOx affects the distribution of reaction channels. In this chapter, C_{10} HOM-ON, HOM-PP and HOM-RO_2 as well as C_{20} accretion products will be analysed in detail using family analysis.

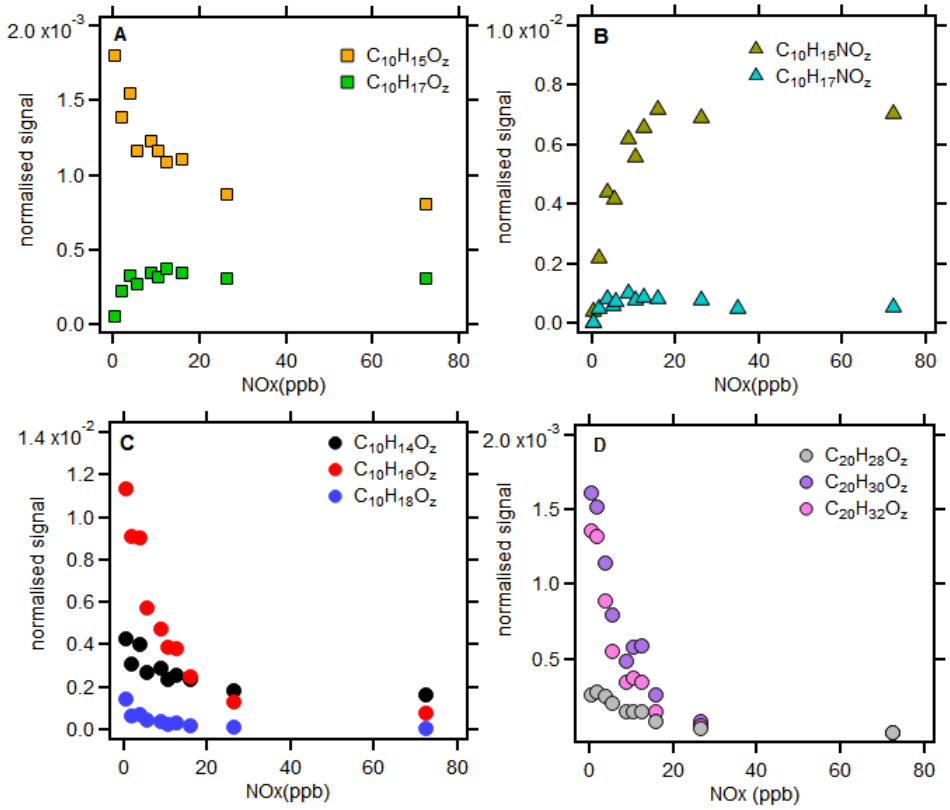

Figure 4.12: The normalised signals of C_{10} and C_{20} families as a function of NOx. Panel A shows the $C_{10}H_{15}O_z$ family (orange squares) and $C_{10}H_{17}O_z$ (green squares) family which was attributed to peroxy radicals. Panel B shows the HOM-ON familes $C_{10}H_{15}NO_z$ (olive green triangle) and $C_{10}H_{17}NO_z$ (turquoise triangle). Panel C shows HOM-PP families $C_{10}H_{14}O_z$ (black filled circles), $C_{10}H_{16}O_z$ (red filled circles), and $C_{10}H_{18}O_z$ (blue filled circles). In panel D, three families of C_{20} accretion products are shown. They are $C_{20}H_{28}O_z$ (grey filled circles), $C_{20}H_{30}O_z$ (purple filled circles) and $C_{20}H_{32}O_z$ (pink filled circles).

Figure 4.12 displays the normalised signal of C_{10} monomer and C_{20} accretion product families as a function of NOx. Panel A shows a normalised signal of the $C_{10}H_{15}O_z$ and $C_{10}H_{17}O_z$ families which are attributed to peroxy radicals. The $C_{10}H_{15}O_z$ peroxy radicals showed a decrease as NOx concentration increased in the system. On the other hand, $C_{10}H_{17}O_z$ peroxy radicals were showing an increase with increasing NOx concentration. There is no clear explanation at the moment why the peroxy radicals should behave like this. However, some explanations can be inferred from the observations. $C_{10}H_{15}O_z$ peroxy radicals are formed from the OH oxidation (likely H-abstraction) of α-pinene oxidation products such as pinonaldehyde. Pinonaldehyde is produced via the first generation peroxy radical $C_{10}H_{17}O_3$. We can construct a line from $C_{10}H_{17}O_3$ to pinonaldehyde (and similar products) and to $C_{10}H_{15}O_z$ by

secondary oxidation by OH. Therefore, it could be possible that $C_{10}H_{17}O_3$ radicals did not follow the route to pinonaldehyde but underwent preferably an alkoxy-peroxy pathway. It is already shown that oxidation is carried out to a high O:C ratio in the presence of NOx. The number of family members of detected $C_{10}H_{17}O_z$ peroxy radicals increased compared to the OH varying experiment series.

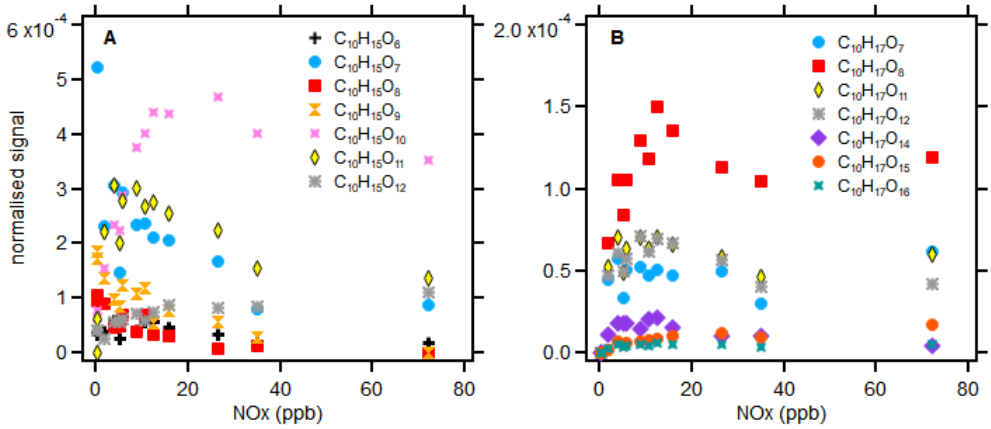

Figure 4.13: The normalised signal of family members of $C_{10}H_{15}O_z$ family (in panel A) and $C_{10}H_{17}O_z$ family (in panel B) as a function of NOx.

Figure 4.13 shows the family members of peroxy radical families. In panel A, there are seven members detected from $C_{10}H_{15}O_z$ family. The $C_{10}H_{15}O_7$ which was the peroxy radical with the highest concentration when no NOx was added became the fourth highest peroxy radical at the highest NOx level. $C_{10}H_{15}O_{10,11,12}$ peroxy radicals which have higher O:C ratio became the most prominent peroxy radicals in NOx experiments. Again, the higher oxidization effect caused by alkoxy-peroxy pathway was observed.

In panel B from figure 4.13, there were seven members detected in $C_{10}H_{17}O_z$ family. In the $J(O_1D)$ experiment, there was only one family member which was detected, $C_{10}H_{17}O_{10}$ (Figure 3.12, panel B). In the presence of NOx, more members and more highly oxygenated $C_{10}H_{17}O_z$ peroxy radicals were detected at high NOx. Peroxy radicals with up to 16 O-atoms were observed. From this observation, it can be claimed that by introducing NOx in the system, the chemistry of peroxy radicals is widened. Since the importance of alkoxy radicals increases with increasing NOx, an early alkoxy step in the alkoxy-peroxy pathway might be the key to facilitate autoxidation of the $C_{10}H_{17}O_3$ peroxy radical. After forming the series of HOM-RO_2, $C_{10}H_{17}O_z$ peroxy radicals finally terminated with NO or other peroxy radicals. This leads then to the already discussed higher oxygenated HOM-PP and HOM-ON in the presence NOx compared to the $J(O_1D)$ experiments. Such alkoxy enhancement of oxidation should be also effective for the $C_{10}H_{15}O_z$ family. However, the $C_{10}H_{15}O_z$ family was suppressed by 30% at the

highest NOx concentrations. This suggest that the enhancement of oxidation by the alokoxy-peroxy path must set on within the radical chain after $C_{10}H_{17}O_3$ formation and before its termination to pinonaldhyde.

In Figure 4.12, panel B shows both $C_{10}H_{15}NO_z$ and $C_{10}H_{17}NO_z$ families which were attributed to organic nitrates. Both families increased with the NOx concentration. This is an understandable result since more NO or NO_2 in the system will result in more RO_2 terminated by NO or NO_2. It is remarkable that the $C_{10}H_{15}NO_z$ family increased as NOx increased although $C_{10}H_{15}O_z$ family decreased. This result reflects that an increasing fraction of $C_{10}H_{15}O_z$ peroxy radicals reacted with NO or NO_2 on the cost of of HOM-PP formation channels.

The decrease of HOM-PP is shown in Figure 4.12, panel C. The $C_{10}H_{14}O_z$ family which was attributed to carbonyl compounds went through a slight maximum at around 10 ppb NOx before it dropped moderately. This maximum reflects that with increasing NOx also [OH] and related photochemical activity passed through a maximum. This can be also recognized by the maximum in HO_2 at about the same NOx in Figure 4.14. It seems that increasing NOx does not have strong effects on the $C_{10}H_{14}O_z$ family. $C_{10}H_{18}O_z$, which was attributed to alcohols and hydroperoxides, and even more so $C_{10}H_{16}O_z$, which was attributed to a mixture of carbonyl compounds, alcohols and hydroperoxides showed a decrease with increasing NOx. In contrast to $C_{10}H_{14}O_z$, here the competition with the termination reaction by NO seems to overcome the maximum of peroxy radical production by OH radicals. The decrease of $C_{10}H_{16}O_z$ family concentration was very strong, while the decrease $C_{10}H_{18}O_z$ concentration was relatively moderate. At 26 ppb and 72 ppb NOx the $C_{10}H_{14}O_z$ family showed greater normalised signal than $C_{10}H_{16}O_z$ family.

By looking at the HO_2/RO_2 ratio, provided by the model simulation of the NOx experiments (Silvia Proff Master thesis 2020), it can derived if increasing the rates of RO_2 + RO_2 reactions is the reason for a increase of relative importance of $C_{10}H_{14}O_z$ among HOM-PP. Figure 4.14 shows the modeled HO_2 radicals and RO_2 radicals and their ratio as a function of NOx. The RO_2 concentration decreased with increasing NOx concentration. HO_2 increased until around 8 ppb NOx and decreased at higher NOx concentration. However, the ratio of HO_2/RO_2 first increased with NOx and finally showed a constant level at high NOx levels. This means there were increasing chances to terminate peroxy radicals by HO_2 and to form hydroperoxides rather than carbonyl compounds or alcohols. As a consequence, $C_{10}H_{14}O_z$ having higher signal than $C_{10}H_{16}O_z$ cannot be the result of increased RO_2+RO_2 termination reactions.

At this point, one pathway of alkoxy radicals may give an explanation. Alkoxy radicals can react with O_2 producing carbonyl compounds and HO_2 radicals. This pathway is more important for small alkoxy radicals. However, in case an H-shift within the alkoxy radical is slow because of a lack of suited H-atoms, the reaction with O_2 may play a role also for larger alkoxy radicals and the O_2 pathway may be competitive with the alkoxy-peroxy pathway. (Decomposition is a third pathway but only the C_{10} monomers are treated in here) The increasing formation of carbonyl compounds by the O_2 pathway with increasing NOx might explain the only minor decrease of the $C_{10}H_{14}O_z$ family. The $C_{10}H_{18}O_z$ family also showed a mild decrease

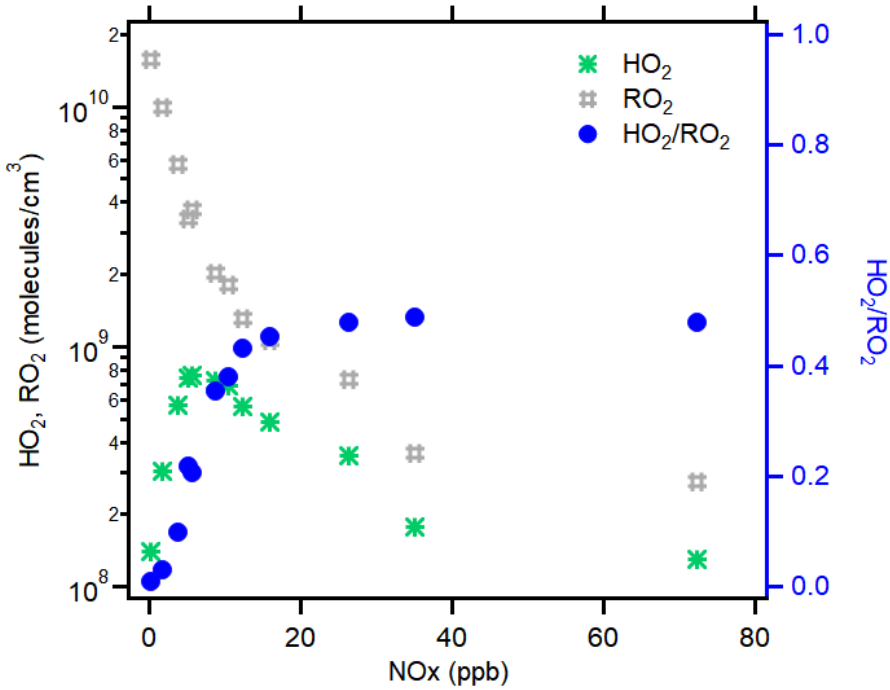

Figure 4.14: Modeled HO_2 radicals and RO_2 radicals and the ratio of HO_2/RO_2 are displayed as a function of NOx. Light green stars represent HO_2 radicals and grey hashs represent RO_2 radicals. Blue filled circles show the ratio of HO_2 and RO_2 radicals. (Data were provided by S.Proff)

and that is probably because of an increase of the $C_{10}H_{17}O_z$ peroxy radical family with NOx and hydroperoxide formation.

Panel D in Figure 4.12 shows the decrease of the concentration of the C_{20} accretion product families with increasing NOx. The $C_{20}H_{30}O_z$ and $C_{20}H_{32}O_z$ families showed dramatic decrease as NOx concentration increased. The $C_{20}H_{28}O_z$ family seems to be less affected by NOx and the question arises if this related to the relatively less suppressed concentration of the $C_{10}H_{14}O_z$ family. Formation of $C_{20}H_{28}O_z$ likely involves $C_{10}H_{13}O_z$ radicals. As a result, relatively milder suppressed concentration of the $C_{20}H_{28}Oz$ accretion products compared to other accretion products might be related to the increase of $C_{10}H_{13}O_z$ peroxy radicals. In addition, $C_{10}H_{13}Oz$ peroxy radicals can contribute to the formation of $C_{10}H_{14}O_z$ family by the alcohol from the disproportionation reaction and by hydroperoxide formation. As a consequence, there are chances that the relative importance of $C_{10}H_{13}O_z$ peroxy radical increased with increasing NOx concentration. All three families approached zero at the highest NOx concentration, again demonstrating the strong suppression of accretion products in the presence of NOx.

4.6 Concluding the effect of NOx on α-pinene photooxidation

It should be noted that oxidation of unsaturated VOC by the NO_3 radical in the atmosphere leads to organic nitrates and SOA formation as well. In that case, NO_3 the nitrate functionality is introduced by addition of the NO_3 to the double bonds (Hallquist *et al.*, 1999; Fry *et al.*, 2009; Fry *et al.*, 2014; Ng *et al.*, 2017). Many studies (Presto, Huff Hartz, and Donahue, 2005; Kroll *et al.*, 2006; Eddingsaas *et al.*, 2012; Sarrafzadeh *et al.*, 2016) reported a decrease of the SOA mass yield when NOx was present in the system. In this thesis, the ***daytime photochemistry*** was investigated when organic nitrates are formed by termination reactions of RO_2 radicals. And, the effect of NOx on the photochemistry of α-pinene OH oxidation was shown, specifically the effect on HOM formation. Knowing that HOM make up a large fraction of SOA (Ehn *et al.*, 2014; Zhang *et al.*, 2017; Roldin *et al.*, 2019), this is a key to understand SOA yields on a molecular level.

Adding NOx to the system changed the monomer distribution and altered the importance of reaction pathways. At very low NOx, HOM peroxy radicals tend to react with other peroxy radicals as well as with HO_2, and produce HOM carbonyl compounds, HOM alcohols and HOM hydroperoxides. However, when there was a certain amount of NOx in the system, the dominant reaction pathway was the reaction with NO or NO_2. These reactions do not only result in an increase of organic nitrate formation but also in an increase of alkoxy radical formation. The latter led to an increasing importance of alkoxy fragmentation, which was detected by increasing concentrations of $C_{5\text{-}9}$ HOM monomers and by an increase of $C_{11\text{-}19}$ compared to C_{20} accretion products.

The change of the monomer product distribution towards HOM-ON did not much affect the SOA yield. The reason is that effective uptake coefficient and volatility for HOM arising from the same precursor peroxy radical do not depend much on the type of the final termination group (Figure 4.3).

Increasing fragmentation via alkoxy radicals took place with increasing NOx. This may have led to some decrease of the SOA yield, however, it was not very critical because products resulting from fragmentation processes were also highly functionalised HOM and were thus still able to participate in SOA mass formation (Figure 4.6, $C_{5\text{-}9}$ HOM mass concentration was even increased).

Despite the increasing importance of alkoxy radicals with increasing NOx, not all monomers were decomposition products even at the highest NOx concentration. That was the case because effective H-shifts in alkoxy radicals prevent that all alkoxy radicals are falling apart (Vereecken and Peeters, 2010). Autoxidation of the resulting peroxy radicals enabled a continuation of the radical chain, a process called the alkoxy-peroxy pathway. By this, the carbon backbone of the molecule was maintained. This was detected by a high fraction of HOM-peroxy radicals and HOM-PP even at the highest NOx concentrations. In conclusion, the reaction with NO was able to compete with reactions of HOM-RO_2 with other peroxy radicals, but not with the autoxidation itself. The alkoxy-peroxy pathway effectively competed with

alkoxy fragmentation and led to a higher degree of oxidation of HOM monomers, which made a reduction of SOA yield with increasing NOx even less.

The major reason why the SOA mass yield was decreasing with increasing NOx was the suppression of accretion products. Especially, C_{20} accretion products remarkably decreased with increasing NOx concentration. Reduction of accretion products is the result of the effective competition between the RO_2 + NO channel and the RO_2 + RO_2 channels. Less oxygenated peroxy radicals participated in accretion product formation which was shown by the lower O:C ratio in accretion products compared to that of monomers. Therefore, the mechanism behind the effect of suppression of accretion products is preventing less oxygenated peroxy radicals to participate in SOA mass formation.

Chapter 5

Summary, conclusion and outlook

In this work, the mechanisms of HOM formation were investigated for the example of α-pinene photooxidation. The basis analysis tool was a high-resolution mass spectrometry. The HR analysis was conducted by separating and analysing monomers, accretion products, and their product distributions of four different chemical regimes. In the experiments either the OH concentration was varied, or the HO_2/RO_2 ratio by addition of CO, or the concentration of small RO_2 by addition of isoprene. Finally, the importance of the formation of organic nitrates and alkoxy radicals was investigated by the addition of NOx.

Methods to cluster HOM according to their termination group were developed. HOM monomers and HOM accretion products were classified in families according to the number of C- and H-atoms as well as the parity of the O-atom number. The family analysis and the detailed analysis of prominent individual compounds (markers) provide a rationale of HOM formation mechanisms. The analysis of the accretion products and accretion product families was developed to confirm and to complement the direct measurements of specific RO_2 including RO_2 with $C_{<10}$ that arise from fragmentation of alkoxy radicals.

The mechanistic findings were worked out semi-quantitatively along the Master Chemical Mechanism (MCM v3.3.1.). The analysis of the observed data was supported quite well by model calculations for HO_2 and RO_2 concentrations in four experimental time series by MCM v3.3.1. (Master thesis Silvia Proff).

In summary, this thesis showed clearly the importance of secondary oxidation to HOM formation and the importance of alkoxy radicals in the continuation of the radical chain in the autoxidation process. In addition, it was shown that changes in the HOM product distribution, namely the suppression of accretion products, reduced SOA formation and SOA yield. This effect was observed in the presence of isoprene (McFiggans *et al.*, 2019) and NOx (Pullinen *et al.*, 2020). NOx scavenges HOM peroxy radicals in a similar manner as isoprene peroxy radicals.

A non-linear relation between α-pinene turnover and HOM concentration was observed with increasing oxidation by OH radicals due to an increasing secondary oxidation. The concentration of HOM increased with [OH] because of the increase of RO_2 production rate with increasing turnover. More RO_2 also resulted in an increase of monomers ($C_{<10}$) and accretion

products ($C_{<20}$) resulting from fragmentation processes. An explanation of the enhanced fragmentation is the alkoxy radical formation from RO_2 + RO_2 reactions. The enhanced alkoxy radical formation was also recognisable in the distribution of markers for both C_{10} and C_{20} compounds: involvement of an alkoxy radical step, i.e. HOM formation via the alkoxy-peroxy pathway, was also indicated by changes of the parity of oxygen in the HOM.

The family analysis of C_{10} and C_{20} compounds showed that $C_{10}H_{15}O_z$ peroxy radicals were the most important HOM-RO_2 family. Obviously, $C_{10}H_{17}O_z$ peroxy radicals, the primary peroxy radicals in α-pinene OH oxidation, were less important for HOM formation. $C_{10}H_{15}O_z$ peroxy radicals must come from the secondary OH oxidation of first generation oxidation products such as pinonaldehyde, since OH can attack the products again by H-abstraction. The OH oxidation mass spectrum of pinonaldehyde confirmed that $C_{10}H_{15}O_z$ peroxy radicals could indeed come from secondary oxidation of pinonaldehyde. The importance of $C_{10}H_{15}O_z$ was also revealed by the fact that $C_{10}H_{16}O_z$ and $C_{10}H_{14}O_z$ were the most important closed shell products. Among C_{10} families, the $C_{10}H_{16}O_z$ family was the most prominent family which is mostly formed from $C_{10}H_{15}O_z$ peroxy radicals in form of hydroperoxides or alcohols. A contribution of carbonyls from $C_{10}H_{17}O_z$ peroxy radicals could not be excluded, though.

The relatively small importance of $C_{10}H_{17}O_z$ peroxy radicals for the formation of HOM monomers was confirmed by only minor contributions of closed shell products like $C_{10}H_{18}O_z$ and $C_{10}H_{17}O_z$. However, the relative importance of $C_{10}H_{17}O_z$ radicals in general, is reflected in the accretion product family ($C_{20}H_{32}O_z$). Based on the fact that highly oxygenated $C_{10}H_{15}O_z$ peroxy radicals were observed and model simulation showed increasing $C_{10}H_{17}O_3$ concentrations with increasing OH, increasing $C_{20}H_{32}O_z$ could be explained by recombination of highly oxygenated $C_{10}H_{15}O_z$ peroxy radicals and lower oxygenated $C_{10}H_{17}O_z$ peroxy radicals.

In a similar way some importance of $C_{10}H_{13}O_z$ peroxy radicals could be shown, which are not included in MCM. $C_{10}H_{13}O_z$ peroxy radicals were not detected directly but detected as accretion products $C_{20}H_{28}O_z$ resulting from $C_{10}H_{13}O_z$ + $C_{10}H_{15}O_z$. Indeed, analysing accretion products proved to be a good hint for investigating the chemistry of peroxy radicals.

The fate of peroxy radicals is dependent on the HO_2/RO_2 ratio. Increasing the HO_2/RO_2 ratio at the same OH concentration by the addition of CO reduced the overall HOM concentration. The reduction was higher for monomers $C_{<10}$ and accretion products $C_{<20}$ that went through alkoxy radical fragmentation, compared to C_{10} and C_{20} non-fragmented products. The reason is the reduced formation of alkoxy radicals from the reaction R1.2.10. Parity of O-atoms in the products showed that the concentration of HOM that require an alkoxy radical step during their formation decreased strongly while the concentration of other compounds were reduced only by a minor amount or even increased.

Higher importance of $C_{10}H_{17}O_z$ peroxy radicals at high HO_2/RO_2 was reflected by the higher concentration of $C_{10}H_{18}O_z$ which are either hydroperoxides or alcohols. The C_{20} family analysis confirmed an increased the importance of $C_{10}H_{17}O_z$ peroxy radicals more clearly. The concentration of $C_{20}H_{32}O_z$ and $C_{20}H_{34}O_z$ increased at high HO_2/RO_2 as both are formed from

$C_{10}H_{17}O_z$ by the recombination with $C_{10}H_{15}O_z$ or $C_{10}H_{17}O_z$. In contrast, $C_{10}H_{15}O_z$ and their accretion products $C_{20}H_{30}O_z$ were smaller at the higher HO_2/RO_2 ratio. However, it remained unclear why $C_{10}H_{17}O_z$ was not detected in higher quantities.

Isoprene was introduced to investigate the effect of small peroxy radicals on the photochemical oxidation of α-pinene. The suppression of monomers and accretion products were observed. Isoprene addition had two impacts on the system of α-pinene and OH oxidation, OH scavenging and product scavenging. Isoprene has a two times higher reaction rate towards OH radicals than α-pinene. Therefore, the α-pinene turnover is decreased because of the lower OH radical concentration in the mixed system of α-pinene and isoprene (at the same OH radical source strength).

In addition, there was a stronger suppression of HOM for monomers and accretion products in the isoprene addition experiment at the same OH concentration compared to the $j(O^1D)$ experiment. The product scavenging effect is responsible for this observation. Formation of HOM peroxy radicals originating from α-pinene was suppressed by termination reactions with small chained peroxy radicals originating from isoprene. The suppression effect was more severe for accretion products than monomers. This was confirmed by the increasing fraction of $C_{11\text{-}15}$ accretion products. These smaller accretion products are more volatile and therefore less likely to condense on the particles. Suppression of accretion products was the major reason why SOA was suppressed in the presence of isoprene.

The presence of NOx in the system induced significant changes in the HOM pattern: it increased the formation of organic nitrates and suppressed the accretion product formation (and SOA formation). Moreover, it increased the degree of oxidation but also the importance of fragmentation. NOx changed the monomer product distribution from hydroperoxides, alcohols, and carbonyl compounds to organic nitrates, but invariant γ_{eff} for all termination groups prevent that this change affected the SOA mass yields significantly. This is because of the multifunctional character of HOM which are essentially multiple hydroperoxides.

NOx addition increased fragmentation due to a higher formation of alkoxy radicals. The effect of alkoxy fragmentation was observed by increasing fractions of fragmented monomers $C_{<10}$ and accretion products $C_{11\text{-}15}$. Increasing fragmentation can lower SOA mass yields since smaller molecules are more volatile. However, here fragmentation did not affect the SOA yield significantly, because those detected smaller products were still highly functionalised and likely to condense on the particles.

In addition, alkoxy radicals did not only undergo fragmentation but also performed H-shifts which kept the carbon number intact. The resulting peroxy radicals pushed the autoxidation to a higher degree competing with alkoxy decomposition. By this alkoxy-peroxy pathway many C_{10} compounds survived even at the very high NOx concentration and as a consequence the total HOM concentration changed only by about 20 %. Thus, the alkoxy-peroxy pathways led to positive contributions to SOA mass yield.

The decrease of the HOM concentration with an increasing NOx concentration was mainly caused by strong suppression of accretion product formation and that is the main reason for the suppression effect of NOx on SOA mass yields. Especially, C_{20} accretion products are suppressed to almost zero and only $C_{11\text{-}15}$ accretion products survived at high NOx conditions. Only when HOM peroxy radicals capture less oxygenated peroxy radicals in accretion products, less oxygenated compounds are capable to condense on particles. The involvement of less oxygenated peroxy radicals in the accretion product formation was detected by low O:C ratios of accretion products and was also found in the $j(O^1D)$ experiments.

By classifying compound families and using the marker analysis, new fundamental insights in a HOM chemistry and its role for SOA formation could be achieved from the HR mass spectra as previously summarised. However, it was difficult to overcome the restriction to qualitative and semi-quantitative results. This was due to different reasons besides the inherent limitation that HR mass spectrometry delivers only molecular formulas without further speciation.

Whenever the chemical system was disturbed by adding a second component, expected changes were induced, but at the same time chemical complexity increased. As could be seen in the analysis (Chapter 3 and 4), the complex chemistry made it difficult to workout explicit explanations and a quantitative mechanistic analysis. Moreover, there is still a lot of unexplored chemistry involved such as the autoxidation itself or accretion product formation from peroxy radicals. (Iyer, Rissanen, and Kurtén, 2019; Berndt *et al.*, 2018b; Møller *et al.*, 2020; Vereecken and Nozière, 2020; Rolletter *et al.*, 2019; Praske *et al.*, 2018). Therefore, mainly qualitative conclusions were obtained in this work together with educated speculations.

Modeling of the experiments added information about radicals and compounds that could not be detected by highly selective CIMS. However, the current version of the MCM lacks information such as rate coefficients for autoxidation, accretion product formation, or alkoxy rearrangement. There are structure activity relationships (Vereecken and Peeters, 2009; Vereecken and Peeters, 2010; Vereecken and Nozière, 2020) and current efforts were made to model near explicitly HOM formation (Weber *et al.*, 2020). Moreover, MCM v3.3.1. provides possibly incorrect product branching ratios, e.g. for pinonaldehyde (Rolletter *et al.*, 2019), and underestimates pathways, e.g. via the primary 6-OH-menthen-8-(per)oxy radical ($C_{10}H_{17}O_3$, APINCO2 in MCM v3.3.1.). This menthen channel should open more pathways of autoxidation (Xu *et al.*, 2019; Vereecken, Müller, and Peeters, 2007).

As shown in this thesis, autoxidation of $C_{10}H_{17}O_3$ with or without the alkoxy-peroxy path is not so much required. However, Vereecken, Müller, and Peeters, 2007 proposed that the menthen pathway should also result in products of the $C_{10}H_{16}O_z$ family. Further reactions by H-abstraction would be in accordance with the finding made here about the central importance of the $C_{10}H_{15}O_z$ peroxy radical family. Mechanistic updates may thus change the detailed compounds where autoxidation and HOM formation is linked to, but it will not affect principal findings in this thesis.

This thesis provides a data base of molecular formulae for several hundreds of HOM species, wherein dozens are highly abundant in different chemical regimes. Concepts of analysis were elaborated and possible reaction pathways for HOM formation were proposed. The material presented in this thesis and the concepts developed can serve as starting point for detailed mechanism development for the formation and the chemical fate of HOM as well as for the evaluation of the respective chemical models.

Bibliography

Atkinson, R *et al.* (2004), Evaluated kinetic and photochemical data for atmospheric chemistry: Volume I-gas phase reactions of Ox, HOx, NOx and SOx species, *Atmospheric chemistry and physics* 4.6, pp. 1461–1738.

Atkinson, R. and J. Arey (2003), Atmospheric degradation of volatile organic compounds, *Chemical reviews* 103.12, pp. 4605–4638.

Berndt, T. *et al.* (2015), Gas-phase ozonolysis of cycloalkenes: formation of highly oxidized RO2 radicals and their reactions with NO, NO2, SO2, and other RO2 radicals, *The Journal of Physical Chemistry A* 119.41, pp. 10336–10348.

Berndt, T. *et al.* (2016), Hydroxyl radical-induced formation of highly oxidized organic compounds, *Nature communications* 7, p. 13677.

Berndt, T. *et al.* (2018a), Accretion product formation from ozonolysis and OH radical reaction of α-pinene: mechanistic insight and the influence of isoprene and ethylene, *Environmental science & technology* 52.19, pp. 11069–11077.

Berndt, T. *et al.* (2018b), Accretion Product Formation from Self-and Cross-Reactions of RO2 Radicals in the Atmosphere, *Angewandte Chemie International Edition* 57.14, pp. 3820–3824.

Bianchi, F. *et al.* (2016), New particle formation in the free troposphere: A question of chemistry and timing, *Science* 352.6289, pp. 1109–1112.

Bianchi, F. *et al.* (2019), Highly oxygenated organic molecules (HOM) from gas-phase autoxidation involving peroxy radicals: A key contributor to atmospheric aerosol, *Chemical reviews* 119.6, pp. 3472–3509.

Capouet, M. *et al.* (2004), Alpha-pinene oxidation by OH: simulations of laboratory experiments.

Carrasquillo, A. J. *et al.* (2014), Secondary organic aerosol formation via the isolation of individual reactive intermediates: role of alkoxy radical structure, *The Journal of Physical Chemistry A* 118.38, pp. 8807–8816.

Criegee, R. (1975), Mechanism of ozonolysis, *Angewandte Chemie International Edition in English* 14.11, pp. 745–752.

Crounse, J. D. *et al.* (2012), Atmospheric fate of methacrolein. 1. Peroxy radical isomerization following addition of OH and O2, *The Journal of Physical Chemistry A* 116.24, pp. 5756–5762.

Crounse, J. D. *et al.* (2013), Autoxidation of organic compounds in the atmosphere, *The Journal of Physical Chemistry Letters* 4.20, pp. 3513–3520.

De Gouw, J. and J. L. Jimenez (2009), *Organic aerosols in the Earth's atmosphere*.

Donahue, N. M. *et al.* (2012a), A two-dimensional volatility basis set–Part 2: Diagnostics of organic-aerosol evolution.

Donahue, N. M. *et al.* (2012b), Aging of biogenic secondary organic aerosol via gas-phase OH radical reactions, *Proceedings of the National Academy of Sciences* 109.34, pp. 13503–13508.

Eddingsaas, N. *et al.* (2012), α-pinene photooxidation under controlled chemical conditions–Part 2: SOA yield and composition in low-and high-NO_x environments, *Atmospheric Chemistry and Physics* 12.16, pp. 7413–7427.

Ehn, M *et al.* (2012), Gas phase formation of extremely oxidized pinene reaction products in chamber and ambient air, *Atmospheric chemistry and physics* 12.11, pp. 5113–5127.

Ehn, M. *et al.* (2014), A large source of low-volatility secondary organic aerosol, *Nature* 506.7489, p. 476.

Eisele, F. and D. Tanner (1993), Measurement of the gas phase concentration of H2SO4 and methane sulfonic acid and estimates of H2SO4 production and loss in the atmosphere, *Journal of Geophysical Research: Atmospheres* 98.D5, pp. 9001–9010.

Elshorbany, Y. F. *et al.* (2012), HOx budgets during HOxComp: A case study of HOx chemistry under NOx-limited conditions, *Journal of Geophysical Research: Atmospheres* 117.D3.

Finlayson, B., J. Pitts Jr, and H Akimoto (1972), Production of vibrationally excited OH in chemiluminescent ozone-olefin reactions, *Chemical Physics Letters* 12.3, pp. 495–498.

Finlayson-Pitts, B. J. and J. N. Pitts Jr (1999), *Chemistry of the upper and lower atmosphere: theory, experiments, and applications*, Elsevier.

Frege, C. *et al.* (2018), submitter: Influence of temperature on the molecular composition of ions and charged clusters during pure biogenic nucleation, *Atmos. Chem. Phys.* 18, pp. 65–79.

Fry, J. *et al.* (2009), Organic nitrate and secondary organic aerosol yield from NO 3 oxidation of β-pinene evaluated using a gas-phase kinetics/aerosol partitioning model. *Atmospheric Chemistry & Physics* 9.4.

Fry, J. L. *et al.* (2014), Secondary organic aerosol formation and organic nitrate yield from NO3 oxidation of biogenic hydrocarbons, *Environmental science & technology* 48.20, pp. 11944–11953.

Guenther, A. *et al.* (2012), The Model of Emissions of Gases and Aerosols from Nature version 2.1 (MEGAN2. 1): an extended and updated framework for modeling biogenic emissions, *Geoscientific Model Development* 5.6, pp. 1471–1492.

Hadley, M. B., J. Baumgartner, and R. Vedanthan (2018), Developing a clinical approach to air pollution and cardiovascular health, *Circulation* 137.7, pp. 725–742.

Hall IV, W. A. and M. V. Johnston (2011), Oligomer content of α-pinene secondary organic aerosol, *Aerosol Science and Technology* 45.1, pp. 37–45.

Hallquist, M. *et al.* (1999), Aerosol and product yields from NO3 radical-initiated oxidation of selected monoterpenes, *Environmental science & technology* 33.4, pp. 553–559.

Hallquist, M. *et al.* (2009), The formation, properties and impact of secondary organic aerosol: current and emerging issues, *Atmospheric chemistry and physics* 9.14, pp. 5155–5236.

Hoyle, C. R. *et al.* (2011), A review of the anthropogenic influence on biogenic secondary organic aerosol, *Atmospheric Chemistry and Physics* 11.1, pp. 321–343.

Hyttinen, N. *et al.* (2015), Modeling the charging of highly oxidized cyclohexene ozonolysis products using nitrate-based chemical ionization, *The Journal of Physical Chemistry A* 119.24, pp. 6339–6345.

Hyttinen, N. *et al.* (2017), Computational comparison of different reagent ions in the chemical ionization of oxidized multifunctional compounds, *The Journal of Physical Chemistry A* 122.1, pp. 269–279.

Iyer, S., M. P. Rissanen, and T. Kurtén (2019), Reaction between peroxy and alkoxy radicals can form stable Adducts, *The journal of physical chemistry letters* 10.9, pp. 2051–2057.

Jenkin, M. E. *et al.* (2019), Estimation of rate coefficients and branching ratios for reactions of organic peroxy radicals for use in automated mechanism construction, *Atmospheric Chemistry and Physics*, pp. 7691–7717.

Jimenez, J. L. *et al.* (2009), Evolution of organic aerosols in the atmosphere, *Science* 326.5959, pp. 1525–1529.

Johnson, D. and G. Marston (2008), The gas-phase ozonolysis of unsaturated volatile organic compounds in the troposphere, *Chemical Society Reviews* 37.4, pp. 699–716.

Jokinen, T *et al.* (2012), Atmospheric sulphuric acid and neutral cluster measurements using CI-APi-TOF, *Atmospheric Chemistry and Physics* 12.9, pp. 4117–4125.

Jokinen, T. *et al.* (2014), Rapid autoxidation forms highly oxidized RO2 radicals in the atmosphere, *Angewandte Chemie International Edition* 53.52, pp. 14596–14600.

Jokinen, T. *et al.* (2015), Production of extremely low volatile organic compounds from biogenic emissions: Measured yields and atmospheric implications, *Proceedings of the National Academy of Sciences* 112.23, pp. 7123–7128.

Junninen, H. *et al.* (2010), A high-resolution mass spectrometer to measure atmospheric ion composition, *Atmospheric Measurement Techniques* 3.4, pp. 1039–1053.

Kalberer, M. *et al.* (2004), Identification of polymers as major components of atmospheric organic aerosols, *Science* 303.5664, pp. 1659–1662.

Kanaya, Y., J. Matsumoto, and H. Akimoto (2002), Photochemical ozone production at a subtropical island of Okinawa, Japan: Implications from simultaneous observations of HO2 radical and NOx, *Journal of Geophysical Research: Atmospheres* 107.D19, ACH–2.

Kiendler-Scharr, A. *et al.* (2009), New particle formation in forests inhibited by isoprene emissions, *Nature* 461.7262, pp. 381–384.

Kirkby, J. *et al.* (2016), Ion-induced nucleation of pure biogenic particles, *Nature* 533.7604, p. 521.

Kristensen, K. *et al.* (2013), Formation and occurrence of dimer esters of pinene oxidation products in atmospheric aerosols, *Atmos. Chem. Phys* 13.7, pp. 3763–3776.

Kristensen, K. *et al.* (2014), Dimers in α-pinene secondary organic aerosol: effect of hydroxyl radical, ozone, relative humidity and aerosol acidity, *Atmos. Chem. Phys* 14.8, pp. 4201–4218.

Kristensen, K. *et al.* (2016), High-molecular weight dimer esters are major products in aerosols from α-pinene ozonolysis and the boreal forest, *Environmental Science & Technology Letters* 3.8, pp. 280–285.

Kroll, J. H. and J. H. Seinfeld (2008), Chemistry of secondary organic aerosol: Formation and evolution of low-volatility organics in the atmosphere, *Atmospheric Environment* 42.16, pp. 3593–3624.

Kroll, J. H. *et al.* (2006), Secondary organic aerosol formation from isoprene photooxidation, *Environmental science & technology* 40.6, pp. 1869–1877.

Kroll, J. H. *et al.* (2011), Carbon oxidation state as a metric for describing the chemistry of atmospheric organic aerosol, *Nature chemistry* 3.2, p. 133.

Kulmala, M. *et al.* (2004), Formation and growth rates of ultrafine atmospheric particles: a review of observations, *Journal of Aerosol Science* 35.2, pp. 143–176.

Kulmala, M. *et al.* (2013), Direct observations of atmospheric aerosol nucleation, *Science* 339.6122, pp. 943–946.

Kurtén, T. *et al.* (2015), Computational study of hydrogen shifts and ring-opening mechanisms in α-pinene ozonolysis products, *The Journal of Physical Chemistry A* 119.46, pp. 11366–11375.

Kurtén, T. *et al.* (2016), α-Pinene autoxidation products may not have extremely low saturation vapor pressures despite high O: C ratios, *The Journal of Physical Chemistry A* 120.16, pp. 2569–2582.

Landrigan, P. J. *et al.* (2018), The Lancet Commission on pollution and health, *The lancet* 391.10119, pp. 462–512.

Lelieveld, J. *et al.* (2008), Atmospheric oxidation capacity sustained by a tropical forest, *Nature* 452.7188, pp. 737–740.

McDonald, B. C. *et al.* (2018), Volatile chemical products emerging as largest petrochemical source of urban organic emissions, *Science* 359.6377, pp. 760–764.

McFiggans, G. *et al.* (2019), Secondary organic aerosol reduced by mixture of atmospheric vapours, *Nature* 565.7741, p. 587.

Mentel, T. *et al.* (2015), Formation of highly oxidized multifunctional compounds: autoxidation of peroxy radicals formed in the ozonolysis of alkenes–deduced from structure–product relationships, *Atmospheric chemistry and physics* 15.12, pp. 6745–6765.

Metzger, A. *et al.* (2010), Evidence for the role of organics in aerosol particle formation under atmospheric conditions, *Proceedings of the National Academy of Sciences* 107.15, pp. 6646–6651.

Mohr, C. *et al.* (2017), Ambient observations of dimers from terpene oxidation in the gas phase: Implications for new particle formation and growth, *Geophysical Research Letters* 44.6, pp. 2958–2966.

Møller, K. H. *et al.* (2020), Double Bonds Are Key to Fast Unimolecular Reactivity in First-Generation Monoterpene Hydroxy Peroxy Radicals, *The Journal of Physical Chemistry A* 124.14, pp. 2885–2896.

Molteni, U. *et al.* (2019), Formation of Highly Oxygenated Organic Molecules from α-Pinene Ozonolysis: Chemical Characteristics, Mechanism, and Kinetic Model Development, *ACS Earth and Space Chemistry* 3.5, pp. 873–883.

Müller, L *et al.* (2008), Unambiguous identification of esters as oligomers in secondary organic aerosol formed from cyclohexene and cyclohexene/?-pinene ozonolysis.

Mutzel, A. *et al.* (2015), Highly oxidized multifunctional organic compounds observed in tropospheric particles: A field and laboratory study, *Environmental science & technology* 49.13, pp. 7754–7761.

Ng, N. L. *et al.* (2017), Nitrate radicals and biogenic volatile organic compounds: oxidation, mechanisms, and organic aerosol, *Atmospheric chemistry and physics* 17.3, p. 2103.

Orlando, J. J. and G. S. Tyndall (2012), Laboratory studies of organic peroxy radical chemistry: an overview with emphasis on recent issues of atmospheric significance, *Chemical Society Reviews* 41.19, pp. 6294–6317.

Ostrom, E. *et al.* (2017), Modeling the role of highly oxidized multifunctional organic molecules for the growth of new particles over the boreal forest region, *Atmospheric Chemistry and Physics*.

Otkjær, R. V. *et al.* (2018), Calculated hydrogen shift rate constants in substituted alkyl peroxy radicals, *The Journal of Physical Chemistry A* 122.43, pp. 8665–8673.

Paasonen, P. *et al.* (2010), On the roles of sulphuric acid and low-volatility organic vapours in the initial steps of atmospheric new particle formation.

Peeters, J., L. Vereecken, and G. Fantechi (2001), The detailed mechanism of the OH-initiated atmospheric oxidation of α-pinene: a theoretical study, *Physical Chemistry Chemical Physics* 3.24, pp. 5489–5504.

Praske, E. *et al.* (2018), Atmospheric autoxidation is increasingly important in urban and suburban North America, *Proceedings of the National Academy of Sciences* 115.1, pp. 64–69.

Presto, A. A., K. E. Huff Hartz, and N. M. Donahue (2005), Secondary organic aerosol production from terpene ozonolysis. 2. Effect of NO x concentration, *Environmental Science & Technology* 39.18, pp. 7046–7054.

Pullinen, I. *et al.* (2020), Impact of NO_x on secondary organic aerosol (SOA) formation from α-pinene and β-pinene photo-oxidation: the role of highly oxygenated organic nitrates, *Atmospheric Chemistry and Physics Discussions*, pp. 1–40.

Pullinen, L. I. M. (2016), *Photochemistry of highly oxidized multifunctional organic molecules: a chamber study*, vol. 387, Forschungszentrum Jülich.

Pye, H. O. *et al.* (2019), Anthropogenic enhancements to production of highly oxygenated molecules from autoxidation, *Proceedings of the National Academy of Sciences* 116.14, pp. 6641–6646.

Ren, X. *et al.* (2003), HOx concentrations and OH reactivity observations in New York City during PMTACS-NY2001, *Atmospheric Environment* 37.26, pp. 3627–3637.

Riccobono, F. *et al.* (2014), Oxidation products of biogenic emissions contribute to nucleation of atmospheric particles, *Science* 344.6185, pp. 717–721.

Riipinen, I *et al.* (2011), Organic condensation: a vital link connecting aerosol formation to cloud condensation nuclei (CCN) concentrations.

Riipinen, I. *et al.* (2012), The contribution of organics to atmospheric nanoparticle growth, *Nature Geoscience* 5.7, pp. 453–458.

Rissanen, M. P. *et al.* (2014), The formation of highly oxidized multifunctional products in the ozonolysis of cyclohexene, *Journal of the American Chemical Society* 136.44, pp. 15596–15606.

Rissanen, M. P. *et al.* (2015), Effects of chemical complexity on the autoxidation mechanisms of endocyclic alkene ozonolysis products: From methylcyclohexenes toward understanding α-pinene, *The Journal of Physical Chemistry A* 119.19, pp. 4633–4650.

Riva, M. *et al.* (2019), Evaluating the performance of five different chemical ionization techniques for detecting gaseous oxygenated organic species, *Atmospheric Measurement Techniques*.

Roldin, P. *et al.* (2019), The role of highly oxygenated organic molecules in the Boreal aerosol-cloud-climate system, *Nature communications* 10.1, pp. 1–15.

Rolletter, M. *et al.* (2019), Investigation of the α-pinene photooxidation by OH in the atmospheric simulation chamber SAPHIR, *Atmospheric Chemistry and Physics* 19.18, pp. 11635–11649.

Sarrafzadeh, M. *et al.* (2016), Impact of NO x and OH on secondary organic aerosol formation from β-pinene photooxidation, *Atmospheric Chemistry and Physics* 16.17, pp. 11237–11248.

Saunders, S. M. *et al.* (2003), Protocol for the development of the Master Chemical Mechanism, MCM v3 (Part A): tropospheric degradation of non-aromatic volatile organic compounds.

Schobesberger, S. *et al.* (2013), Molecular understanding of atmospheric particle formation from sulfuric acid and large oxidized organic molecules, *Proceedings of the National Academy of Sciences* 110.43, pp. 17223–17228.

Shah, R. U. *et al.* (2019), Urban oxidation flow reactor measurements reveal significant secondary organic aerosol contributions from volatile emissions of emerging importance, *Environmental Science & Technology* 54.2, pp. 714–725.

Shilling, J. E. *et al.* (2013), Enhanced SOA formation from mixed anthropogenic and biogenic emissions during the CARES campaign, *Atmospheric Chemistry and Physics* 13.4, pp. 2091–2113.

Sindelarova, K. *et al.* (2014), Global data set of biogenic VOC emissions calculated by the MEGAN model over the last 30 years.

Sipilä, M. *et al.* (2010), The role of sulfuric acid in atmospheric nucleation, *Science* 327.5970, pp. 1243–1246.

Spracklen, D. *et al.* (2011), Aerosol mass spectrometer constraint on the global secondary organic aerosol budget, *Atmospheric Chemistry and Physics* 11.23, pp. 12109–12136.

Stark, H. *et al.* (2015), Methods to extract molecular and bulk chemical information from series of complex mass spectra with limited mass resolution, *International Journal of Mass Spectrometry* 389, pp. 26–38.

Steinfeld, J. I., J. S. Francisco, and W. L. Hase (1999), *Chemical kinetics and dynamics*, Prentice Hall Upper Saddle River, NJ.

Stocker, T. F. *et al.* (2013), Climate change 2013: The physical science basis, *Contribution of working group I to the fifth assessment report of the intergovernmental panel on climate change* 1535.

Stone, D *et al.* (2010), HOx observations over West Africa during AMMA: impact of isoprene and NOx, *Atmospheric Chemistry and Physics* 10.19, pp. 9415–9429.

Tröstl, J. *et al.* (2016), The role of low-volatility organic compounds in initial particle growth in the atmosphere, *Nature* 533.7604, p. 527.

Valiev, R. R. *et al.* (2019), Intersystem Crossings Drive Atmospheric Gas-Phase Dimer Formation, *The Journal of Physical Chemistry A* 123.30, pp. 6596–6604.

Vereecken, L. and B. Nozière (2020), H migration in peroxy radicals under atmospheric conditions, *Atmospheric Chemistry and Physics* 20.12, pp. 7429–7458, DOI: 10.5194/acp-20-7429-2020.

Vereecken, L. and J. S. Francisco (2012), Theoretical studies of atmospheric reaction mechanisms in the troposphere, *Chemical Society Reviews* 41.19, pp. 6259–6293.

Vereecken, L., J.-F. Müller, and J. Peeters (2007), Low-volatility poly-oxygenates in the OH-initiated atmospheric oxidation of α-pinene: impact of non-traditional peroxyl radical chemistry, *Physical Chemistry Chemical Physics* 9.38, pp. 5241–5248.

Vereecken, L. and J. Peeters (2009), Decomposition of substituted alkoxy radicals—part I: a generalized structure–activity relationship for reaction barrier heights, *Physical Chemistry Chemical Physics* 11.40, pp. 9062–9074.

— (2010), A structure–activity relationship for the rate coefficient of H-migration in substituted alkoxy radicals, *Physical Chemistry Chemical Physics* 12.39, pp. 12608–12620.

Viggiano, A. *et al.* (1997), Rate Constants for the Reactions of XO3-(H2O) n (X= C, HC, and N) and NO3-(HNO3) n with H2SO4: Implications for Atmospheric Detection of H2SO4, *The Journal of Physical Chemistry A* 101.44, pp. 8275–8278.

Weber, J. *et al.* (2020), CRI-HOM: A novel chemical mechanism for simulating Highly Oxygenated Organic Molecules (HOMs) in global chemistry-aerosol-climate models, *Atmospheric Chemistry and Physics Discussions* 2020, pp. 1–31, DOI: 10.5194/acp-2020-154.

Weber, R. *et al.* (1996), Measured atmospheric new particle formation rates: Implications for nucleation mechanisms, *Chemical Engineering Communications* 151.1, pp. 53–64.

Wildt, J *et al.* (2014), Suppression of new particle formation from monoterpene oxidation by NO x, *Atmospheric chemistry and physics* 14.6, pp. 2789–2804.

Xu, L. *et al.* (2019), Unimolecular reactions of peroxy radicals formed in the oxidation of α-pinene and β-pinene by hydroxyl radicals, *The Journal of Physical Chemistry A* 123.8, pp. 1661–1674.

Zhang, Q. *et al.* (2007), Ubiquity and dominance of oxygenated species in organic aerosols in anthropogenically-influenced Northern Hemisphere midlatitudes, *Geophysical research letters* 34.13.

Zhang, R. *et al.* (2015), Formation of urban fine particulate matter, *Chemical Reviews* 115.10, pp. 3803–3855.

Zhang, X. *et al.* (2017), Highly oxygenated multifunctional compounds in α-pinene secondary organic aerosol, *Environmental science & technology* 51.11, pp. 5932–5940.

Zhao, D. *et al.* (2018), Effects of NO_X and SO_2 on the secondary organic aerosol formation from photooxidation of α-pinene and limonene, *Atmospheric Chemistry and Physics* 18.3, pp. 1611–1628.

Zhao, D. *et al.* (2015), Secondary organic aerosol formation from hydroxyl radical oxidation and ozonolysis of monoterpenes. *Atmospheric Chemistry & Physics* 15.2.

Zhao, J. *et al.* (2013), Dependence of particle nucleation and growth on high-molecular-weight gas-phase products during ozonolysis of α-pinene, *Atmos. Chem. Phys* 13.15, pp. 7631–7644.

Appendix A

Peaklists

A.1 α-pinene OH oxidation

A.2 α-pinene OH oxidation in the presence of CO

A.3 α-pinene OH oxidation in the presence of isoprene

A.4 α-pinene OH oxidation in the presence of NOx

Table A.1: Peaklist from α-pinene OH oxidation.

Molecule	Detected Mass (Th)	Molecule	Detected Mass (Th)
$C_5H_5O_7$	238.991894	$C_7H_9O_7$	267.023194
$C_5H_6O_6$	224.004804	$C_8H_{10}O_4$	232.046275
$C_5H_6O_7$	239.999719	$C_8H_{10}O_5$	248.04119
$C_5H_6O_8$	255.994634	$C_8H_{10}O_6$	264.036104
$C_5H_7O_6$	225.012629	$C_8H_{10}O_7$	280.031019
$C_5H_7O_7$	241.007544	$C_8H_{10}O_8$	296.025934
$C_5H_8O_7$	242.015369	$C_8H_{11}O_7$	281.038844
$C_6H_{10}O_5$	224.04119	$C_8H_{12}O_4$	234.061925
$C_6H_{10}O_6$	240.036104	$C_8H_{12}O_5$	250.05684
$C_6H_{10}O_7$	256.031019	$C_8H_{12}O_6$	266.051755
$C_6H_{11}NO_6$	255.047003	$C_8H_{12}O_7$	282.046669
$C_6H_{12}O_6$	242.051755	$C_8H_{12}O_8$	298.041584
$C_6H_6O_5$	220.00989	$C_8H_{14}O_7$	284.062319
$C_6H_6O_7$	251.999719	$C_8H_{14}O_8$	300.057234
$C_6H_7O_7$	253.007544	$C_8H_8O_6$	262.020454
$C_6H_8O_5$	222.02554	$C_8H_8O_7$	278.015369
$C_6H_8O_6$	238.020454	$C_8H_9O_8$	295.018109
$C_6H_8O_7$	254.015369	$C_9H_{10}O_7$	292.031019
$C_6H_9O_7$	255.023194	$C_9H_{11}O_7$	293.038844
$C_7H_{10}O_4$	220.046275	$C_9H_{12}O_5$	262.05684
$C_7H_{10}O_5$	236.04119	$C_9H_{12}O_6$	278.051755
$C_7H_{10}O_6$	252.036104	$C_9H_{12}O_7$	294.046669
$C_7H_{10}O_7$	268.031019	$C_9H_{13}O_6$	279.05958
$C_7H_{10}O_8$	284.025934	$C_9H_{13}O_7$	295.054494
$C_7H_{10}O_9$	300.020848	$C_9H_{13}O_8$	311.049409
$C_7H_{11}O_6$	253.043929	$C_9H_{13}O_9$	327.044323
$C_7H_{12}O_4$	222.061925	$C_9H_{14}O_4$	248.077575
$C_7H_{12}O_5$	238.05684	$C_9H_{14}O_5$	264.07249
$C_7H_{12}O_6$	254.051755	$C_9H_{14}O_6$	280.067405
$C_7H_7O_8$	281.002459	$C_9H_{14}O_7$	296.062319
$C_7H_8O_4$	218.030625	$9\,H_{14}O_8$	312.057234
$C_7H_8O_5$	234.02554	$C_9H_{14}O_9$	328.052148
$C_7H_8O_6$	250.020454	$C_9H_{14}O_{10}$	344.047063
$C_7H_8O_7$	266.015369	$C_9H_{16}O_6$	282.083055
$C_7H_8O_8$	282.010284	$C_9H_{16}O_7$	298.077969

Table A.2: Peaklist from α-pinene OH oxidation (Continued).

Molecule	Detected Mass (Th)	Molecule	Detected Mass (Th)
$C_{10}H_{14}O_6$	292.067405	$C_{13}H_{20}O_{12}$	430.083842
$C_{10}H_{14}O_7$	308.062319	$C_{13}H_{26}O_{10}$	404.140963
$C_{10}H_{14}O_8$	324.057234	$C_{14}H_{18}O_{11}$	424.073278
$C_{10}H_{14}O_9$	340.052148	$C_{14}H_{20}O_9$	394.099099
$C_{10}H_{14}O_{10}$	356.047063	$C_{14}H_{20}O_{11}$	426.088928
$C_{10}H_{14}O_{11}$	372.041978	$C_{14}H_{20}O_{12}$	442.083842
$C_{10}H_{14}O_{12}$	388.036892	$C_{14}H_{22}O_9$	396.114749
$C_{10}H_{15}O_6$	293.07523	$C_{14}H_{22}O_{11}$	428.104578
$C_{10}H_{15}O_7$	309.070144	$C_{14}H_{22}O_{12}$	444.099493
$C_{10}H_{15}O_8$	325.065059	$C_{14}H_{22}O_{13}$	460.094407
$C_{10}H_{15}O_9$	341.059973	$C_{15}H_{20}O_{10}$	422.094013
$C_{10}H_{15}O_{10}$	357.054888	$C_{15}H_{22}O_9$	408.114749
$C_{10}H_{15}O_{11}$	373.049803	$C_{15}H_{22}O_{10}$	424.109663
$C_{10}H_{16}O_4$	262.093225	$C_{15}H_{22}O_{11}$	440.104578
$C_{10}H_{16}O_5$	278.08814	$C_{15}H_{22}O_{12}$	456.099493
$C_{10}H_{16}O_6$	294.083055	$C_{15}H_{22}O_{13}$	472.094407
$C_{10}H_{16}O_7$	310.077969	$C_{15}H_{24}O_8$	394.135484
$C_{10}H_{16}O_8$	326.072884	$C_{15}H_{24}O_{10}$	426.125313
$C_{10}H_{16}O_9$	342.067798	$C_{15}H_{24}O_{11}$	442.120228
$C_{10}H_{16}O_{10}$	358.062713	$C_{15}H_{24}O_{12}$	458.115143
$C_{10}H_{16}O_{11}$	374.057628	$C_{15}H_{28}O_{10}$	430.156613
$C_{10}H_{16}O_{12}$	390.052542	$C_{16}H_{22}O_9$	420.114749
$C_{10}H_{17}O_{10}$	359.070538	$C_{16}H_{22}O_{10}$	436.109663
$C_{10}H_{18}O_6$	296.098705	$C_{16}H_{24}O_8$	406.135484
$C_{10}H_{18}O_7$	312.093619	$C_{16}H_{24}O_9$	422.130399
$C_{10}H_{18}O_8$	328.088534	$C_{16}H_{24}O_{10}$	438.125313
$C_{10}H_{18}O_9$	344.083449	$C_{16}H_{24}O_{11}$	454.120228
$C_{10}H_{18}O_{10}$	360.078363	$C_{16}H_{24}O_{12}$	470.115143
$C_{10}H_{18}O_{11}$	376.073278	$C_{16}H_{24}O_{13}$	486.110057
$C_{10}H_{18}O_{12}$	392.068192	$C_{16}H_{26}O_9$	424.146049
$C_{12}H_{18}O_{10}$	384.078363	$C_{16}H_{26}O_{11}$	456.135878
$C_{12}H_{20}O_{12}$	418.083842	$C_{16}H_{26}O_{12}$	472.130793
$C_{13}H_{18}O_{10}$	396.078363	$C_{16}H_{28}O_9$	426.161699
$C_{13}H_{20}O_{10}$	398.094013	$C_{16}H_{28}O_{13}$	490.141357
$C_{13}H_{20}O_{11}$	414.088928	$C_{17}H_{22}O_{10}$	448.109663

Table A.3: Peaklist from α-pinene OH oxidation (Continued).

Molecule	Detected Mass (Th)	Molecule	Detected Mass (Th)
$C_{17}H_{24}O_9$	434.130399	$C_{19}H_{26}O_6$	412.161305
$C_{17}H_{24}O_{10}$	450.125313	$C_{19}H_{26}O_8$	444.151134
$C_{17}H_{24}O_{11}$	466.120228	$C_{19}H_{26}O_9$	460.146049
$C_{17}H_{24}O_{12}$	482.115143	$C_{19}H_{26}O_{15}$	556.115537
$C_{17}H_{24}O_{13}$	498.110057	$C_{19}H_{28}O_8$	446.166784
$C_{17}H_{24}O_{14}$	514.104972	$C_{19}H_{28}O_9$	462.161699
$C_{17}H_{26}O_8$	420.151134	$C_{19}H_{28}O_{10}$	478.156613
$C_{17}H_{26}O_9$	436.146049	$C_{19}H_{28}O_{11}$	494.151528
$C_{17}H_{26}O_{10}$	452.140963	$C_{19}H_{28}O_{12}$	510.146443
$C_{17}H_{26}O_{11}$	468.135878	$C_{19}H_{28}O_{13}$	526.141357
$C_{17}H_{26}O_{12}$	484.130793	$C_{19}H_{28}O_{14}$	542.136272
$C_{17}H_{26}O_{13}$	500.125707	$C_{19}H_{28}O_{15}$	558.131187
$C_{17}H_{26}O_{14}$	516.120622	$C_{19}H_{28}O_{16}$	574.126101
$C_{17}H_{26}O_{15}$	532.115537	$C_{19}H_{30}O_7$	432.18752
$C_{17}H_{26}O_{16}$	548.110451	$C_{19}H_{30}O_8$	448.182434
$C_{17}H_{28}O_{12}$	486.146443	$C_{19}H_{30}O_9$	464.177349
$C_{18}H_{24}O_7$	414.140569	$C_{19}H_{30}O_{10}$	480.172264
$C_{18}H_{26}O_8$	432.151134	$C_{19}H_{30}O_{11}$	496.167178
$C_{18}H_{26}O_{10}$	464.140963	$C_{19}H_{30}O_{12}$	512.162093
$C_{18}H_{26}O_{11}$	480.135878	$C_{19}H_{30}O_{13}$	528.157007
$C_{18}H_{26}O_{12}$	496.130793	$C_{19}H_{30}O_{14}$	544.151922
$C_{18}H_{26}O_{13}$	512.125707	$C_{19}H_{30}O_{15}$	560.146837
$C_{18}H_{28}O_7$	418.17187	$C_{19}H_{30}O_{16}$	576.141751
$C_{18}H_{28}O_8$	434.166784	$C_{19}H_{32}O_{10}$	482.187914
$C_{18}H_{28}O_9$	450.161699	$C_{20}H_{28}O_{11}$	506.151528
$C_{18}H_{28}O_{12}$	498.146443	$C_{20}H_{28}O_{12}$	522.146443
$C_{18}H_{28}O_{13}$	514.141357	$C_{20}H_{28}O_{13}$	538.141357
$C_{18}H_{28}O_{14}$	530.136272	$C_{20}H_{28}O_{14}$	554.136272
$C_{18}H_{28}O_{15}$	546.131187	$C_{20}H_{28}O_{15}$	570.131187
$C_{18}H_{28}O_{16}$	562.126101	$C_{20}H_{28}O_{16}$	586.126101
$C_{18}H_{30}O_{11}$	484.167178	$C_{20}H_{28}O_{17}$	602.121016
$C_{18}H_{30}O_{12}$	500.162093		

Table A.4: Peaklist from α-pinene OH oxidation (Continued).

Molecule	**Detected Mass (Th)**	**Molecule**	**Detected Mass (Th)**
$C_{20}H_{30}O_8$	460.182434	$C_{20}H_{29}O_{17}$	603.128841
$C_{20}H_{30}O_9$	476.177349	$C_{20}H_{32}O_8$	462.198084
$C_{20}H_{30}O_{10}$	492.172264	$C_{20}H_{32}O_9$	478.192999
$C_{20}H_{30}O_{11}$	508.167178	$C_{20}H_{32}O_{10}$	494.187914
$C_{20}H_{30}O_{12}$	524.162093	$C_{20}H_{32}O_{11}$	510.182828
$C_{20}H_{30}O_{13}$	540.157007	$C_{20}H_{32}O_{12}$	526.177743
$C_{20}H_{30}O_{14}$	556.151922	$C_{20}H_{32}O_{13}$	542.172657
$C_{20}H_{30}O_{15}$	572.146837	$C_{20}H_{32}O_{14}$	558.167572
$C_{20}H_{30}O_{16}$	588.141751	$C_{20}H_{32}O_{15}$	574.162487
$C_{20}H_{30}O_{17}$	604.136666	$C_{20}H_{32}O_{16}$	590.157401
$C_{20}H_{29}O_{12}$	523.154268	$C_{20}H_{32}O_{17}$	606.152316
$C_{20}H_{29}O_{13}$	539.149182	$C_{20}H_{34}O_8$	464.213734
$C_{20}H_{29}O_{14}$	555.144097	$C_{20}H_{34}O_9$	480.208649
$C_{20}H_{29}O_{15}$	571.139012	$C_{20}H_{34}O_{10}$	496.203564
$C_{20}H_{29}O_{16}$	587.133926		

Table A.5: Peaklist from α-pinene OH oxidation in the presence of CO.

Molecule	Detected Mass (Th)	Molecule	Detected Mass (Th)
$C_4H_4O_7$	225.984069	$C_8H_{13}O_{10}$	331.039238
$C_5H_6O_6$	224.004804	$C_8H_{13}O_{11}$	347.034153
$C_5H_6O_7$	239.999719	$C_8H_{14}O_7$	284.062319
$C_6H_7O_8$	269.002459	$C_8H_{14}O_8$	300.057234
$C_6H_7O_9$	284.997373	$C_8H_{14}O_9$	316.052148
$C_6H_8O_8$	270.010284	$C_8H_{14}O_{11}$	348.041978
$C_7H_7O_8$	281.002459	$C_9H_{11}O_{13}$	389.008332
$C_7H_8O_4$	218.030625	$C_9H_{12}O_6$	278.051755
$C_7H_8O_5$	234.02554	$C_9H_{12}O_7$	294.046669
$C_7H_8O_7$	266.015369	$C_9H_{13}O_7$	295.054494
$C_7H_8O_8$	282.010284	$C_9H_{14}O_6$	280.067405
$C_7H_8O_9$	298.005198	$C_9H_{14}O_7$	296.062319
$C_7H_9O_7$	267.023194	$C_9H_{14}O_8$	312.057234
$C_7H_9O_8$	283.018109	$C_9H_{14}O_9$	328.052148
$C_7H_{10}O_4$	220.046275	$C_9H_{14}O_{10}$	344.047063
$C_7H_{10}O_7$	268.031019	$C_9H_{14}O_{11}$	360.041978
$C_7H_{10}O_8$	284.025934	$C_9H_{15}O_7$	297.070144
$C_7H_{10}O_9$	300.020848	$C_9H_{15}O_{10}$	345.054888
$C_7H_{10}O_{10}$	316.015763	$C_9H_{16}O_7$	298.077969
$C_7H_{11}O_7$	269.038844	$C_9H_{16}O_8$	314.072884
$C_7H_{12}O_7$	270.046669	$C_9H_{16}O_9$	330.067798
$C_8H_{10}O_4$	232.046275	$C_9H_{16}O_{10}$	346.062713
$C_8H_{10}O_5$	248.04119	$C_9H_{18}O_{13}$	396.063107
$C_8H_{10}O_7$	280.031019	$C_{10}H_{14}O_7$	308.062319
$C_8H_{11}O_7$	281.038844	$C_{10}H_{14}O_8$	324.057234
$C_8H_{11}O_8$	297.033759	$C_{10}H_{14}O_9$	340.052148
$C_8H_{11}O_{11}$	345.018503	$C_{10}H_{14}O_{10}$	356.047063
$C_8H_{12}O_4$	234.061925	$C_{10}H_{14}O_{11}$	372.041978
$C_8H_{12}O_6$	266.051755	$C_{10}H_{15}O_8$	325.065059
$C_8H_{12}O_7$	282.046669	$C_{10}H_{15}O_9$	341.059973
$C_8H_{12}O_8$	298.041584	$C_{10}H_{15}O_{10}$	357.054888
$C_8H_{12}O_9$	314.036498	$C_{10}H_{16}O_5$	278.08814
$C_8H_{12}O_{10}$	330.031413	$C_{10}H_{16}O_6$	294.083055
$C_8H_{12}O_{11}$	346.026328	$C_{10}H_{16}O_7$	310.077969
$C_8H_{13}O_7$	283.054494	$C_{10}H_{16}O_8$	326.072884

Table A.6: Peaklist from α-pinene OH oxidation in the presence of CO (Continued).

Molecule	Detected Mass (Th)	Molecule	Detected Mass (Th)
$C_{10}H_{16}O_9$	342.067798	$C_{14}H_{20}O_{10}$	410.094013
$C_{10}H_{16}O_{10}$	358.062713	$C_{14}H_{21}O_{11}$	427.096753
$C_{10}H_{16}O_{11}$	374.057628	$C_{14}H_{22}O_8$	380.119834
$C_{10}H_{16}O_{12}$	390.052542	$C_{14}H_{22}O_9$	396.114749
$C_{10}H_{17}O_{10}$	359.070538	$C_{14}H_{22}O_{10}$	412.109663
$C_{10}H_{18}O_7$	312.093619	$C_{14}H_{22}O_{11}$	428.104578
$C_{10}H_{18}O_8$	328.088534	$C_{14}H_{22}O_{13}$	460.094407
$C_{10}H_{18}O_9$	344.083449	$C_{15}H_{19}O_9$	405.091274
$C_{10}H_{18}O_{10}$	360.078363	$C_{15}H_{20}O_9$	406.099099
$C_{11}H_{11}O_5$	285.049015	$C_{15}H_{20}O_{10}$	422.094013
$C_{11}H_{17}O_{10}$	371.070538	$C_{15}H_{22}O_9$	408.114749
$C_{11}H_{17}O_{11}$	387.065453	$C_{15}H_{22}O_{11}$	440.104578
$C_{11}H_{17}O_{12}$	403.060367	$C_{15}H_{22}O_{14}$	488.089322
$C_{11}H_{17}O_{13}$	419.055282	$C_{15}H_{24}O_9$	410.130399
$C_{11}H_{17}O_{14}$	435.050197	$C_{15}H_{24}O_{13}$	474.110057
$C_{11}H_{18}O_{10}$	372.078363	$C_{15}H_{24}O_{14}$	490.104972
$C_{11}H_{18}O_{11}$	388.073278	$C_{16}H_{18}O_8$	400.088534
$C_{11}H_{18}O_{12}$	404.068192	$C_{16}H_{18}O_9$	416.083449
$C_{11}H_{18}O_{13}$	420.063107	$C_{16}H_{24}O_{10}$	438.125313
$C_{11}H_{18}O_{14}$	436.058022	$C_{16}H_{24}O_{11}$	454.120228
$C_{11}H_{19}O_7$	325.101444	$C_{16}H_{24}O_{12}$	470.115143
$C_{11}H_{19}O_9$	357.091274	$C_{16}H_{24}O_{13}$	486.110057
$C_{11}H_{19}O_{13}$	421.070932	$C_{16}H_{26}O_{10}$	440.140963
$C_{11}H_{20}O_8$	342.104184	$C_{16}H_{26}O_{13}$	488.125707
$C_{11}H_{20}O_9$	358.099099	$C_{16}H_{26}O_{15}$	520.115537
$C_{11}H_{24}O_{13}$	426.110057	$C_{17}H_{20}O_8$	414.104184
$C_{11}H_{24}O_{14}$	442.104972	$C_{17}H_{24}O_{12}$	482.115143
$C_{12}H_{18}O_{10}$	384.078363	$C_{17}H_{24}O_{16}$	546.094801
$C_{12}H_{20}O_{13}$	434.078757	$C_{17}H_{26}O_8$	420.151134
$C_{12}H_{26}O_{14}$	456.120622	$C_{17}H_{26}O_9$	436.146049
$C_{12}H_{26}O_{15}$	472.115537	$C_{17}H_{26}O_{10}$	452.140963
$C_{13}H_{20}O_9$	382.099099	$C_{17}H_{26}O_{11}$	468.135878
$C_{13}H_{20}O_{10}$	398.094013	$C_{17}H_{26}O_{12}$	484.130793
$C_{13}H_{20}O_{12}$	430.083842	$C_{17}H_{26}O_{13}$	500.125707
$C_{13}H_{24}O_{13}$	450.110057	$C_{17}H_{28}O_8$	422.166784

Table A.7: Peaklist from α-pinene OH oxidation in the presence of CO (Continued).

Molecule	Detected Mass (Th)	Molecule	Detected Mass (Th)
$C_{17}H_{28}O_{10}$	454.156613	$C_{19}H_{30}O_{11}$	496.167178
$C_{17}H_{28}O_{11}$	470.151528	$C_{19}H_{30}O_{12}$	512.162093
$C_{17}H_{28}O_{12}$	486.146443	$C_{19}H_{30}O_{13}$	528.157007
$C_{18}H_{20}O_{6}$	394.114355	$C_{19}H_{30}O_{14}$	544.151922
$C_{18}H_{20}O_{10}$	458.094013	$C_{19}H_{32}O_{11}$	498.182828
$C_{18}H_{22}O_{9}$	444.114749	$C_{19}H_{32}O_{12}$	514.177743
$C_{18}H_{26}O_{10}$	464.140963	$C_{19}H_{32}O_{13}$	530.172657
$C_{18}H_{28}O_{7}$	418.17187	$C_{19}H_{32}O_{14}$	546.167572
$C_{18}H_{28}O_{8}$	434.166784	$C_{19}H_{32}O_{15}$	562.162487
$C_{18}H_{28}O_{9}$	450.161699	$C_{19}H_{32}O_{16}$	578.157401
$C_{18}H_{28}O_{10}$	466.156613	$C_{19}H_{32}O_{17}$	594.152316
$C_{18}H_{28}O_{11}$	482.151528	$C_{20}H_{29}O_{13}$	539.149182
$C_{18}H_{28}O_{12}$	498.146443	$C_{20}H_{29}O_{14}$	555.144097
$C_{18}H_{28}O_{13}$	514.141357	$C_{20}H_{29}O_{15}$	571.139012
$C_{18}H_{28}O_{14}$	530.136272	$C_{20}H_{29}O_{16}$	587.133926
$C_{18}H_{30}O_{10}$	468.172264	$C_{20}H_{29}O_{17}$	603.128841
$C_{18}H_{30}O_{11}$	484.167178	$C_{20}H_{30}O_{8}$	460.182434
$C_{18}H_{30}O_{12}$	500.162093	$C_{20}H_{30}O_{9}$	476.177349
$C_{18}H_{30}O_{13}$	516.157007	$C_{20}H_{30}O_{10}$	492.172264
$C_{18}H_{30}O_{15}$	548.146837	$C_{20}H_{30}O_{11}$	508.167178
$C_{18}H_{32}O_{8}$	438.198084	$C_{20}H_{30}O_{12}$	524.162093
$C_{19}H_{22}O_{7}$	424.124919	$C_{20}H_{30}O_{13}$	540.157007
$C_{19}H_{24}O_{8}$	442.135484	$C_{20}H_{30}O_{14}$	556.151922
$C_{19}H_{24}O_{9}$	458.130399	$C_{20}H_{30}O_{15}$	572.146837
$C_{19}H_{26}O_{9}$	460.146049	$C_{20}H_{30}O_{16}$	588.141751
$C_{19}H_{28}O_{7}$	430.17187	$C_{20}H_{30}O_{17}$	604.136666
$C_{19}H_{28}O_{8}$	446.166784	$C_{20}H_{30}O_{18}$	620.13158
$C_{19}H_{28}O_{9}$	462.161699	$C_{20}H_{31}O_{11}$	509.175003
$C_{19}H_{28}O_{10}$	478.156613	$C_{20}H_{31}O_{12}$	525.169918
$C_{19}H_{28}O_{11}$	494.151528	$C_{20}H_{31}O_{13}$	541.164832
$C_{19}H_{30}O_{6}$	416.192605	$C_{20}H_{31}O_{14}$	557.159747
$C_{19}H_{30}O_{7}$	432.18752	$C_{20}H_{31}O_{15}$	573.154662
$C_{19}H_{30}O_{8}$	448.182434	$C_{20}H_{31}O_{16}$	589.149576
$C_{19}H_{30}O_{9}$	464.177349	$C_{20}H_{31}O_{17}$	605.144491
$C_{19}H_{30}O_{10}$	480.172264		

Table A.8: Peaklist from α-pinene OH oxidation in the presence of CO (Continued).

Molecule	**Detected Mass (Th)**	**Molecule**	**Detected Mass (Th)**
$C_{20}H_{32}O_7$	446.20317	ceC20H33O12	527.185568
$C_{20}H_{32}O_8$	462.198084	ceC20H33O13	543.180482
$C_{20}H_{32}O_9$	478.192999	ceC20H33O14	559.175397
$C_{20}H_{32}O_{10}$	494.187914	ceC20H33O15	575.170312
$C_{20}H_{32}O_{11}$	510.182828	ceC20H34O8	464.213734
$C_{20}H_{32}O_{12}$	526.177743	ceC20H34O10	496.203564
$C_{20}H_{32}O_{13}$	542.172657	ceC20H34O11	512.198478
$C_{20}H_{32}O_{14}$	558.167572	ceC20H34O12	528.193393
$C_{20}H_{32}O_{15}$	574.162487	ceC20H34O13	544.188308
$C_{20}H_{32}O_{16}$	590.157401	ceC20H34O14	560.183222
$C_{20}H_{32}O_{17}$	606.152316	ceC20H34O15	576.178137

Table A.9: Peaklist from α-pinene OH oxidation in the presence of Isoprene.

Molecule	Detected Mass (Th)	Molecule	Detected Mass (Th)
$C_4H_4O_7$	225.984069	$C_7H_{10}O_9$	300.020848
$C_4H_6O_{10}$	275.984463	$C_7H_{11}O_6$	253.043929
$C_4H_6O_6$	212.004804	$C_7H_{12}O_4$	222.061925
$C_5H_5O_7$	238.991894	$C_7H_{12}O_5$	238.05684
$C_5H_6O_6$	224.004804	$C_7H_{12}O_6$	254.051755
$C_5H_6O_7$	239.999719	$C_7H_7O_8$	281.002459
$C_5H_6O_8$	255.994634	$C_7H_8O_4$	218.030625
$C_5H_7O_6$	225.012629	$C_7H_8O_5$	234.02554
$C_5H_7O_7$	241.007544	$C_7H_8O_6$	250.020454
$C_5H_8O_7$	242.015369	$C_7H_8O_7$	266.015369
$C_5H_8O_8$	258.010284	$C_7H_8O_8$	282.010284
$C_5H_8O_9$	274.005198	$C_7H_9O_4$	219.03845
$C_5H_9O_8$	259.018109	$C_7H_9O_7$	267.023194
$C_5H_9O_9$	275.013023	$C_8H_8O_6$	262.020454
$C_5H_{10}O_7$	244.031019	$C_8H_8O_7$	278.015369
$C_5H_{10}O_8$	260.025934	$C_8H_{10}O_4$	232.046275
$C_5H_{10}O_9$	276.020848	$C_8H_{10}O_5$	248.04119
$C_6H_6O_5$	220.00989	$C_8H_{10}O_6$	264.036104
$C_6H_6O_7$	251.999719	$C_8H_{10}O_7$	280.031019
$C_6H_7NO_7$	267.010618	$C_8H_{10}O_8$	296.025934
$C_6H_7O_7$	253.007544	$C_8H_{11}O_7$	281.038844
$C_6H_8O_5$	222.02554	$C_8H_{12}O_4$	234.061925
$C_6H_8O_6$	238.020454	$C_8H_{12}O_5$	250.05684
$C_6H_8O_7$	254.015369	$C_8H_{12}O_6$	266.051755
$C_6H_9O_7$	255.023194	$C_8H_{12}O_7$	282.046669
$C_6H_{10}O_5$	224.04119	$C_8H_{12}O_8$	298.041584
$C_6H_{10}O_6$	240.036104	$C_8H_{14}O_7$	284.062319
$C_6H_{10}O_7$	256.031019	$C_8H_{14}O_8$	300.057234
$C_6H_{11}NO_6$	255.047003	$C_9H_{10}O_7$	292.031019
$C_6H_{12}O_6$	242.051755	$C_9H_{11}O_6$	277.043929
$C_7H_{10}O_4$	220.046275	$C_9H_{11}O_7$	293.038844
$C_7H_{10}O_5$	236.04119	$C_9H_{12}O_5$	262.05684
$C_7H_{10}O_6$	252.036104	$C_9H_{12}O_6$	278.051755
$C_7H_{10}O_7$	268.031019	$C_9H_{12}O_7$	294.046669
$C_7H_{10}O_8$	284.025934	$C_9H_{13}O_6$	279.05958

Table A.10: Peaklist from α-pinene OH oxidation in the presence of Isoprene (Continued).

Molecule	Detected Mass (Th)	Molecule	Detected Mass (Th)
$C_9H_{13}O_8$	311.049409	$C_{10}H_{16}O_{12}$	390.052542
$C_9H_{13}O_9$	327.044323	$C_{10}H_{17}O_{10}$	359.070538
$C_9H_{14}O_4$	248.077575	$C_{10}H_{17}O_{13}$	407.055282
$C_9H_{14}O_5$	264.07249	$C_{10}H_{17}O_{14}$	423.050197
$C_9H_{14}O_6$	280.067405	$C_{10}H_{18}O_6$	296.098705
$C_9H_{14}O_7$	296.062319	$C_{10}H_{18}O_7$	312.093619
$C_9H_{14}O_8$	312.057234	$C_{10}H_{18}O_8$	328.088534
$C_9H_{14}O_9$	328.052148	$C_{10}H_{18}O_9$	344.083449
$C_9H_{14}O_{10}$	344.047063	$C_{10}H_{18}O_{10}$	360.078363
$C_9H_{16}O_6$	282.083055	$C_{10}H_{18}O_{11}$	376.073278
$C_9H_{16}O_7$	298.077969	$C_{10}H_{18}O_{12}$	392.068192
$C_{10}H_{12}O_5$	274.05684	$C_{10}H_{18}O_{13}$	408.063107
$C_{10}H_{14}O_6$	292.067405	$C_{10}H_{18}O_{14}$	424.058022
$C_{10}H_{14}O_7$	308.062319	$C_{11}H_{16}O_{12}$	402.052542
$C_{10}H_{14}O_8$	324.057234	$C_{11}H_{16}O_{13}$	418.047457
$C_{10}H_{14}O_9$	340.052148	$C_{12}H_{18}O_{10}$	384.078363
$C_{10}H_{14}O_{10}$	356.047063	$C_{12}H_{18}O_{11}$	400.073278
$C_{10}H_{14}O_{11}$	372.041978	$C_{12}H_{18}O_{12}$	416.068192
$C_{10}H_{14}O_{12}$	388.036892	$C_{12}H_{18}O_{13}$	432.063107
$C_{10}H_{14}O_{14}$	420.026722	$C_{12}H_{20}O_{12}$	418.083842
$C_{10}H_{15}O_6$	293.07523	$C_{13}H_{16}O_{10}$	394.062713
$C_{10}H_{15}O_7$	309.070144	$C_{13}H_{20}O_{10}$	398.094013
$C_{10}H_{15}O_8$	325.065059	$C_{13}H_{20}O_{11}$	414.088928
$C_{10}H_{15}O_9$	341.059973	$C_{13}H_{20}O_{12}$	430.083842
$C_{10}H_{15}O_{10}$	357.054888	$C_{13}H_{26}O_{10}$	404.140963
$C_{10}H_{15}O_{11}$	373.049803	$C_{14}H_{20}O_9$	394.099099
$C_{10}H_{15}O_{13}$	405.039632	$C_{14}H_{20}O_{10}$	410.094013
$C_{10}H_{16}O_4$	262.093225	$C_{14}H_{20}O_{11}$	426.088928
$C_{10}H_{16}O_5$	278.08814	$C_{14}H_{20}O_{12}$	442.083842
$C_{10}H_{16}O_6$	294.083055	$C_{14}H_{20}O_{15}$	490.068586
$C_{10}H_{16}O_7$	310.077969	$C_{14}H_{22}O_8$	380.119834
$C_{10}H_{16}O_8$	326.072884	$C_{14}H_{22}O_9$	396.114749
$C_{10}H_{16}O_9$	342.067798	$C_{14}H_{22}O_{10}$	412.109663
$C_{10}H_{16}O_{10}$	358.062713	$C_{14}H_{22}O_{11}$	428.104578
$C_{10}H_{16}O_{11}$	374.057628	$C_{14}H_{22}O_{12}$	444.099493

Table A.11: Peaklist from α-pinene OH oxidation in the presence of Isoprene (Continued).

Molecule	Detected Mass (Th)	Molecule	Detected Mass (Th)
$C_{14}H_{22}O_{13}$	460.094407	$C_{16}H_{28}O_{9}$	426.161699
$C_{14}H_{24}O_{12}$	446.115143	$C_{17}H_{22}O_{8}$	416.119834
$C_{14}H_{26}O_{9}$	400.146049	$C_{17}H_{22}O_{9}$	432.114749
$C_{15}H_{18}O_{10}$	420.078363	$C_{17}H_{22}O_{10}$	448.109663
$C_{15}H_{20}O_{10}$	422.094013	$C_{17}H_{24}O_{8}$	418.135484
$C_{15}H_{21}O_{9}$	407.106924	$C_{17}H_{24}O_{9}$	434.130399
$C_{15}H_{21}O_{10}$	423.101838	$C_{17}H_{24}O_{10}$	450.125313
$C_{15}H_{22}O_{9}$	408.114749	$C_{17}H_{24}O_{11}$	466.120228
$C_{15}H_{22}O_{10}$	424.109663	$C_{17}H_{24}O_{12}$	482.115143
$C_{15}H_{22}O_{11}$	440.104578	$C_{17}H_{24}O_{13}$	498.110057
$C_{15}H_{22}O_{12}$	456.099493	$C_{17}H_{24}O_{14}$	514.104972
$C_{15}H_{22}O_{13}$	472.094407	$C_{17}H_{26}O_{8}$	420.151134
$C_{15}H_{23}O_{11}$	441.112403	$C_{17}H_{26}O_{9}$	436.146049
$C_{15}H_{24}O_{8}$	394.135484	$C_{17}H_{26}O_{10}$	452.140963
$C_{15}H_{24}O_{9}$	410.130399	$C_{17}H_{26}O_{11}$	468.135878
$C_{15}H_{24}O_{10}$	426.125313	$C_{17}H_{26}O_{12}$	484.130793
$C_{15}H_{24}O_{11}$	442.120228	$C_{17}H_{26}O_{13}$	500.125707
$C_{15}H_{24}O_{12}$	458.115143	$C_{17}H_{26}O_{14}$	516.120622
$C_{15}H_{24}O_{14}$	490.104972	$C_{17}H_{26}O_{15}$	532.115537
$C_{15}H_{24}O_{15}$	506.099886	$C_{17}H_{26}O_{16}$	548.110451
$C_{15}H_{26}O_{8}$	396.151134	$C_{17}H_{28}O_{12}$	486.146443
$C_{15}H_{26}O_{10}$	428.140963	$C_{18}H_{24}O_{6}$	398.145655
$C_{15}H_{26}O_{11}$	444.135878	$C_{18}H_{24}O_{7}$	414.140569
$C_{15}H_{26}O_{13}$	476.125707	$C_{18}H_{24}O_{8}$	430.135484
$C_{15}H_{26}O_{14}$	492.120622	$C_{18}H_{26}O_{8}$	432.151134
$C_{16}H_{20}O_{8}$	402.104184	$C_{18}H_{26}O_{10}$	464.140963
$C_{16}H_{22}O_{10}$	436.109663	$C_{18}H_{26}O_{11}$	480.135878
$C_{16}H_{24}O_{8}$	406.135484	$C_{18}H_{26}O_{12}$	496.130793
$C_{16}H_{24}O_{9}$	422.130399	$C_{18}H_{26}O_{13}$	512.125707
$C_{16}H_{24}O_{10}$	438.125313	$C_{18}H_{28}O_{8}$	434.166784
$C_{16}H_{24}O_{11}$	454.120228	$C_{18}H_{28}O_{9}$	450.161699
$C_{16}H_{24}O_{12}$	470.115143	$C_{18}H_{28}O_{12}$	498.146443
$C_{16}H_{24}O_{13}$	486.110057	$C_{18}H_{28}O_{13}$	514.141357
$C_{16}H_{26}O_{11}$	456.135878	$C_{18}H_{28}O_{14}$	530.136272
$C_{16}H_{26}O_{12}$	472.130793	$C_{18}H_{28}O_{15}$	546.131187

Table A.12: Peaklist from α-pinene OH oxidation in the presence of Isoprene (Continued).

Molecule	Detected Mass (Th)	Molecule	Detected Mass (Th)
$C_{18}H_{28}O_{16}$	562.126101	$C_{20}H_{28}O_{17}$	602.121016
$C_{18}H_{30}O_{11}$	484.167178	$C_{20}H_{29}O_{12}$	523.154268
$C_{18}H_{30}O_{12}$	500.162093	$C_{20}H_{29}O_{13}$	539.149182
$C_{19}H_{26}O_{6}$	412.161305	$C_{20}H_{29}O_{14}$	555.144097
$C_{19}H_{26}O_{9}$	460.146049	$C_{20}H_{29}O_{15}$	571.139012
$C_{19}H_{26}O_{12}$	508.130793	$C_{20}H_{29}O_{16}$	587.133926
$C_{19}H_{26}O_{15}$	556.115537	$C_{20}H_{29}O_{17}$	603.128841
$C_{19}H_{28}O_{8}$	446.166784	$C_{20}H_{30}O_{8}$	460.182434
$C_{19}H_{28}O_{9}$	462.161699	$C_{20}H_{30}O_{9}$	476.177349
$C_{19}H_{28}O_{10}$	478.156613	$C_{20}H_{30}O_{10}$	492.172264
$C_{19}H_{28}O_{11}$	494.151528	$C_{20}H_{30}O_{11}$	508.167178
$C_{19}H_{28}O_{12}$	510.146443	$C_{20}H_{30}O_{12}$	524.162093
$C_{19}H_{28}O_{13}$	526.141357	$C_{20}H_{30}O_{13}$	540.157007
$C_{19}H_{28}O_{14}$	542.136272	$C_{20}H_{30}O_{14}$	556.151922
$C_{19}H_{28}O_{15}$	558.131187	$C_{20}H_{30}O_{15}$	572.146837
$C_{19}H_{28}O_{16}$	574.126101	$C_{20}H_{30}O_{16}$	588.141751
$C_{19}H_{30}O_{8}$	448.182434	$C_{20}H_{30}O_{17}$	604.136666
$C_{19}H_{30}O_{9}$	464.177349	$C_{20}H_{32}O_{6}$	430.208255
$C_{19}H_{30}O_{10}$	480.172264	$C_{20}H_{32}O_{8}$	462.198084
$C_{19}H_{30}O_{11}$	496.167178	$C_{20}H_{32}O_{9}$	478.192999
$C_{19}H_{30}O_{12}$	512.162093	$C_{20}H_{32}O_{10}$	494.187914
$C_{19}H_{30}O_{13}$	528.157007	$C_{20}H_{32}O_{11}$	510.182828
$C_{19}H_{30}O_{14}$	544.151922	$C_{20}H_{32}O_{12}$	526.177743
$C_{19}H_{30}O_{15}$	560.146837	$C_{20}H_{32}O_{13}$	542.172657
$C_{19}H_{30}O_{16}$	576.141751	$C_{20}H_{32}O_{14}$	558.167572
$C_{19}H_{32}O_{10}$	482.187914	$C_{20}H_{32}O_{15}$	574.162487
$C_{20}H_{28}O_{11}$	506.151528	$C_{20}H_{32}O_{16}$	590.157401
$C_{20}H_{28}O_{12}$	522.146443	$C_{20}H_{32}O_{17}$	606.152316
$C_{20}H_{28}O_{13}$	538.141357	$C_{20}H_{34}O_{8}$	464.213734
$C_{20}H_{28}O_{14}$	554.136272	$C_{20}H_{34}O_{9}$	480.208649
$C_{20}H_{28}O_{15}$	570.131187	$C_{20}H_{34}O_{10}$	496.203564
$C_{20}H_{28}O_{16}$	586.126101		

Table A.13: Peaklist from α-pinene OH oxidation in the presence of NOx.

Molecule	Detected Mass (Th)	Molecule	Detected Mass (Th)
$C_3H_5NO_7$	229.992003	$C_6H_7O_{11}$	317.984237
$C_4H_4O_7$	226.981104	$C_6H_8O_5$	223.022575
$C_4H_5NO_6$	225.997088	$C_6H_8O_6$	239.017489
$C_4H_5NO_7$	241.992003	$C_6H_8O_7$	255.012404
$C_4H_5O_7$	227.988929	$C_6H_8O_9$	287.002233
$C_4H_6NO_7$	242.999828	$C_6H_8O_{10}$	302.997148
$C_4H_6O_7$	228.996754	$C_6H_8O_{11}$	318.992062
$C_4H_7NO_6$	228.012738	$C_6H_8O_{12}$	334.986977
$C_4H_7O_{10}$	277.989323	$C_6H_9NO_{13}$	365.992791
$C_4H_8NO_6$	229.020563	$C_6H_9NO_6$	254.028388
$C_5H_5NO_7$	253.992003	$C_6H_9O_{11}$	319.999887
$C_5H_5NO_9$	285.981832	$C_6H_9O_{12}$	335.994802
$C_5H_5O_8$	255.983843	$C_6H_{10}O_{11}$	321.007712
$C_5H_6O_5$	209.006925	$C_6H_{10}O_{12}$	337.002627
$C_5H_6O_6$	225.001839	$C_6H_{10}O_4$	209.04331
$C_5H_6O_7$	240.996754	$C_6H_{10}O_5$	225.038225
$C_5H_7NO_6$	240.012738	$C_6H_{11}NO_{10}$	320.023697
$C_5H_7NO_7$	256.007653	$C_6H_{11}NO_6$	256.044038
$C_5H_7NO_8$	272.002568	$C_6H_{11}NO_7$	272.038953
$C_5H_7NO_9$	287.997482	$C_6H_{11}O_{10}$	306.020623
$C_5H_7O_{10}$	289.989323	$C_6H_{12}O_{10}$	307.028448
$C_5H_7O_{11}$	305.984237	$C_6H_{13}NO_7$	274.054603
$C_5H_7O_9$	273.994408	$C_7H_{10}O_4$	221.04331
$C_5H_8NO_7$	257.015478	$C_7H_{10}O_5$	237.038225
$C_5H_8O_{11}$	306.992062	$C_7H_{10}O_6$	253.033139
$C_5H_9NO_6$	242.028388	$C_7H_{10}O_7$	269.028054
$C_5H_9O_{10}$	292.004973	$C_7H_{10}O_8$	285.022969
$C_5H_9O_9$	276.010058	$C_7H_{10}O_9$	301.017883
$C_6H_6O_5$	221.006925	$C_7H_{10}O_{10}$	317.012798
$C_6H_6O_6$	237.001839	$C_7H_{10}O_{12}$	349.002627
$C_6H_6O_7$	252.996754	$C_7H_{11}NO_6$	268.044038
$C_6H_6O_9$	284.986583	$C_7H_{11}NO_7$	284.038953
$C_6H_7NO_8$	284.002568	$C_7H_{11}O_7$	270.035879
$C_6H_7O_8$	269.999494	$C_7H_{11}O_8$	286.030794
$C_6H_7O_{10}$	301.989323	$C_7H_{11}O_9$	302.025708

Table A.14: Peaklist from α-pinene OH oxidation in the presence of NOx (Continued).

Molecule	Detected Mass (Th)	Molecule	Detected Mass (Th)
$C_7H_{11}O_{10}$	318.020623	$C_7H_{13}O_{11}$	336.031188
$C_7H_{11}O_{11}$	334.015538	$C_7H_{14}O_{10}$	321.044098
$C_7H_{11}O_{13}$	366.005367	$C_8H_9NO_6$	278.028388
$C_7H_{12}O_4$	223.05896	$C_8H_9O_{10}$	328.004973
$C_7H_{12}O_5$	239.053875	$C_8H_{10}O_4$	233.04331
$C_7H_{12}O_6$	255.048789	$C_8H_{10}O_5$	249.038225
$C_7H_{12}O_7$	271.043704	$C_8H_{10}O_6$	265.033139
$C_7H_{12}O_8$	287.038619	$C_8H_{10}O_7$	281.028054
$C_7H_{12}O_9$	303.033533	$C_8H_{10}O_8$	297.022969
$C_7H_{12}O_{10}$	319.028448	$C_8H_{10}O_9$	313.017883
$C_7H_{12}O_{11}$	335.023363	$C_8H_{10}O_{11}$	345.007712
$C_7H_6O_7$	264.996754	$C_8H_{10}O_{12}$	361.002627
$C_7H_7NO_4$	232.022909	$C_8H_{11}NO_6$	280.044038
$C_7H_7NO_6$	264.012738	$C_8H_{11}NO_7$	296.038953
$C_7H_7NO_7$	280.007653	$C_8H_{11}NO_{10}$	344.023697
$C_7H_7NO_8$	296.002568	$C_8H_{11}NO_{11}$	360.018612
$C_7H_7O_8$	281.999494	$C_8H_{11}NO_{12}$	376.013526
$C_7H_8O_5$	235.022575	$C_8H_{11}NO_{13}$	392.008441
$C_7H_8O_6$	251.017489	$C_8H_{12}O_4$	235.05896
$C_7H_8O_7$	267.012404	$C_8H_{12}O_5$	251.053875
$C_7H_8O_9$	299.002233	$C_8H_{12}O_6$	267.048789
$C_7H_8O_{10}$	314.997148	$C_8H_{12}O_8$	299.038619
$C_7H_8O_{11}$	330.992062	$C_8H_{12}O_9$	315.033533
$C_7H_8O_{12}$	346.986977	$C_8H_{11}O_{12}$	362.010452
$C_7H_9NO_6$	266.028388	$C_8H_{11}O_{13}$	378.005367
$C_7H_9NO_7$	282.023303	$C_8H_{11}O_{14}$	394.000281
$C_7H_9NO_8$	298.018218	$C_8H_{11}O_{15}$	409.995196
$C_7H_9NO_9$	314.013132	$C_8H_{12}O_{10}$	331.028448
$C_7H_9NO_{10}$	330.008047	$C_8H_{12}O_{11}$	347.023363
$C_7H_9NO_{11}$	346.002961	$C_8H_{12}O_{12}$	363.018277
$C_7H_9O_6$	252.025314	$C_8H_{12}O_{13}$	379.013192
$C_7H_9O_7$	268.020229	$C_8H_{12}O_{14}$	395.008106
$C_7H_9O_9$	300.010058	$C_8H_{13}NO_6$	282.059688
$C_7H_9O_{10}$	316.004973	$C_8H_{13}NO_8$	314.049518
$C_7H_9O_{12}$	347.994802	$C_8H_{13}NO_9$	330.044432

Table A.15: Peaklist from α-pinene OH oxidation in the presence of NOx (Continued).

Molecule	Detected Mass (Th)	Molecule	Detected Mass (Th)
$C_8H_{13}NO_{10}$	346.039347	$C_9H_{13}NO_{14}$	422.019005
$C_8H_{13}O_8$	300.046444	$C_9H_{13}O_5$	264.0617
$C_8H_{13}O_9$	316.041358	$C_9H_{13}O_9$	328.041358
$C_8H_{13}O_{10}$	332.036273	$C_9H_{13}O_{15}$	424.010846
$C_8H_{13}O_{11}$	348.031188	$C_9H_{14}O_5$	265.069525
$C_8H_{13}O_{12}$	364.026102	$C_9H_{14}O_6$	281.06444
$C_8H_{13}O_{13}$	380.021017	$C_9H_{14}O_7$	297.059354
$C_8H_{13}O_{14}$	396.015931	$C_9H_{14}O_8$	313.054269
$C_8H_{14}O_7$	285.059354	$C_9H_{14}O_9$	329.049183
$C_8H_{14}O_8$	301.054269	$C_9H_{14}O_{10}$	345.044098
$C_8H_{14}O_9$	317.049183	$C_9H_{14}O_{11}$	361.039013
$C_8H_{14}O_{11}$	349.039013	$C_9H_{15}NO_5$	280.080424
$C_8H_{14}O_{12}$	365.033927	$C_9H_{15}NO_6$	296.075339
$C_8H_{14}O_{13}$	381.028842	$C_9H_{15}NO_9$	344.060082
$C_8H_{15}O_8$	302.062094	$C_9H_{15}NO_{10}$	360.054997
$C_8H_{15}O_{14}$	398.031581	$C_9H_{15}NO_{13}$	408.039741
$C_8H_{16}O_8$	303.069919	$C_9H_{15}O_5$	266.07735
$C_8H_{16}O_{10}$	335.059748	$C_9H_{15}O_7$	298.067179
$C_8H_{16}O_{13}$	383.044492	$C_9H_{15}O_{12}$	378.041752
$C_9H_{10}O_7$	293.028054	$C_9H_{15}O_{13}$	394.036667
$C_9H_{11}NO_8$	324.033868	$C_9H_{15}O_{14}$	410.031581
$C_9H_{11}O_7$	294.035879	$C_9H_{16}O_7$	299.075004
$C_9H_{11}O_8$	310.030794	$C_9H_{16}O_8$	315.069919
$C_9H_{11}O_{11}$	358.015538	$C_9H_{16}O_9$	331.064833
$C_9H_{12}O_4$	247.05896	$C_9H_{16}O_{10}$	347.059748
$C_9H_{12}O_5$	263.053875	$C_9H_{16}O_{12}$	379.049577
$C_9H_{12}O_6$	279.048789	$C_9H_{16}O_{13}$	395.044492
$C_9H_{12}O_7$	295.043704	$C_9H_{16}O_{14}$	411.039407
$C_9H_{12}O_8$	311.038619	$C_9H_{18}O_{14}$	413.055057
$C_9H_{12}O_9$	327.033533	$C_{10}H_{10}O_4$	257.04331
$C_9H_{12}O_{10}$	343.028448	$C_{10}H_{12}O_7$	307.043704
$C_9H_{12}O_{14}$	407.008106	$C_{10}H_{12}O_8$	323.038619
$C_9H_{13}NO_5$	278.064774	$C_{10}H_{12}O_9$	339.033533
$C_9H_{13}NO_8$	326.049518	$C_{10}H_{12}O_{10}$	355.028448
$C_9H_{13}NO_9$	342.044432	$C_{10}H_{12}O_{11}$	371.023363

Table A.16: Peaklist from α-pinene OH oxidation in the presence of NOx (Continued).

Molecule	Detected Mass (Th)	Molecule	Detected Mass (Th)
$C_{10}H_{13}NO_7$	322.054603	$C_{10}H_{15}O_{12}$	390.041752
$C_{10}H_{13}NO_8$	338.049518	$C_{10}H_{16}O_4$	263.09026
$C_{10}H_{13}NO_9$	354.044432	$C_{10}H_{16}O_5$	279.085175
$C_{10}H_{13}NO_{10}$	370.039347	$C_{10}H_{16}O_6$	295.08009
$C_{10}H_{13}NO_{11}$	386.034262	$C_{10}H_{16}O_7$	311.075004
$C_{10}H_{13}NO_{12}$	402.029176	$C_{10}H_{16}O_8$	327.069919
$C_{10}H_{13}O_6$	292.056614	$C_{10}H_{16}O_9$	343.064833
$C_{10}H_{13}O_7$	308.051529	$C_{10}H_{16}O_{10}$	359.059748
$C_{10}H_{14}O_5$	277.069525	$C_{10}H_{16}O_{11}$	375.054663
$C_{10}H_{14}O_6$	293.06444	$C_{10}H_{16}O_{12}$	391.049577
$C_{10}H_{14}O_7$	309.059354	$C_{10}H_{16}O_{13}$	407.044492
$C_{10}H_{14}O_8$	325.054269	$C_{10}H_{16}O_{14}$	423.039407
$C_{10}H_{14}O_9$	341.049183	$C_{10}H_{16}O_{15}$	439.034321
$C_{10}H_{14}O_{10}$	357.044098	$C_{10}H_{17}NO_7$	326.085903
$C_{10}H_{14}O_{11}$	373.039013	$C_{10}H_{17}NO_8$	342.080818
$C_{10}H_{14}O_{12}$	389.033927	$C_{10}H_{17}NO_{11}$	390.065562
$C_{10}H_{14}O_{13}$	405.028842	$C_{10}H_{17}NO_{12}$	406.060476
$C_{10}H_{14}O_{14}$	421.023756	$C_{10}H_{17}NO_{13}$	422.055391
$C_{10}H_{15}NO_6$	308.075339	$C_{10}H_{17}NO_{14}$	438.050306
$C_{10}H_{15}NO_7$	324.070253	$C_{10}H_{17}NO_{15}$	454.04522
$C_{10}H_{15}NO_8$	340.065168	$C_{10}H_{17}O_7$	312.082829
$C_{10}H_{15}NO_9$	356.060082	$C_{10}H_{17}O_8$	328.077744
$C_{10}H_{15}NO_{10}$	372.054997	$C_{10}H_{17}O_{11}$	376.062488
$C_{10}H_{15}NO_{11}$	388.049912	$C_{10}H_{17}O_{12}$	392.057402
$C_{10}H_{15}NO_{12}$	404.044826	$C_{10}H_{17}O_{14}$	424.047232
$C_{10}H_{15}NO_{13}$	420.039741	$C_{10}H_{17}O_{15}$	440.042146
$C_{10}H_{15}NO_{14}$	436.034655	$C_{10}H_{17}O_{16}$	456.037061
$C_{10}H_{15}NO_{15}$	452.02957	$C_{10}H_{18}O_8$	329.085569
$C_{10}H_{15}NO_{16}$	468.024485	$C_{10}H_{18}O_9$	345.080483
$C_{10}H_{15}O_6$	294.072265	$C_{10}H_{18}O_{10}$	361.075398
$C_{10}H_{15}O_7$	310.067179	$C_{10}H_{18}O_{11}$	377.070313
$C_{10}H_{15}O_8$	326.062094	$C_{10}H_{18}O_{12}$	393.065227
$C_{10}H_{15}O_9$	342.057008	$C_{10}H_{18}O_{13}$	409.060142
$C_{10}H_{15}O_{10}$	358.051923	$C_{11}H_{13}O_{10}$	368.036273
$C_{10}H_{15}O_{11}$	374.046838	$C_{11}H_{13}O_{11}$	384.031188

Table A.17: Peaklist from α-pinene OH oxidation in the presence of NOx (Continued).

Molecule	Detected Mass (Th)	Molecule	Detected Mass (Th)
$C_{11}H_{13}O_{12}$	400.026102	$C_{12}H_{18}O_9$	369.080483
$C_{11}H_{14}O_8$	337.054269	$C_{12}H_{17}O_{10}$	384.067573
$C_{11}H_{14}O_9$	353.049183	$C_{12}H_{17}O_{11}$	400.062488
$C_{11}H_{14}O_{10}$	369.044098	$C_{12}H_{17}O_{15}$	464.042146
$C_{11}H_{14}O_{11}$	385.039013	$C_{12}H_{17}O_{16}$	480.037061
$C_{11}H_{14}O_{12}$	401.033927	$C_{12}H_{17}O_{17}$	496.031975
$C_{11}H_{14}O_{13}$	417.028842	$C_{12}H_{18}O_{10}$	385.075398
$C_{11}H_{14}O_{14}$	433.023756	$C_{12}H_{18}O_{11}$	401.070313
$C_{11}H_{15}NO_{12}$	416.044826	$C_{12}H_{18}O_{12}$	417.065227
$C_{11}H_{15}NO_{13}$	432.039741	$C_{12}H_{18}O_{13}$	433.060142
$C_{11}H_{15}NO_{14}$	448.034655	$C_{12}H_{19}NO_{13}$	448.071041
$C_{11}H_{15}O_{13}$	418.036667	$C_{12}H_{20}O_{12}$	419.080877
$C_{11}H_{15}O_{14}$	434.031581	$C_{12}H_{20}O_{13}$	435.075792
$C_{11}H_{15}O_{15}$	450.026496	$C_{12}H_{20}O_{14}$	451.070707
$C_{11}H_{15}O_{16}$	466.021411	$C_{12}H_{22}O_{13}$	437.091442
$C_{11}H_{15}O_{18}$	498.01124	$C_{13}H_{17}NO_{11}$	426.065013
$C_{11}H_{16}O_8$	339.069919	$C_{13}H_{17}NO_{12}$	442.060476
$C_{11}H_{16}O_9$	355.064833	$C_{13}H_{17}O_{10}$	396.067573
$C_{11}H_{16}O_{10}$	371.059748	$C_{13}H_{17}O_{12}$	428.057402
$C_{11}H_{16}O_{13}$	419.044492	$C_{13}H_{17}O_{14}$	460.047232
$C_{11}H_{16}O_{14}$	435.039407	$C_{13}H_{18}O_8$	365.085569
$C_{11}H_{16}O_{15}$	451.034321	$C_{13}H_{18}O_9$	381.080483
$C_{11}H_{16}O_{16}$	467.029236	$C_{13}H_{18}O_{10}$	397.075398
$C_{11}H_{16}O_{17}$	483.02415	$C_{13}H_{18}O_{12}$	429.065227
$C_{12}H_{15}NO_{13}$	444.039741	$C_{13}H_{18}O_{13}$	445.060142
$C_{12}H_{15}O_9$	366.057008	$C_{13}H_{18}O_{14}$	461.055057
$C_{12}H_{15}O_{12}$	414.041752	$C_{13}H_{19}NO_{10}$	412.086297
$C_{12}H_{15}O_{13}$	430.036667	$C_{13}H_{19}O_{10}$	398.083223
$C_{12}H_{16}O_9$	367.064833	$C_{13}H_{19}O_{11}$	414.078138
$C_{12}H_{16}O_{11}$	399.054663	$C_{13}H_{19}O_{13}$	446.067967
$C_{12}H_{16}O_{12}$	415.049577	$C_{13}H_{19}O_{14}$	462.062882
$C_{12}H_{16}O_{13}$	431.044492	$C_{13}H_{19}O_{16}$	494.052711
$C_{12}H_{16}O_{16}$	479.029236	$C_{13}H_{20}O_8$	367.101219
$C_{12}H_{18}O_7$	337.090654	$C_{13}H_{20}O_9$	383.096134
$C_{12}H_{18}O_8$	353.085569	$C_{13}H_{20}O_{10}$	399.091048

Table A.18: Peaklist from α-pinene OH oxidation in the presence of NOx (Continued).

Molecule	Detected Mass (Th)	Molecule	Detected Mass (Th)
$C_{13}H_{20}O_{11}$	415.085963	$C_{15}H_{17}O_{12}$	452.057402
$C_{13}H_{20}O_{12}$	431.080877	$C_{15}H_{18}O_{9}$	405.080483
$C_{13}H_{20}O_{13}$	447.075792	$C_{15}H_{18}O_{10}$	421.075398
$C_{13}H_{23}O_{17}$	514.078926	$C_{15}H_{18}O_{13}$	469.060142
$C_{13}H_{26}O_{11}$	421.132913	$C_{15}H_{18}O_{14}$	485.055057
$C_{14}H_{17}O_{14}$	472.047232	$C_{15}H_{19}NO_{12}$	468.076126
$C_{14}H_{17}O_{15}$	488.042146	$C_{15}H_{19}O_{16}$	518.052711
$C_{14}H_{17}O_{16}$	504.037061	$C_{15}H_{19}O_{17}$	534.047625
$C_{14}H_{18}O_{14}$	473.055057	$C_{15}H_{20}O_{9}$	407.096134
$C_{14}H_{18}O_{17}$	521.0398	$C_{15}H_{20}O_{10}$	423.091048
$C_{14}H_{19}O_{13}$	458.067967	$C_{15}H_{20}O_{15}$	503.065621
$C_{14}H_{19}O_{14}$	474.062882	$C_{15}H_{20}O_{16}$	519.060536
$C_{14}H_{19}O_{15}$	490.057796	$C_{15}H_{21}NO_{12}$	470.091776
$C_{14}H_{19}O_{16}$	506.052711	$C_{15}H_{21}O_{11}$	440.093788
$C_{14}H_{19}O_{17}$	522.047625	$C_{15}H_{21}O_{12}$	456.088702
$C_{14}H_{20}O_{8}$	379.101219	$C_{15}H_{21}O_{14}$	488.078532
$C_{14}H_{20}O_{9}$	395.096134	$C_{15}H_{21}O_{15}$	504.073446
$C_{14}H_{20}O_{10}$	411.091048	$C_{15}H_{22}O_{9}$	409.111784
$C_{14}H_{20}O_{11}$	427.085963	$C_{15}H_{22}O_{10}$	425.106698
$C_{14}H_{20}O_{12}$	443.080877	$C_{15}H_{22}O_{11}$	441.101613
$C_{14}H_{20}O_{13}$	459.075792	$C_{15}H_{22}O_{12}$	457.096527
$C_{14}H_{20}O_{14}$	475.070707	$C_{15}H_{22}O_{13}$	473.091442
$C_{14}H_{21}O_{12}$	444.088702	$C_{15}H_{22}O_{14}$	489.086357
$C_{14}H_{21}O_{14}$	476.078532	$C_{15}H_{22}O_{15}$	505.081271
$C_{14}H_{21}O_{15}$	492.073446	$C_{15}H_{23}NO_{16}$	536.087085
$C_{14}H_{21}O_{16}$	508.068361	$C_{15}H_{23}O_{10}$	426.113975
$C_{14}H_{22}O_{8}$	381.116869	$C_{15}H_{23}O_{11}$	442.109438
$C_{14}H_{22}O_{9}$	397.111784	$C_{15}H_{23}O_{12}$	458.104353
$C_{14}H_{22}O_{10}$	413.106698	$C_{15}H_{23}O_{13}$	474.099267
$C_{14}H_{22}O_{11}$	429.101613	$C_{15}H_{24}O_{10}$	427.122348
$C_{14}H_{23}O_{11}$	430.109438	$C_{15}H_{24}O_{11}$	443.117263
$C_{14}H_{23}O_{17}$	526.078926	$C_{15}H_{24}O_{12}$	459.112178
$C_{14}H_{24}O_{10}$	415.122348	$C_{15}H_{24}O_{13}$	475.107092
$C_{14}H_{26}O_{11}$	433.132913	$C_{15}H_{24}O_{16}$	523.091836
$C_{15}H_{17}O_{10}$	420.067573	$C_{15}H_{25}NO_{13}$	490.117991

Table A.19: Peaklist from α-pinene OH oxidation in the presence of NOx (Continued).

Molecule	Detected Mass (Th)	Molecule	Detected Mass (Th)
$C_{15}H_{25}O_{10}$	428.130173	$C_{16}H_{25}O_{14}$	504.109832
$C_{15}H_{25}O_{12}$	460.120003	$C_{16}H_{25}O_{15}$	520.104746
$C_{15}H_{26}O_{11}$	445.132913	$C_{16}H_{26}O_{11}$	457.132913
$C_{15}H_{26}O_{12}$	461.127828	$C_{16}H_{26}O_{12}$	473.127828
$C_{15}H_{26}O_{13}$	477.122742	$C_{16}H_{26}O_{13}$	489.122742
$C_{15}H_{26}O_{16}$	525.107486	$C_{16}H_{26}O_{14}$	505.117657
$C_{15}H_{27}O_{13}$	478.130567	$C_{16}H_{26}O_{15}$	521.112571
$C_{15}H_{27}O_{17}$	542.110226	$C_{16}H_{26}O_{16}$	537.107486
$C_{15}H_{28}O_{10}$	431.153648	$C_{16}H_{26}O_{17}$	553.102401
$C_{15}H_{28}O_{13}$	479.138392	$C_{16}H_{26}O_{18}$	569.097315
$C_{16}H_{20}O_{16}$	531.060536	$C_{16}H_{27}NO_{16}$	552.118385
$C_{16}H_{21}O_{13}$	484.083617	$C_{16}H_{27}NO_{17}$	568.1133
$C_{16}H_{21}O_{14}$	500.078532	$C_{16}H_{27}O_{13}$	490.130567
$C_{16}H_{21}O_{15}$	516.073446	$C_{16}H_{28}O_{13}$	491.138392
$C_{16}H_{21}O_{16}$	532.068361	$C_{17}H_{20}O_{18}$	575.050365
$C_{16}H_{22}O_{11}$	453.101613	$C_{17}H_{21}O_{15}$	528.073446
$C_{16}H_{22}O_{14}$	501.086357	$C_{17}H_{21}O_{17}$	560.063276
$C_{16}H_{22}O_{16}$	533.076186	$C_{17}H_{22}O_{10}$	449.106698
$C_{16}H_{23}O_{13}$	486.099267	$C_{17}H_{22}O_{11}$	465.101613
$C_{16}H_{23}O_{14}$	502.094182	$C_{17}H_{22}O_{13}$	497.091442
$C_{16}H_{23}O_{17}$	550.078926	$C_{17}H_{23}NO_{13}$	512.102341
$C_{16}H_{24}O_{9}$	423.127434	$C_{17}H_{23}NO_{15}$	544.09217
$C_{16}H_{24}O_{10}$	439.122348	$C_{17}H_{23}O_{11}$	466.109438
$C_{16}H_{24}O_{11}$	455.117263	$C_{17}H_{23}O_{12}$	482.104353
$C_{16}H_{24}O_{12}$	471.112178	$C_{17}H_{23}O_{13}$	498.099267
$C_{16}H_{24}O_{13}$	487.107092	$C_{17}H_{23}O_{15}$	530.089096
$C_{16}H_{24}O_{14}$	503.102007	$C_{17}H_{23}O_{16}$	546.084011
$C_{16}H_{24}O_{15}$	519.096921	$C_{17}H_{23}O_{17}$	562.078926
$C_{16}H_{24}O_{16}$	535.091836	$C_{17}H_{23}O_{18}$	578.07384
$C_{16}H_{24}O_{17}$	551.086751	$C_{17}H_{24}O_{10}$	451.122348
$C_{16}H_{25}NO_{10}$	454.133247	$C_{17}H_{24}O_{11}$	467.117263
$C_{16}H_{25}NO_{17}$	566.09765	$C_{17}H_{24}O_{12}$	483.112178
$C_{16}H_{25}O_{11}$	456.125088	$C_{17}H_{24}O_{13}$	499.107092
$C_{16}H_{25}O_{12}$	472.120003	$C_{17}H_{24}O_{14}$	515.102007
$C_{16}H_{25}O_{13}$	488.114917	$C_{17}H_{24}O_{16}$	547.091836

Table A.20: Peaklist from α-pinene OH oxidation in the presence of NOx (Continued).

Molecule	Detected Mass (Th)	Molecule	Detected Mass (Th)
$C_{17}H_{24}O_9$	435.127434	$C_{18}H_{25}NO_{19}$	622.087479
$C_{17}H_{24}O_{17}$	563.086751	$C_{18}H_{25}NO_{20}$	638.082394
$C_{17}H_{24}O_{18}$	579.081665	$C_{18}H_{25}O_{12}$	496.120003
$C_{17}H_{25}O_{10}$	452.130173	$C_{18}H_{25}O_{14}$	528.109832
$C_{17}H_{25}O_{11}$	468.125088	$C_{18}H_{25}O_{16}$	560.099661
$C_{17}H_{25}O_{14}$	516.109832	$C_{18}H_{25}O_{17}$	576.094576
$C_{17}H_{25}O_{15}$	532.104746	$C_{18}H_{25}O_{18}$	592.08949
$C_{17}H_{25}O_{16}$	548.099661	$C_{18}H_{26}O_{11}$	481.132913
$C_{17}H_{25}O_{17}$	564.094576	$C_{18}H_{26}O_{13}$	513.122742
$C_{17}H_{25}O_{18}$	580.08949	$C_{18}H_{26}O_{14}$	529.117657
$C_{17}H_{26}O_9$	437.143084	$C_{18}H_{26}O_{15}$	545.112571
$C_{17}H_{26}O_{10}$	453.137998	$C_{18}H_{26}O_{16}$	561.107486
$C_{17}H_{26}O_{11}$	469.132913	$C_{18}H_{26}O_{17}$	577.102401
$C_{17}H_{26}O_{12}$	485.127828	$C_{18}H_{27}NO_{19}$	624.103129
$C_{17}H_{26}O_{13}$	501.122742	$C_{18}H_{27}O_9$	450.150909
$C_{17}H_{26}O_{14}$	517.117657	$C_{18}H_{27}O_{11}$	482.140738
$C_{17}H_{26}O_{15}$	533.112571	$C_{18}H_{27}O_{13}$	514.130567
$C_{17}H_{26}O_{16}$	549.107486	$C_{18}H_{27}O_{14}$	530.125482
$C_{17}H_{26}O_{17}$	565.102401	$C_{18}H_{27}O_{15}$	546.120396
$C_{17}H_{26}O_{18}$	581.097315	$C_{18}H_{27}O_{17}$	578.110226
$C_{17}H_{27}O_{11}$	470.140738	$C_{18}H_{28}O_9$	451.158734
$C_{17}H_{27}O_{12}$	486.135653	$C_{18}H_{28}O_{10}$	467.153648
$C_{17}H_{27}O_{13}$	502.130567	$C_{18}H_{28}O_{11}$	483.148563
$C_{17}H_{27}O_{14}$	518.125482	$C_{18}H_{28}O_{12}$	499.143478
$C_{17}H_{27}O_{15}$	534.120396	$C_{18}H_{28}O_{13}$	515.138392
$C_{17}H_{27}O_{16}$	550.115311	$C_{18}H_{28}O_{14}$	531.133307
$C_{17}H_{27}O_{18}$	582.10514	$C_{18}H_{28}O_{15}$	547.128222
$C_{17}H_{28}O_{12}$	487.143478	$C_{18}H_{28}O_{16}$	563.123136
$C_{17}H_{28}O_{13}$	503.138392	$C_{18}H_{28}O_{17}$	579.118051
$C_{17}H_{28}O_{14}$	519.133307	$C_{18}H_{29}NO_{15}$	562.139121
$C_{17}H_{28}O_{17}$	567.118051	$C_{18}H_{29}O_{11}$	484.156388
$C_{17}H_{28}O_{18}$	583.112965	$C_{18}H_{29}O_{12}$	500.151303
$C_{18}H_{24}O_{20}$	623.071494	$C_{18}H_{29}O_{13}$	516.146217
$C_{18}H_{25}NO_{12}$	510.123077	$C_{18}H_{30}O_{12}$	501.159128
$C_{18}H_{25}NO_{16}$	574.102735	$C_{18}H_{31}O_{12}$	502.166953

Table A.21: Peaklist from α-pinene OH oxidation in the presence of NOx (Continued).

Molecule	Detected Mass (Th)	Molecule	Detected Mass (Th)
$C_{19}H_{24}O_6$	411.14269	$C_{19}H_{29}O_{12}$	512.151303
$C_{19}H_{24}O_{12}$	507.112178	$C_{19}H_{29}O_{13}$	528.146217
$C_{19}H_{25}NO_{11}$	506.128162	$C_{19}H_{29}O_{14}$	544.141132
$C_{19}H_{25}NO_{14}$	554.112906	$C_{19}H_{29}O_{15}$	560.136047
$C_{19}H_{25}NO_{16}$	586.102735	$C_{19}H_{29}O_{16}$	576.130961
$C_{19}H_{25}NO_{18}$	618.092564	$C_{19}H_{30}O_8$	449.179469
$C_{19}H_{25}NO_{19}$	634.087479	$C_{19}H_{30}O_9$	465.174384
$C_{19}H_{25}O_8$	444.140344	$C_{19}H_{30}O_{10}$	481.169298
$C_{19}H_{26}O_7$	429.153255	$C_{19}H_{30}O_{11}$	497.164213
$C_{19}H_{26}O_{11}$	493.132913	$C_{19}H_{30}O_{12}$	513.159128
$C_{19}H_{26}O_{12}$	509.127828	$C_{19}H_{30}O_{13}$	529.154042
$C_{19}H_{26}O_{14}$	541.117657	$C_{19}H_{30}O_{14}$	545.148957
$C_{19}H_{26}O_{15}$	557.112571	$C_{19}H_{30}O_{15}$	561.143872
$C_{19}H_{26}O_{16}$	573.107486	$C_{19}H_{30}O_{16}$	577.138786
$C_{19}H_{26}O_{17}$	589.102401	$C_{19}H_{31}O_{11}$	498.172038
$C_{19}H_{27}O_8$	446.155994	$C_{19}H_{31}O_{13}$	530.161867
$C_{19}H_{27}O_9$	462.150909	$C_{19}H_{31}O_{16}$	578.146611
$C_{19}H_{27}O_{11}$	494.140738	$C_{19}H_{32}O_{15}$	563.159522
$C_{19}H_{27}O_{13}$	526.130567	$C_{20}H_{27}NO_{15}$	584.123471
$C_{19}H_{27}O_{15}$	558.120396	$C_{20}H_{27}NO_{16}$	600.118385
$C_{19}H_{28}O_8$	447.163819	$C_{20}H_{27}NO_{17}$	616.1133
$C_{19}H_{28}O_9$	463.158734	$C_{20}H_{27}NO_{18}$	632.108214
$C_{19}H_{28}O_{11}$	495.148563	$C_{20}H_{27}O_{12}$	522.135653
$C_{19}H_{28}O_{12}$	511.143478	$C_{20}H_{27}O_{13}$	538.130567
$C_{19}H_{28}O_{13}$	527.138392	$C_{20}H_{27}O_{15}$	570.120396
$C_{19}H_{28}O_{14}$	543.133307	$C_{20}H_{27}O_{17}$	602.110226
$C_{19}H_{28}O_{15}$	559.128222	$C_{20}H_{28}O_9$	475.158734
$C_{19}H_{28}O_{16}$	575.123136	$C_{20}H_{28}O_{11}$	507.148563
$C_{19}H_{28}O_{17}$	591.118051	$C_{20}H_{28}O_{12}$	523.143478
$C_{19}H_{28}O_{18}$	607.112965	$C_{20}H_{28}O_{13}$	539.138392
$C_{19}H_{28}O_{20}$	639.102795	$C_{20}H_{28}O_{14}$	555.133307
$C_{19}H_{29}NO_{16}$	590.134035	$C_{20}H_{28}O_{15}$	571.128222
$C_{19}H_{29}NO_{19}$	638.118779	$C_{20}H_{28}O_{16}$	587.123136
$C_{19}H_{29}O_8$	448.171644	$C_{20}H_{28}O_{17}$	603.118051
$C_{19}H_{29}O_{10}$	480.161473	$C_{20}H_{28}O_{18}$	619.112965

Table A.22: Peaklist from α-pinene OH oxidation in the presence of NOx (Continued).

Molecule	Detected Mass (Th)	Molecule	Detected Mass (Th)
$C_{20}H_{28}O_{19}$	635.10788	$C_{20}H_{30}O_{15}$	573.143872
$C_{20}H_{29}NO_{11}$	522.159462	$C_{20}H_{30}O_{16}$	589.138786
$C_{20}H_{29}NO_{13}$	554.149291	$C_{20}H_{30}O_{17}$	605.133701
$C_{20}H_{29}NO_{14}$	570.144206	$C_{20}H_{30}O_{18}$	621.128615
$C_{20}H_{29}NO_{15}$	586.139121	$C_{20}H_{30}O_{19}$	637.12353
$C_{20}H_{29}NO_{16}$	602.134035	$C_{20}H_{31}O_{9}$	478.182209
$C_{20}H_{29}NO_{17}$	618.12895	$C_{20}H_{31}O_{10}$	494.177124
$C_{20}H_{29}NO_{18}$	634.123864	$C_{20}H_{31}O_{11}$	510.172038
$C_{20}H_{29}O_{9}$	476.166559	$C_{20}H_{31}O_{12}$	526.166953
$C_{20}H_{29}O_{10}$	492.161473	$C_{20}H_{31}O_{13}$	542.161867
$C_{20}H_{29}O_{11}$	508.156388	$C_{20}H_{31}O_{14}$	558.156782
$C_{20}H_{29}O_{12}$	524.151303	$C_{20}H_{31}O_{15}$	574.151697
$C_{20}H_{29}O_{13}$	540.146217	$C_{20}H_{31}O_{17}$	606.141526
$C_{20}H_{29}O_{14}$	556.141132	$C_{20}H_{31}O_{18}$	622.13644
$C_{20}H_{29}O_{15}$	572.136047	$C_{20}H_{32}O_{9}$	479.190034
$C_{20}H_{29}O_{16}$	588.130961	$C_{20}H_{32}O_{10}$	495.184949
$C_{20}H_{29}O_{17}$	604.125876	$C_{20}H_{32}O_{11}$	511.179863
$C_{20}H_{29}O_{18}$	620.12079	$C_{20}H_{32}O_{12}$	527.174778
$C_{20}H_{29}O_{19}$	636.115705	$C_{20}H_{32}O_{13}$	543.169692
$C_{20}H_{30}O_{8}$	461.179469	$C_{20}H_{32}O_{14}$	559.164607
$C_{20}H_{30}O_{9}$	477.174384	$C_{20}H_{32}O_{15}$	575.159522
$C_{20}H_{30}O_{10}$	493.169298	$C_{20}H_{32}O_{16}$	591.154436
$C_{20}H_{30}O_{11}$	509.164213	$C_{20}H_{32}O_{18}$	623.144266
$C_{20}H_{30}O_{12}$	525.159128	$C_{20}H_{33}O_{10}$	496.192774
$C_{20}H_{30}O_{13}$	541.154042	$C_{20}H_{33}O_{16}$	592.162261
$C_{20}H_{30}O_{14}$	557.148957		

Appendix B

CIMS analyzer

B.1 CIMS analyzer

Figure B.1 shows how CIMS analyzer control panel looks like. The upper half which has light violet colour is for data preparation and selection. Ion names, mass per charge ratio, and date/time will be given as input so that the program can find original time series. The program generates raw, normalised, and mass weighted data based on the original time series created by Tofware. Raw data are a copy of the original time series from Tofware. normalised data are the original time series divided by the sum of reagent ions or sum of all ions depending on the option which was chosen on the right upper corner. Mass weighted data comprise time series multiplied by the molecular mass of the species they represent. Here we give an example for $C_{10}H_{16}O_7$. If C10H16O7 is the original time series from the Tofware, it will be copied under the same name into the raw folder. C10H16O7 stored in the normalised folder is the signal of the original C10H16O7 time series divided by the sum of the reagent ion or sum of all ions. C10H16O7 under the mass weighted folder is the product of C10H16O7 time series and 248.08964 Da, which is the mass of the assigned molecular formula $C_{10}H_{16}O_7$. Note that the ion names are the assigned molecular formulas and thus contain chemical information in string form.

Based on the chemical formula, each species is assigned to one of three classes, HOM-PP, HOM-ON, or HOM-RO_2. Accretion products are classified as HOM-PP since they are products of the permutation reaction of RO_2. In detail the classification is performed as follows. The first step is to find the time series of the species in the list of ion names provided by Tofware. The ion name of the species is anylsysed in terms of presence and number of C, H, O, and N atoms. If the species has an even number of hydrogen, it is classified as HOM-PP(e.g., C10H16O7). If species has an odd number of hydrogen and containing N-atom in the molecular formula, it is classified as HOM-ON (e.g., C10H15NO8). If species has an odd number of hydrogen without N-atom in the molecular formula, it is classified as HOM-RO_2 (e.g., C10H15O7).

This is simple as long as the species appeared as a cluster with NO_3^-. If the species clustered with the dimer of the reagent ion, the parity counts became the opposite. For example, $C_{10}H_{16}O_7$ clustering with dimer reagent ion had the ion name '(NO3)2_C10H17O6' given by Tofware naming system. Since the ion name already indicates a cluster with the reagent dimer

ion, it will be correctly classified as HOM-PP, despite the odd number of hydrogen in the molecular formula.
The classification of species is used further to calculate (automatically) the relative fraction of each class or the absolute sum of each classes for raw, normalised, and mass weighted signals. Data selection can be done within a mass per charge range of interest by setting boundary values. In addition, outliers can be excluded by entree in a black list. The data on the black list will be excluded from any other calculations. Furthermore, mass spectra (both unit mass and high resolution) can be averaged for a certain time period. Depending on the chosen data set in the data selection section, high resolution mass spectra or unit mass resolution spectra for the time period of interest can be displayed. In addition, high resolution stick mass spectrum can be obtained as shown in Figure B.2.

Figure B.2 shows a high resolution stick mass spectrum for the example of α-pinene OH oxidation in the presence of NOx. Each peak is colour coded according to its class membership. The plot allows for easy recognizing the importance of the classes are dominant for the experimental conditions and the time of interest.

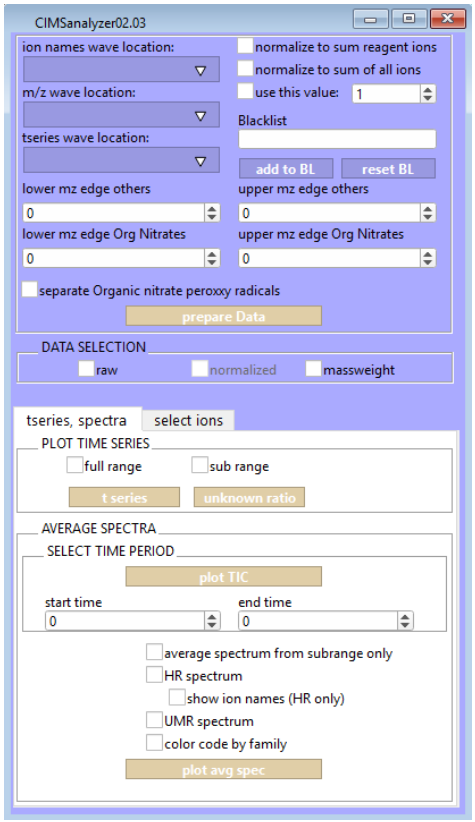

Figure B.1: CIMS analyzer panel. In upper three sections on the left, data generated by Tofware (ion name, mass per charge of ion, and date/time) can be selected as input. On the right side, one can choose different methods to generate normalised data. Outliers can be added to the blacklist and be excluded. The mass range for HOM-ON and others can be set for data selection. After the preparation of the data, time series of the sum of raw, normalised, or mass weighted data can be plotted. On the bottom, the time of interest can be selected and various types of mass spectra can be selected for plotting. (The program was written by Sebastian Schmitt.)

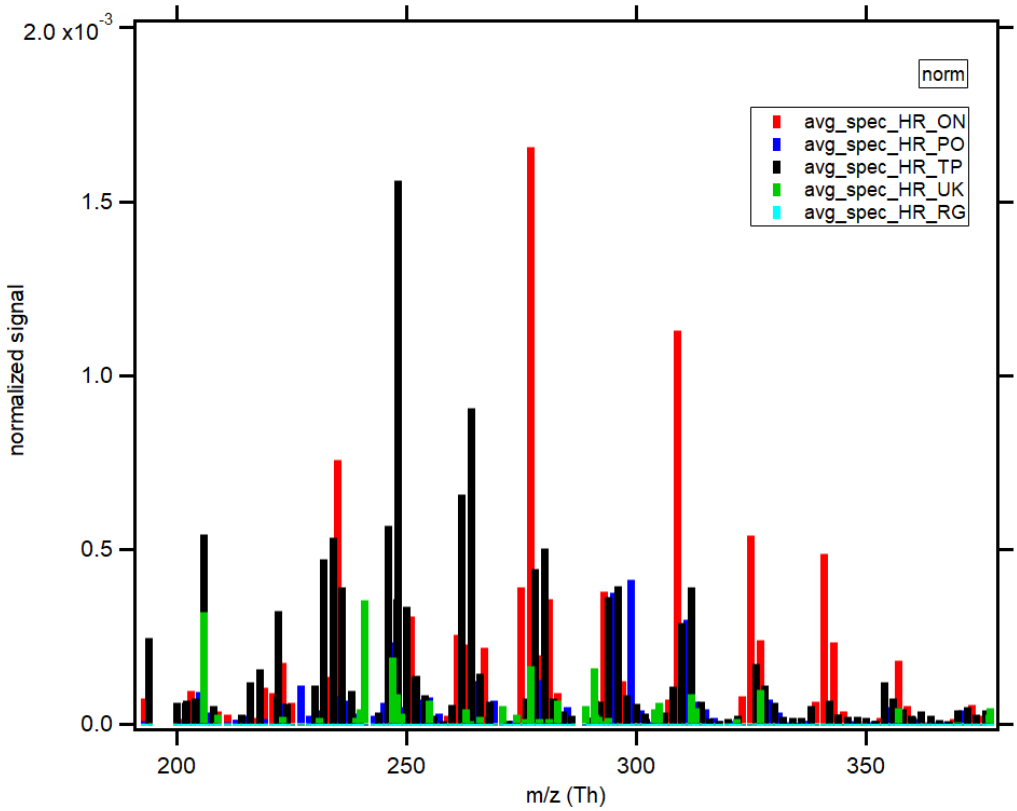

Figure B.2: The example of high resolution stick mass spectrum obtained by CIMS analyzer program. The x-axis shows mass per charge ratio and y-axis shows normalised signals. Peaks are colour coded according their class. Red(avg_spec_HR_ON) represents organic nitrates and blue(avg_spec_HR_PO) represents peroxy radicals. Black(avg_spec_HR_TP) represents permutation products i.e., HOM-PP. Green(avg_spec_HR_UK) represents unknown peaks and light blue(avg_spec_HR_RG) represents reagent ion.

Appendix C

Abbreviation

VOC Volatile Organic Compounds

BVOC Biogenic Volatile Organic Compounds

AVOC Anthropogenic Volatile Organic Compounds

OVOC Oxygenated Volatile Organic Compounds

OA Organic Aerosol

POA Primary Organic Aerosol

SOA Secondary Organic Aerosol

HOM Highly Oxygenated Organic Molecules

PAN Peroxy Acyl Nitrates

CI Criegee Intermediates

PRIP Peroxy Radical Organic Compounds

LVOC Low Volatile Organic Compounds

ELVOC Extremely Low Volatile Organic Compounds

NPF New Particle Formation

HOM-RO_2 HOM-peroxy radicals

HOM-PP HOM- Permutation Products

HOM-ON HOM-Organic Nitrates

HOM-ACC HOM-Accretion products

Band / Volume 543
Processing and creep resistance of short SiC fiber containing Ti_3SiC_2 MAX phase composites
A. Dash (2021), vii, 125 pp
ISBN: 978-3-95806-558-1

Band / Volume 544
Synthese und Charakterisierung von Geopolymeren für die Entsorgung der Spaltprodukte ^{137}Cs und ^{90}Sr
S. K. Weigelt (2021), VI, 186 pp
ISBN: 978-3-95806-559-8

Band / Volume 545
Potential depletion of ozone in the mid-latitude lowermost stratosphere in summer under geoengineering conditions
S. Robrecht (2021), 185 pp
ISBN: 978-3-95806-563-5

Band / Volume 546
Two-phase Flow in Porous Transport Layers of Polymer Electrolyte Membrane Electrolysers
D. Borah (2021), xi, 196 pp
ISBN: 978-3-95806-564-2

Band / Volume 547
Effects of root temperature on food quality of horticultural crops
F. He (2021), V, 143 pp
ISBN: 978-3-95806-565-9

Band / Volume 548
Verhalten und Kontrolle von Schlacken des bioliq®-Vergasers
K. Mielke (2021), 162, XXXV pp
ISBN: 978-3-95806-566-6

Band / Volume 549
Gravity waves resolved in Numerical Weather Prediction products
C. Strube (2021), iii, 139 pp
ISBN: 978-3-95806-567-3

Band / Volume 550
Experimental study of the chemical degradation of biogenic volatile organic compounds by atmospheric OH radicals
M. Rolletter (2021), XIII, 199 pp
ISBN: 978-3-95806-568-0

Band / Volume 551
Infiltrated Positive Electrodes for All-Solid-State Sodium Batteries
T. Lan (2021), vi, 104 pp
ISBN: 978-3-95806-576-5

Band / Volume 552
Trajectory Analysis on the Asian Tropopause Aerosol Layer (ATAL) based on Balloon Measurements at the Foothills of the Himalayas
S. Hanumanthu (2021), xiv, 147 pp
ISBN: 978-3-95806-578-9

Band / Volume 553
Field assisted sintering of yttria ceramics for plasma etching applications
M. Kindelmann (2021), VI, 122, XXX pp
ISBN: 978-3-95806-579-6

Band / Volume 554
Characterisation of the effect of redox potential on the emission of greenhouse gases using wireless sensing techniques
J. Wang (2021), XIV, 104 pp
ISBN: 978-3-95806-581-9

Band / Volume 555
Stability assessment of variably saturated hillslopes using coupled hydromechanical models
S. Moradi (2021), xxxii, 123 pp
ISBN: 978-3-95806-583-3

Band / Volume 556
Catalytic-doping of Silicon Alloys for the Use in Silicon Heterojunction Solar Cells
Y. Liu (2021), 126 pp
ISBN: 978-3-95806-591-8

Band / Volume 557
Formation of highly oxygenated organic molecules from α-pinene photochemistry
S. Kang (2021), xvii, 156 pp
ISBN: 978-3-95806-596-3

Weitere ***Schriften des Verlags im Forschungszentrum Jülich*** unter
http://wwwzb1.fz-juelich.de/verlagextern1/index.asp

Energie & Umwelt / Energy & Environment
Band / Volume 557
ISBN 978-3-95806-596-3

Mitglied der Helmholtz-Gemeinschaft

JÜLICH
Forschungszentrum